Investigation of local inhomogeneous ignition in fuel/air mixtures in a high-pressure shock tube

Von der Fakultät für Ingenieurwissenschaften, Abteilung Maschinenbau und Verfahrenstechnik

der

Universität Duisburg-Essen

zur Erlangung des akademischen Grades

eines

Doktors der Ingenieurwissenschaften

Dr.-Ing.

genehmigte Dissertation

von

Philipp Niegemann
aus
München

Gutachter: Prof. Dr. Christof Schulz
Prof. Dr. Alexander Heufer
Tag der mündlichen Prüfung: 24.09.2021

„Was einmal gedacht wurde, kann nicht mehr zurückgenommen werden“ –
Friedrich Dürrenmatt – Die Physiker (Diogenes Verlag, Neufassung 1980)

Kurzfassung

Strengere Emissionsvorschriften weltweit, gerade im Automobilmarkt, sorgte für steigende Effizienz des Verbrennungsmotors und wichtigen Entwicklungen in der Abgasnachbehandlung. Diese Zielvorgaben erfordern eine Erhöhung des Wirkungsgrades bei gleichzeitigem Einsatz erneuerbarer Energieträger wie biologischer Brennstoffe oder synthetischer Kraftstoffe. Technologisch haben die Forderungen zu zwei Trends in der Motorenauslegung geführt: Downsizing, d. h. Reduktion des Hubvolumens bei gleichbleibender Leistung und Downspeeding, d. h. Verringerung der Motordrehzahl bei gesteigertem Drehmoment. Verbunden mit diesen Änderungen der Betriebsparameter ist das Auftreten von Zündphänomenen in Otto-Motoren beobachtet worden, welche zu Detonation mit extremen Druckoszillationen und einer Schädigung des Motors führen können. Diese Zündphänomene unterscheiden sich vom klassischen Klopfen einerseits durch vielfach höhere Druckanstiege und andererseits durch ihr zufälliges Auftreten unabhängig vom Zündwinkel. Weil diese unnormale Verbrennung zufällig unter geringer Motordrehzahl und hoher Last auftritt, wird diese „Low-speed pre-ignition (LSPI)“ genannt.

Es wird vermutet, dass lokale Zündquellen wie Partikel, Schmieröltropfen oder heiße Oberflächen die Zündung im Kompressionstakt initiieren. In dieser Arbeit wurden lokale Zündungen in homogenen Gasmischungen und der Einfluss von lokalen Zündquellen wie Partikel, heiße Oberflächen und Schmieröl auf die Zündverzugszeit in einem Hochdruckstoßwellenrohr zum ersten Mal untersucht. Stoßwellenrohre vereinfachen ideal die Bedingungen in einem Motor (vernachlässigen den Einfluss von Transportprozessen), was die Untersuchung von reaktiven Kraftstoffmischungen unter konstantem Druck und Temperaturen nach nahezu instantaner Kompression erlaubt.

In einem ersten Schritt wurde die Zündverzugszeit, die Lokalität und Homogenität der Zündung des primären Referenzkraftstoffs PRF95 (95 Vol.% iso-Oktan und 5 Vol.% n-Heptan) und von Ethanol in Luft bei einem Äquivalenzverhältnis (ϕ) von 1 unter motorischen Bedingungen ($p_5 = 20$ bar, $T_5 = 750$–950 K) untersucht. Hierfür wurde das Hochdruckstoßwellenrohr mit einer optisch zugänglichen Endwand ausgestattet. Die Zündung wurde gleichzeitig von zwei Hochgeschwindigkeitskameras, eine im sichtbaren (VIS) und eine im ultravioletten (UV) Spektrum, beobachtet.

Untersuchungen der Gasphasenzündung haben gezeigt, dass abhängig vom Temperaturbereich die Zündung nicht vollständig homogen für unverdünnte Mischungen ist. Lokale Zündungen in der Nähe der Seitenwand, nahe der Endwand wie auch weit entfernt (verursacht durch heiße Partikel), wurden beobachtet. Es wurde herausgefunden, dass die heißen Membranpartikel nicht die Zündverzugszeit beeinflussen. Im Gegensatz, lokale Gasphasenzündung ergab eine Reduktion der Zündverzugszeit. Gezielte Verdünnung der reaktiven Gasmischung mit Komponenten, die entweder die Wärmekapazität oder die Wärmeleitfähigkeit der Mischung steigern, ermöglichen die Prävention lokaler Zündungen in der reinen Gasphase.

Der Einfluss definierter Inhomogenitäten auf die Selbstzündung der genannten Kraftstoff/Luft Mischungen wurde untersucht. Der Einfluss einer heißen Oberfläche auf die Zündverzugszeit wurde bestimmt durch das Einführen einer Glühkerze in die Seitenwand des Stoßwellenrohres und das damit einhergehende nicht homogene Temperaturfeld. Die nicht homogene Temperaturverteilung, hervorgerufen durch die heiße Oberfläche, führt zu lokalen Zündungen für Gastemperaturen hinter der reflektierten Stoßwelle ($T5$) unter 850 K und Oberflächentemperaturen (T_S) über 1000 K. Es wurde kein Einfluss auf die Zündverzugszeit beobachtet.

Vorherige Studien haben gezeigt, dass in Motorversuchen die Zusammensetzung des Schmieröls einen Einfluss auf die Frequenz von LSPI Ereignissen hat. Es ist unklar, ob das Schmieröl zersetzt wird und Oxidationsprodukte die lokale Zündung begünstigen oder ob Prozesse in der flüssigen

Phase des Tropfens wichtiger sind. Für die Klärung wurde das Problem in dieser Arbeit in drei Schritten untersucht.
In einem ersten Schritt wurden Schmierölproben mit thermogravimetrische Analyse (TGA) und differential scanning Kalorimetrie (DSC) in Kombination mit Quadrupol-Massenspektroskopie (QMS) analysiert. Zündverzugszeit-Messungen von PRF95/Luft Mischungen bei $\phi = 1$ mit bis zu 1000 ppm der schwefelhaltigen, potenziell begünstigenden Moleküle, zeigten keinen Effekt. Zur Nachahmung des Prozesses, in welchem Öltropfen in den Verbrennungsraum unter repräsentativen und wiederholbaren Bedingungen geschleudert werden, wurden einzelne Tropfen hinter der reflektierten Stoßwelle durch einen Zugang in der Seitenwand in das Hochdruckstoßwellenrohr eingespritzt. Die Tropfen bestanden aus n-Dodekan, Basis-Schmieröl und/oder verschiedenen einzelnen Zusätzen und/oder flüssigem PRF95. Die eingespritzten Tropfen wurden beobachtet durch Laser induzierte Fluoreszenz in Kombination mit hoch repetitiver Bildgebung. Hierfür wurde jede Probe mit 0,1 mmol/l Pyrromethene 597 dotiert. Die lokale Zündung, Ausbreitung und volumetrische Zündung wurde beobachtet und die Zündverzugszeit über der Temperatur für jede Probe bestimmt. Tropfen von n-Dodekan und Basis-Öl zugesetzt mit Anti Abrieb Zusatz, basierend auf Zink Diphosphat (ZDDP) oder Seife-Zusätzen, basierend auf Kalzium zeigten, signifikant schneller lokale Zündverzugszeiten, als die Anwesenheit von puren Basis-Öltropfen und beschleunigten die volumetrische Zündverzugszeit signifikant verglichen zu Fällen ohne Einspritzung von Tropfen.

Abstract

Stringent emission requirements around the world, particularly in the automotive market lead to increasing efficiency of internal combustion (IC) engines and major developments in the exhaust after-treatment. The set targets require an increase in efficiency with the simultaneous use of renewable energy like biomass -derived or synthetic fuels. Technologically, the requirements have led to two trends in IC engines design: Downsizing, i.e., reducing the stroke volume while maintaining the same power, and down-speeding, i.e., reducing the engine speed (RPM) while increasing the torque. The increase in power density is achieved by increasing the boost pressure and the associated temperature rise. In conjunction with these changes in operating parameters, abnormal ignition phenomena have been observed in spark ignition (SI) engines that can lead to detonation with extreme pressure oscillations and engine damage. These ignition phenomena differ from classical knock on the one hand by much higher pressure rises and on the other hand by their random occurrence independent of the ignition angle. Because this abnormal combustion occurs randomly under operation of low engine speed and high load, it is called low-speed pre-ignition (LSPI).

It is assumed that local ignition sources like particles, lubricant oil droplets or hot surfaces can initiate ignition in the compression stroke. In the present work, local ignition in homogeneous gas mixtures and the influence of local ignition sources like particles, hot surfaces and lubricant oil on the ignition delay time were investigated in a high-pressure shock tube for the first time. Shock tubes ideally simplify the conditions in an engine (approaching the influence of transport processes), which allow the investigation of reactive fuel mixtures at constant pressure and temperature after nearly instantaneous compression.

In a first step, the ignition delay time, spot and homogeneity of the ignition of the primary reference fuel PRF95 (95 vol. % isooctane and 5 vol. % n-heptane) and of ethanol in air at equivalence ratios (ϕ) of 1 was investigated under engine-like conditions ($p_5 = 20$ bar, $T_5 = 750$–950 K). Therefore, the high-pressure shock tube was equipped with an optic accessible endwall. The ignition was observed by two high-speed cameras one in the visible (VIS) and one in the ultraviolet (UV) spectrum simultaneously.

Investigations of the gas-phase ignition have shown, that depending on the temperature range, the ignition is not fully homogeneous for the undiluted mixtures. Local ignition near the wall in the vicinity of the endwall as well as upstream (caused by hot particles) were observed. The hot membrane particles were found not to influence the ignition delay time. In contrast, local gas-phase ignition resulted in a reduction of the ignition delay times. Targeted dilution of the reactive gas mixture with components that either increase the heat capacity or the thermal diffusivity of the mixture enabled the prevention of local ignition in the pure gas phase.

The influence of defined inhomogeneities on the auto-ignition of the mentioned fuel/air mixtures was analyzed. The influence of a hot surface on the ignition delay time was determined by inserting a glow plug in the sidewall of the shock tube and the associated non-uniformity of the temperature field. Non-uniform temperature distribution induced by the hot surface led to local ignition for gas temperatures behind the reflected shock wave (T_5) below 850 K and surface temperatures T_s above 1000 K. No influence on the ignition delay time was observed.

Previous studies have shown that the formulation of lubricant oil influences the frequency of LSPI events in engine experiments. It is unclear whether the lubricant oil is decomposed, and oxidation products favor the local ignition or if processes in the liquid phase of the droplet are more important. For clarification, the problem was investigated in this work in three steps.

In a first step, lubricant oil samples were analyzed by thermogravimetric analysis (TGA) and differential scanning calorimetry (DSC) in combination with quadrupole mass spectroscopy (QMS).

Ignition delay time measurements of PRF95/air mixture at $\phi = 1$ plus up to 1000 ppm of molecules identified as potential promotors containing sulfur showed no effect.
To mimic the process of oil droplets that are hurled into the combustion chamber under representative and repeatable conditions, single droplets were injected behind the reflected shock wave through a sidewall port into the high-pressure shock tube. The droplets contained n-dodecane, lubricant base oil, and/or different single additives and/or liquid PRF95. The injected droplets were observed by laser induced fluorescence in combination with a high-repetitive imaging. Therefore, each sample was doped with 0.1 mmol/l of pyrromethene 597. The local ignition, propagation and volumetric ignition was observed and ignition delay times over temperature were determined for each sample. Droplets of n-dodecane and base oil with the addition of an anti-wear additive based on zinc diphosphate (ZDDP) or a detergent additive based on calcium showed significantly faster local ignition delay times than the presence of pure base oil droplets and accelerated the volumetric ignition delay time significantly compared to cases without injection of droplets.

Symbols

Symbol	Meaning	Unit
A	Pre-exponential factor	
C_D	Dragging forces at the droplet	
c_p	Heat capacity at constant pressure	J/K
c_V	Heat capacity at constant volume	J/K
D	Diameter	m
d	Distance between droplet centers	m
d_0	Diameter at time zero (nozzle diameter)	m
E	Internal energy	W
f	Number of degrees of freedom	
G	Combustion number according to Chiu et al.	
g	Gravitational constant	m/s^2
h	Enthalpy	J
h_c	Enthalpy of combustion	J
k	Thermal conductivity	W/(m K)
L	Characteristic length of the droplet or wave	m
Le	Lewis number	
l	Length	m
m	Mass	kg
m_D	Mass of droplet	kg
$\dot{m}_F$	Mass rate of diffusion	kg/s
M	Mach number	
N	Total number of droplet or total number of data points	
Nu	Nusselt number	
n	Number of samples	
Oh	Ohnesorge number	
p	Pressure	Pa or bar
p_σ	Surface tension pressure	Pa
Pr	Prandtl number	
q	Exponential growth rate	
R	Universal gas constant	J/(mol K)
Re	Reynolds number	
r	Radius	m
r_l	Radius of droplet	m

Sc	Schmidt number	
S	Standard deviation of the samples	
T	Statistic t-value	
t	Time	s
T	Temperature	K
U	Voltage DC	V
u	Velocity	m/s
V	Voltage AC	V
We	Weber number	
x	Distance	m
x_x	Sample of the population called x	
$\bar{x}$	Mean of samples	
Z_F	Impedance	Pa s/m^3

Greek symbols

Symbol	Meaning	Unit
α	Thermal diffusivity	m^2/s
α	Convective heat transfer coefficient	$W/(m^2\ K)$
δ	Maximum error	
δ_{flame}	Flame thickness	Mm
Φ	Heat flux	W/m^2
ϕ	Equivalence ratio	
η_L	Dynamic viscosity	Pa s
κ	Isentropic exponent	
λ	Wavelength or constant evaporation rate	Nm
μ	Mean of population	
ρ	Density	kg/m^2
σ	Surface tension	J/m^2
σ	Standard deviation	
σ^2	Variance	
τ_{ign}	Volumetric ignition delay time determined by PMT	ms
τ_{local}	Local ignition delay time determined by imaging	ms
$\tilde{\nu}$	Wave number	m^{-1}
ν_i	Stoichiometric coefficient	
υ_L	Kinematic viscosity	m^2/s
ω	Angular velocity	s^{-1}
χ^2	Chi square goodness of a distributions	
χ_x	Statistic population named x	

Abbreviations and acronyms

API	American Petroleum Institute
CVC	Constant volume chamber
HPST	High-pressure shock tube
IC engine	Internal combustion engine
IQT	Ignition quality tester
IVG	Institute for Combustion and Gas Dynamics
LIF	Laser-induced fluorescence
LSPI	Low-speed pre-ignition
MON	Motor octane number
NTC	Negative temperature coefficient
PMT	Photomultiplier
PRF	Primary reference fuel
QMS	Quadrupole mass spectrometry
RCEM	Rapid-compression-expansion machine
RCM	Rapid compression machine
RON	Research octane number
RPM	Revolutions per minute

Table of Contents

Kurzfassung ..... **V**
Abstract ..... **VII**
Symbols ..... **IX**
Greek symbols ..... **XI**
Abbreviations and acronyms ..... **XIII**
Table of Contents ..... **XV**
1 Introduction **1**
2 Theory and state of the art **5**
2.1 Reaction kinetics of ignition 5
2.2 Theory of shock tubes 8
2.3 Pre-ignition and inhomogeneous ignition phenomena 12
2.3.1 Inhomogeneities in shock tube 12
2.3.2 Mimic inhomogeneous ignition by intentionally introduced inhomogeneities 13
2.4 Optical detection methods of ignition phenomena 22
2.4.1 Chemiluminescence in combustion 22
2.4.2 Laser-induced fluorescence (LIF) 23
2.4.3 Incandescence of hot particles 25
3 Experiment **27**
3.1 High-pressure shock tube facility 27
3.1.1 Surface-induced ignition 28
3.1.2 Generation of single droplets against high pressure 29
3.1.3 Measurement techniques 31
3.2 High-pressure cell 37
3.3 Offline sample analysis 38
3.3.1 Thermogravimetry 39
3.3.2 Differential scanning calorimetry 39
3.3.3 Quadrupole mass spectrometry 40
4 Autoignition of homogeneous fuel/air mixtures **41**
4.1 Homogeneous and inhomogeneous autoignition of PRF95 41
4.2 Homogeneous and inhomogeneous autoignition of ethanol 45
4.3 Interpretation of fuel/air ignition results 56
5 Ignition experiments with defined inhomogeneities **59**
5.1 Impact of hot local surfaces on homogeneous autoignition 59
5.1.1 Interpretation of hot surface-induced ignition 70
5.2 Pre-ignition triggered by droplets 71
5.2.1 Decomposition of oil samples 73
5.2.2 Potential impact of oil decomposition products on the autoignition of iso-octane 80
5.2.3 Impact of single droplets on homogeneous autoignition 81
5.2.4 Discussion and outcomes of the impact of lubricant oil/compounds or droplets on the ignition of PRF95/air 102
6 Conclusions and outlook **105**
7 Publications **107**
8 References **109**
9 Appendices **119**
9.1 Appendix A: Uncertainty and error calculation 119
9.2 Appendix B: Significance analysis of ignition delay times 123

1 Introduction

The assumption that the increase of CO_2-concentration in the lower atmosphere of the earth is a main reason for climate change has a direct influence on today's passenger car market. Stricter regulations for reduced emission limits of harmful substances in specific test cycles result in development efforts for improved powertrains in particular for the combustion engine. While the number of particles and HC, CO, and NO_x concentrations can be reduced by filtering and catalysts, CO_2 emissions can be reduced by increased efficiency only. For a spark ignition (SI) engine fueled by hydrocarbons, ideally one CO_2 molecule is formed from each carbon atom present in the fuel. Therefore, maximizing the conversion of energy from fossil fuels to mechanical power is a necessary measure on the short term to reduce CO_2 emission. On an intermediate timescale, biofuels and electrochemically-generated synthetic fuels can be one way towards CO_2 neutral processes. The efficiency of electric powertrains for CO_2 reduction is limited by the energy mix on which the electricity generation is based. Additional disadvantages in power-density and infrastructure require parallel development of different powertrains and justify the efforts to exploit the full potential of the combustion engine.

Engine downsizing in combination of downspeeding is a successful way to increase efficiency [1]. Over the last years, engines with direct injection and high boosting pressures above 2 bar or increased compression ratios of 10.5 entered the market. However, combustion phenomena with extreme knock are reported in SI engines since 2006 [2] at these operating conditions.

These extreme knock phenomena differ from the classic knock, which has been known in IC engines for a long time. These combustion abnormalities appear in sets of several knocking cycles alternating with normal cycles, although the spark timing is shifted by the engine control to avoid knock. Detailed descriptions, correlations of event frequencies with RON and MON, and potential ignition sources for pre-ignition were described by Dahnz and Spicher in 2010 [3, 4]. Amann et al. investigated the impact factors of the these ignition sources on the *pre-ignition* [5] and found that direct injection by itself does not increase the number of LSPI events [6]. In 2011, the expression Low-Speed Pre-Ignition (LSPI) was introduced to describe combustion phenomena that result in extreme knock. The name refers to the operation range of low engine speed and high load when ignition is observed in advance of the spark timing. Early ignition was detected by measuring the pressure which strongly increases in the compression stroke due to heat release from combustion.The following impact factors on the number of LSPI events were postulated:

- Boosting pressure
- Liner wetting
- Cooling temperature
- Piston crevice
- Lubricant oil composition

Dahnz et al. [4] postulated that engine oil that is released from the piston top land might be one of the casual factors for LSPI. This hypothesis was extended in the following years, [7-11]. In general, the developed hypothesis says: It is likely that lubricant oil or a mixture of lubricant oil and fuel is splashed into the combustion chamber and initiates local ignition shown in figure 1. This local ignition is followed by flame propagation through the fuel/air mixture. The deflagrating flame leads to the increase in pressure by heat release. Additional compression by the up-moving piston and finally the spark that initiates an additional flame that can lead to a transition from deflagration to detonation. In 2015, Kalghatgi described theoretically the transition from deflagration to detonation of a hot pocket in an IC engine [12].

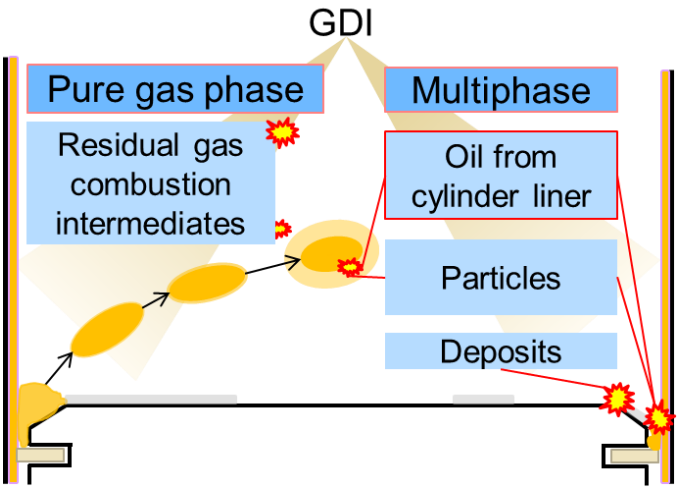

Figure 1: Schematics of a gasoline direct injection (GDI) combustion chamber of an engine with various causes of pre-ignition [13].

Whereas the ignition is certainly triggered by local autoignition in the compression stroke, it is unclear whether the local ignition is triggered by a particle or deposit removed from the combustion chamber or piston surface or a droplet. Furthermore, it is unclear whether droplets interact with the surrounding fuel/air mixture promote local autoignition or if gas-phase species formed from the decomposition of the oil droplets initiate the ignition. Hot particles or deposits released from the piston surface can act as ignition sources, too. In 2017, Wang et al. [14] summarized various aspects of LSPI in a comprehensive review.

Because of the complexity of ignition phenomena in SI engines, a separation of single aspects and idealization of processes is the approach for a better understanding of ignition. Decoupling flow and mixing processes from chemical kinetics is one major step.

The choice of the experiment therefore also determines the degree of idealization. Compared to a commercial engine, a research engine is the first step giving more details about in cylinder processes, by sensors or optical access. This influences the thermodynamics properties of the system at the same time by geometrical and material changes. There are different types of research engines in various levels of idealization, but overall four stroke engine systems include all four strokes and the fuel/oxidizer mixing process in a multi-dimensional operation map. To dramatically reduce the complexity, rapid compression machines (RCM) can be used, reducing the number of moving parts and therefore the flow and mixing process. Here, fuel and oxidizer are premixed and compressed by a piston similar to a piston engine. In contrast to an engine, the piston of an RCM is held in the top position to observe the ignition and combustion of the gas mixture at nearly constant volume in absence of mixing processes. For further decoupling from flow and wall interactions, shock tubes enable extremely fast compression of premixed fuel/oxidizer mixture. Therefore, the shock-heated and compressed gas can be studied decoupled from transport processes at nearly adiabatic conditions for a certain time span. Thus, processes that are assumed to be critical in the compression stroke become frozen and only the chemical reactivity can be measured in time.

As described above, LSPI depends on many factors that depend on the specific engine. To find the critical conditions for LSPI of the fuel/oxidizer mixture, engine-like conditions were mapped in a shock tube in this work. At these critical conditions (near autoignition), ignition sources like hot surfaces or lubricant oil droplets were introduced into the shock tube to investigate their impact on autoignition.

In a first step, the ignition of the primary reference fuel PRF95 (95% vol.%. iso-octane and 5 vol.% n-heptane) mixed with synthetic air at an equivalence ratio $\phi = 1$ was studied. PRF95 represents

gasoline with an octane rating of 95 regarding to RON and MON. Synthetic air was used to control the oxidizer composition and to be close to the conditions of normal engine operation. Current European regulations prescribe to run the engine at $\phi = 1$ at any time. Additional to the pressure traces and chemiluminescence measurements, the ignition process was imaged by simultaneous high-repetition-rate imaging in the visible and UV spectral range through a transparent endwall. To mimic engine-relevant conditions the pressure was set to 20 bar and pre-ignition temperatures were varied. In addition, the same experimental setup was used to study the ignition of ethanol/air mixtures because ethanol is known to be sensitive to surface ignition [15, 16] and inhomogeneous ignition [17, 18]. Ethanol/air mixtures at different dilution levels were studied too. The results of both, PRF95/air and the ethanol/air mixtures serve as reference for the second step of the study, where the impact of well-defined inhomogeneities on the ignition process was investigated by inserting local sources of interference.

This required the development of a new test aperture. The influence of hot surfaces and local temperature non-uniformity on the ignition delay time was determined by inserting a glow plug in the sidewall of the shock tube. This uncovers the potential effect of hot surfaces like spark plugs, outlet valves, particles, or deposits as an ignition source on a physical basis neglecting chemical reactions with the surface material.

The droplet hypothesis was investigated in two steps: On the one hand, a pure gas-phase study focusing on the local ignition triggered by gaseous substances potentially formed during the decomposition/evaporation of lubricant oil droplets with extremely high reactivity; on the other hand, the more complex process of single droplets flying through the gas mixture was elucidated. Oil samples were examined for their decomposition/evaporation properties by thermogravimetric analysis (TGA) in combination with differential scanning calorimetric (DSC). The outgas products were analyzed by quadrupole mass spectrometry (QMS). Potential species that interact in the ignition were then added to the reference PRF95/air mixture in potentially occurring concentrations and the impact on the ignition delay time was studied.

To study the potential impact of droplets on the ignition, a test method was developed to inject single droplets behind the reflected shock wave into quiescent gas at constant conditions. The on-demand released droplets were visualized by laser-induced fluorescence (LIF) and imaged to follow the droplets, the local ignition, and link the observed processes with the impact on the ignition delay time. The liquid samples were n-dodecane, base oil, and different oil additives that were dissolved in the base oil. In addition, liquid PRF95 was mixed into the oil samples. For the LIF base imaging of the droplets 0.1 mmol/l pyrromethene 597 was added to samples. The LIF was recorded by a high-speed camera in the visible (VIS) range. For more information about the ignition process high speed imaging in the ultraviolet range (UV) was performed simultaneously. The local observations of the droplets and the ignition enabled the investigation of the droplets impact volumetric ignition, and therefore to gain the understanding of LSPI in engines.

2 Theory and state of the art

In this chapter, the theory on which the experiments of this work are based is summarized. The todays understanding of gas-phase ignition, ignition specific reaction kinetics, and shock-tube based measurement techniques around the ignition process are outlined. Principles of the shock-tube technique are presented and the fundamental equations applicable for understanding the procedure are introduced. The focus is directed on the state-of-the-art of shock-tube applications and investigations on the influence of perturbations. In addition, the principles of the measurement techniques are described.

2.1 Reaction kinetics of ignition

Parts of this chapter are based on the book "Combustion" by Warnatz, Maas, and Dibble [19], while specific points refer to additional references. The combustion process can be described by the thermodynamics of the system which is influenced by diffusion, heat conduction, and flow. From a chemical perspective, combustion can be described by the underlying kinetics mechanism. Reaction mechanisms describe the process in a uniform infinitesimal volume that includes the rates of relevant elementary reactions. Macroscopic observations like the ignition delay time (described later) follow the rate laws as a consequence of the underlying microscopic phenomena of collisions between molecules [19]. The rate laws describe an empirical formulation of the reaction rate of a species in a chemical reaction. In terms of fuel chemistry, the number of reactions increases dramatically with the size of the fuel molecules. Both the elementary reaction kinetics as well as the global combustion phenomena were studied over the last decades to develop and validate reaction mechanisms which are fundamental for simulations and process optimization.

Ignition is defined as the time-dependent process starting with reactants and evolving in time towards a steadily burning flame [19]. Ignition processes can be induced locally, or start homogeneously under autoignition conditions, as is the case in this work. Autoignition plays an important role in many applications regarding safety considerations or ignition processes in combustion systems. An ignitable mixture will ignite after a **certain ignition delay time** (τ_{ign}) also called **induction time** at a certain pressure and temperature. The ignition limits of a specific mixture are the result of the competing processes of chain branching in the gas phase forming radicals and the chain termination for example by diffusion, transporting radicals to the boundary of the homogeneous system [20]. While the explosion limits of hydrogen/oxygen mixtures at constant temperature are separated by three explosion limits (1st chain explosion, 2nd stationary reaction, and 3rd thermal explosion), ignition limits for hydrocarbons exhibit more complex shapes. The more complex explosion limits are governed by the underlying chemical reactions. At low temperatures and high-pressure, cool flame regimes [21] followed by multistage ignition [22] are observed.

According to the fundamental theory of hydrocarbon oxidation referred to its inventor the "Semenov theory" [23]. The principles of branched-chain reactions are summed up by Pilling [24] in five steps:

(1) Primary initiation (radicals formed from parent molecules)
(2) Propagation of the chain (no change in the number of radicals)
(3) Termination of radical chain (removal of radicals)
(4) Chain branching (Multiplication of the number of radicals)
(5) Secondary initiation (or degenerate branching), where new radicals are formed from a "stable" intermediate product

The primary initiation reactions for hydrocarbon ignition are the reactions (R1) and (R1A):

(R1) $RH + O_2 \rightarrow R + HO_2$

(R1A) $RH \rightarrow R' + R''$

These initiation reactions (chain reactions) are endothermic and dominate the first phase of the reaction process. The number of formed radicals increases exponentially through chain branching. At high temperatures, the branching reaction (R2) is important for the increase in radical concentration. Therefore, this temperature regime is called high-temperature chemistry.

(R2) $H + O_2 \rightarrow OH + O$

With decreased temperature and/or increased pressure, the formation of HO_2 becomes more dominant, which is followed by slow branching reactions. The reaction (R2) competes with the radical recombination (R3) forming HO_2 followed by H abstraction (R4) with stable intermediates (R5).

(R3) $H + O_2 + M \rightarrow HO_2 + M$

(R4) $RH + HO_2 \rightarrow R + H_2O_2$

(R5) $H_2O_2 + M \rightarrow OH + OH + M$

The HO_2 and H_2O_2 chemistry separates the high-temperature chemistry (small radicals) by the strongly temperature/pressure dependent equilibrium of (R3). At even lower temperatures, alkyl radicals R) form peroxy radicals by addition of O_2. These peroxy radicals are able to isomerize. The formation of RO_2 competes with the termination reaction forming HO_2, CH_3, and CH_3OO while decreasing temperature shifts the equilibrium to the formation of RO_2. The peroxy radical chemistry is also called “low-temperature chemistry” often seen in n-heptane oxidation. The low-temperature pathways of n-heptane oxidation are shown in figure 2.

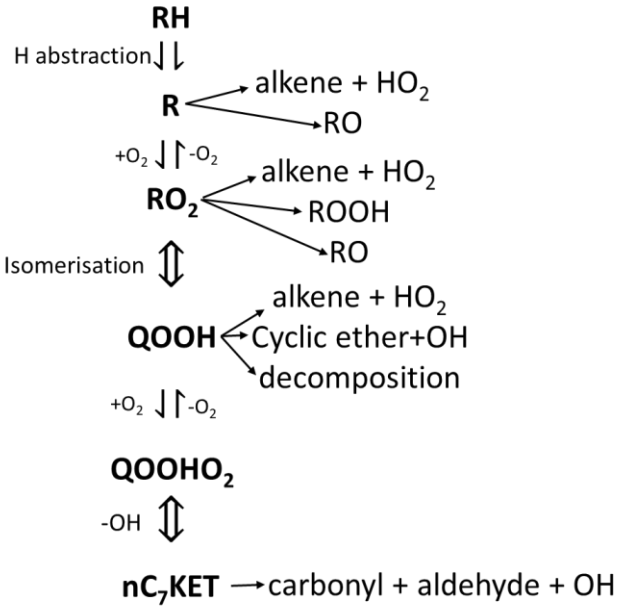

Figure 2: Low-temperature oxidation pathways of n-heptane [25].

The temperature regimes of the different chemistry processes are described in the book of “Low-temperature combustion and autoignition” by Pilling [24] and illustrated as a function of pressure.

The low-temperature chemistry produces large amounts of unstable intermediates being essential in the process of autoignition. These together with the heat release shift the system from low temperature to intermediate temperatures. As a consequence, the mixture ignites. The characteristic time of the ignition is seen in figure 3. The induction time is shorter in the low-temperature regime than in the intermediate, while the high-temperature chemistry is even faster. This behavior of negative trend in ignition delay time where the reactivity increases with decreased temperature is called **negative temperature coefficient** (NTC) behavior or NTC regime characteristic of many hydrocarbons.

Ciezki and Adomeit [26] measured ignition delay times of n-heptane/air mixtures at $\phi = 1$ over a wide temperature and pressure range and compared their results with the results of the low-temperature reaction mechanism developed by Warnatz and coworkers [27, 28]. With increased pressure the reaction rates of peroxy chemistry is reduced which results in a flattening of the NTC behavior.

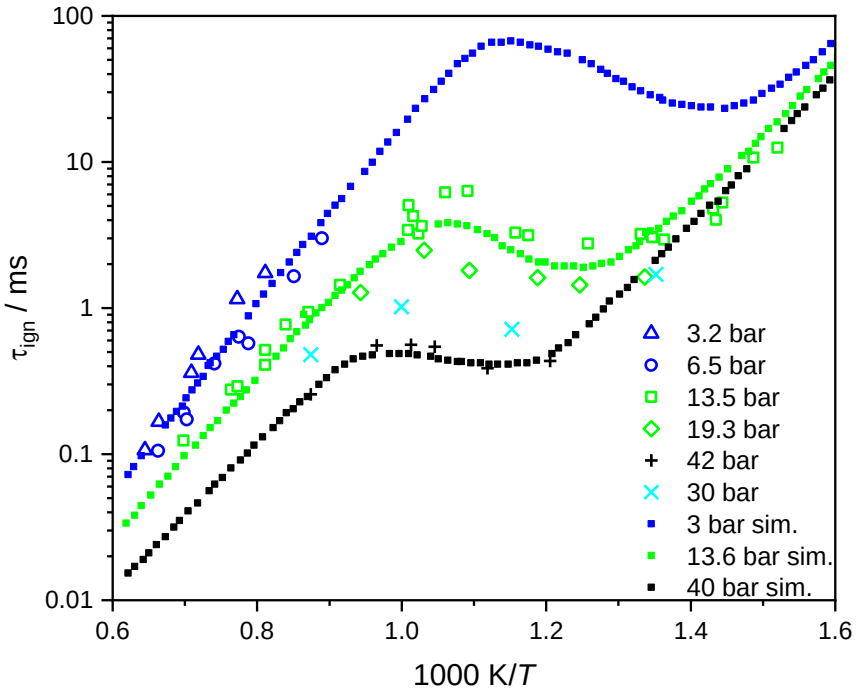

Figure 3: Ignition delay times of stoichiometric n-heptane/air mixtures; experimental results from Ciezki and Adomeit [26] and simulations from Warnatz et al. [27, 28].

Shock tubes have a long history in chemical kinetics studies. The method's merit is the capability to generate nearly ideal conditions (homogeneous gas mixture in terms of concentration, temperature, and pressure) by adiabatic gas compression through shock waves. The fundamentals of shock-tube experiments are explained in section 3.1.

While the autoignition of homogenous gas mixtures has been intensively studied in shock tubes, combustion in many application processes are initiated by local ignition sources like sparks, pilot flames, or glow plugs. The pre-ignition sources in engines mentioned in the introduction could act like an ignition source. For an analytical description of such an ignition source and resulting ignition the ignition source can be esteem as a spot energy source. An analytical model that describes the threshold ignition energy is discussed by Williams [29], Glassman [30], and Turns [31], and is summarized in the dissertation of Bane [32]. A spherical volume of gas is ignited by a point spark with a critical radius r_{crit}. In order not to be extinguished, the heat release according to Semenov [23] from chemical reactions inside the gas volume needs to be at least equal to the heat loss to the surrounding:

$$\frac{-dm_{\mathrm{fuel}}^{m}}{dt}\Delta h_{\mathrm{c}}\left(\frac{4}{3}\pi r_{\mathrm{crit}}^{3}\right)\approx -k\left.\frac{dT}{dr}\right|_{r_{\mathrm{crit}}}(4\pi r_{\mathrm{crit}}^{2}) \quad (1)$$

where $m_{\mathrm{fuel}}^{\mathrm{m}}$ is the fuel mass per unit volume, Δh_{c} is the enthalpy difference due to combustion, and *k* is the thermal conductivity. By several approximations explained in detail in ref. [32], the critical flame radius (i.e., the smallest flame that can exist and grow) can be found according to equation (2):

$$r_{\mathrm{crit}}\approx\sqrt{6}\frac{\alpha}{s_{\mathrm{L}}}\approx\sqrt{6}\frac{\delta_{\mathrm{flame}}}{2} \quad (2)$$

with the thermal diffusivity α, the laminar flame speed $s_L \approx \left(\frac{-2m\alpha}{\rho_{\mathrm{u}}}\frac{dm_{\mathrm{fuel}}'''}{dt}\right)^{\frac{1}{2}}$, and the flame thickness δ_{flame}.
Understanding inhomogeneity during the physiochemical processes is essential because in combustion applications this makes the difference between desired and arbitrary combustion events.

2.2 Theory of shock tubes

Shock tubes are well-established to investigate the chemical kinetics of fast high-temperature reactions in absence of transport processes. The obtained experimental data provide targets such as rate constants, ignition delay times and time dependent species concentrations for the validation of detailed chemical kinetics mechanisms. The theory of shock tubes was developed based on the Rankine-Hugoniot conditions as a result of the work of Hugoniot [33] and Rankine [34]. More details about the application are summarized by Oertel in “Stoßrohre, Theorie, Praxis, Anwendung” [35].
The type of shock tube covered in this work consists of two tube sections separated by a diaphragm, both ends of the tube are closed by endwalls. The right tube section at the top of figure 4 contains the test gas, the left section is filled by the driver gas. The pressure increase in the driver section causes the diaphragm to burst followed by the expansion of the driver gas into the test section resulting in local thermodynamic equilibrium. From the burst diaphragm, compression waves are released, which then propagate into the test-gas section. The compression of the test gas by the shock waves increases the pressure and temperature of the test gas behind the incident shock waves, increasing the Mach number of each following shock wave. Therefore, each following shock wave is faster than the previous one, so that the shock waves outrun each other after a certain distance of about 10 times the diameter and form a shock front traveling through the test gas with the supersonic velocity u_2.

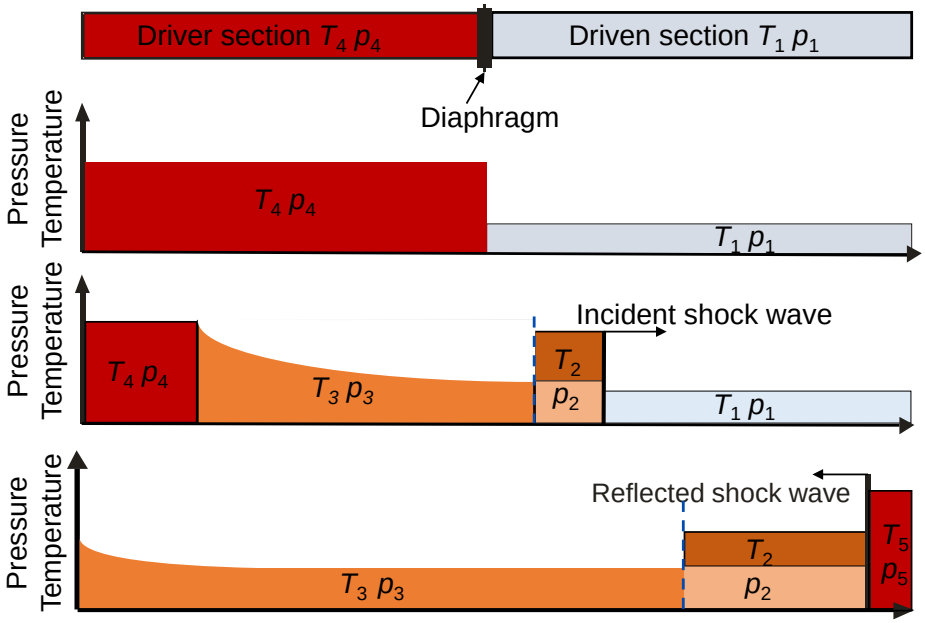

Figure 4: Pressure and temperature diagram of the five conditions in shock tubes [36].

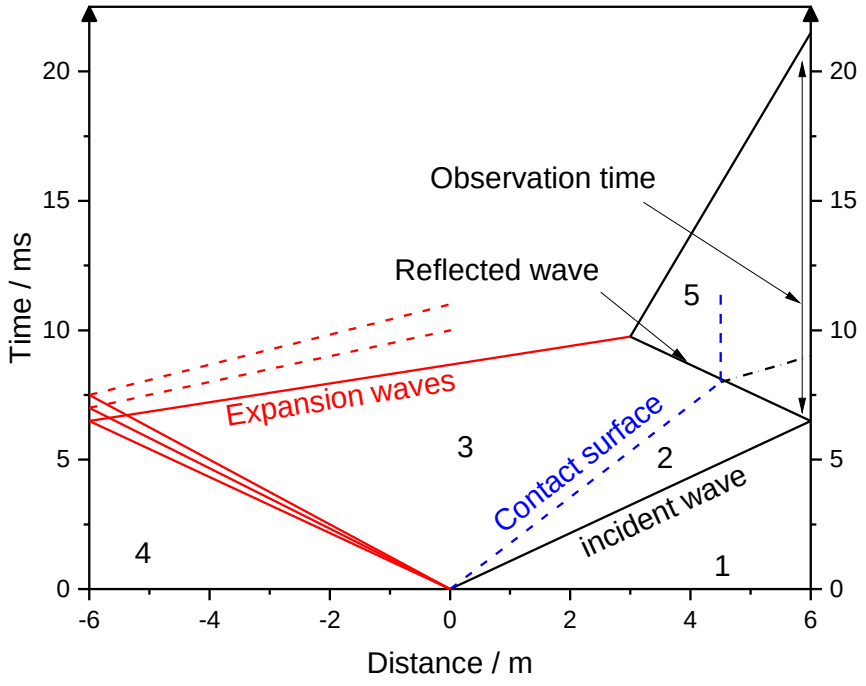

Figure 5: *x-t* diagram representing the propagation of the shock wave and other waves over time [36].

In figure 4, the conditions in the shock tube at different points of time are shown. figure 5 shows the *x-t* diagram of the different waves. Behind the incident shock wave, the medium interface (contact surface between the test gas and the driver gas) propagates with the velocity u_3. The shock wave is reflected at the endwall. According to Oertel [35], the conservation of mass, momentum, and energy with the term for the specific mass density, u for the velocity, p for the pressure, E for the internal energy per unit of mass and h for the enthalpy per unit of mass with

$$\rho_1 u_1 = \rho_2 u_2 \tag{3}$$

$$\rho_1 u_1^2 + p_1 = \rho_2 u_2^2 + p_2 \tag{4}$$

$$\frac{1}{2}u_1^2 + h_1 = \frac{1}{2}u_2^2 + h_2 \tag{5}$$

respectively.

$$h_1 + \frac{u_1^2}{2} = h_2 + \frac{u_2^2}{2} \tag{6}$$

Assuming ideal gases without dissociation and ionization:

$$p_1 = \rho_2 R T_2 \tag{7}$$

with the universal constant $R = 8.314$ J/(K mol) and the equation for the internal energy of ideal gases

$$E_2 - E_1 = c_V(T_2 - T_1) \tag{8}$$

with c_V, the specific heat (heat capacity at constant volume). This leads to a system of equations with four unknowns (ρ_2, p_2, u_1 and u_2). For its solution, it is common practice to measure the velocity u_1 in an experiment. Applying

$$c_V = \frac{f}{2}R \tag{9}$$

and

$$c_p = \frac{2+f}{2}R \tag{10}$$

(c_V and c_p are constant at low temperature). With f as number of degrees of freedom of the gas molecules ($f = 3$ for monatomic gases, $f = 5$ for linear molecules and $f = 6$ for multi-atomic molecules) follows:

$$\kappa = \frac{f+2}{f} \tag{11}$$

i.e., $\kappa = 5/3$ for atoms, $\kappa = 7/5$ for molecules with two atoms, and $\kappa = 4/3$ for molecules with three or more atoms). After transformation the following relations apply:

$$p_2 = p_1 \frac{2\kappa \mathrm{M}_1^2 - (\kappa - 1)}{\kappa + 1} \tag{12}$$

$$\rho_2 = \rho_1 \frac{(\kappa+1)\mathrm{M}_1^2}{(\kappa-1)\mathrm{M}_1^2 + 2} \tag{13}$$

$$T_2 = T_1 \left[\frac{2\kappa \mathrm{M}_1^2 - (\kappa-1)}{\kappa+1}\right]\left[\frac{(\kappa-1)\mathrm{M}_1^2 + 2}{(\kappa+1)\mathrm{M}_1^2}\right] \tag{14}$$

with the Mach Number $\mathrm{M}_1 = u_1/u_s$, where u_s is the velocity of sound in the test gas under condition 1. Accordingly, the condition behind the shock wave can be determined. In order to

determine the condition behind the reflected shock wave, the Rankine-Hugoniot equations need to be applied leading to the following thermodynamic values in condition 5:

$$p_5 = p_1 \frac{\left(\frac{3\kappa-1}{\kappa-1}\right)\mathrm{M}_1^2 - 2\frac{2\kappa}{\kappa-1}\mathrm{M}_1^2 - 1}{M_1^2 + \frac{2}{\kappa-1}\qquad\left(\frac{\kappa+1}{\kappa-1}\right)} \tag{15}$$

$$\rho_5 = \rho_1 \frac{\mathrm{M}_1^2\left(\frac{\kappa+1}{\kappa-1}\right)}{\mathrm{M}_1^2 + \frac{2}{\kappa-1}} \frac{\left(\frac{2\kappa}{\kappa-1}\right)\mathrm{M}_1^2 - 1}{2\mathrm{M}_1^2 + \frac{3-\kappa}{\kappa-1}} \tag{16}$$

$$T_5 = T_1 \frac{\left[\left(\frac{3\kappa-1}{\kappa-1}\right)\mathrm{M}_1^2 - 2\right]\left[2\mathrm{M}_1^2 + \frac{3-\kappa}{\kappa-1}\right]}{\left(\frac{\kappa+1}{\kappa-1}\right)^2 \mathrm{M}_1^2} \tag{17}$$

Condition 5 will remain constant until the reflected shock wave hits the contact surface of the medium moving in the direction of the endwall. This point in time is shown in figure 5, when the blue dashed line crosses the black line. The observation time lasts for typically 1–4 ms in state-of-the-art shock tubes depending on the conditions and length of the shock tube. Then the reflected shock wave matches the contact surface of the medium and is reflected back into the reaction segment, illustrated by the dashed black line in Figure 5 or the gas expands. The reason for this is the difference in impedance of the media in which the shock wave penetrates. To extend the observation time, the method of driver-gas tailoring [37] by adapting the sound velocity of the driver gas. A sound wave penetrates a homogeneous medium with a specific wave characteristic. The transition into a second medium (contact surface) impacts the sound wave depending on the difference in impedance. In case, both medias have the same impedance (ZF), the sound-wave velocity does not change. Larger differences in the impedance lead to a reflection of the sound wave at the interface. Therefore, ideally the impedance of the driver gas in condition ZF (3) equals that of the test gas under condition ZF (2). To achieve that, the general impedance equation must be applied:

$$Z_\mathrm{F} = \frac{p}{u} \tag{18}$$

The impedance is the ratio of acoustic pressure and velocity. It is assumed that the heat capacity is independent of the temperature according to:

$$T_{43} = \left(\frac{p_{41}}{p_{21}}\right)^{2\beta_4} \tag{19}$$

$$T_{21} = \frac{p_{41}(\alpha_1 + p_{21})}{(\alpha|1p_{21} + 1)} \tag{20}$$

With $\beta = (\kappa - 1)/2\,\kappa$, $\alpha = (\kappa + 1)/(\kappa - 1)$ and p_{41} is related to p_{21} by the equation for the ideal membrane:

$$p_{41} = \frac{p_{21}}{\left(1 - (p_{21} - 1)\left[\frac{\beta_4 E_{14}}{\alpha_1 p_{21} + 1}\right]^{1/2}\right)^{1/\beta_1}} \tag{21}$$

Palmer and Knox solved the test- and driver-gas condition terms leading to an equation of mass fraction of two species driver-gas composition for a given pressure and temperature, with equal acoustic impedance in the driver gas and in the test gas in condition 2.

$$E_{32} = \frac{c_{V3} T_3}{c_{V2} T_2} = \frac{(\alpha_3 p_{52} + 1)}{(\alpha_2 p_{52} + 1)} = 1 \quad (22)$$

For a case using a mixture of helium and argon for the driver gas, for example, the portion of helium is given by:

$$X_{\mathrm{He}} = \frac{M_1}{M_4} \quad (23)$$

With driver-gas tailoring, the observation time in the high-pressure shock tube at the IVG can be extended up to 15 ms, enabling investigations of dynamic processes in reacting gases at long timescales and low temperatures.

2.3 Pre-ignition and inhomogeneous ignition phenomena

Pre-ignition is the premature ignition of a combustible mixture prior to the main ignition, the term is likewise used in context to low-speed pre-ignition (LSPI) meaning the ignition prior to the spark at low engine speed. This work concentrates on the application aspect where pre-ignition in IC engines results in “super knock”, using shock tube techniques at conditions that prevail in combustion engines. Therefore, it is not possible to investigate general valid impact factors in an engine. In contrast shock tubes enables to study general valid ignition behavior under specific thermodynamic conditions. The impact of artificial introduced ignition sources along with the inhomogeneous conditions on local and volumetric ignition is directly compared to identical measurements without perturbation.

2.3.1 Inhomogeneities in shock tube

The shock tube is usually interpreted as an ideal or nearly ideal reactor to study chemical kinetics such as ignition processes. However, observations have shown that the post-reflected conditions are subject of non-idealities. Especially ignition delay time studies at low temperatures with long ignition delay times and high fuel concentrations can be strongly affected by these non-ideal effects, leading to discrepancies in the predicted values of the reaction mechanism with the experiments. Ideally, the shock tube theory predicts homogeneous pressure-temperature conditions behind the reflected shock wave. The post-shock conditions depend mainly on the shock wave velocity and flow conditions as viscosity of the gas which is influenced by the friction at the wall of the tube. Due to viscosity a boundary layer forms and grows with time. The effect of boundary layer formation can be seen by shock attenuation of the incident waves [38] and on the time-dependent variation of the pressure where a gradual pressure increase over time called d*p*/d*t* is observed especially at high pressures [39, 40].
In some cases, the reflected shock wave can interact with the boundary layer causing bifurcation [41]. Shock bifurcation leads to the formation of vortices and an inhomogeneous temperatures field behind the reflected shock wave and complicates the determination of time zero from the pressure profiles. In some cases, the dynamic pattern of shock determines the nature of ignition. Khokhlov et al. [42] and Lipkowicz et al. [43] simulated the ignition starting at small kernels that slowly burn the gas called *mild ignition*. Mild ignition was reported by Fieweger et al. [44] for experiments at high pressure and temperatures where peroxy chemistry plays an important role. But these experiments did not show features of bifurcation, instead shadowgraphy images indicate local spots of ignition similar to the ignition spots from inhomogeneous temperature fields in the low-pressure simulation from Lipkowicz et al. [43].

Local ignition spots can lead to a flame-like deflagrating spread of the ignition [44] that can transit to detonation in the unburned gas. In shock-tube studies, pre-reaction heat release leads to an early rise in the pressure trace before the main ignition, called pre-ignition [45]. The source of these early reactions is still under debate, but facility-related effects in terms of pressure rise (dp/dt) are unlikely. The pre-ignition manifests itself as *remote ignition*, which is the ignition that starts in the core of the shock tube upstream from the endwall due to temperature non-uniformity. Hanson et al.[46] developed a constrained volume shock-tube technique called CRV to avoid a pressure increase due to growing boundary layer and consequently also remote ignition. However, the processes around remote ignition is not fully understood. Lipkowicz et al. [43] have recently investigated remote ignition in more detail by numerical simulation.

2.3.2 Mimic inhomogeneous ignition by intentionally introduced inhomogeneities

Pre-ignition occurs in shock tubes as described above due to inhomogeneous conditions in the shock-heated gas. Pre-ignition in an SI engines is the ignition prior the spark timing because of local exceeding the conditions of autoignition [47]. Pre-ignition in shock tube studies can be identified, however, by different measurement techniques. In engines the occurrence of pre-ignition is on the one hand dependent on the operation conditions. On the other hand, many parameters are engine specific. Therefore, it is not possible to investigate general valid impact factors in an engine. In contrast, shock tubes enable to study general valid ignition behavior under specific thermodynamic conditions. The impact of artificial introduced ignition sources along with the inhomogeneous conditions on local and volumetric ignition is directly compared to identical measurements without perturbation.

2.3.2.1 Ignition induced by a hot surface

The following chapter is a reprint of selected paragraphs from the publication Niegemann et al. 2018 [48] as main author. The respective parts are entirely based on my own work. The final version of the paper was written together with the coauthors who also have contributed to the conception, structuring and substantial revision of the article.

Hot surface ignition of ignitable fuel/air mixtures was studied in the context of safety [49-51] as well as in fuel science for application in IC engines and aviation [52, 53]. Ignition of fuel/air mixtures on hot surfaces was studied at atmospheric and high pressure and low gas temperature [49, 54]. Roth et al. [55] have investigated ignition from mechanical sparks using ceramic bearing balls placed in various quiescent and explosive combustibles. The particles were exposed to intense radiation resulting in rapid temperature rise that induces ignition of the gas-phase. The particle temperature was simulated using 1D approaches with detailed transport and chemistry models. In an earlier study [55] it was the thermal ignition of hydrogen/air mixtures by small hot particles was characterized and found that the particle temperature at ignition increases as the particle size decreases.

The influence of hot surfaces on the ignition process in the presence of hot compressed gases has rarely been studied systematically. Hot-surface ignition was investigated by droplets in contact with a hot surface [56, 57] and surface ignition of sprays was investigated by Adomeit et al. [58] who studied the advanced ignition behavior of ethanol mixtures in a high-temperature high-pressure vessel initiated by a ceramic glow plug. Menon et al. [59] studied near-wall ignition of n-hexane/air mixtures at low pressure and various equivalence ratios. In their study, they provided simulated temperature fields and included a detailed chemical mechanism for n-heptane [60] as a surrogate for n-hexane. Simulations reveal a two-stage ignition, however, that deviates from the two-stage ignition observed in a homogeneous reactor due to diffusive and convective processes. Boeck et al. [50] experimentally studied the ignition of fuel/air mixtures (hydrogen/air, ethylene/air, n-hexane/air) from a heated cylinder situated inside a closed combustion vessel. A

heated surface was used to provide spatially uniform temperature. The threshold temperature at the time of ignition was measured by two-color pyrometry.
Hot-surface ignition has been studied in engines in the context of cold start [61] and has been observed in various engine experiments. A recent study of Budak et al. [62] investigated experimentally and numerically hot-surface ignition of ethanol, E10, and iso-octane in a single-cylinder engine equipped with a heated plug. To date, however, there is no established method to investigate hot-surface ignition under in-cylinder conditions decoupled from the mixture inhomogeneities and turbulent flows that exist in an engine. Such a method, however, is required to systematically investigate the propensity of various fuels compression ignition or surface ignition for practically relevant conditions.

2.3.2.2 Ignition induced by low-volatile liquids

Zahdeh et al. [63] shed light onto parameters and features associated with pre-ignition in boosted SI engines, such as cylinder liner wetting, low liner temperatures, and high end-of-compression gas temperatures through increased compression ratio and lean combustion. The influence of the lubricant oil composition on the frequency of low-speed pre-ignition (LSPI) was studied by Takeuchi et al. [7]. The fuel properties discussed by Zahdeh were investigated further by Sasaki et al. who found correlations between pre-ignition temperature and RON for several fuels [64]. A theoretical study by Kalghatgi et al. [65, 66] of the development of detonation was complemented by an experimental study by Wang et al. [67-69] who described the relationship between super-knock and pre-ignition. The development of detonation starts as local pre-ignition followed by flame propagation and subsequent transition into detonation. Similar results recorded in a single-cylinder research engine are reported by Miyasaka et al. and Dingle et al. [10, 70] for various fuels doped with lubricant oil or oil additives based on calcium salicylate.
Single-droplet injection into an RCM was presented by Ohtomo et al. [71]. Oil and oil/fuel mixtures injected into methane/air and PRF/air mixtures were investigated in a constant volume chamber (CVC) and a rapid-compression-expansion machine (RCEM) by Kassai et al. [72]. The reactivity of the base oil was found to be sufficient to initiate pre-ignition that can result in LSPI, and the type of the base oil had a stronger influence than the additive package. In methane/air mixtures, a reduction of ignition delay times by calcium-based additives was not observed. The study by Yuusuke et al. [73] quantified the influence of lubricant oil, lubricant oil mixed with iso-octane, as well as the influence of icosane and calcium sulfonate injected into an iso-octane/air mixture on ignition delay times in an RCM. It was found that the presence of lubricant oil reduced the ignition delay time. Oil with calcium compounds further reduced the ignition delay time for some fuels. Works by Yuusuke et al. [73] and Kassai et al. [72] found that fuel mixed with lubricant oil increases the number of LSPI events and shortens the ignition delay time in an RCM. Recently, a reaction mechanism for fuel/lubricant-oil mixtures was presented in [74], based on a reduced iso-octane reaction mechanism by Wang et al. [80] combined with the mechanism by Sarathy et al. [75]. This mechanism was compared with measurements by Kuti et al. [76] who injected oil and oil surrogates into hot air in an ignition quality tester (IQT), and shock-tube ignition delay-time data on iso-octane/air-mixtures from Fieweger et al. [44]. The comparison showed good agreement.
To study the influence of liquids on the ignition under well-defined conditions, single droplets were injected into shock heated fuel/air mixtures at engine relevant conditions in this work. Single droplets had to be injected in a challenging environment of post reflected shock waves (high-pressure, rapid dynamic). Therefore, fundamental knowledge of lubricant oils, droplet generation and break-up, and droplet ignition and evaluation were essential.

2.3.2.2.1 Lubricant oil composition

This work focuses on the influence of lubricant oil on the ignition process at conditions close to the end of compression in modern IC engines. Today's lubricating oils in IC engines prepossess an extremely narrow ranged specification of composition on the one hand, while achieving requirements of specific engines on the other hand. It is obvious that a single fraction of crude oil is not able to fit to all these specifications. Lubricating engine oils in general consist of base oil of 85–95 wt.%. and an additive package of 5–15 wt.%. The base oil is the main amount, but for the right fitting, additive formulation gains the desired properties. The American Petroleum Institute (API) defines five groups of base stocks. The first three base stocks are even called mineral oils. A Group I base stock is the product of a four-step extraction from petroleum crude oil. In the first step, the oil gases and lube fraction of the crude oil is extracted by distillation, which is cleaned by solvent extraction in a second step. The solvents mainly remove aromatics, polar hydrocarbons, sulfur, and nitrogen compounds. Afterwards, the oil is dewaxed by cooling down to –10 to –20°C. In the last step, the amount of aromatics and heterocyclic compounds is reduced by hydro-fishing to improve the oxidation stability of the base oil, which is important to avoid sludge formation and ensure storage stability [77].
While Group I base oils are solvent-refined, Group II base oils are hydrotreated and cracked, which reduces the amount of sulfur, nitrogen and ring structures. For Group III base oils, the conditions of hydrotreating and cracking are more severe in temperature and pressure, resulting in additional oxidation stability. The Group IV base oils are poly-alpha-olefins called PAOs or synthetic oils. PAOs are synthesized by polymerization of oil gases to generate saturated hydrocarbons called polyolefins. In the case of PAOs, an alpha-olefin (double bond between the first and second carbon molecules) is polymerized to form an alkyl branched polymer [78]. The benefit of this production process is a base oil without ring structures, double bonds (besides the α–olefin), sulfur, nitrogen or waxy hydrocarbons. Group V base oils includes all base stocks that do not fit into the classification of group I–IV. To name some examples: silicone oils, phosphate esters, polyolester, bio lubricants, etc. All groups are specified in composition and performance in specified tests in appendix E of API 1509 [79]. IC engines of the current generation use lubricant oils based on stocks from Group IV only. Because of the poor performance in regard to oxidation likelihood of Group I base oils described above, test samples in this work are from a base stock of Group I.
The amount and composition of the additive package vary from product to product. There are different ways to categorize the additives, by their function or by their chemical properties. Both methods are not able to generate an unequivocal structure, because several properties are necessary for one function and the chemical properties influence each other. The task of the main oil is the reduction of friction by lubrication. The lubricating properties of the oil are dominated by the composition of additives. The basis to enhance the reduction of friction are anti-wear or extreme-pressure additives. The group of anti-wear additives are based on sulfur or phosphorus containing molecules as different forms of sulfurized olefins or phosphate esters. To generate the convenable properties in terms of mechanical stress and transport the viscosity and film-forming properties are very important. A wide range of different viscosity modifiers exist. Some are metal-based polymers that act as antioxidant dispersants, too. Others are linear polymers made from three classes of hydrocarbon side chains. These properties get lost with the degradation of the oil, mainly by oxidation which forms deposits and finally sludge. An IC engine is a perfect reactor for oxidation, by operating at high temperatures, offering high reactive radicals and combustion intermediates by blowby and metallic surfaces. The deposit additives make the largest amount of the additive package. The book “Lubricant Additives – Chemistry and Applications“ edited by L. R. Rudnick [80] count three different deposit control additives. The first antioxidants are mostly based on sulfur or sulfur-nitrogen or sulfur-phosphorus compounds. As an

example, dialkylphenol sulfide or dithiocarbonate ester is used. Combining phosphorus and sulfur in one molecule is more powerful as an antioxidant than containing only one type. Different types of metal dialkyldithiophosphates exist, but the zinc salts of dialkyldithiophosphoric acid (ZDDP) are the most cost-effective antioxidants and therefore commonly used.
The second and third group of additives inhibit deposit formation in the form of detergents and dispersants. In the oxidation process, the oil decomposes to highly polar materials, separating from the bulk lubricant and forming surface deposits. The separation of the undesirable polar products in the nonpolar environment is slowed down by detergents and dispersants [81]. Detergents and dispersants are even called stabilizers and deposit control agents. Detergents are metal salts of organic acids that frequently contain associated excess base, usually in the form of carbonate [80] (Page 124). The amount of metal is important to form a neutral salt, referred to as neutral detergent or soap. “If the metal is present in excess, the detergents are called basic, overbased, or superbased” [82, 83]. The reserve base of the detergent neutralizes the acids from combustion and oil decomposition to form salts, while the organic portion of the detergent keeps the salts suspended in the lubricant.
In contrast to the detergent, dispersants are metal-free additives with high molecular weight consisting of three structural features: a hydrocarbon group, a polar group, and a connecting group. Their function is the inclusion of undesirable polar species into micelles, associating with colloidal particles to prevent them from aggregation, suspending the aggregates, and lowering the surface/interfacial energy of the polar species to prevent their adherence to metal surfaces.
Especially the ZDDP and the detergents play an important role in the context of pre-ignition as different studies have shown that these additives have a significant influence on the number of LSPI events in different engine tests [7, 8, 10, 67, 72].

2.3.2.2.2 Fundamentals of the formation of single droplets clusters and spray

The formation of a droplet depends on the “attacking forces” such as the external aerodynamic pressure p_A and the surface tension pressure p_σ. A droplet formed out of a constant falling jet (gravitation g) with a geometric diameter of d_0 has a mass m_D:

$$m_D = \frac{\pi\, d_0\, p_\sigma}{g} \tag{24}$$

For a spherical droplet that forms out of a falling jet, the diameter D is defined as:

$$D = \left(\frac{6\, d_0\, p_\sigma}{\rho_L\, g}\right)^{\frac{1}{3}} \tag{25}$$

With the specific density of the liquid ρ_L.
For applications like injectors for spray formation and for very small droplets of the size of 1 to 300 µm, gravitational forces becomes negligible [84]. The size of the droplet depends on the break-up regime. Therefore, the droplet is pushed instead of falling through the quiescent air. The relative velocity u_{rel} becomes important while g becomes negligible.
For a cylindrical jet formed in a typical cylindrical nozzle, the competition between cohesive and disruptive forces on the jet surface affects the oscillation and perturbation of the jet. Most studies refer to a combination of liquid as dispersed phase and gas as continuous phase, usually air. The first experimental studies were carried out by Bidone [85] and Savart [86], while Rayleigh [87] established the basics of theoretical mathematical tools to describe the observations in the experiments. The surface energy is directly proportional to the surface area and the surface tension of the liquid.

$$E_s = \frac{\pi\,\sigma}{2\,d_0}(\gamma^2 + n^2 - 1)b_n^2 \tag{26}$$

Here E_s is the potential surface energy, d_0 is the nozzle = jet diameter, b_n is the constant in Fourier series expansion, $\gamma = 2\pi/\lambda$ the dimensionless wave number, λ is the wavelength of the disturbance in the jet and n is any positive integer (including zero).
If b_n is proportional to exp(qt) with q the exponential growth rate of disturbance, the exponential growth rate is given by:

$$q_{\max} = 0.97\left(\frac{\sigma}{\rho_L {d_0}^3}\right) \tag{27}$$

Corresponding to q_{max}, the optimum wavelength λ_{opt} is:

$$\lambda_{opt} = 4.5\; l\; d_0 \tag{28}$$

After break-up the cylindrical jet of 4.5 l d_0 a spherical drop is formed:

$$4.5\; d_0 \frac{\pi}{4} d_0^2 = \frac{\pi}{6} D^3 \tag{29}$$

$$D = 1.89\; d_0 \tag{30}$$

The theoretical results were confirmed experimentally by Tyler [88]. Rayleigh's theory found general acceptance, although it neglects viscosity turbulence and influence of the surrounding air. He recognized that the break-up of jets is a dynamic problem and the rate of collapse is important. Therefore, Weber [89] extended Rayleigh's theory for viscous liquids. For a viscous liquid with dynamic viscosity η_L, there is an optimal wavelength λ_{opt} most favorable for droplet formation:

$$\lambda_{opt} = \sqrt{2}\pi d_0 \left(1 + \frac{3\eta_L}{\sqrt{\rho_L \sigma d_0}}\right)^{0.5} \tag{31}$$

Considering the air resistance on the disintegration of jets into droplets, the air friction shortens the optimum wavelength depending on the relative air velocity. Besides the theoretical values based on the Weber number, Haenlein [98] provided experimental results for liquids with various viscosities and surface tensions. The disintegration of liquid jets was classified into four regimes, while there was no sharp line for allocation. Ohnesorge proposed the commonly used ratio criteria of equation (32) and equation (33) for classification described in Ref. [90]. He classified three regimes of jet disintegration by using the dimensionless number Z also known as Ohnesorge number Oh versus Reynolds number Re.

$$\mathrm{Oh} = Z = \left(\frac{u_L^2 \rho_L d_0}{\sigma}\right)^{0.5} \left(\frac{u_L d_0 \rho_L}{\eta_L}\right)^{-1} = \frac{\eta_L}{(\rho_L \sigma d_0)^{0.5}} \tag{32}$$

With the velocity u_L.
The Reynolds number describes the flow pattern and is used in experiments by breaking the conditions down to a comparable well-known standard case. It is also applicable to describe a liquid that is flowing through a nozzle. In this case, the Reynolds number is the product of the relative velocity u_{rel}, the characteristic length (diameter of the nozzle d_0) and the density of the injected

liquid ρ_L divided by the dynamic viscosity of the liquid η_L. Using the kinematic viscosity of the liquid υ_L the density is canceled.

$$\mathrm{Re} = \frac{\rho_L u_{rel} d_0}{\eta_L} = \frac{u_{rel} d_0}{\upsilon_L} \tag{33}$$

Because of uncertainties and disagreement to the Ohnesorge limit for the transition from sinus wave break-up to atomization, Reitz [91] proposed a distinction into four regimes that consider his own results and those from many others, like Giffen and Muraszew [92], and Haenlein [93].

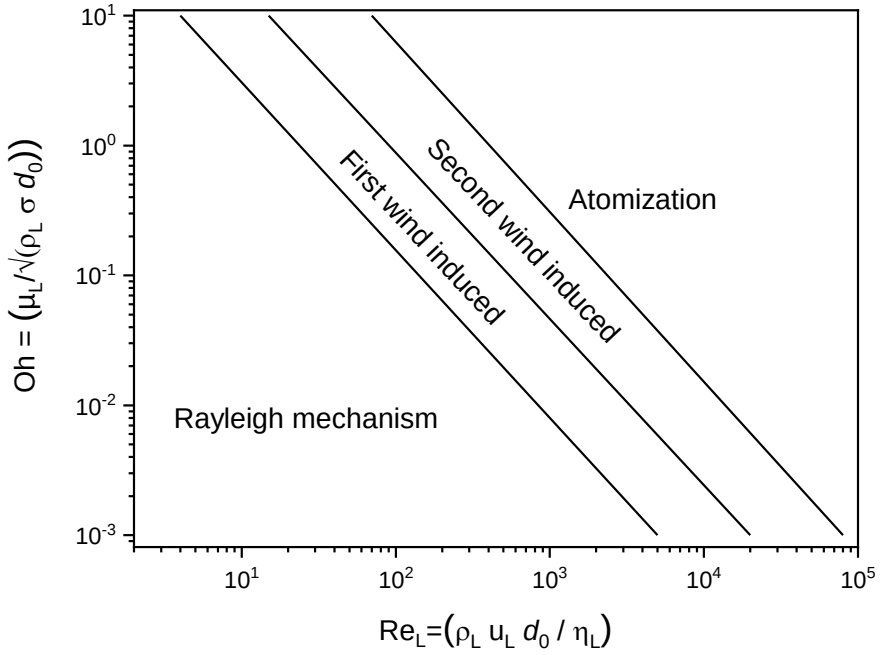

Figure 6: Ohnesorge diagram classification of disintegration modes modified by Reitz [91].

For practical use, the break-up length is important, which is not linear for an increasing jet velocity. Dumouchel reviewed the experimental investigation on primary atomization recently [94]. The four regimes of jet disintegration together with the addition of the dripping regime for no jet velocity are shown as break-up length Z_b over velocity V in Figure 6. The break-up length is defined as the length of the continuous jet; from to the nozzle tip to the position where the jet breaks up into a droplet. Besides the dripping process, the formation of droplets for very low jet velocities is in the Rayleigh mechanism. With increasing jet velocity, the break-up length increases until the transition to the first wind induces break-up. In this regime a further increase in jet velocity decreases the break-up length. The minimum break-up length is about the same length as it is for the lowest jet speed. Then the transition to the second wind-induced break-up takes place. In the Rayleigh and first wind-induced regime the jet velocity changes the break-up length linearly, but in the second wind-induced breakup regime the influence is logarithmic with a fluent transition to the atomization regime.

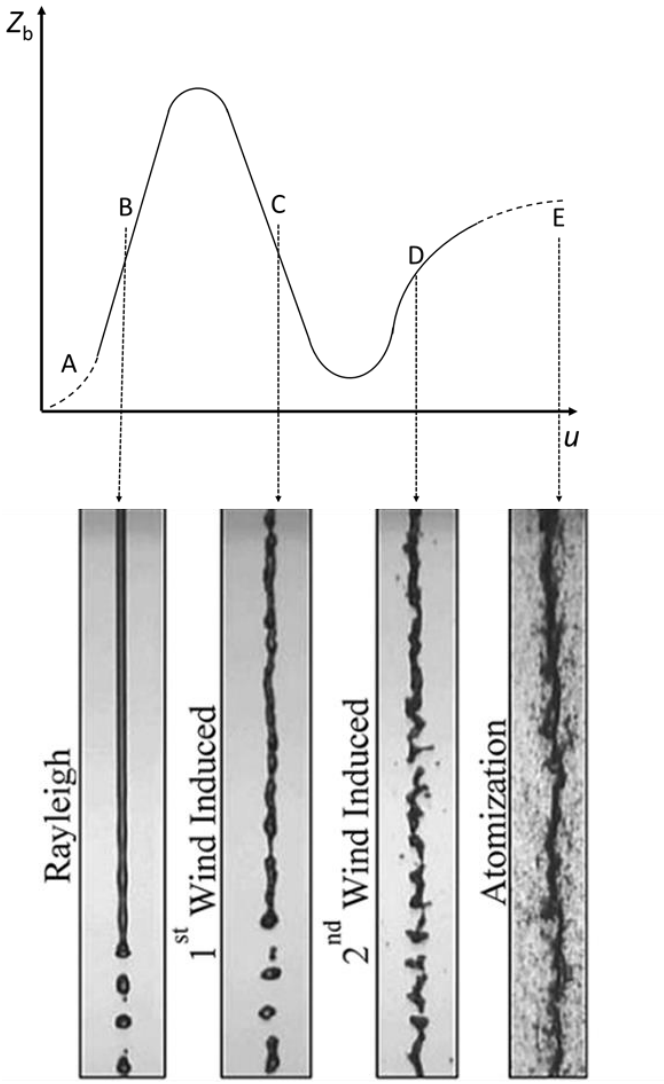

Figure 7: Cylindrical jet behavior. Top: stability curve, bottom: example of visualizations (from left to right): Rayleigh regime (region B) $Re_L = 790$, $We_G = 0.06$; first wind-induced regime (region C) $Re_L = 5{,}500$, $We_G = 2.7$; second wind-induced regime (region D) $Re_L = 16{,}500$, $We_G = 24$; atomization regime (region E) $Re_L = 28{,}000$, $We_G = 70$ [95].

Besides the first formation of the droplet out of a jet the droplet itself is stable in an equilibrium of inner and outer acting forces:

$$C_D \frac{\pi D^2}{4} 0.5\, \rho_A\, u_{rel}^2 = \pi\, D\, \sigma \tag{34}$$

C_D are the dragging forces and ρ_A the density of the continuous phase.
If this is not the case, the droplet flattens and will break-up. To describe the critical conditions of droplet break-up called secondary break-up, two cases must be distinguished:

1. The droplet in a continuous flow field with and without viscosity of the dispersant and continuous phase.
2. The droplet in a turbulent flow field.

For the non-viscous case the critical relative velocity $u_{rel.\ crit}$ is defined as[84]:

$$u_{\mathrm{rel.crit}} = \left(\frac{8\sigma}{C_D \rho_A D}\right)^{0.5} \tag{35}$$

To consider the viscosity, Hinze [96] uses the assumption of viscosity group that represents the internal viscosity forces to interfacial surface tension forces [90].

$$Z = \frac{\sqrt{\mathrm{We}}}{\mathrm{Re}} \tag{36}$$

The Weber number describes the deformation of a droplet. With higher Weber number the deformation increases till the droplet breaks up into several smaller droplets. The general form of the Weber number is shown in equation (37). Using equations (35), (36), and (37) the critical Weber number can be calculated, see equation (38)

$$\mathrm{We} = \frac{p_A {u_{\mathrm{rel}}}^2 D}{\sigma} = \frac{8}{C_D} \tag{37}$$

$$\mathrm{We}_{\mathrm{crit}} = \dot{\mathrm{We}}_{\mathrm{crit}}[1 + f(\mathrm{Oh})] \tag{38}$$

with the critical Weber number for the non-viscous case $\dot{\mathrm{We}}_{\mathrm{crit}}$.

Experimental data for viscosities of the dispersed and the continuous-phases with variation in viscosity ratio were published by Meister and Scheele [97] with the result that variation in the continuous-phase has no appreciable effect on the atomization process, while an increase in viscosity of the dispersed phase delays the break-up at higher velocities. Taylor's [98] theory was modified by Rumscheidt and Mason [99], so that the critical Weber number varies between 1 and 0.84 for a viscosity ratio η_L/η_a from zero to infinity.

$$\mathrm{We}_{\mathrm{crit}} = \frac{1 + \left(\frac{\eta_L}{\eta_A}\right)}{1 + \left(\frac{19}{16}\right)\left(\frac{\eta_L}{\eta_A}\right)} \tag{39}$$

In general, Taylor's experiments show that it is difficult to atomize liquids with high viscosity ratios.

For a turbulent flow field, experimental results and calculations vary between the different experimental settings and assumptions. Hinze [96] used Clay's [100] experimental data to calculate a We_{crit} of 1.18 while Sevik and Park [101] calculated a We_{crit} of 1.04 that corresponds to their own and Clay's experimental data.

For the later experimental study, critical conditions were identified based on the described relationships. Temperature, pressure and gas composition of the continuous phase were set to be representative for conditions at the end of compression in IC engines. The liquid phase changes from sample to sample.

Heat transfer and evaporation of droplets

The ignition process of liquids is dominated by the heat transfer, evaporation and mixing process with the oxidizer. All three processes are closely linked together and mainly influenced by the conditions like temperature difference of the phases or flow conditions. The theory of heat transfer and diffusion are equivalent. Depending on the accuracy that must be reached in the calculations, the approaches range from simple quasi-steady-state to transient analysis. Because of the complexity of the problem, this work only deals with the fundamental approach of convective droplet evaporation and heating under ideal post-reflected conditions. The theory of convective

droplet evaporation, heating and acceleration are summarized by Sirignano in the second and third chapters of "Fluid Dynamics and Transport of Droplets and Sprays" [102].
In a first step, the steady-state evaporation considers a quasi-steady-state gas phase with the mass and thermal diffusion processes with reasonable mass evaporation rates and droplet life-times. For this process a constant evaporation λ is assumed for the D^2-law with the start droplet diameter D_0 with changing diameter D over time t:

$$D_0^2 - D^2 = \lambda t \tag{40}$$

For further calculation of the droplet evaporation and heating, the following assumptions are made:

1. The droplet is spherical
2. The liquid has a well-defined boiling point
3. Radiation heat transfer is negligible

Based on the work of Faeth [103] the droplet is heated by the surrounding gas. With increasing temperature, vapor is formed at the droplet surface. The vaporization of the liquid consumes the main part of the heat transferred to the droplet, while the outward flow of vapor mitigates the heat transfer to the droplet.
The theoretical and experimental results and correlations are well explained by Lefebvre in "Atomization and Sprays" who summarized the work of Feath [103], Goldsmith and Penner [104], Kanury [105], Spalding [106], and Williams [107]. The fundamental result of droplet heat-up and evaporation including transient conditions is described as the mass rate of diffusion per unit area $\dot{m}_\mathrm{F}$:

$$\dot{m}_\mathrm{F} = 2\pi D \left(\frac{\kappa}{c_\mathrm{p}}\right)_\mathrm{g} ln\,(1 + B_\mathrm{M}) \tag{41}$$

D is the diameter of the droplet; κ is the isotropic exponent and c_p the heat capacity of the gas. B_M can be calculated by the mass fraction of the liquid at the surface $Y_{\mathrm{F_s}}$:

$$B_\mathrm{M} = \frac{Y_{\mathrm{F_s}}}{1 - Y_{\mathrm{F_s}}} \tag{42}$$

The droplet is injected into pressurized gas. The relative motion is equal to the velocity of the droplet. The motion of the droplet is the driving factor for heat and mass transfer rates in the gas film surrounding it. To correct the influence of the flow field conditions the correlation from Ranz and Marshall [108] can be used:

$$\dot{m} = \dot{m}_\mathrm{F} \tag{43}$$

Droplet combustion modes

Droplets, in particular droplets in sprays, play a major role in combustion of liquid fuels. Therefore, a large number of works has been performed in the field of spray and single droplet combustion. Ignition phenomena of single droplets and combustion are outlined in Sirignano's book: "Fluid dynamics and transport of droplets and sprays" [102]. The theories of Chiu and co-workers [109-111] apply under some assumptions: The Nusselt number and the vaporization law depend on the spacing between the single droplets, while the spacing is only considered as an averaged value. The theories are based on a quasi-steady assumption, so that changes of parameters over time are not considered. The studies postulate four different combustion regimes. The regimes are separated by the group combustion number G and can be visualized over the non-dimensional separation between the droplets S and the total number of droplets N as shown in Figure

8. The group combustion number *G* describes the ratio of rate of vaporization to the transport of gaseous species by diffusion and is calculated by the dimensionless numbers: Re (Reynolds number), Sc (Schmidt number), Le (Lewis number), *N* (total number of droplets), r_l (radius of the droplets, and d (distance between the droplet centers).

$$G = 3\left(1 + 0.276\,\mathrm{Re}^{1/2}\,\mathrm{Sc}^{1/3}\right) \leq N^{2/3}\left(\frac{r_l}{d}\right) \tag{44}$$

For large *G* numbers, external sheath combustion occurs. With decreasing value for *G,* the combustion switches over external (*G* > 1) and internal group combustion to isolated droplet combustion typical for values less than 10^{-2}. The results of Chiu and coworkers were confirmed by Labowsky and Rosner [112].

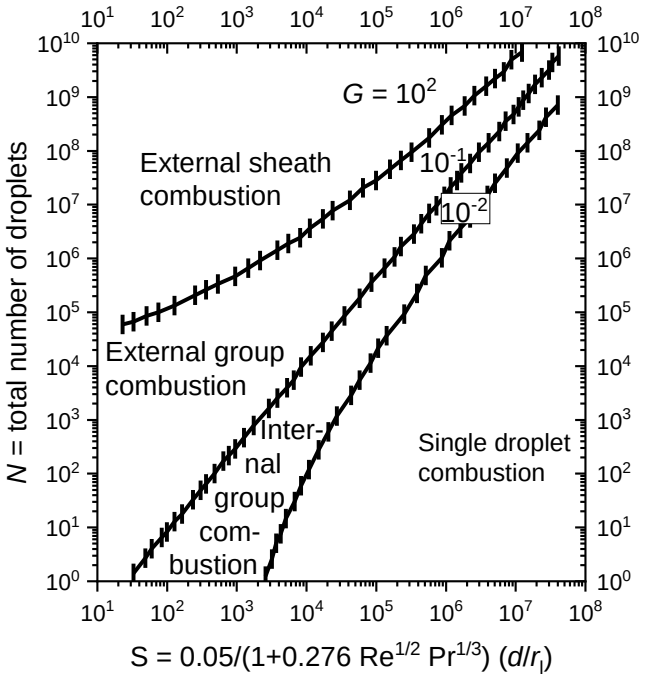

Figure 8: Four group-combustion modes of a droplet cloud [109].

2.4 Optical detection methods of ignition phenomena

Optical measurement techniques are used to follow the ignition process and the injected droplets. The detected radiation ranges from the ultraviolet (UV) to the near infrared (NIR). Three different luminescence phenomena were measured:

1. Chemiluminescence
2. Incandescence of hot particles
3. Laser-induced fluorescence

2.4.1 Chemiluminescence in combustion

Chemiluminescence is the emission of light due to chemical reactions. Different forms of chemiluminescence are known for different phases. In context of combustion, the formation of excited intermediates formed according to (R7) represents only ~1 % of the oxidation pathway. In case of OH* formation, the pathway leading to ground-state OH results in an energy release of –429.9 kJ mol^{-1}, while the R7 pathway leading to OH* releases only –36.7 kJ mol^{-1} [57].

(R6) $O + H + M \rightarrow OH + M$

(R7) $O + H + M \rightarrow OH^* + M$

Besides OH*, more electronically-excited species are formed in the oxidation of fuels like CH*, C_2*, or CO_2*. The electronically-excited molecules have two possibilities to return to their respective ground state. (i) Collisions with other molecules transfer the excess energy to their partner through collisional quenching or (ii) by emission of a photon. Usually, process (i) is more likely. The energy difference between the ground and excited energy levels in combination with the energy levels distribution lead to a characteristic emission spectrum. Figure 9 shows the chemiluminescence spectra of a CH_4/O_2 flame with 30% H_2 addition [113]. In addition Kathrotia et al. [114] published a literature review on chemiluminescence studies. Bozkurt et al. [115] determined reaction rates and implemented those to model for hydrogen oxidation by measuring OH*.

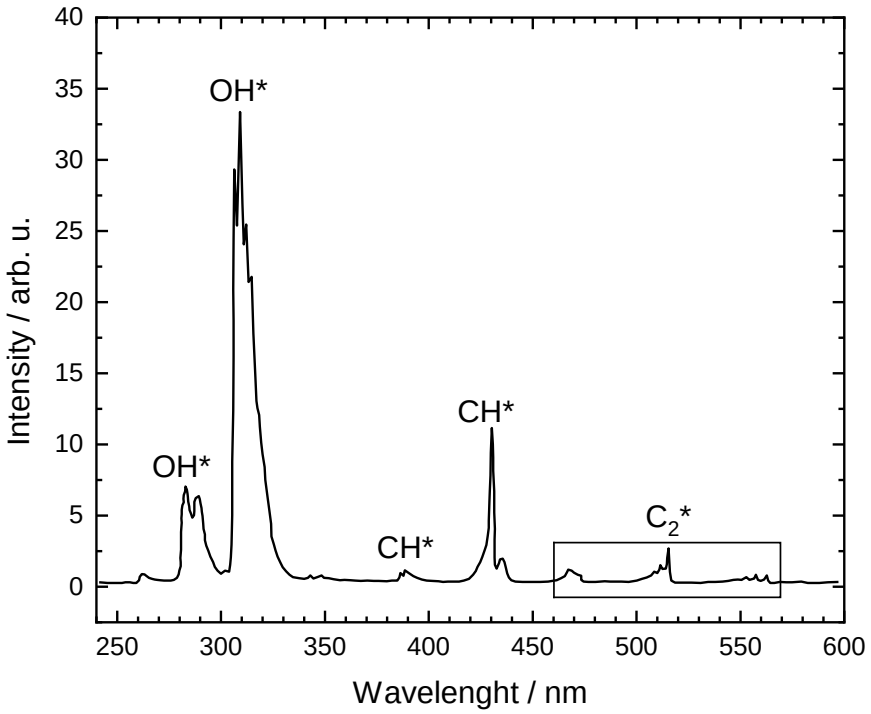

Figure 9: Chemiluminescence spectrum of a CH_4/O_2 flame with 30% H_2 addition [114].

These chemiluminescing species are suitable markers for oxidation. Furthermore, a specific detection by spectral filtering is possible. However, quantitative measurements require very complex calibration strategies [115]. The thermal energy in flames excites all kinds of molecules frequently, but at the start of ignition the gas is comparably cold. The local energy release of the reaction leads to very specific excitation of a few molecules like OH and CH. Therefore, OH* and CH* are good markers for the ignition with highest formation rates of all excited molecules. The detection methods are described in section 3.1.

2.4.2 Laser-induced fluorescence (LIF)

Fluorescence from excited states pumped by electromagnetic radiation from a low band is called laser-induced fluorescence (LIF). The photophysical effect of LIF is explained by the simplified Jablonski diagram shown in Figure 10. A molecule in the ground state S_0 populates different vibrational energy levels according to the Boltzmann distribution. At room temperature, the vibrational ground state is populated almost exclusively. The energetic difference of the S_0 and the first excited state S_1 is specific for the molecule and corresponds to the absorption characteristics of the molecule. In Figure 10 the green wave lines illustrate the excitation by a laser. In most applications, the pumping energy is higher than the energy difference between the vibrational ground levels of S_0 to S_1. Therefore, higher vibrational levels are populated on the S_1 level than

on the S_0 level. By vibrational relaxation, the molecule will reach thermal equilibrium. To return to the S_0 level the excited molecule reduces its energy by releasing a photon. The released photon is of longer wavelength than the pumping radiation because when returning to the ground state higher vibrational levels are populated mostly. Vibrational relaxation in the S_0 level achieves thermalization. Because of the lower energy relative to the initially populated levels, the fluorescence the light is red-shifted compared to the light/energy of the absorption. The vibrational relaxation in the S_1 level strongly depends on the state of phase. In liquids, the vibrational relaxation is very fast, so the fluorescence mainly starts from the ground level of S1, while the fluorescence and the vibrational relaxation appear on similar times scales in the gas phase. Further effects are not explained here but can be found in "Principles of Fluorescence Spectroscopy" by Lakwicz [116].

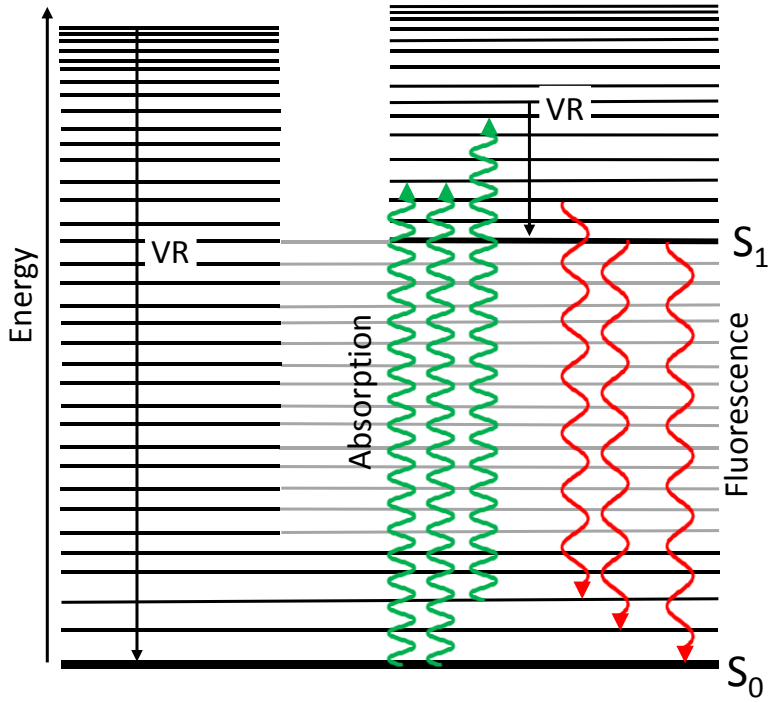

Figure 10: Simplified Jablonski diagram based on Ref. [117].

LIF is used in many fields from standard devices to very specific applications in science. The best-known devices are dye-lasers, which use a laser dye as laser medium, while different laser dyes can be used to address specific output wavelength. Very well-known are laser dyes of different types of coumarin and rhodamine. In their pure form they are present as solids but can be dissolved in solvents like ethanol.

LIF as a measurement technique for combustion systems found its application in different fields to study the structure of molecules, detection of specific species or flow visualization. In case the system of interest has no fluorescence properties, so-called "tracers" can be added in small amounts. The choice of tracer has to fit to the spectral requirements on the one hand and should have physio chemical properties similar to the system of interest on the other hand to minimize the influence of the tracer on the behavior of the original system. A detailed review of tracer based LIF techniques in combustion systems is given by Schulz and Sick [118]. For example, aromatics like toluene [119] or naphthalene [120] are high relevant because of their absorption and fluorescence characteristic in the UV and near UV, respectively.

Base oils shown very low fluorescence, while the oil additives show significant stronger fluorescence when excited in the UV-range [121]. The absorption and fluorescence properties overlap with those of classical tracers like aromatics [122].

Therefore, aromatic tracers and the fluorescence properties of oil additives are not suitable to use these to track oil droplets in a gas phase fuel/air mixture while ignition occurs. Different tracers with longer fluorescence wavelength were tested for the separation of the different emission sources from each other. Several laser dyes in the spectral range of 450–600 nm are commercially available. Pyrromethene 597 shows the highest quantum efficiency at relevant conditions and therefore fits well for the later experimental application. The absorption and fluorescence properties are shown in Figure 11.

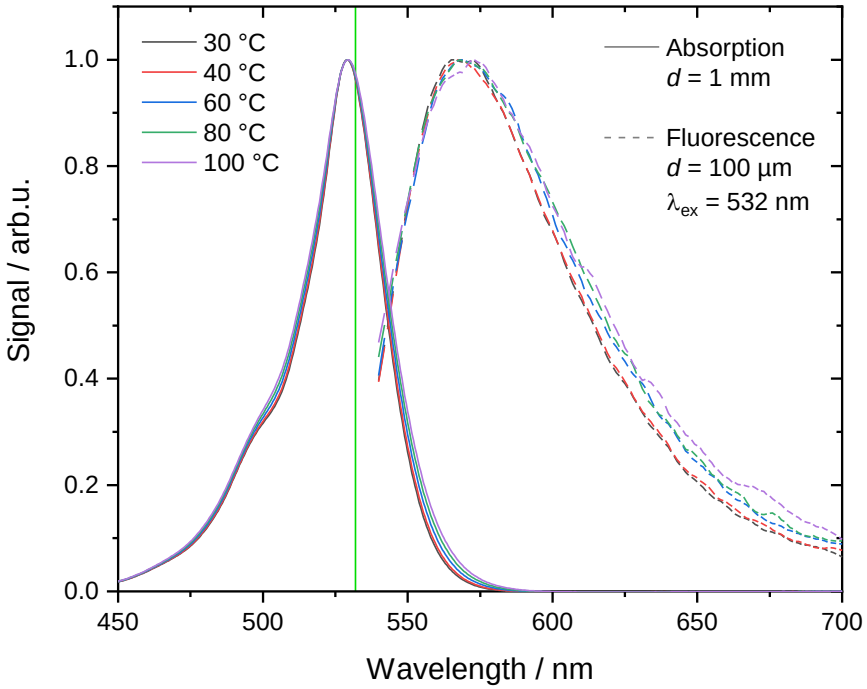

Figure 11: Absorption and fluorescence spectra of pyrromethene 597 in PAO (0.1 mmol/l) at temperatures from 30–100°C, absorption and fluorescence are normalized to the peak maximum.

2.4.3 Incandescence of hot particles

The third light-emitting phenomenon of importance in the following study occurs later in the combustion processes and is called soot incandescence. Thermal radiation is electromagnetic radiation from surfaces of all kinds. The best-characterized case is the black body radiation from a black body ($\alpha = \epsilon = 1$) in thermodynamic equilibrium where the Planck law describes the emission spectra dependent on temperature. The peak in thermal radiation is in the near IR spectrum and shifts more to the visible spectrum with increasing temperature. The deviation in wavelength of incandescence to the previously described luminescing phenomena enabled a separation of the emission sources in case selected detection in the fully visible range. By incandescence hot particles were identified already before the ignition.

3 Experiment

To study the pre-ignition of fuels decoupled from pressure/temperature history, shock tubes are nearly ideal test reactors. Conditions similar to the end of compression can be realized in high-pressure shock tubes like the one presented below. To study the impact of hot surfaces and lubricant oil droplets two new experimental modifications will be introduced.
The local pre-reactions and the development of volumetric ignition are followed by different imaging setups. Pre-studies for the characteristic of the hot surface or the droplet injector are described briefly. Thermo gravimetric analysis of the oil samples was performed too, to generate information about the samples with an undefined composition (Table 2).

3.1 High-pressure shock tube facility

The investigations presented in this work were carried out in the high-pressure shock tube of the "Institute for Combustion and Gas Dynamics – Reactive Fluids" – Duisburg. A sketch of the shock tube is shown in Figure 12. The shock tube consists of a stainless-steel tube with an inner diameter of 90 mm, divided into two sections by a diaphragm. The diaphragm is an aluminum disk of 2.5 mm thickness with a cross milled into the surface for reproducible uniform opening at set driver gas pressure. Typically, pressures of 20 bar behind the reflected shock wave (p_5) can be reached using a 2.5 mm thick diaphragm. The jumps in pressure are followed by an increase over time dp/dt less than 2–3 % / ms. The increase in dp/dt is linear for about 3 ms. Afterwards, the pressure is constant, while a small variation is observed in the experiments by quality variation of the tailored interface. Other thicknesses can be used to achieve other peak pressure ranges. The right section of the tube in Figure 12 is the driven section with the initial conditions of the test gas p_1 and T_1 mentioned in section 2.2. The test gas is prepared manometrically in a stainless-steel mixing vessel measuring the pressure with a pressure gauge 0–1 bar and a pressure transmitter (Keller type PAA-35XHTC). For homogeneous mixing, an electrical steerer is installed that mixes the gases at least 2 h and thus well-defined gas mixture is after filled in into the driven section. The driver section, the driven section and the mixing vessel are pumped by a dry pump system of a claw pump (Edwards QDP80) in combination with a roots pump. The mixing vessel is pumped to 2 10^{-2} mbar before preparing the mixture. The driver section is pumped to 7×10^{-2} mbar and the driven section is pumped to 8×10^{-2} mbar in a first step and down to 6×10^{-5} mbar by a diffusion pump in a second step to ensure high vacuum. The driver section is filled *in situ* with a helium/argon mixture by two high-pressure mass flow controllers (consisting of Bronkhorst flowmeters and Flowsurf regulator valves) to extend the measuring time up to 15 ms by driver gas tailoring. The required He/Ar composition is calculated applying the equation (24) and (25) from Palmer and Knox [37] based on the calculated experimental conditions using the zero-dimensional shock-tube code CHEMKIN [123] based on the shock equations from Oertel [35] explained in detail in 2.2. The real experimental conditions were post calculated with the speed of the incident shock wave. Therefore, four pressure transducers (PCB 112 A05) are mounted in the sidewall at a distance of 108.5, 89.5, 61.5, and 1.5 cm of the endwall to detect this speed. The pressure detection has a time resolution of 1 µs. The delta time between the pressure rise of the different pressure transducers is used to calculate the velocity of the incident shock wave using the least-squares method and considers an attenuation of 1–2%.

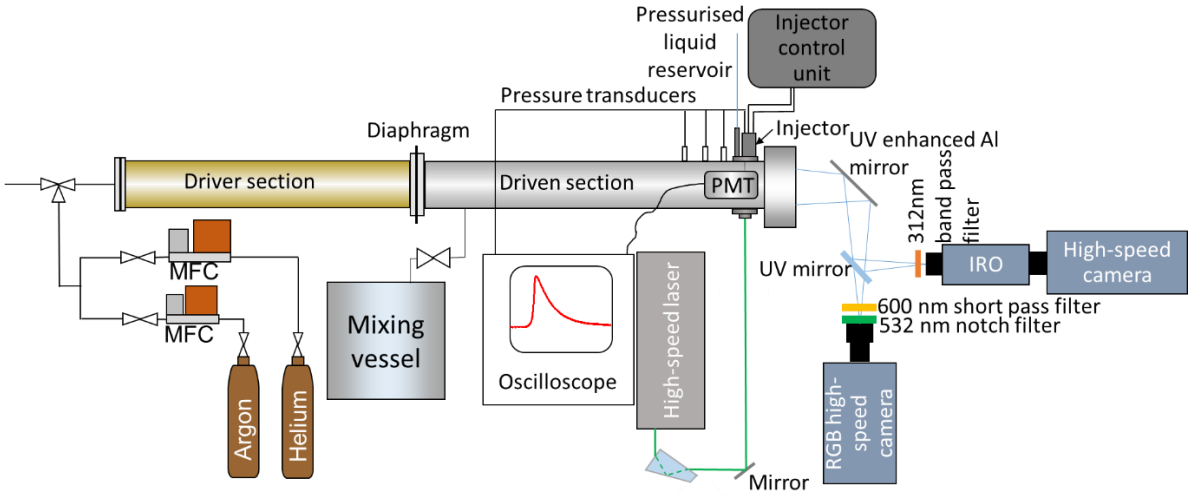

Figure 12: High-pressure shock tube with a single-droplet injector and high-speed imaging through the endwall [124].

The pressure transducer in the measurement section is placed 15 mm from the endwall and is used to track the pressure over the observation time. The pressure transducer was shielded by RTV silicon to protect it from thermal effect over time. Besides the pressure sensor, three additional ports are symmetrically located in the sidewall in the measuring plane. Figure 12 shows the scheme of the shock tube with the injector mounted in the sidewall further described in section 3.1.2. This port could be replaced by an optical one for line-of-sight chemiluminescence measurements or by a glow plug holder described in section 3.1.1. One CH* or OH* sensitive photomultiplier (PMT) was mounted in the top position. More details about the studies with the mounted glow plug using sidewall imaging from the opposite port can be seen in section 3.1.3.1. In this case, the endwall was made from metal. For optical observations from the endwall a new endwall was manufactured which is described in detail in section 3.1.3.2.

3.1.1 Surface-induced ignition

To generate a local hot surface area, a commercial high-temperature glow plug used for engine applications (BERU Type GE101) was introduced in the sidewall port opposite to an endoscope holder. A glow plug holder was constructed as shown in Figure 13 to place the hemisphere tip of the plug (radius of 1.5 mm) flush with the shock tube sidewall. Further details of the glow plug and the operation were published by Niegemann et al. [48]. The following section is a reprint of paragraphs of the publication [48]. This glow plug reaches temperatures over 1200 K within a rise-time of 5 s according to its specifications [125]. For faster heat-up and defined maximum temperature, the glow plug was operated outside its specifications by powering it with an external power supply.

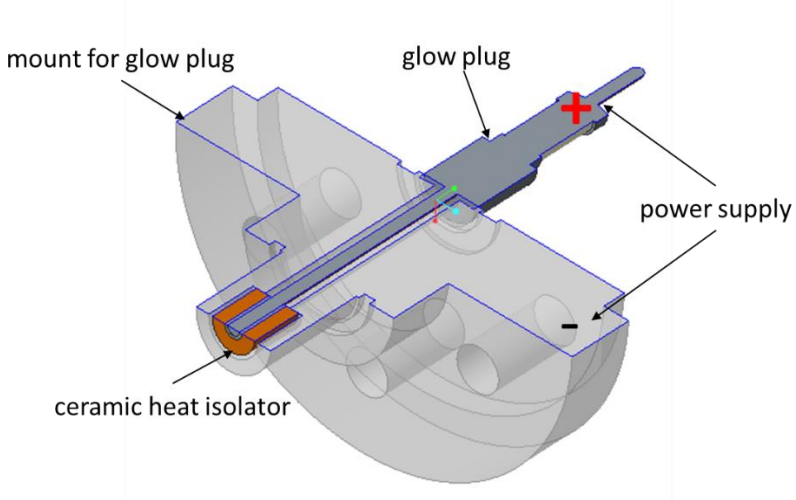

Figure 13: Arrangement of the glow plug for generating a locally hot surface [48].

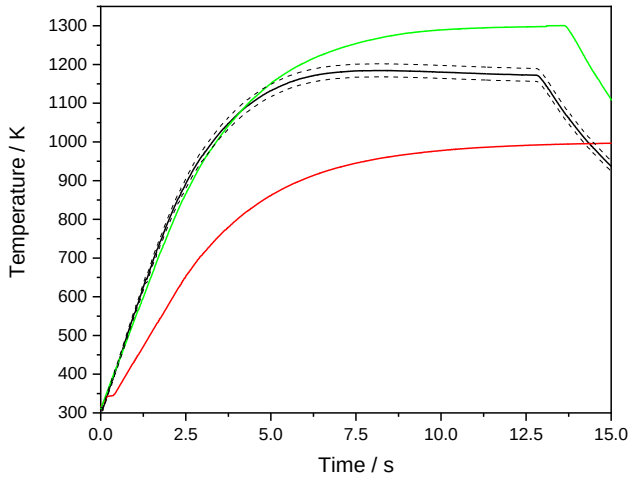

Figure 14: Measured temperature evolution of the glow plug with an emissivity of 0.88 operated with 8 V and 13 A (black line); 6 V and 1 A (red line); 8 V and 16 A (green line)[48].

The current and voltage were varied in a parameter study to determine the optimal settings for fast heat-up to a defined temperature. The surface temperature of the glow plug was measured with two different two-color pyrometers (Sensortherm MI18 (1.8 µm wavelength) and MI16 (1.6 µm wavelength). Both pyrometers were calibrated by the manufacturer with a black-body radiation source. The emissivity ε of silicon nitride is 0.88±0.05 depending on temperature and wavelength according to Ref. [126]. Figure 14 shows the heating characteristics of the glow plug determined for different end temperatures. The uncertainty in emissivity would result in uncertainty of ±18 K after 5 s heat-up time (dashed line). The uncertainty of the pyrometer system is about 4 % (related to the values in °C).
Approximately 5 s before the burst of the shock-tube diaphragm, the heating of the hot plug is started to reach the set temperature of the glow plug. The time required for the diaphragm to burst was measured as a function of filling pressure to determine the instant for manually switching on the glow-plug power.

3.1.2 Generation of single droplets against high pressure

To investigate the influence of liquid droplets on the ignition of fuel/air mixtures, droplets were injected into post-shock-heated gas at high pressure. The used injector is an adapted type of a commercial micro-dispensing injector (MDV3300+, Vermes GmbH). In Figure 15, a picture of the assembled injector is shown in the center. On the left, the inner parts of the injector that are in

contact with the fluid are shown. On the right, a sketch of a cut through the injector front end is shown. High-precision dosing of the liquid is achieved by a piezo-stack driven actor that is cooled by air through an in- and outlet port. An actor mechanics drives the needle, which is the only connecting part between the electric and fluid transport part. The top sealing ring seals the needle to keep liquid from entering the electric device. After filling the fluid reservoir, the pressure tubing is connected to a nitrogen gas supply with pressure of up to 21 bar.
To avoid any back flow from the shock tube into the fluid reservoir, the pressure of the fluid reservoir was set ~0.1 bar higher compared to the pressure in the shock tube during an experiment. For this purpose, the original parts were replaced against a metal one to sustain high pressures. When the needle is operated, the liquid flows through the tubing that connect the reservoir with the nozzle parts and the actor mechanics, called fluidic shown in Figure 15, along with the cylinder liner that holds the nozzle with a diameter of 45 µm. Different nozzles diameters are available. The smallest one (45 µm opening) was chosen to generate the desired small droplets. The finally formed droplets will be larger than the nozzle diameter for droplets formed in the Rayleigh and first wind-induced break-up regimes (see section 2.3.2.2). The liquid flows between the cylinder liner and the needle, shown in Figure 15 on the right side. When the control unit of the injector is switched on, the needle is in the bottom position. After adjustment of the needle height, the needle perfectly sits in the nozzle and is leak-proofed against high vacuum and pressure. This adjustment can be implemented at operating temperatures without liquid. The injector is a type with adjustment from the top, i.e., one can change the position of the needle with the mechanical actor by a screw on the top of the injector. Other types are adjusted by the thread of the cylinder and fluidic which is not possible with the used holder system when mounted in the shock tube. The fluid is kept in the crevice between the needle and the liner until the actor starts to move. The outer sealing ring seals the injector in the injector holder for operation in the high-pressure shock tube.

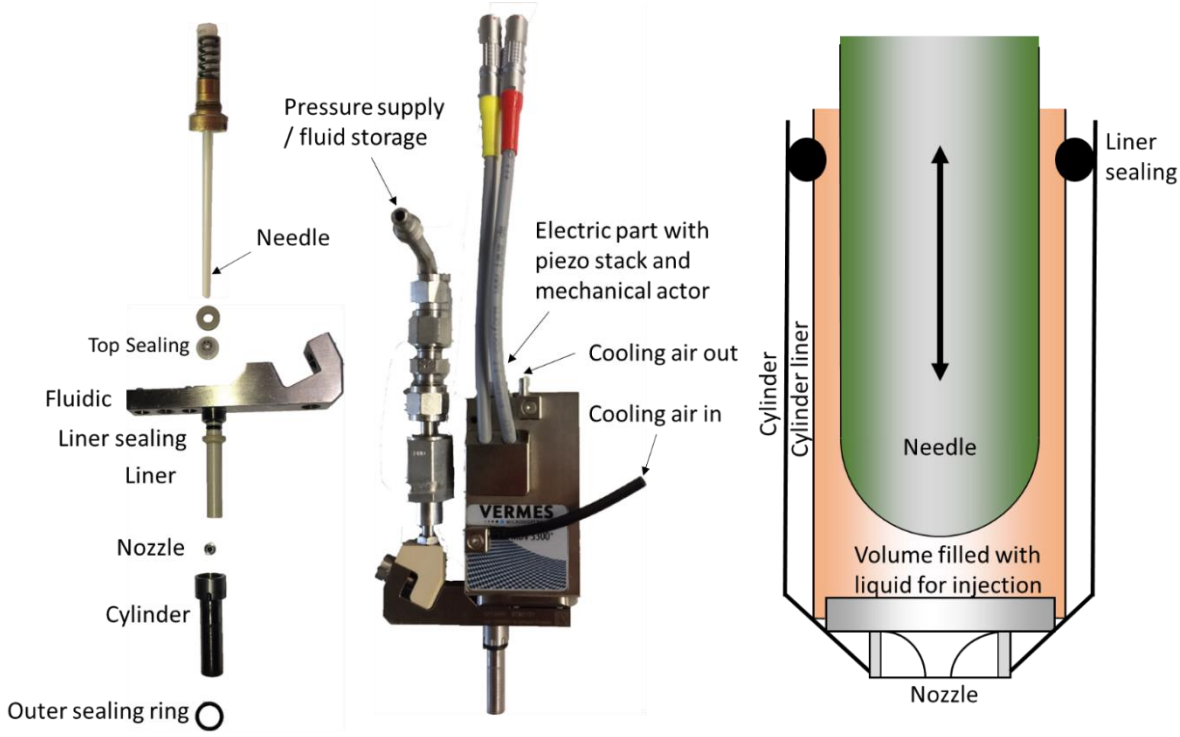

Figure 15: Left: Disassembled liquid carrying parts of injector; Center: Complete assembled injector; Right: Sketch of a cut through the injector front end [124].

The injection procedure is divided into three steps: starting in the bottom position, the needle seals the nozzle. The measurement system is triggered by the pressure transducer in the

measuring plane. It is possible to inject droplets before the incident shock wave (using a different trigger system) or behind the reflected shock wave. However, it was preferred to proceed the injection behind the reflected shock wave because interaction with the incident shock wave would disperse the droplets [127, 128]. When the injector is triggered, the needle lifts (Figure 16, phase I). The level of lift can be set in percentage by the control unit to adjust the filling volume of the fluid. The time it takes the needle to reach the top position is called “rising time” and can be varied. After this step, the “open time” of the injection begins (phase II). In time, the liquid flows into the volume between the needle and the nozzle. Because of the very narrow tubing, the pressure in the reservoir is not sufficient to press the liquid through the nozzle. Experimental observations have shown that vibrations can eventually lead to a release of liquid material. In phase III “falling slope”, the needle moves downwards and pushes the liquid through the nozzle. The injector rests in the bottom position for a span of time until the next trigger signal. This procedure can be repeated, depending on the number of injections that are set in the control unit.
All these parameters have an impact on the droplets and their formation. Because the variation of all parameters results in too many combinations, only those with major impact were varied. The “falling time” in combination with the “needle lift” is the most important parameter. While the “falling time” determines the time the needle moves, the “needle lift” determines the distance. Therefore, the combination results in the velocity of the needle. Additionally, the “needle lift” controls the injected mass which influences the momentum of the injected droplets.
Whenever refilling the empty injector with liquid, the procedure was run continuously for 500 cycles to flush all the air out of the fluid system. Changing the liquid requires to disassemble all parts to be cleaned and re-adjusted. Details about the droplet formation are shown in section 5.2.3.1.

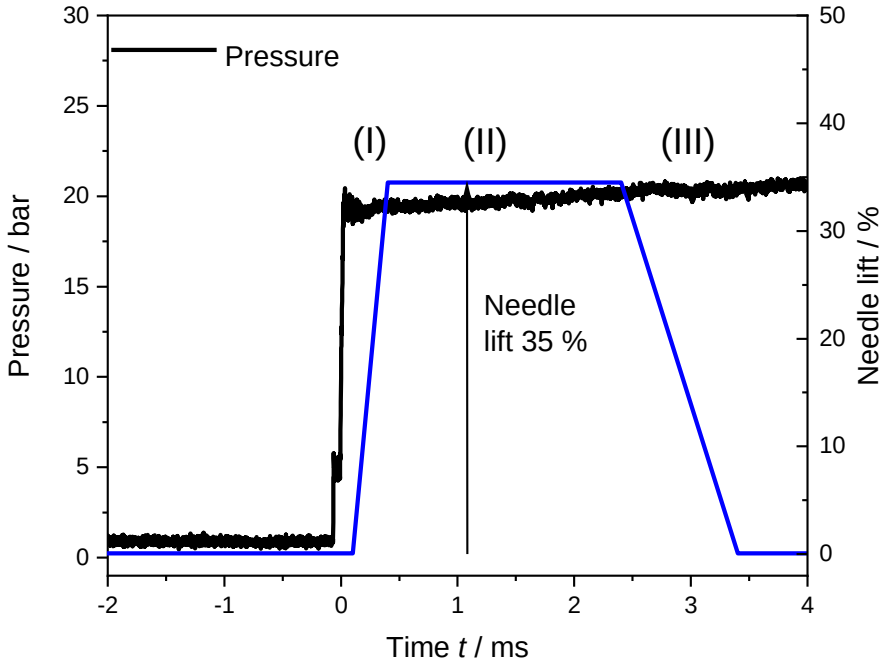

Figure 16: Operation principle of the injector showing the different steps of the injection after the arrival of the shock wave[124].

3.1.3 Measurement techniques

Beside the pressure measurement chemiluminescence measurements are standard tools for ignition studies especially in the field of kinetics. In shock-tube studies the pressure trace shows characteristics (jumps) like the first increase by the incident wave and a second rise about double the amount by the reflected shock wave. When shock attenuation and boundary layer effects

(resulting d*p*/d*t*) are ignored, the pressure ideally stays constant for a non-reactive gas mixture with tailored driver gas until the first expansion wave reaches the measurement plane. In a reactive mixture the heat release is directly linked to the pressure, if the reactive volume is assumed adiabatic. The shock tube is not a real constant volume reactor although this assumption is often made as a simplification in simulations with constant volume and constant energy. Due to the fact that in reality the shock tube is not a perfect constant volume reactor, the measured pressure trace is less than the expected pressure based on the volume work.

In this work, OH* and CH* were detected by a photomultiplier (Hamamatsu 1P21) with a bandpass filter for 310±5 nm through a window situated on top of the shock tube and a photomultiplier tube of the same type with a bandpass filter 430±5 nm located at the left side, respectively. This PMT can be replaced by the injector or the glow plug as shown in Figure 18. The signals of the pressure and the two photomultipliers were used for monitoring the ignition delay times of homogeneous gas mixtures. The endwall and the left window were closed by non-optical stainless-steel dummy flanges.

To determine the ignition delay time, the pressure and chemiluminescence traces were used. Figure 17 shows the trace of pressure and the chemiluminescence signals of CH* and OH*, respectively. The ignition delay time is defined as the time the reflected shock wave passes the measurement plane and the steepest rise in OH* or CH* extrapolated to the ground level.

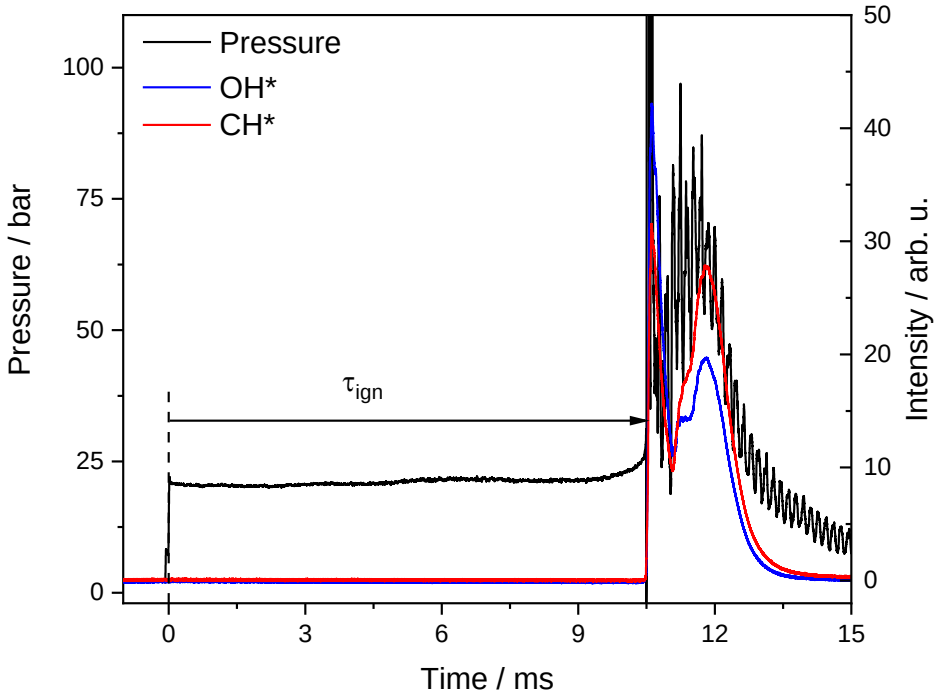

Figure 17: Determination of ignition delay time by chemiluminescence and pressure trace.

3.1.3.1 High-speed imaging from the sidewall

For sidewall imaging, a UV-transmitting endoscope with a front diameter of 10 mm and a field lens [135-137] was used. Chemiluminescence of the ignition was detected in the visible light range. The endoscope was chosen for its wide-angle characteristics to detect low light levels from a large field of view.

A standard camera lens (Nikkor $f = 50$ mm, $f_{\#} = 1.8$) and a 30 mm ring were used to relay the real image from the field lens of the endoscope onto the detector of a Phantom V7.3 high-speed camera. This combination results in a projected pixel size of 0.338 mm/pixel and an imaged area

of 120 mm in diameter along the opposite sidewall that is detected. The endoscope was directly mounted on the shock tube while the camera and the relay lens were separated from the shock tube allowing the optical elements to float against each other and thus accommodate for the vibration of the shock tube during shock arrival. Consequently, a slight drift of the image out of the optical axis is caused that was corrected by post-processing. To detect the full image of the field lens at any time of the experiment, the detected area is wider than the image of the field lens itself.

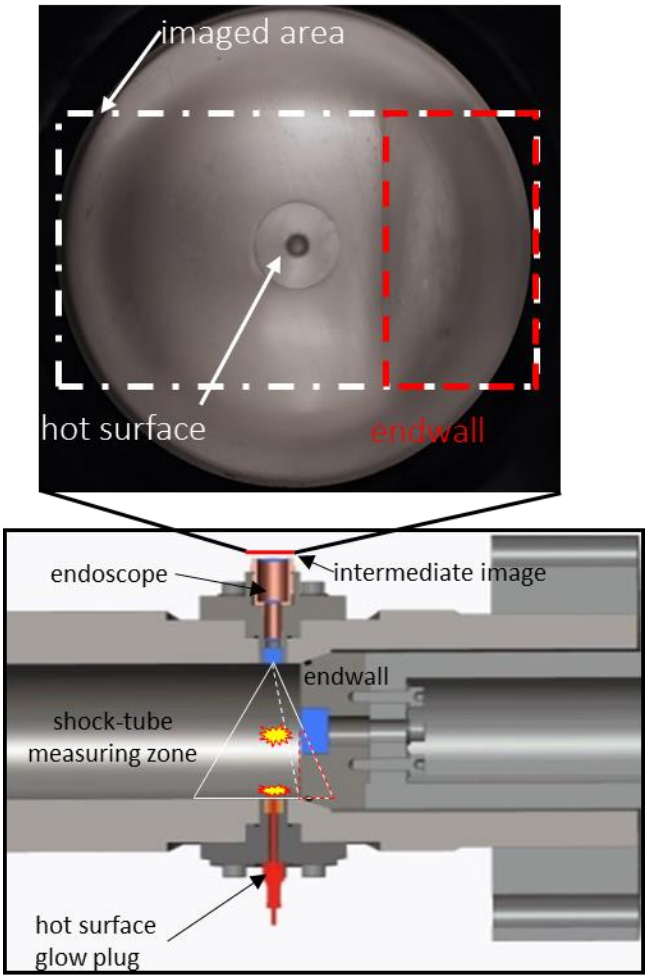

Figure 18: Photo through the endoscope optics (top). Because of the wide-angle characteristics of the endoscope, the endwall is seen as an extended area on the right side of the image. The left end of the endwall is marked at the position where it intersects with the shock-tube wall 15 mm downstream of the glow-plug position (bottom) [48].

The images were used to localize the starting point and the propagation of the combustion process in time. The image sequences clarify whether or not ignition occurred behind the incident shock wave – here, typically the reactive gas is not quiescent and has a much lower temperature – or behind the reflected shock wave, where the gas is quiescent.

3.1.3.2 High-speed imaging from the endwall

To detect local ignition, imaging was required. In the context of this work, an optical endwall was designed as shown in Figure 20. The transparent endwall consists of a stainless-steel holder-ring and a mounting tube piston with a 70 mm diameter aperture the holder ring is screwed on. On the chamfering side of the ring, an o-ring was placed in a groove to seal the holder ring on the outer side and the inner shock tube wall. In the ring, a 30 mm thick sapphire window with a diameter of 80 mm was glued by an industrial glue (Stycast 2850 FT). Behind the shock tube, a

45° UV-enhanced Al mirror was placed to direct the light to a color high-repetition-rate camera (Phantom 1216) that is placed at a 90° angle to the shock tube. The camera is equipped with a macro lens (Tokina, $f = 100$ mm, $f_{\#} = 2.8$ lens). In front of the lens, a 532 nm notch filter was mounted to suppress scattered laser light. In some cases of n-dodecane and base oil injection, an additional 600 nm short-pass filter was mounted to block the high intense incandescence from local soot formation. The sensor response of the color high-speed camera and the filter curves are shown in Figure 22.
In the above-mentioned cases, an additional intensified high-repetition-rate camera (Photron SA-Z) was used. With the second camera, OH* high-repetition-rate imaging was obtained simultaneously. A UV mirror was used as a beam splitter placed between the UV enhanced Al mirror and the filter of the color camera at a 45° angle. A 312 nm (35 nm FWHM) bandpass filter separated the OH* line from the broad-band emission. An 85 mm, $f_{\#} = 2.8$ UV lens (LaVision) in combination with a high-repetition-rate intensifier (LaVision) was used. Both cameras were synchronized in Davis 10 and operated at 30 kHz. The focal plane of both cameras was set to the measurement plane 15 mm from the endwall. The position is marked by a white dashed line in Figure 20 and is the cutting plane of the drawing in Figure 21. A target was used to focus the camera optics and a variety of positions was recorded to estimate the depth of field. Based on the images shown in Figure 19 a relatively sharp image is created in a depth of field of about 20 mm.

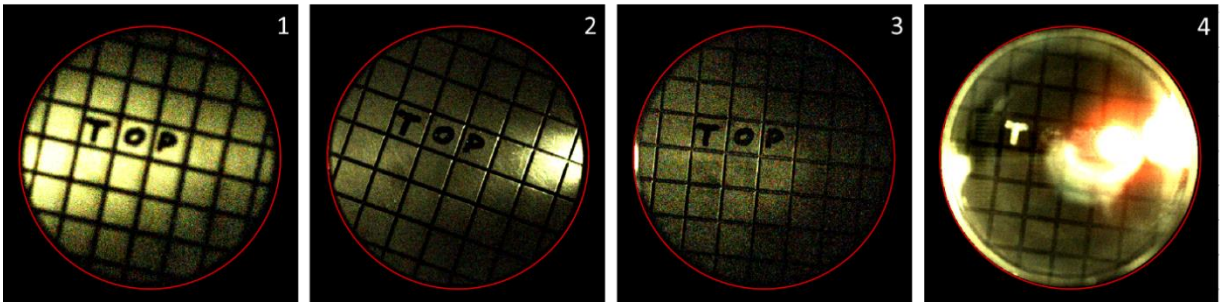

Figure 19: Target images 0-, 15-, 35-, and 70-mm distance from the endwall.

This setup was used in two different versions. Without the intensified camera, homogeneous PRF95 ignition was studied as well as the ignition of PRF95 with injection of oil-based samples. With the intensified camera, the ignition of ethanol and the ignition of PRF95 with injection of base oil and dodecane was studied.

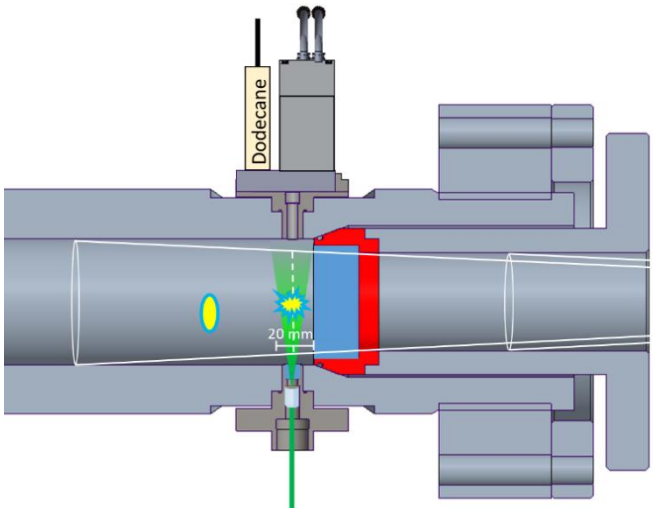

Figure 20: Sketch of the measurement section with the transparent endwall as a cut along the shock tube [124].

3.1.3.2.1 Droplet visualization by laser-induced fluorescence (LIF)

For the observation and detection of the droplets, an illumination system was necessary that works for very short exposure times. The laser-induced fluorescence technique was chosen because it provides a high signal intensity on very short time scales. The laser dye pyrromethene 597 was mixed into each sample at a concentration of 0.1 mmol/l to visualize the droplets. The first published work using this technique stemmed from Thirouard et al. [129] who investigated the transport processes in the piston ring pack. The absorption and fluorescence spectrum of pyrromethene 597 dissolved in polyalphaolefine (PAO) at a temperature of 100°C is shown in Figure 22. In the experiments, different samples were mixed with the dye. The absorption and fluorescence characteristics are known for a solvent in PAO, but were not measured for the different samples pyrromethane 597 was dissolved in. The effect on absorbance of different solvents was negligible in this study because the technique was not used for quantification based on signal intensity. All samples containing different additives were dissolved in API Group I base oil. Group I base oils are of a mineral base, while the PAO is synthetic and therefore contains no Sulfur (chaptor 2.3.2.2).
The dye excited by light from a high-repetition-rate, frequency-doubled, pulsed Nd:YAG laser at 532 nm (EdgeWave IS16II-E) with a repetition rate of 15 kHz. The laser beam was focused by lenses onto a meniscus lens located in front of the sidewall window. This front lens expanded the beam to illuminate a large area in the tube as shown in Figure 21.

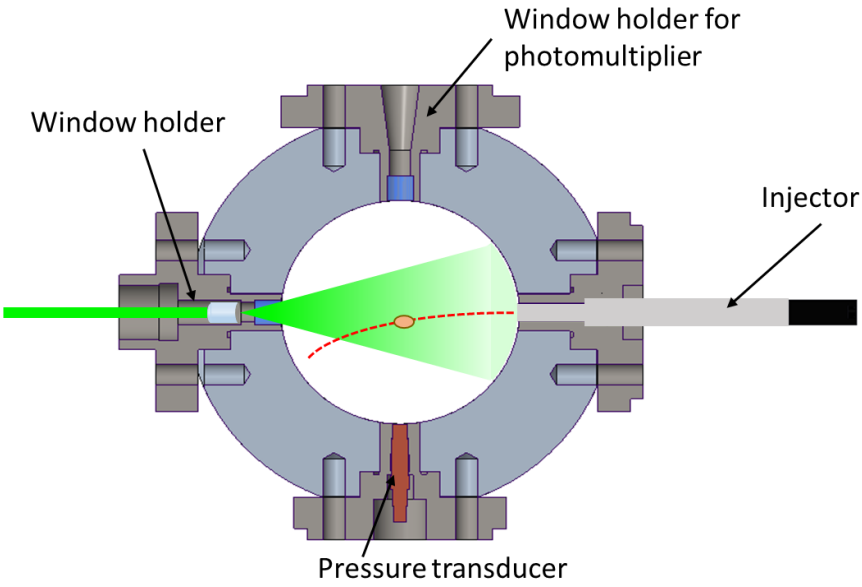

Figure 21: Cut through the measurement plane of the high-pressure shock tube (view from the endwall) [124].

The expanded beam is directed to the injector tip located on the opposite sidewall. The fluorescence signal fits well to the sensor response in the green and red channels of the color camera.

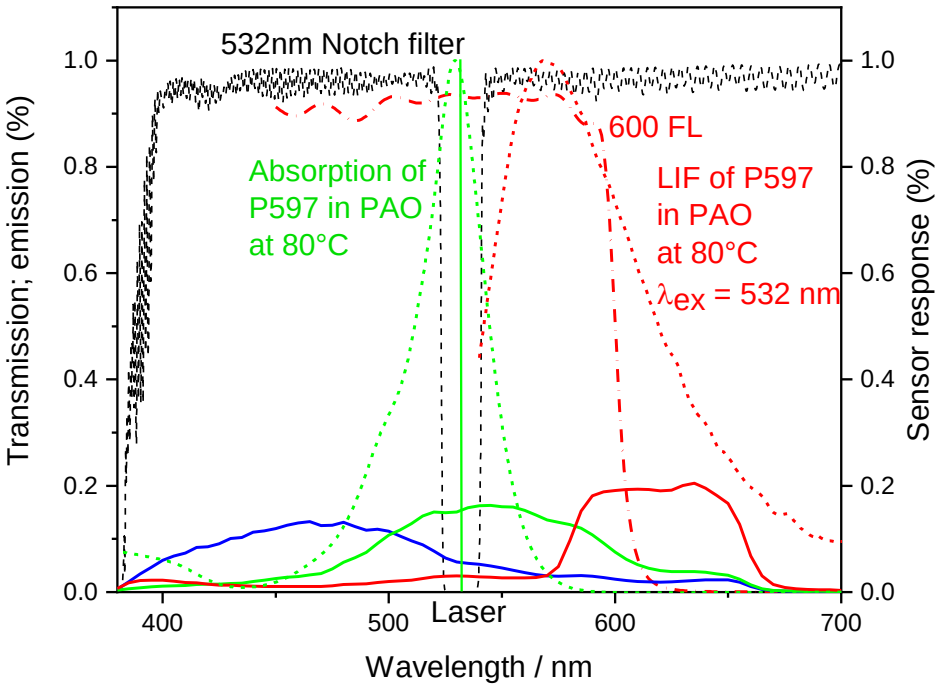

Figure 22: Absorption/fluorescence spectra of the dissolved dye (dot green/red line);
the absorption lines of the notch 532 and short pass 600 filters (dot dash black/red line);
and sensor response of each channel of the phantom 1216 (solid red/green/blue line).

The spectral properties were not sufficient to identify the droplet in a reactive gas mixture at autoignition conditions, because local ignition around particles was observed in experiments without injection in the same spectral range as the fluorescence of the droplets. To distinguish between a droplet, an igniting droplet or a local gas ignition triggered by a particle, a skipped illumination was used to identify the droplet before it ignites. The high-repetition laser runs at a frequency of 15 kHz while the camera runs at 30 kHz. If a green spot appears in an image like in Figure 23, disappears in the next frame when the laser is off and appears again when the laser is on again, then it can be identified as a droplet. In the frame at 2.72 ms (frame 4) the droplet is not visible because the laser is off, but at the position of the droplet, a blue area appears that grows in the following frames. This is the local ignition which reaches the droplet at 2.8 ms. The subsequent injected liquid is shown in bright green before it is consumed by the combustion.

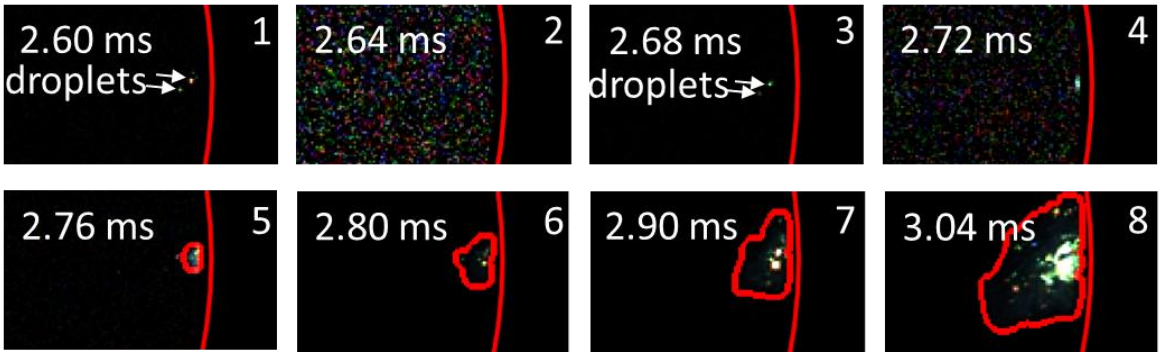

Figure 23: Section of the observed area close to the injector tip, showing the local droplet igniting [124].

3.1.3.2.2 Image post-processing

All images were processed in Matlab to correct the background of the images and extract the relevant information. A background correction by subtraction of an average image of 300 background images was performed. No correction in color was run, so that the images appear blue-shifted because the short-pass filter suppressed the emitted light of wavelengths longer than

600 nm. The impact of the narrow band 532 nm notch filter on the resulting color impression is small.
OH* images are background corrected to minimize artefacts of signal, due to remaining light that is not emitted by the experimental process. Additionally, a white-field correction was performed to correct signal differences from location depend transfer function of the optics. Therefore, the OH* images (*I*) were subtracted by an averaged background image ($\overline{I_{\mathrm{BG}}}$), consisting of 300 background frames. A white field image was recorded by placing a UV mercury lamp far upstream in the shock tube. 1000 images were averaged to generate a white field image ($\overline{I_{\mathrm{WF}}}$).

$$\frac{I_x - \overline{I_{\mathrm{BG}}}}{\overline{I_{\mathrm{WF}}} - \overline{I_{\mathrm{BG}}}} = I_{\mathrm{corr.}} \tag{45}$$

The corrected Images $(I_x)_{\mathrm{corr.}}$ were further processed: The blue channel of the RGB images and the OH* images were used for the detection of flame edge using an algorithm based on a binarization according to the multi-threshold Otsu method [130]. The fundamental structure is described by Shawal et al. [131] to correlate flame properties like area, mass fraction burned, average growth rate with crank angle or pressure. The area of the flame or **burned area** (BA) is located by the number of pixels in the contour. The detected flame contour is illustrated in each image as an additional red line. The inner part of the shock tube that was observed by the cameras is called the **observed area** (OA). This is marked by a red circular line in the images while the outer area is blacked. The **normalized burned area** was calculated:

$$\frac{BA}{OA} = (BA)_{\mathrm{norm}} \tag{46}$$

The normalized burned area was traced over time to determine the onset of the first local flame occurrence. In studies without droplet injection, the **local ignition delay time** was defined as the time of constant conditions until the first local flame found by an increase in normalized burned area occurs.
In case of droplet injection, the droplets were found by an alternating pattern in image intensity. Then the onset of droplet ignition was determined when the flame edge detection algorithm captures the droplet for the first time. More general details about high-speed imaging are summarized in ref. [141].

3.2 High-pressure cell

The injector has many parameters to cover a wide field of applications. To generate droplets of 50–250 µm in diameter against high pressure, a parameter study was necessary. The range of 50–250 µm was chosen based on the results from Ohtomo et al. [71] and analytic calculations based on the work from Kalghatgi and Bradley [65]. Shock-tube experiments are costly and time-consuming; therefore, a pressure cell was built to study the injector parameters in a continuous way. The cell was designed with vertical long windows for observation of the injection. The cell allowed pressures up to 25 bar at a temperature of 100°C. The goal was to find the injector settings which generate small single droplets and reach a depth of penetration of 45 mm in about 10 ms under post reflected shock conditions. The combination of pressure and temperature result in a gas density which is the main parameter to describe the friction between the gas and the droplet. Hence, an equal density was realized by adjustment of pressure at room temperature to reach densities of $\rho = 7–10$ kg/m^3.
A schlieren high-repetition-rate imaging optics was set up as shown in Figure 24 (view from the top). It consists of an LED as a light source with a pinhole in the front. At 15 mm distance a $f = 15$ mm convex lens was located to generate nearly parallel light beams. The parallel beams

pass the cell and the two parallel windows in the cell and are focused by an additional convex lens $f = 15$ mm. In the focal plane of this lens, another pinhole was located and could be adjusted to set the sensitivity of the schlieren setup. A high-speed camera phantom V7.3 in combination with a macro lens, (Tokina, $f = 100$ mm, $f_{\#} = 2.8$) was used for the imaging.

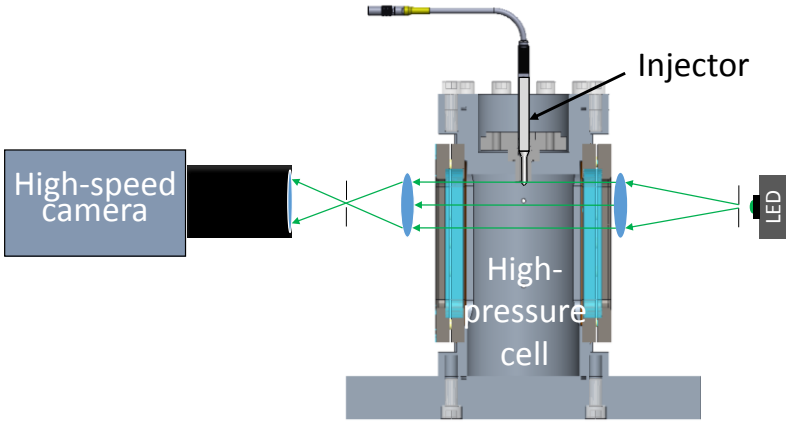

Figure 24: View from the top of the schlieren setup of a high-pressure cell with the injector mounted in the endwall.

The optics were placed on rails to move it along the optical windows to measure at different positions from the injector tip. The droplets' release and their interaction with the ambient gas were observed at three different distances from the injector, first close to the tip (0–14 mm), at a distance of about 30 mm and about 45 mm equivalent to the central axis in the shock tube. Additionally, the injected amount of liquid was measured by injecting 500 times into a shell and measuring the amount by weight to estimate the droplet mass.
The schlieren images were post-processed in Matlab using in-house functions based on different Matlab implemented functions. The tracking of the droplets for determining the speed and size is done in five steps:

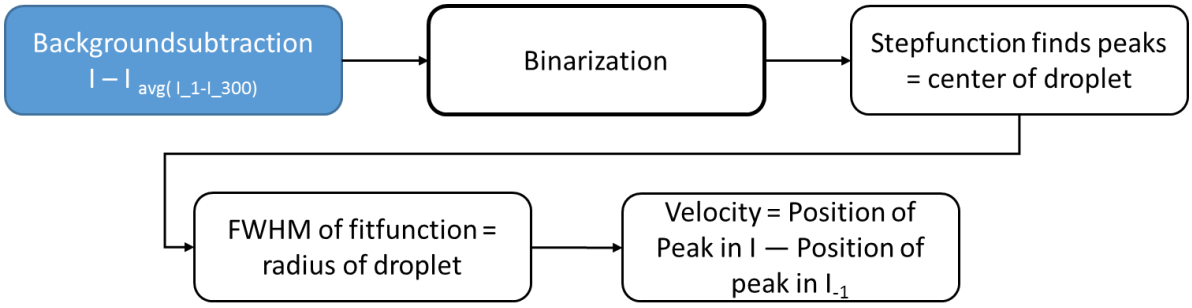

Figure 25: Correction and calculation algorithm for droplet speed.

1. The images were subtracted from an averaged background image
2. The corrected images were binarized using image segmentation
3. Finally, the droplets were detected using the Matlab implemented vision package step-function. The step-function locates local peaks in a two-dimensional matrix.
4. The local maxima were determined as the center of the droplet. To determine the diameter, the FWHM of a Gaussian-fit through the line of the center was used.
5. The speed was calculated from the change in maxima position and time difference by the frame rate.

3.3 Offline sample analysis

For the thermo-gravimetric analysis of the liquid oil samples, a commercial device was used. The NETZSCH STA 449 F1 Jupiter is an analytical device for thermogravimetric analysis (TGA) in

combination with a differential thermal analysis (DTA) or differential scanning calorimeter (DSC). In a first step, basically the weight loss over temperature or time is measured by a balance. In this study, the DSC configuration was used with aluminum crucibles to measure the energy absorption/release rate. For the identification of evaporated compounds, a mass spectrometer was coupled. Because the device is commercially available, the description in this chapter is limited to the measurement principle and the used procedure.
The samples were tested in an inert atmosphere of argon and oxidative atmosphere of synthetic air. For the protection of the balance and electronic devices, a safety volume flow of 20 ml/min of argon was used in all measurements. For inert atmosphere, a purging gas flow of additional 50 ml/min of argon and for the oxidative cases 50 ml/min of synthetic air were used. All measurements were performed with the same temperature ramp of 10 K/min with a starting temperature of 35°C and an end temperature of 550°C. The maximum operating temperature of the crucible is 610°C. A safety margin of 60 K was chosen in the heating ramp, in case of exothermic reactions of the oil samples. For each measurement, a new set of crucibles was used, and the thermal characteristic was found by a baseline measurement heating each sample carrying and reference crucible in the TGA/DSC once. The repeatability of the base line of the crucible was proven once, running several cycles of heating and cooling in a row. The sample crucible was filled by 5–10 mg sample material, however, for consistency a weight close to 7.5 mg was kept constant for the entire series of experiments. All measured values in the TGA/DSC were corrected by the baseline in the NETZSCH software. The transfer capillary and the sampling volume of the QMA were heated to a constant temperature of 250°C. The maximum temperature was 300°C which was chosen to clean the capillary and the sampling volume between the different samples, and the oven was heated to 1000°C for 15 minutes when changing the sampling material.

3.3.1 Thermogravimetry

Thermogravimetric analysis is a thermal method to investigate the physicochemical properties of a system of elements as a function of increasing temperature [132]. The thermogravimetry is closely linked with the differential scanning.
Further description of the method can be found in the review of Coats and Redfern [133]. For the thermogravimetry only a precision balance and an oven with programmable temperature increase are necessary. The weight loss with temperature or time which is equivalent to a constant linear temperature ramp is measured. Results in changing weight are caused by thermal decomposition. There is a leak inaccuracy based on the assumption that the sample has the same temperature as the oven although the oven temperature changes continuously. This means that the weight loss over temperature is strongly dependent on the temperature ramp itself and on other facility effects like the type of crucible as discussed in ref. [134-136] and referred to as the decomposition temperature. Pellon and Carpenter [137] use a cumulative weight loss of 10 % as a definition for the decomposition temperature that will be used here as well.

3.3.2 Differential scanning calorimetry

The differential scanning calorimetry is a complementary technique that can be used in thermogravimetry analysis to measure the amount of energy transfer of the sample as a function of temperature. The description is limited to the heat flux DSC technique as it was used also in this study. The measurement principle was documented in a patent in 1966 by Watson and O'Neill [138] and is still used with small modifications. While only one crucible is necessary for the thermogravimetry, a second one is necessary as a reference. Both crucibles are located on a disc of high thermal diffusivity and the discs are linked to a thermocouple. The oven temperature is also measured by a thermocouple. With changing temperature, a certain amount of energy is needed

to heat the crucible which is measured by the thermocouple at the reference crucible. The temperature at the sample will be lower because of the energy needed to heat the sample material. The heat flux of the sample minus the heat flux of the reference is proportional to the temperature interval (ΔT).

$$\Phi_{\mathrm{FP}} - \Phi_{\mathrm{FR}} = \propto \Delta T \tag{47}$$

A change in heat flux to the sample normalized to the weight of the sample enables the detection of endothermic or exothermic reactions of the sample. In combination with the information about the change in weight the type of process taking place can be found. Additionally, the conditions of the atmosphere inert with pyrolysis decomposition or air with oxidative reactions changes the product. Therefore, the exhaust gases is sampled and analyzed by a QMS.

3.3.3 Quadrupole mass spectrometry

The thermogravimetry facility from the lab equipment supplier NETZSCH was coupled to a mass spectrometer QMS 403 D Aëolos also from NETZSCH, while the main component of this mass spectrometer is the quadrupole mass spectrometer (QMS) called QMA 200 from Pfeiffer Vacuum. The NETZSCH QMS device is coupled to the top of the oven of the TGA by a two-meter-long and 75 µm inner diameter heated fused silica capillary. The system consists of the sample volume which is pumped by a vacuum pump. The volume is filled with the sample by the capillary, sucking a very small amount of gas from the oven which contains the crucible. The QMS is flanged to the sample volume. The measurement principle is summarized in “Mass Spectrometry: Instrumentation, Interpretation, and Applications” by Ekman et al. [139].

4 Autoignition of homogeneous fuel/air mixtures

Primary reference fuels are model fuels that represent certain behavior of technical fuels by a smaller number of components and high accuracy in concentration. PRF95 is the primary reference fuel for an octane 95 gasoline fuel consisting of 95 vol. % iso-octane and 5 vol. % n-heptane. To adjust the evaporation properties, additional extension with chemical components having different boiling points can be found in the literature [140]. Ethanol is likewise used as a fuel additive because of its knock resistance and is produced from biomass, therefore it is considered a biofuel. Shock-tube studies are essential for the development and validation of reaction mechanisms. Recently, shock tube data as well as RCM data were subject of discussion because of disagreement to each other and to model predictions. New insight was gained due to new measurement possibilities that lead to in-depth understanding of the ignition inconsistency in particular at low temperatures. Among these techniques high repetitive imaging has contributed to knowledge of the ignition process characteristics. Effects impacting the ignition such as dp/dt and the formation of the boundary layer were studied in refs. [41, 141-144] as well as the effects of membrane particles [145] and specific fuel behavior [146, 147]. An inhomogeneous ignition is an ignition of a reactive mixture that evolves spatially and time-resolved and deviates from the ideal case. An ideal autoignition in a shock tube is an ignition starting in the plane next to the endwall over the entire plane. This ignition follows the reflected shock wave this imposes that the ignition occurs first at the position where the test gas first processed the conditions (T_5, p_5).

4.1 Homogeneous and inhomogeneous autoignition of PRF95

PRF95 was studied at high pressure and moderate temperatures as a reference case to investigate the impact factors that can explain the combustion phenomena mentioned in the introduction. The ignition delay time was determined for post-reflected conditions: pressure of 20 bar and temperatures from 700–1000 K at $\phi = 1$. Figure 26 shows experimental and simulated ignition delay times determined by OH*. For the simulations the mechanism from Cai and Pitsch [148] was used in a 0D adiabatic constant pressure batch reactor (PQ-batch reactor) and constant-volume batch reactor (VQ-batch reactor), but only the simulation results for constant pressure are shown and considered in the following discussions because it fits much better to the experimental results. These simulations were performed with chemical workbench [149] with a dp/dt of 2%/ms for the first 3 ms according to Pang et al. [150, 151]. Taking the experimental dp/dt into account enhances the agreement of experimental and simulated results. The dashed black line is the simulated result without consideration of dp/dt and the solid line considers dp/dt for the first 3 ms and constant afterward. The simulation considering dp/dt fits well to the experimental results over the investigated temperature range.

The experimental data scatter in the range from 780–870 K. The reasons for the scattered data will be discussed later together with the uncertainty calculations. Scatter in ignition delay time means that the ignition randomly occurs earlier due non-uniformity in the mixture (gas pockets, mixture and temperature non-uniformity). To unravel the reason for the difference between the experiments using methods like chemiluminescence detection via photomultiplier or volumetric pressure traces are not suitable because slight rise in chemiluminescence and pressure prior to the main ignition are not detected in all cases with pre-ignition because of the limited detection view.

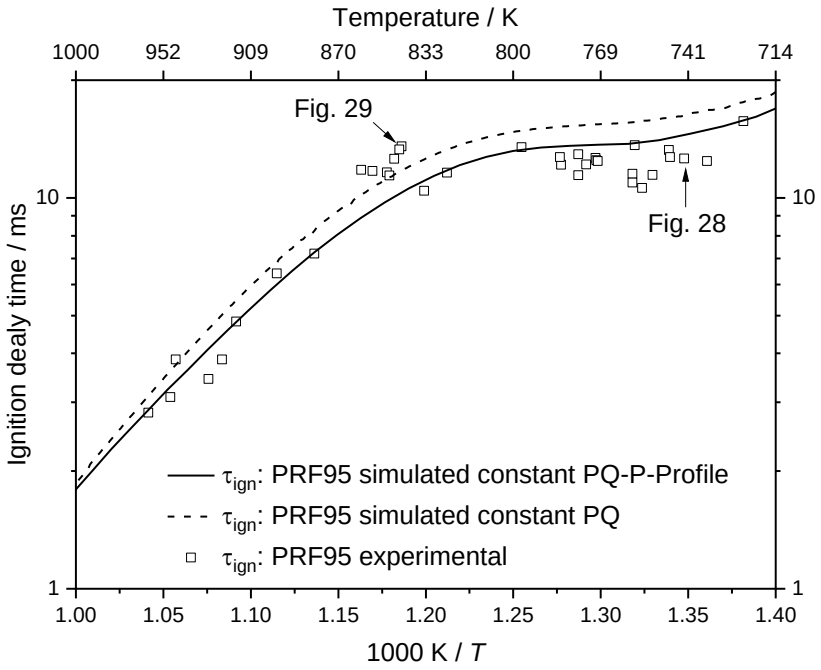

Figure 26: Ignition delay time of PRF95/air at $\phi = 1$ at $p_5 = 20$ bar, black line simulated with mechanism from Cai and Pitsch, black open squares experimental results in HPST.

High-repetition-rate imaging was performed to investigate the evolution of the pre-ignition by spatially resolved measurement. Figure 27 shows the pressure and chemiluminescence traces of homogeneous PRF95/air ignition that end up by a sudden rise in pressure and OH* chemiluminescence after 12.6 ms. The abrupt rise in signal intensity is typical for a homogeneous strong ignition. The simulated OH* and ignition delay time shown in Figure 27 display a longer ignition delay of 14.5 ms. The simulated ignition delay times caches the overall trend of the experiments quite well, while the experimental results scatter at temperature ranges where non-ideal facility effects in shock tubes are known. Whether such effects occur is further investigated in this case. The corresponding sequence of high-speed images are described with nine frames in Figure 28. The red circle is the edge of the endwall window as described in section 3.1.3.2. During the first 8.0 ms, no light emission was detected, then three very weak local luminescence spots appear. The spot marked (a) appears first in the gas-phase, followed by (b) and (c) which stem from the reactive zone located at the sidewall area. The edge of the flame spots is marked by a red contour line using a flame edge detection algorithm explained in section 3.1.3.2. The spots grow laterally and increase in intensity. The ignition area (a) is in the focal plane and shows very sharp yellow spots inside the blue flame in all frames. In frame 5 and onwards, the flame shows more structural features that are very sharp. The positions of ignition areas (b) and (c) are directly in the vicinity of the endwall (upstream the focal length); therefore, they appear a bit blurry. The sensor intensity was integrated and is shown over time in Figure 27 as a green line. Additionally, a new metric was applied to evaluate the portion of ignition equivalent area: this is the “normalized burned area” which is the area showing chemiluminescence (detected by the algorithm in section 3.1.3.2) normalized to the observed area. The result is shown in Figure 27 as a red line.

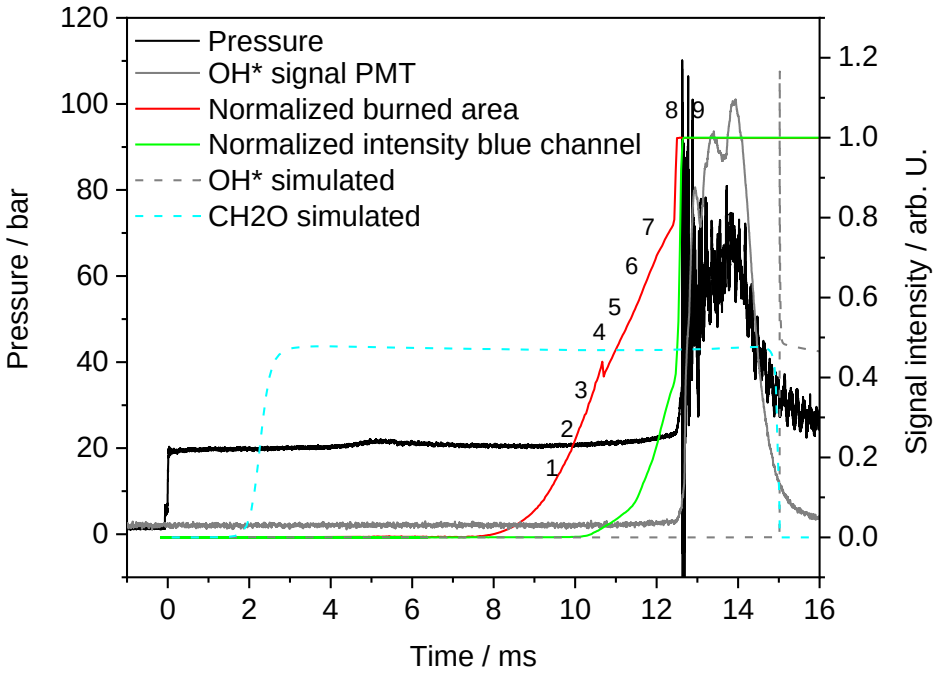

Figure 27: Pressure and chemiluminescence intensity during the ignition of a homogeneous PRF95/air mixture at $\phi = 1$, $T_5 = 740$ K, and $p_5 = 19.4$ bar. Simulated intensities of OH* and HCHO are shown as dashed lines.

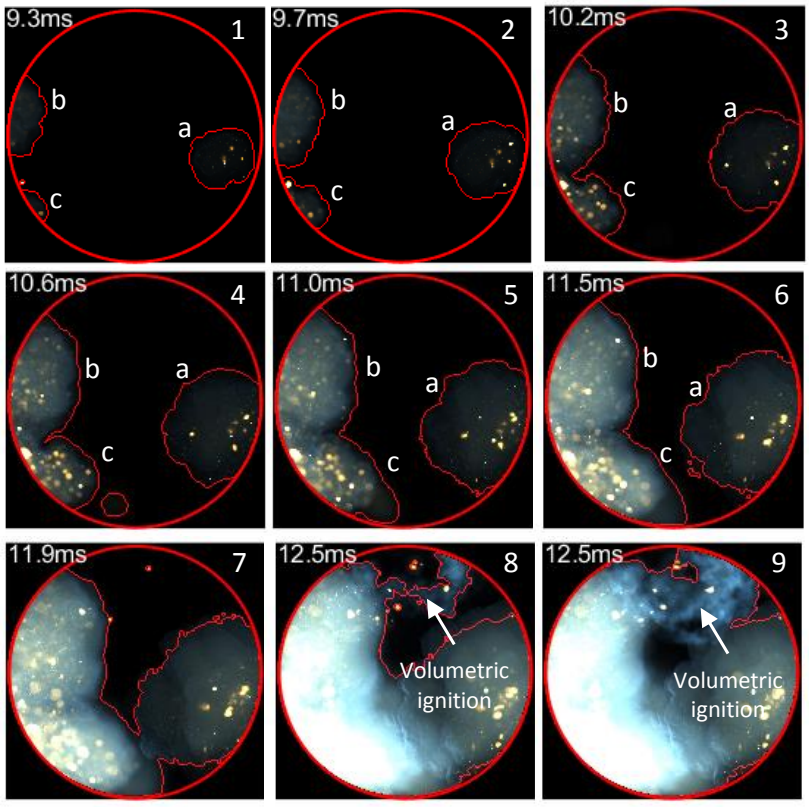

Figure 28: High-repetition-rate image series recorded form the endwall of homogeneous gas mixture of PRF95/air that ignites in inhomogeneous manner at $\phi = 1$, $T_5 = 740$ K, and $p_5 = 19.4$ bar [152].

Over the first 12 ms, no intensity change was detected by the photomultiplier. Since the PMT was placed on the top position with narrow angle of view, any local flames occurrence outside the solid angle cannot be registered. This is where merits of high-repetition-rate imaging from the endwall come into consideration. At 12 ms when the ignition zone propagates axially to the center area, the PMT signal intensity increases to the maximum within 0.1 ms, which agrees well

with frames 8 and 9 when the normalized burned area reaches 100 % of the observed area. Hence, the data from the camera images provide the needed information to follow the local ignition process. One might argue that the observed chemiluminescence originates from a cool flame since the camera detects the full integrated visible spectrum. To check this hypothesis, formaldehyde (HCHO) which is a marker for a cool flame was simulated. The simulation shows that HCHO already appeared after 2 ms while the camera detects the "flame" first after 8 ms. Another argument that refutes the assumption of cool flame detection is the high sensitivity that is accompanied with the cool flame occurrence.

At temperatures higher than 840 K local yellow luminescent spots were observed early before the main ignition. Although the shock tube was cleaned very thoroughly between the experiments, the yellow spots were observed and attributed to diaphragm particles that are heated to their ignition temperature. An example for particle triggered ignition is shown in Figure 29. The first three frames show a yellow luminescent spot initiating the ignition in the surrounding gas. Additional 2 ms later a second yellow spot appears in frame 4 of Figure 29 and initiates the gas ignition and in the following frames mingles with the first flame that reaches the size of ¼ of the observed area.

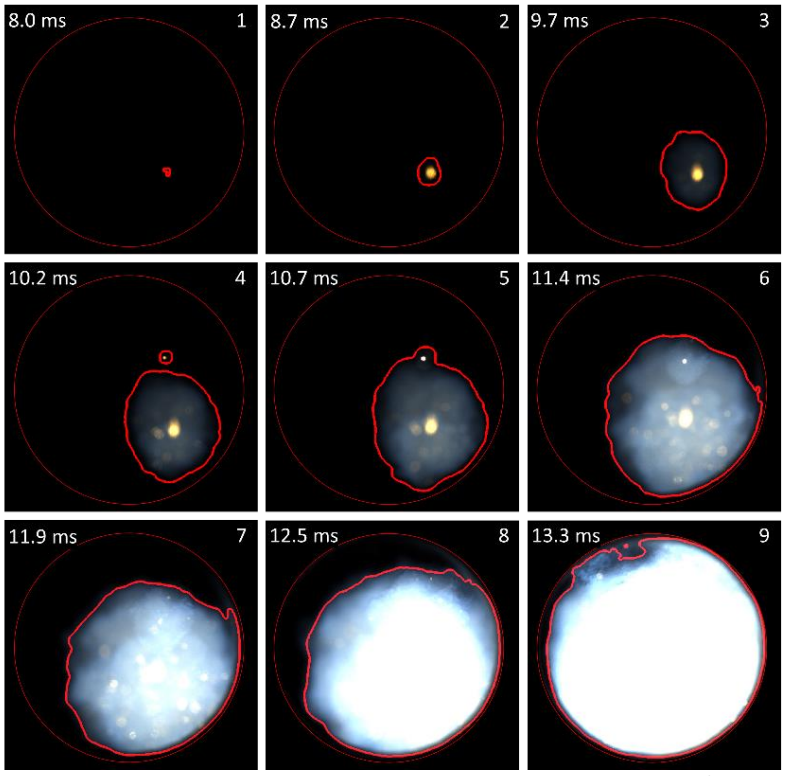

Figure 29: High-speed images from the endwall of homogeneous gas mixture of PRF95/air that ignites in a homogeneous manner at $\phi = 1$, $T_5 = 840$ K, and $p_5 = 19.6$ bar.

The pressure of the above experiment run starts to rise at 9.5 ms while the OH* chemiluminescence signal rises first up 12.5 ms. The deviation in time of the pressure and OH* chemiluminescence signal rise and the associated small increase in the pressure trace shown in Figure 30 is attributed to local pre-ignition. The delayed detection of the ignition by the PMT is caused by the onset of the first local ignition out of the plane of the detection view of the PMT. The ignition delay time of 13.4 ms determined by the PMT agrees well with the high-repetition-rate image series. Even though the yellow spot induces local ignition, the final delay time of the volumetric ignition is not shorter than the one predicted by the mechanism. Instead it is even longer than the prediction of the mechanism without dp/dt correction, which might fit better in this case because the pressure trace was perfectly flat.

Despite the routine cleaning of the shock tube, the presence of particles cannot completely be avoided. Also, new particles are generated each time the membrane bursts. This is seen in frame 2 of Figure 29 as a yellow spot that is attributed to a hot particle that further oxidizes. To identify the origin of the hot spots, a series of experiments was performed without cleaning and only in air. With an increased number of experiments, the number of yellow spots increased. In experiments in nitrogen in contrast, no light emission was observed. This leads to the conclusion that in the shock-heated gases, the diaphragm particles are not heated up to temperatures where incandescence can be observed in the visible. In the presence of oxygen, however, oxidation leads to further particle heating and thus visible emission. Measurements over a wide temperature range have shown that the oxidation of the particles is initiated at temperatures above ~800 K, which is the temperature where aluminum reaches its first oxidation step [31, 153].

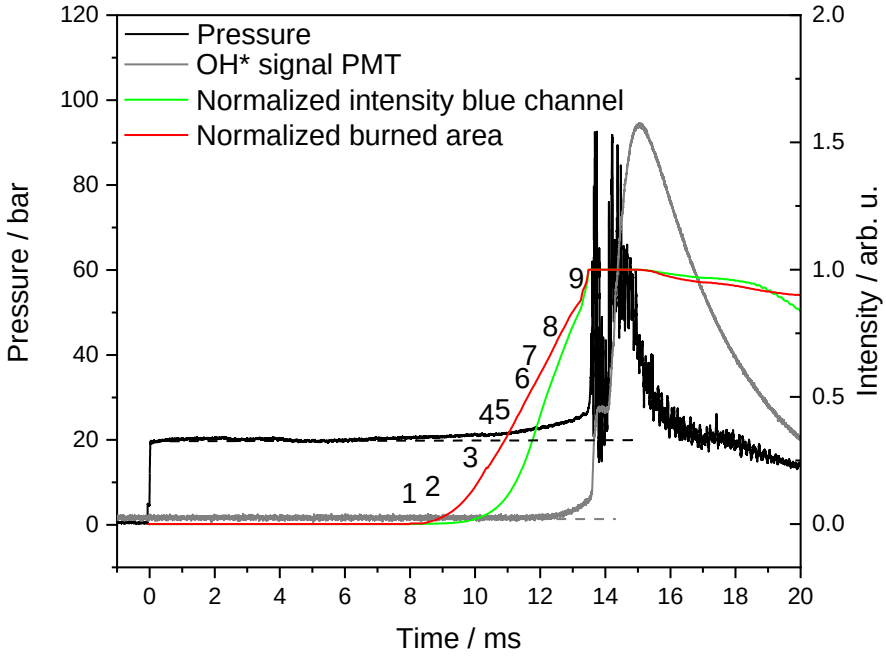

Figure 30: Pressure and chemiluminescence intensity during ignition of a homogeneous PRF95/air mixture at $\phi = 1$, $T_5 = 840$ K, and $p_5 = 19.6$ bar.

The series of experiments was performed at 850 K to prove the repeatability of the facility and investigate the effect of cleaning. With cleaning no promoting effect on the volumetric ignition was observed even though local ignition has still happened. Without cleaning, the ignition delay time drops down by 3 ms/experiment. While the ignition delay time was 13 ms ±0.5°ms in five repetitions with cleaning the cleaning was stopped, and ignition delay time of the following experiment was reduced to 10 ms. The experiment was repeated once again without cleaning. This time the ignition delay time dropped down to 7 ms. Afterwards the shock tube was cleaned, and the experiment was repeated once again. The ignition delay time was 13 ms again. Particle-induced ignition is a statistical local phenomenon that does not necessarily impact the delay time of the volumetric ignition. The effects on the ignition delay time depend on the gas temperature that needs to be high enough for starting the aluminum oxidation. The size of the local ignition spot and the dissipation of energy compete with the chemical reaction of the bulk gas. Therefore, local pre-ignition plays a role for long ignition delay times and low temperature only [154].

4.2 Homogeneous and inhomogeneous autoignition of ethanol

PRF95 is frequently used as a standard representative for gasoline but due to its peroxy chemistry, the interpretation of local ignition is complicated. At gas temperatures in the NTC region,

local ignition can shift the gas state to the rising or declining part of the NTC regime, which then increases or decreases the reactivity of the system. For a linear relation of temperature and kinetics, a fuel that follows the standard Arrhenius behavior is useful and simplifies interpretation. Ethanol is of special interest because of its increasing application in engines as octane booster and its availability as biofuel. On the other side, it is known to be prone to inhomogeneous ignition phenomena [155, 156]. Recently, different groups published work on ethanol ignition including the IVG [18, 157-159]. But still the ignition behavior of ethanol in shock tubes raises questions especially at low temperatures.

For ignition of ethanol/air mixtures, the experimental results deviate from the simulated ones, which was attributed to pre-ignition due to local inhomogeneities. The simulation results based on different published reaction mechanisms deviate from each other, which is described in the following sections in more detail. The following section includes data, figures and text passages that are published in a paper in the Proceedings of the Combustion Institute (first author: Natvel, my own contribution: [160]).

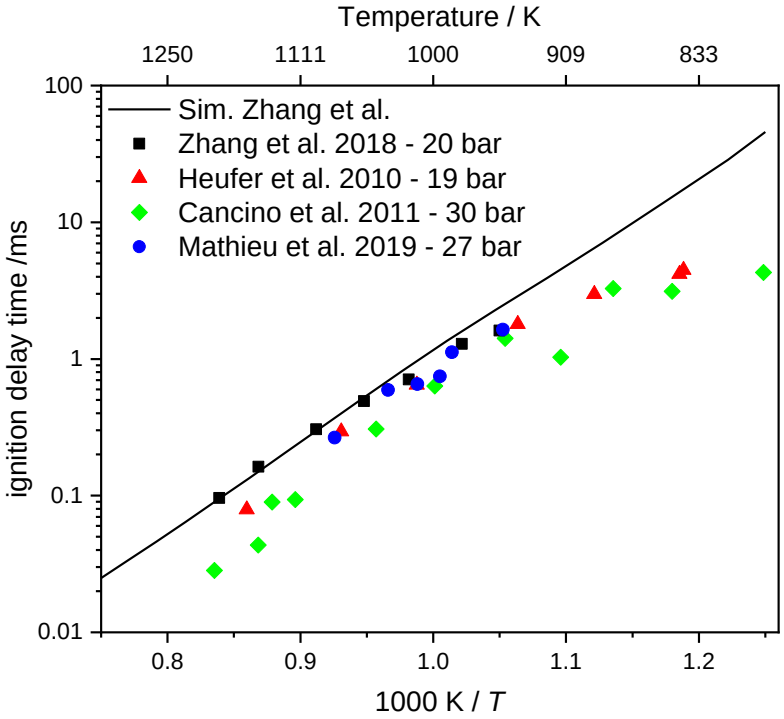

Figure 31: Ignition delay time data from literature and simulation with a recently published mechanism from Zhang et al. [157].

Only few studies measured the ignition delay times of undiluted ethanol/air mixtures at $\phi = 1$, high pressure, and low temperatures. For ignition delay times, Heufer et al. [158] and Cancino et al. [161] measured down to temperatures of 800 K, while Zhang et al. [157] and Mathieu et al. measured down to temperatures of 920 K. At temperatures higher than 920 K the measured ignition delay times agree well with the simulation from Zhang et al. The results form Cancino et al. are shorter because of the slightly higher pressure (30 bar), but the data might have been additionally affected by the pre-ignition at lower temperatures.

For the low-temperature range, the measurements from Heufer et al. and Cancino et al. agree but deviate from the simulations. The reaction mechanism from Zhang et al. was also validated for very low temperatures in RCMs and intermediate and high temperatures in RCMs and shock tubes, while deviations appear only for shock-tube experiments at intermediate temperatures.

Experiments with high fuel concentrations in shock tubes are generally subject to large uncertainties due to the significant heat release that complicates the development of accurate reaction

mechanisms [162]. Earlier works have applied experimental and numerical approaches to mitigate these effects [151, 163]. For experiments with undiluted mixtures, discrepancies appear mainly for longer timescales due to the interaction of chemistry and heat transfer and potential additional interaction with hot particles [154].
As the introduction of this topic shows, different aspects are in discussion to explain discrepancies in the mechanism as well as in the shock-tube experiments. This study focuses on two main aspects of shock-tube experiments in three steps: first to generate repeatable ignition delay time data that fits well to the state of the art chemical simulations; second to classify the different homogeneous and inhomogeneous ignitions by high-repetitive imaging at multi-spectral ranges through the endwall; third the mixture was diluted by helium to adjust the heat conductivity with minimal impact on heat capacity and chemical reactivity.
The in here used fuel/air mixture was diluted by addition of ~15% N_2 with a volumetric ratio of 7.62 for diluent/oxygen (Mixture #1). During the course of the investigation six different mixtures were used, listed in Table 1.

Table 1: Mixture composition (mol%). All mixtures are at $\phi = 1$.

Mixture	Ethanol	O_2	N_2	Ar	He	Diluent/O_2
#1	3.72	11.17	85.11	-	-	7.62
#2	3.72	11.17	-	85.11	-	7.62
#3	6.54	19.63	73.83	-	-	3.76
#4	6.38	19.14	71.98	-	2.5	3.89
#5	6.21	18.64	70.15	-	5.0	4.03
#6	5.89	17.66	66.45	-	10.0	4.33

Figure 32 shows a comparison of the simulated ignition delay times using different mechanisms and experimental results at $p_5 \approx 20$ bar and temperatures from 880–1320 K. Towards lower temperatures, the time range was limited to 15 ms, which is the maximum test time of the IVG shock-tube facility. All three mechanisms and the experimental results agree very well, except the CRECK mechanism that predicts longer ignition delay times for temperatures >1100 K.

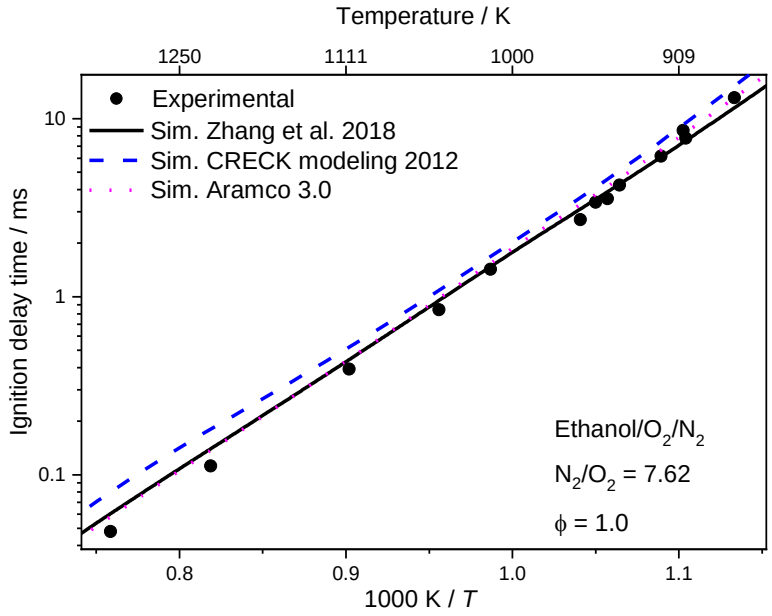

Figure 32: Comparison between experiments and simulations from Zhang et al. [157] (solid lines), CRECK modeling [164] (dashed lines), and Aramco 3.0 [165] (dotted lines).

The results presented in section 4.1 show good agreement of measured and simulated ignition delay times, but do not give any indication that the ignition proceeded homogeneously. Simultaneous RGB and OH* high-repetition-rate imaging shed light on the entire ignition process and confirmed that the ignition was homogeneous over the tested temperature range for ethanol/O_2/N_2 mixtures. Figure 33 shows an image sequence of the ignition at $T_5 = 950$ K that starts homogeneously in the entire test volume as weak blue structure (image 1 to 4), followed by a sudden strong ignition from the core (images 9 and 10). The strong pressure increase leads to a sudden oxidation of the residual fuel and local formation of soot (images 11 and 12). In images 4–8 of the OH* image sequence, the signal increase was very weak and homogeneous. In all frames, the intensity increases with local high-intensity structures that gradually develop and transit in full combustion (images 13–16).

All images shown in this section were recorded with the same camera settings and post-processed in the same way. Thus, the color scales are comparable. Both cameras were set to be sensitive to local ignition phenomena. This high sensitivity allows to characterize weak features in earlier times but leads to saturation when approaching main ignition.

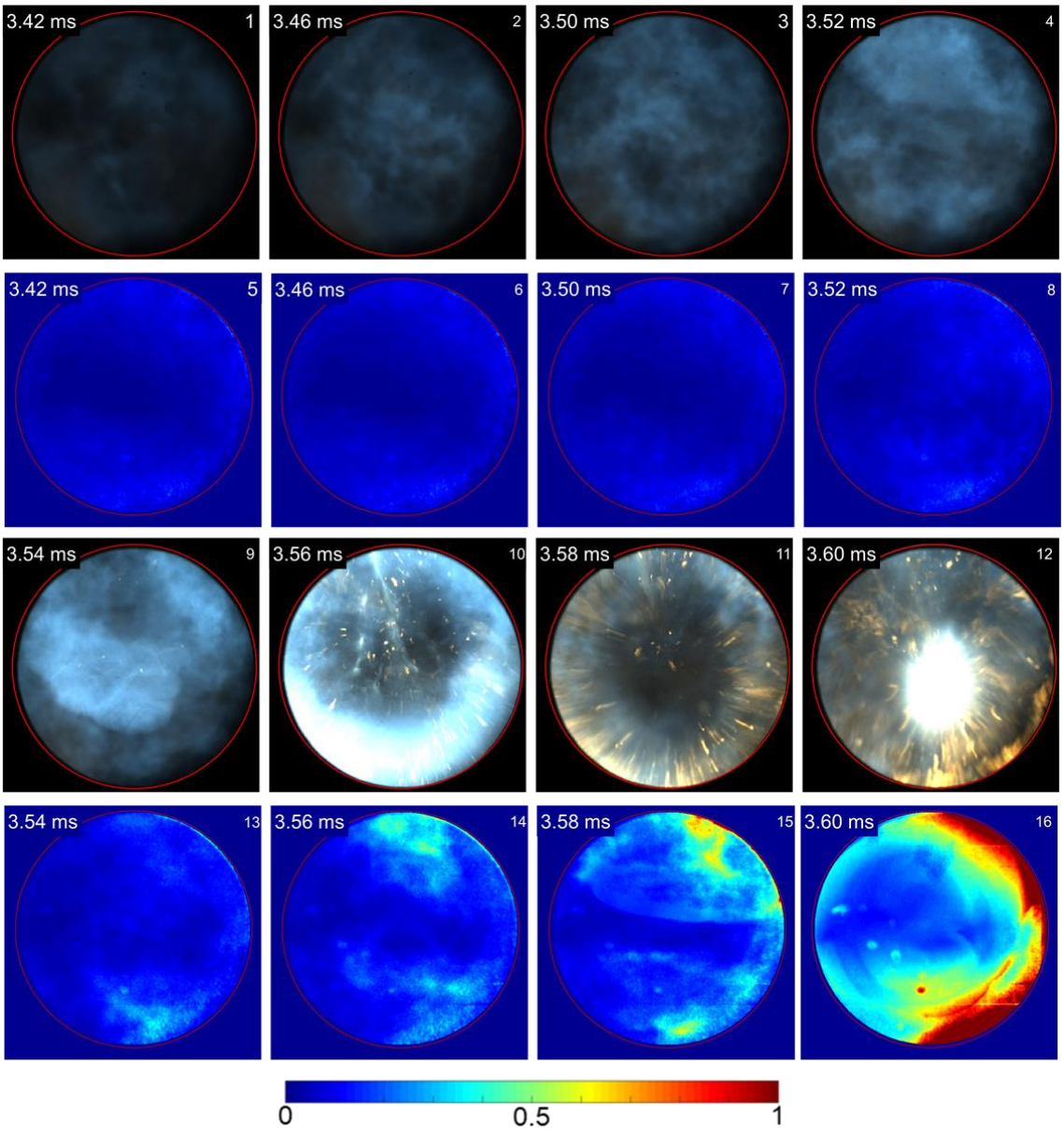

Figure 33: Image sequence at $T_5 = 950$ K and $p_5 = 21$ bar. Frames 1–4 and 9–12: RGB camera, 5–8 and 13–16: OH* camera and the corresponding color scale.

Through dilution with N_2, homogeneous ignition was achieved. It is, however, of interest to find out, which mechanism governs this process and what the relevant factors are (molecular structure, density, temperature, timescale)?
In shock-tube studies, argon is a typically used bath gas to dilute mixtures. High Mach numbers can be achieved with argon because of its low heat capacity. Also, gas dynamics effect such as shock bifurcation are not expected. For consistency, N_2 was replaced by equal volumes of argon (Mixture #2: ethanol/oxygen of $\phi = 1 +$ argon with a representative ratio of 7.62 for diluent/oxygen). The focus was on the experimental data in the low-temperature range where pre-ignition is expected. At first glance, the different mechanisms agree much better for Ar dilution than for N_2 dilution. Below 930 K, the experiments start to deviate from the simulation (Figure 34). This behavior was observed also by Mathieu et al. [146] and Zhang et al. [157].

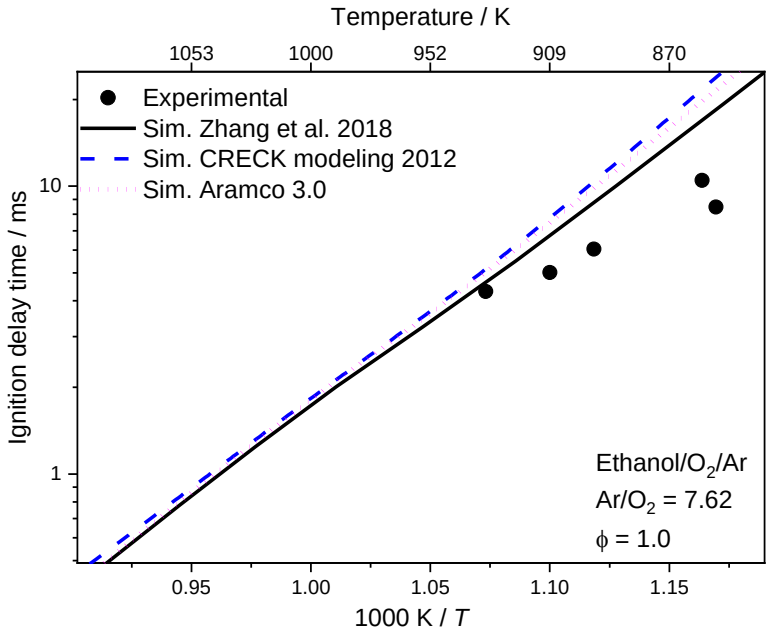

Figure 34: Comparison between experiments [160] and simulation from Zhang et al. [157] (solid lines), CRECK modeling [164] (dashed lines), Aramco 3.0 [165] (dotted lines).

Imaging of the argon-diluted ethanol/oxygen mixture reveals that the discrepancy to the simulation is attributed to the inhomogeneous ignition process. Figure 35 shows inhomogeneous ignition that starts close to the sidewall on the right side, followed by the bottom and left side until bright illumination from the center several centimeters away from the endwall occurs (e.g., frame 3 and 6). This leads to fast ignition of the unburned gas in the measurement section. This type of ignition far from the endwall is referred to as “remote ignition” influenced by boundary layer growth and interaction with the reflected shock wave ref. [166] but could be triggered by other sources like particles that are far upstream as well. Recent CFD simulation showed the impact of gas dynamics on the formation of remote ignition [43].

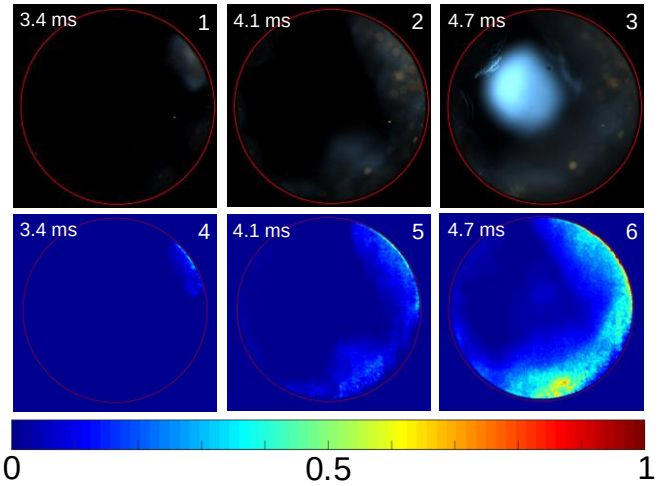

Figure 35: Image series of ethanol/O_2 diluted in argon at 910 K and ≈ 20 bar;
Frames 1–3: RGB Camera, 4–6: OH* camera with corresponding color scale [160].

Mixture #1 and #2 have the same dilution levels, thus, the oxidation reactions release the same amount of heat, but due to different carrier gases with different heat capacity (N_2 and Ar, respectively), mixture #1 results in lower local temperatures than mixture #2. This was observed in different ignition behavior. Comparing Figure 33 and Figure 35 at 880–910 K reveals that ignition in mixture #1 proceeds homogeneously whereas in mixture #2 ignition starts from locations near the sidewall. Also, the measured τ_{ign} at around 860 K (Figure 34) are substantially shorter in mixture #2 (≤10 ms) compared to mixture #1, where no ignition was observed within the test time of the shock tube. This is attributed to the higher thermal diffusivity and heat capacity of N_2 in mixture #1 (vs. Ar in mixture #2) [180] so that pre-ignition does not influence the main ignition because of generally lower temperature and the associated reduced temperature inhomogeneity. The examples show that not only the dilution level but also the type of carrier gas are factors that influence ignition.

Additionally, undiluted stoichiometric ethanol/air (Mixture #3) was studied because the different dilution results were not conclusive. The last study of ethanol by Cancino et al. [159] at the IVG was performed without imaging. In contrast to that study, from the new concept with 2D imaging valuable information about the ignition process itself can be obtained. It was possible to identify different types of inhomogeneous ignition in the present study at temperatures from 800–860 K which can be referred to: *particles-induced ignition*, *local gas ignition*, and *remote ignition*.

The images of the *particle-induced ignition* appear identical to those observed in PRF95/air mixtures. Figure 37 shows the same temperature range for particle-induced ignition (red crossed circles) and the same induction time, the particles need to heat the ambient gas to start the local ignition as it was observed in PRF95/air mixtures. While in the study of PRF95/air only the color camera was used, the distinction of particle/gas ignition was supported in this series of measurements by OH* imaging to clearly identify the gas ignition. The comparison of the simultaneously recorded image types enabled the identification of flame and particle in time. Frame 1 of Figure 36 shows a priori particle that initiates a flame in frame 2. The corresponding OH* frame 5 does not show any features because the hot particles do not emit in the ultraviolet range. This changes in frame 6, when the gas surrounding the particle ignites leading to chemiluminescence emission. In frame 2, a second particle initiates an ignition at the bottom. The initiated flame is more evident in frame 3 and the corresponding frame 7 (OH* signal). The flame covers the entire volume in frames 4 and 8 before the main ignition with ignition delay time of 10.5 ms.

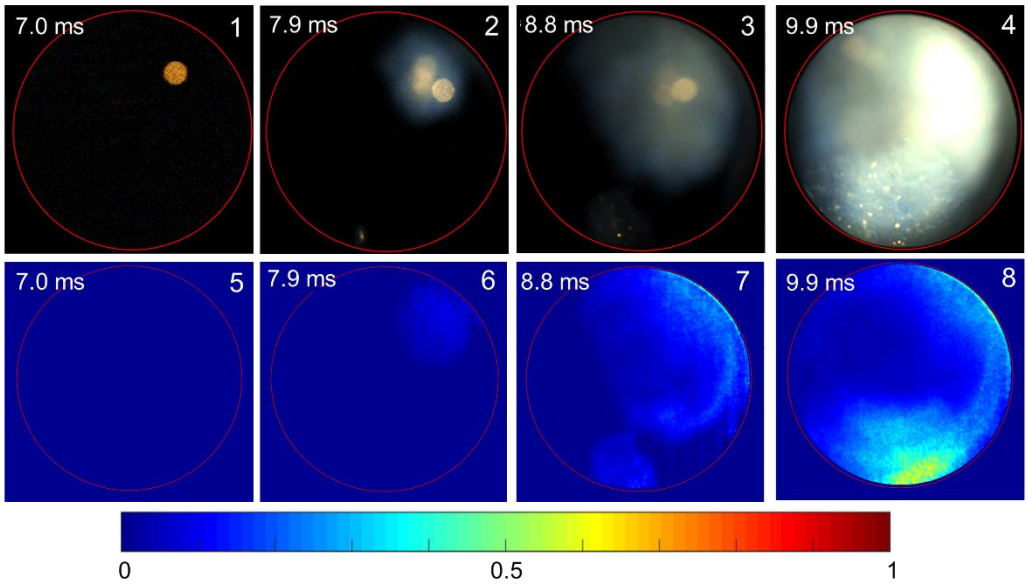

Figure 36: Particle-induced ignition of ethanol/air at $\phi = 1$, $T_5 = 850$ K, and $p_5 = 20$ bar.
Frames 1–4: RGB Camera, 5–8: OH* camera with corresponding color scale.

Local gas ignition was observed over the investigated temperature range with a high impact on the ignition delay time (orange circles in Figure 37). Figure 38 shows local gas ignition that starts in the left bottom, propagating diagonally through the observed volume. Early before the entire observed area was filled by the ignition the volumetric ignition occurs. This is different for particle-induced ignition at the same conditions at which the propagating ignition fills the volume first (Figure 29 and Figure 36). It can be concluded that the particle-induced ignition does not shorten the τ_{ign} because of the restricted timescale of the shock tube measurement: particle ignition appears for delay times > 8 ms. Whether the particle can have an effect or not is dependent on the ignition delay time of the specific fuel at these conditions.
The so-called "**remote ignition**" was observed for very low temperatures provoking ignition in the same time range of particle-induced ignition (green symbols in Figure 37). Remote ignition was observed in all cases of ethanol/Ar/O_2 ignitions (see Figure 34).

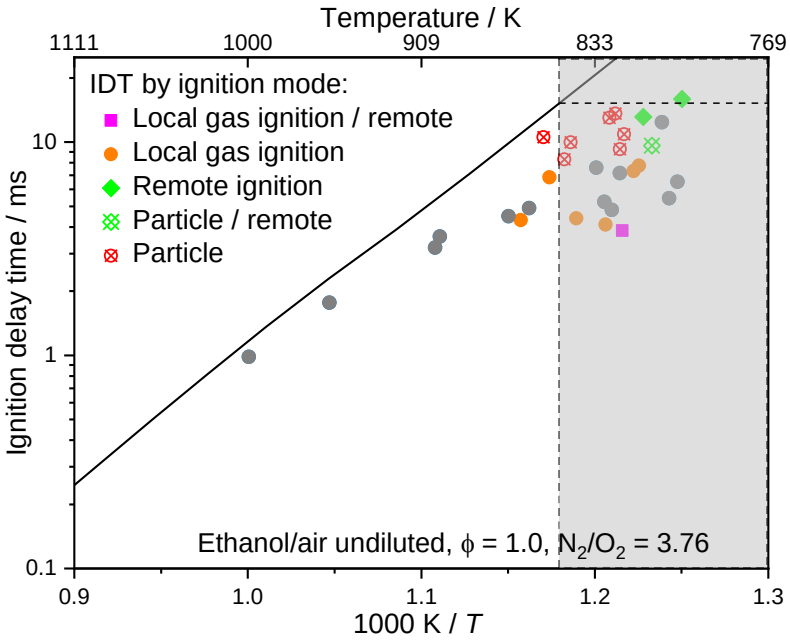

Figure 37: Comparison of ignition delay times of ethanol/air mixture at $\phi = 1$, and $p_5 = 20$ bar, different ignition modes and ideal ignition delay predicted by Zhang et al. [157], ref. [160]

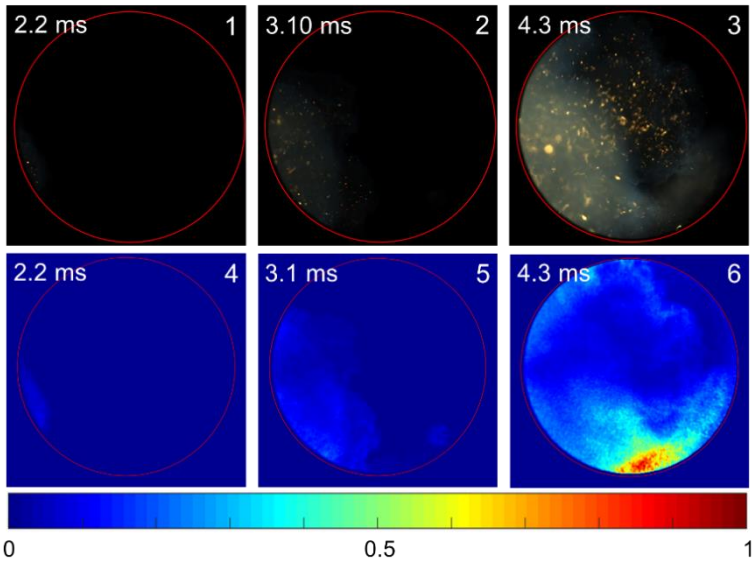

Figure 38: Local gas ignition of ethanol/air mixture at $\phi = 1$, $T_5 = 850$ K, and $p_5 = 20$ bar. Frames 1–3: RGB Camera, 4–6: OH* camera with corresponding color scale.

The grey underlaid rectangle in Figure 37 marks the temperature range in which the mechanism predicts an ignition delay time longer than 15 ms. For the ideal case, no ignition would be observed for temperatures below 850 K due to test time limitation. The experimental results show, however, ignition delay times in this temperature range which are much shorter than 15 ms and the ignition is not influenced by the quenching. An example of local gas ignition with τ_{ign} below 15 ms is shown in Figure 39. The local ignition starts on the left sidewall and propagates sideways to the right resulting in an τ_{ign} of 6.7 ms. A comparison between Figure 38 and Figure 39 shows no essential difference although the temperature of the ignition shown in Figure 39 is 30 K lower and the τ_{ign} decreases by 2.7 ms. The ignition delay times scatter for lower temperatures ($T_5 < 850$ K), where no ignition is expected to occur.

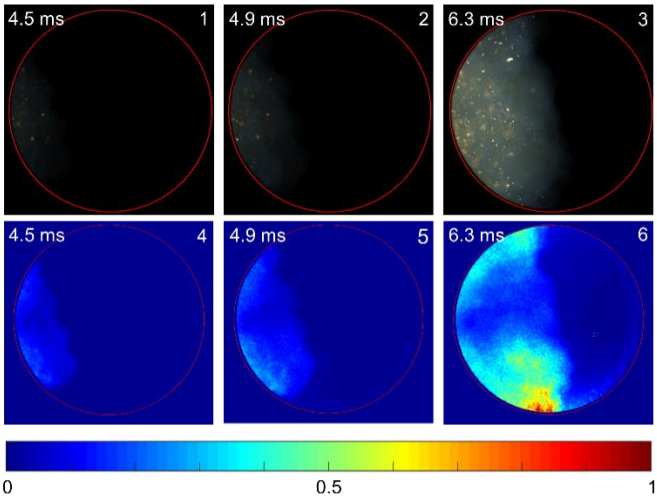

Figure 39: Local gas ignition of ethanol/air mixture at $\phi = 1$, $T_5 = 820$ K, and $p_5 = 20$ bar. Frames 1–3: RGB Camera, 4–6: OH* camera with corresponding color scale.

Discrepancies between experiment and model predictions from the mechanism were observed at higher temperatures from 850–1000 K as well. The observations have shown that the ignition is still subject to non-homogeneous local gas ignition close to the wall.

Helium was recently used by the Hanson group as a diluent gas to stabilize ignition [167] and in an additional study to reduce particle-induced ignition [154]. At the same time, Figueroa-Labastida et al. [18] studied inhomogeneous ignition of different ethanol and methanol mixtures and attempted to find a context in thermal diffusivity/flame thickness and inhomogeneous ignition over temperature and pressure. To systematically understand the link of thermal diffusivity of the mixture and pre-ignition the ignition was studied under the same conditions with different thermal diffusivity by addition of helium. Helium was used because it has very high thermal diffusivity. Figure 40 shows the thermal diffusivity over temperature for the tested mixtures in this work. The undiluted mixture of ethanol in air (Mixture #3) and the mixture diluted in argon (Mixture #2) have the same thermal diffusivity, while the dilution in nitrogen has a higher thermal diffusivity. Adding 2.5 % helium to the ethanol/air mixture has the same effect on thermal diffusivity as the nitrogen dilution, but the absolute value is smaller for the tested conditions because of the lower test temperature. Further addition of helium increases the thermal diffusivity of the mixture.

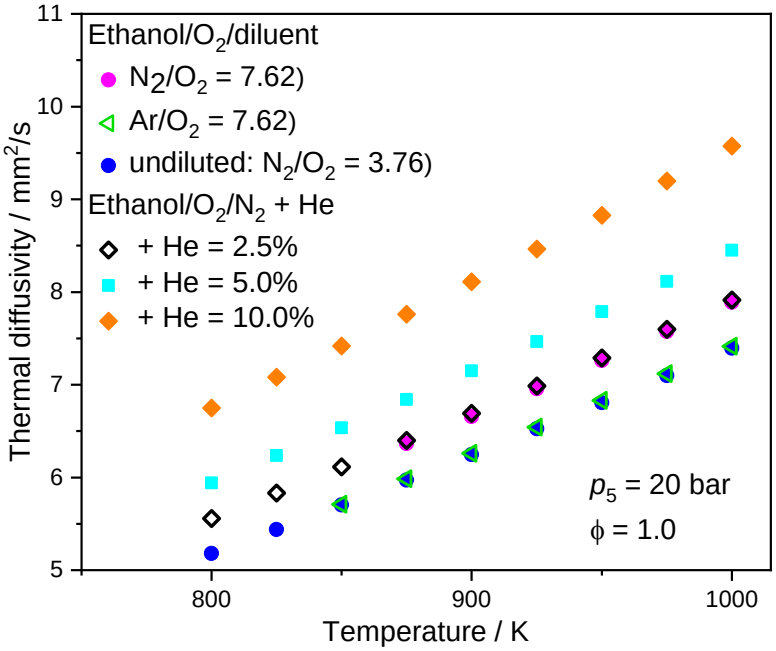

Figure 40: Thermal diffusivity of the studied ethanol mixtures over temperature.

The assumption was that a mixture with high thermal diffusivity will not show pre-ignition because local hot regions (gas pockets) or ignition kernels will quickly dissipate the heat to the surrounding gas. Therefore, the mixtures were investigated at low temperatures where pre-ignition is present due to the timescales coupling between the heat release and heat transfer. The addition of 2.5 % He (Mixture #4) has the same thermal diffusivity as mixture #1, but at 820 K resulted in pre-ignition and τ_{ign} = 5.2 ms. The difference in heat capacity of mixture #1 changes the temperature in the local reaction areas and decides between local ignition or a volumetric homogeneous ignition. With 5 % He (Mixture #5), the experiments showed pre-ignition in one of the three tests. A concentration of 10 % He (Mixture #6) suppressed pre-ignition in the studied temperature range of 800–1000 K. Mixture #6 showed a bending in the investigated temperature range that is underestimated in the simulation. In the simulation of containing 10 % helium the *dp*/*dt* was set as function of temperature (found in non-reactive shocks), in contrast to mixture #3 with constant *dp*/*dt*. Here, ignition delay times of mixture #1 and #6 match for temperatures over 900 K (temperature range where all compared studies agree, see Figure 31). For lower temperatures the ignition delay times of mixture #6 breaks the observed trend to shorter ignition delay times. The effect of dilution seems not to play the dominant role to suppress the local pre-ignition as the dilution by argon (mixture #2) also shows pre-ignition.
Figure 41 shows ignition delay times of the mixture #3, #4, #5, and #6 and the simulation for the pure ethanol/air case (Mixture #3) and the addition of 10% He (Mixture #6).
Adding 10 % He to the mixture reduces ignition inhomogeneities significantly and results in reproducible τ_{ign} measurements. The imaging data shows more homogeneous ignition compared to mixture #3 for all experiments with 10 % He dilution. No particle-induced ignition, remote or local gas ignition was observed contrary to mixture #3. However, the thermal diffusivity cannot be considered as the only parameter influencing ignition homogeneity but instead, it must be considered in conjunction with the heat release. For instance, in case of mixtures #1 (homogeneous ignition) and #3 (inhomogeneous) where $\alpha_{mix\#3} < \alpha_{mix\#1}$, the fact that mixture #3 ignites

inhomogeneously is attributed to cumulative effects governed by the low thermal diffusivity and strong heat release.

In contrast to the runs without helium, the measured τ_{ign} with 10 % He dilution agree much better with the simulations that were validated in RCMs at low temperatures. A good agreement is especially observed from 850–865 K and 950–1000 K. In the 875–900 K range, experiment and simulation deviate up to 45 % range, which is attributed to not fully homogeneous ignition in these cases because of the competition of the heat release and the heat dissipation that changes with temperature and time.

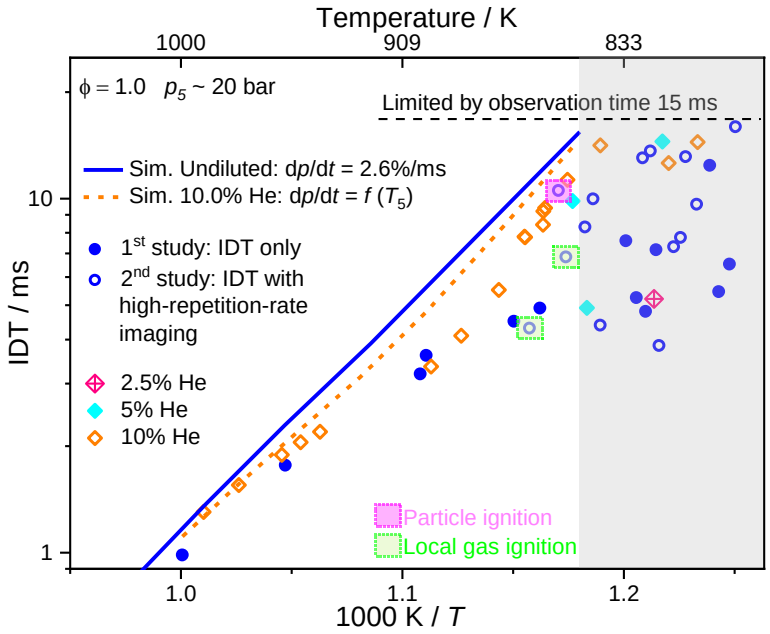

Figure 41: Effect of helium dilution on the τ_{ign} (mixtures #4, #5, and #6) compared to mixture #3 [160]. Simulated τ_{ign} of the mixtures #3, and #6 are based on the Zhang et al. [157].

The image sequence of ignition at 850 K and 10 % He in the mixture is shown in Figure 42. The ignition shows a very weak local ignition in the top left corner that propagates through the reaction volume. It shows also a relatively strong local ignition as a blue flame structure in the center of the tube (image 2). This structure becomes stronger and grows over time resulting in a volumetric ignition. The region in the top left corner is, however, more intense over the process than the rest.

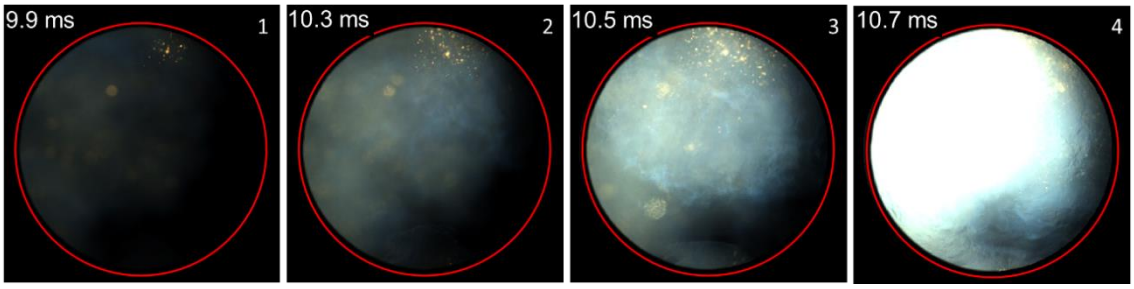

Figure 42: Image sequence of nearly homogeneous ignition of ethanol/air + 10 % He at $\phi = 1$, $T_5 = 850$K, and $p_5 = 20$ bar.

The ignition process is much more homogeneous and shows similarities to the ignition of dilution in nitrogen as shown previously in Figure 33. But the ignition is not perfectly homogeneous although the thermal diffusivity is much higher.

In Figure 41, a quasi-plateau in τ_{ign} is observed at temperatures $T_5 < 850$ K for data with 10 % He dilution which is due to the limitation of our shock tube observation time of roughly 15 ms. In this temperature range, an increase in OH* signal was observed although according to the simulations, ignition is not expected within the observation time of 15 ms. To understand this phenomenon, Figure 43 shows the pressure and OH* traces of a low-temperature case diluted with 10 % He. We observe that the OH* signal starts to increase at $t \approx 16$ ms at a time when the pressure already strongly decreases due to the geometry of the shock tube leading to rapid quenching of the ignition process. The standard analysis of the signal trace that determines ignition from the initial rise in OH* signal is therefore misled and ignition delay times of ~16 ms are reported despite the fact that the main ignition would only occur significantly later (at ~32.5 ms according to simulation based on the measured pressure trace, that was smoothed resulting in two different slopes of increase in *dp*/*dt* for the simulation), which is beyond the test time. Therefore, care has to be taken when interpreting ignition from weak initial signal variations in very sensitive diagnostics like OH* chemiluminescence and late test times.

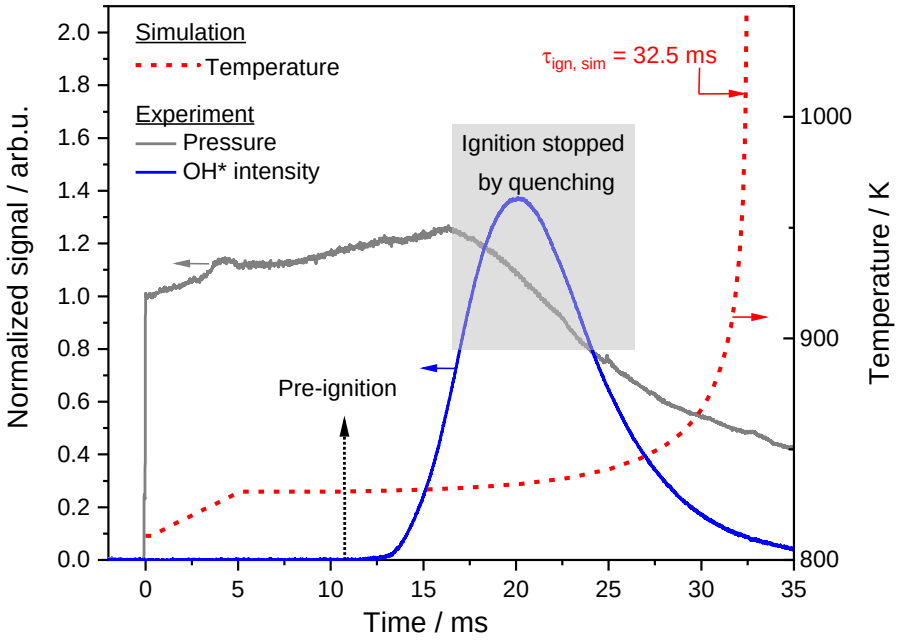

Figure 43: Case of mixture #6 (10 mol % He) at initial T_5 = 811 K and p_5 = 19.1 bar. Left axis: Measured pressure, and OH* signal. Right axis: Simulated temperature using the kinetics mechanism from Zhang et al. [157] and the resulting τ_{ign} from the temperature profile [160].

Considering mixture #3, it can be seen from the analysis of the images and the corresponding pressure profiles that among all τ_{ign} for "particle ignition" cases depicted in Figure 37 and Figure 41, only one (over a total of 32 experiments for mixture #3) was identified as an ignition in the classical way with a strong pressure and chemiluminescence increase (Figure 41 magenta square). In all other particle-driven ignition cases at temperatures between 800 and 850 K) no main ignition was observed due to the limitation of observation time (~15 ms). This confirms that particles have no influence on our measurements at $\tau_{ign} < 8$ ms. Only two cases with local gas ignition at $T_5 > 850$ K were identified as real ignition (Figure 41, green square).

4.3 Interpretation of fuel/air ignition results

How critical the temperature is for the interpretation of ignition delay times can be seen in the results shown in section 4.1 and 4.2. Results of PRF95 and ethanol must be discussed separately because ethanol does not exhibit an NTC behavior. However, in the high temperature region where the ignition delay times are shorter than 7.5 ms (half of the observation time), the scatter

in ignition delay time is in the range of temperature accuracy (see section 9.1 Appendix A). This means that all data points match with the simulation within temperature uncertainties. Although the data scatter a little bit, a trendline can be clearly determined. At low temperatures in the NTC regime of PRF95, the data do not scatter strongly because of temperature non-uniformity (discussed in detail for ethanol in section 4.2). This is due to the less impact of temperature on the ignition delay time at low temperatures (NTC-regime at high pressure shows flattened ignition with temperature variation). At moderate temperatures, the experiments with PRF95 suffer from additional effect of particles which can be minimized by cleaning as it was done in this work. (Further discussion in section 5.1.1.)

The results of homogenous ethanol ignition and the presented study showed different types of ignition, depending on the conditions and gas mixture. The observations cannot be explained by classic analytical calculations and has to be supported by CFD simulation to visualize temperature inhomogeneity due to flow perturbation. Different workarounds were presented here, and multi-color high-repetition-rate imaging was demonstrated as a reliable technique to identify inhomogeneous ignition as a result of non-ideality. Further 3D CFD simulations are needed to analyze the specific effects underlying local inhomogeneities. Experimental design modifications, such as the constrained-volume shock-tube approach [46] can further reduce propensity to remote ignition.

5 Ignition experiments with defined inhomogeneities

Inhomogeneities in gas mixture and temperature can lead to pre-ignition in shock tubes and IC engines. To study the impact of inhomogeneities on the volumetric ignition, defined inhomogeneous conditions were generated in the IVGs high-pressure shock tube. In IC engines, two reasons for pre-ignition are mainly assumed, hot surfaces such as exhaust valves and spark plugs [62, 168] and pre-ignition triggered by lubricant oil spilled into the combustion chamber [7-10, 63, 67, 169]. Both sources of pre-ignition and their impact on ignition delay time were studied in this work.

5.1 Impact of hot local surfaces on homogeneous autoignition

This section of the following chapter is a reprint from the publication Niegemann et al. [48] (2018). The respective parts are entirely based on my own experimental work and a comparison to CFD simulations done by the coauthor I. Wlokas. The final version of the paper was written together with the coauthors who also have contributed to the structuring and wording of the article.

In our experiments, a homogenously premixed fuel/air mixture is shock-heated quasi-instantaneously by a reflected shock wave to a high temperature where autoignition occurs within the 1–100 ms time range (i.e. at 750–1000 K). The temperature can be pre-set depending on the initial pressure of the gases in the driven and the driver section of the shock tube. The shock-tube facility used here is considered to provide homogeneous conditions in the test section close to the endwall with negligible boundary-layer effects because of its comparably large diameter (90 mm). Temperature inhomogeneities are intentionally induced with a rapidly-heated glow plug that was installed in the sidewall 15 mm away from the endwall. The glow plug is permanently in contact with the reactive gas mixture in the test section of the shock tube. During its heating phase (initiated 5 s before the arrival of the shock wave), it locally increases the temperature of the unburned gas mixture. This hot gas volume is compressed and pushed closer towards the endwall by the incident shock wave. At the same time, fresh gas (preheated by the incident shock wave) flows along the heated surface and comes to a rest after the second heating step by the passage of the reflected shock wave. Therefore, three ignition regimes occur simultaneously:

(A) The major part of the shock-heated volume is not affected by the glow plug because the preheated gases are limited to a small volume only and the time before ignition is not sufficient for conductive heating for distances longer than 5 mm. This gas mixture acts as reference for ignition in an undisturbed environment.

(B) A gas cloud is generated with higher gas temperature than (a). This gas has experienced contact with the glow plug before the arrival of the incident wave. Additional to the increased temperature, there is a chance for pre-reactions that have been initiated in the heat-up phase of the glow plug close to the surface. Thus, ignition in this gas volume is affected by combination of processes preventing straight forward analysis.

(C) The immediate vicinity of the glow plug is exposed to the hot surface. Because of the gas-dynamic effects described before, this volume has been purged and the local gases are not affected by the history of the heat-up time of the glow plug. Therefore, this gas provides “clean” conditions for investigating the effect of the hot surface on stagnant gases with post-shock temperatures.

Therefore, the gases in (A) and (C) are nominally identical, with the sole difference of the hot wall being present in (C). The situation in (B) is more complex as consequence of pre-reactions, as well as convective and diffusive transport. For a more detailed separation of the three regimes,

computational fluid dynamics (CFD) simulations were conducted to quantify heat transfer into the gas as well as fluid-dynamic effects by the geometric disturbance imposed by the glow plug. In all cases, the chemiluminescence emission was imaged in the vicinity of the glow plug by a high-speed camera through an UV-transmitting endoscope mounted in the sidewall of the shock tube on the opposite side of the glow-plug. Additionally, the CH* chemiluminescence emission was collected by a photomultiplier with a 431.5 nm narrow bandpass filter (5 nm half width at half maximum, HWHM). Pressure traces were measured with high time resolution to also determine variations in volume-averaged effects as a consequence of surface heating.

The criterion of the occurrence of hot-surface ignition must be related to the balance between the chemical heat release and heat loss in exothermic reactions [170]. This approach considers that ignition occurs when the heat transfer from the reaction from a thin layer in the vicinity of the hot surface exceeds the heat loss from the hot surface to the surrounding gas as discussed in refs. [171-175]. In this work, hot-surface ignition of a reactive mixture was studied for gas temperatures lower than 1050 K behind reflected shock waves and for glow-plug temperatures from 800 to 1200 K. The pressure was chosen around 40 bar. The temperature and pressure for the reactive mixture was chosen to represent IC engine conditions.

A sequence of ten frames of the chemiluminescence imaging is shown in Figure 44. As described above, different types of ignition were observed in the experiments. Without a hot surface, ignition was detected as a sudden rise in homogeneously distributed luminescence starting close to the endwall. No local flame propagation or spread was observed for homogeneous ignition at an imaging rate of 100 kHz for a look from the sidewall. Details about auto-ignition of ethanol mixtures are given in section 4.2. The zone with rising signals follows the reflected shock front with a delay related to the ignition delay time. The time between the frames selected for the figures was adapted to the dynamics of the observed phenomena. Time zero corresponds to the moment where the incident shock wave arrives at the detection plane. The wide-angle characteristics of the endoscope leads to a partial visualization of the endwall (cf. Figure 18) and the red line marks the position where the endwall intersects with the shock-tube wall next to the heated surface. Signal that seemingly appears “beyond” the endwall marker results from (a) emission from gases located between the lens and the endwall and (b) reflection of signal of the endwall. In the outer regions of the detection area, localization of the signal origin becomes more complex, because of the distortion and limited depth of field of the optical system. The camera was focused on the glow-plug plane to best visualize phenomena in the vicinity of the heated surface. The camera signal of each image was averaged and plotted as function of time for cases with a heated surface as shown in Figure 47, Figure 48, and Figure 50.

Differences in ignition phenomena can be detected in shape of the profiles and by the onset of the camera signal in case of local surface ignition described later on.

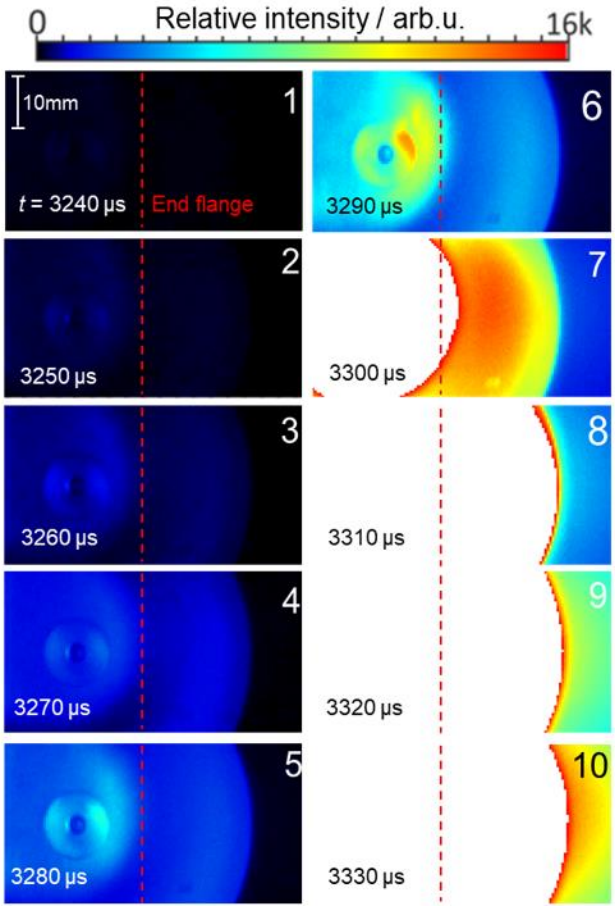

Figure 44: Ten subsequent chemiluminescence images from the shock tube with homogeneous ignition of an ethanol/air mixture at $\phi = 1$, $T_5 = 846$ K, $p_5 = 39$ bar, and $\tau_{ign.} = 3.25$ ms. The glow plug is not heated. The given time represents the time after arrival of the incident shock wave in the measurement plane. For signal at the right of the marked end flange position [48].

With surface temperatures below 800 K, no surface ignition was observed; ignition at these conditions proceeded homogeneously (Figure 44). Ignition delay times were determined both from the photomultiplier signals and by the image sequences. Figure 45 shows a case where the ignition occurs homogeneously, although the temperature of the plug was set to 750 K. The glow plug itself causes a weak signal due to thermal emission centered on the first images. The color scale was reduced to show the entire ignition development, thus in later frames, this weak signal is no longer visible. Although the gas temperature is similar to the surface temperature, the signal intensity close to the glow plug rises more strongly than in the rest of the reaction volume. Preheated gas is transported to the endwall (shown below). Bowlike features that are symmetric from both sides of the plug were observed in this experiment that are not a result of surface reaction but attributed to emission from the volumetric ignition reflected from the endoscope fitting. A correction of this effect was not attempted because the shock tube slightly moves during the experiments preventing the use of simple subtraction algorithms.

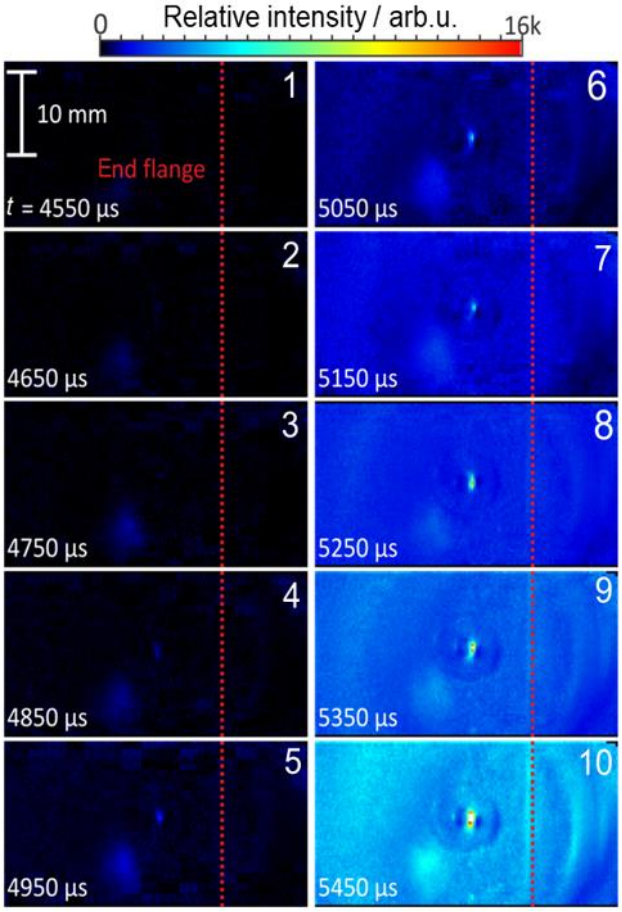

Figure 45: Homogenous ignition of an ethanol/air mixture at $\phi = 1$, $T_5 = 723$ K, $p_5 = 36$ bar, $T_S = 750$ K, and $\tau_{ign.} = 5.92$ ms. For signal at the right of the marked end flange position [48].

In the example shown in Figure 46, the glow plug was heated up to 1200 K. Here, the plug emits light in the visible detected as the spot in the center of the images. At 4.4 ms after the incident wave passes over the glow plug, the area on the glow-plug surface shows chemiluminescence emission that expands radially in time. In this time span, the ignition delay time for volumetric ignition of the gas at the respective temperature is not reached. Frame 10 is 1.3 ms before the main ignition appears as can be observed in the images and the chemiluminescence measurements by the photomultiplier (Figure 46 and Figure 47). The volumetric ignition occurs at 6.8 ms. With the image sequences one can clearly follow the development and growth of the local ignition in the vicinity of the plug described as ignition case c in the introduction.

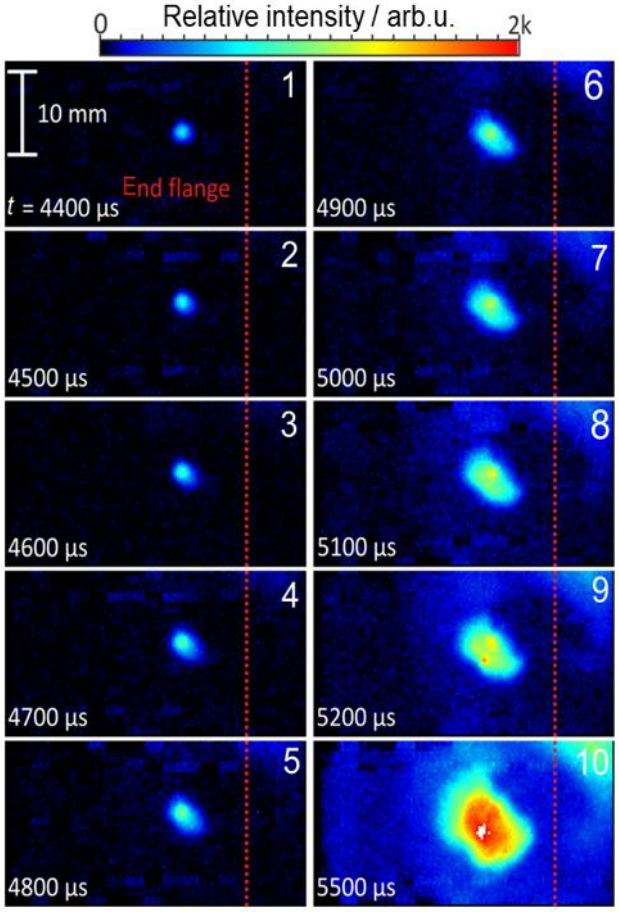

Figure 46: Localized ignition at the glow plug of an ethanol/air mixture at $\phi = 1$, $T_5 = 766$ K, $p_5 = 42$ bar, $T_s = 1200$ K, and $\tau_{ign.} = 6.8$ ms. For signal at the right of the marked end flange position [48].

Optimized detection using different band-pass filters were tested, which results in decrease of signal intensities and blocking the emission of the glowing plug, but no difference in the ignition characteristics was observed, therefore, the measurements were conducted without filtering. At post-shock temperatures higher than 1000 K, the volumetric ignition was too fast (ignition delay times ~700 µs) to observe an effect of the glow plug. Therefore, the focus was on gas temperatures between 700 and 900 K.

In contrast to the photomultiplier measurements, ignition delay times determined from the image sequences allow to provide local information near the spatial temperature inhomogeneity induced by the hot plug. To determine the onset of the main ignition from the camera images, the signal acquired in the images was integrated over the visualized area and plotted as a function of time in Figure 47, and Figure 48. The steady rise in signal from the PMT and integrated image signal shown in Figure 47 is characteristic for surface pre-ignition and is due to the propagation effect leading to a comparably slow increase in the area of the luminous zone followed by the main ignition. The smooth rise in pressure was identified as an indication for local ignition. In contrast, the homogenous autoignition in Figure 48 shows a sudden strong signal rise typical for a homogeneous volumetric ignition.

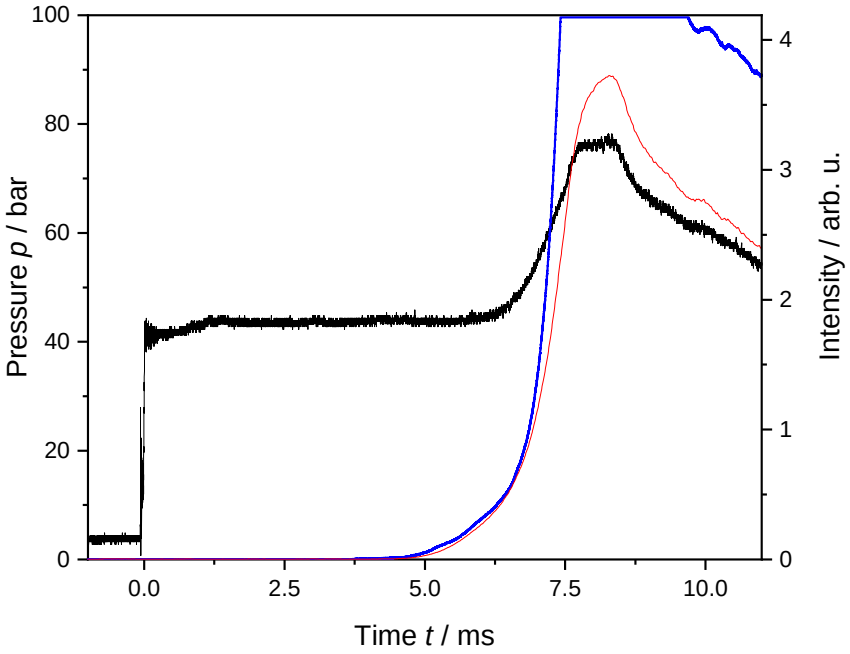

Figure 47: Signal from the high-speed camera detected in the interrogation region as a function of time (red, cf. images from Figure 46); Pressure signal of pressure transducer in measuring plane (black); PMT signal (blue); at $\phi = 1$, $T_5 = 766$ K, $p_5 = 42$ bar, $T_s = 1200$ K, and $\tau_{ign.} = 6.8$ ms [48].

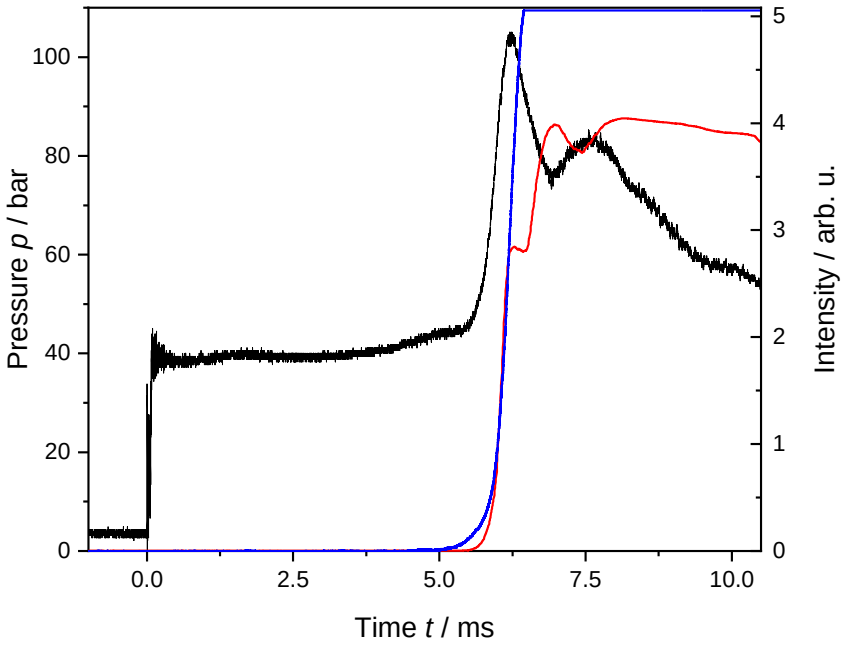

Figure 48: Signal from the high-speed camera detected in the interrogation region as a function of time (red, cf. images from Figure 45); Pressure signal of pressure transducer in measuring plane (black); PMT signal (blue); at $\phi = 1$, $T_5 = 723$ K, $p_5 = 36$ bar, $T_S = 750$ K, and $\tau_{ign.} = 5.92$ ms [48].

At higher temperature (T_5 = 850 K, Figure 49), the additional thermal effects caused by the gas heating around the glow plug before the arrival of the incident shock wave can be visualized. 80 µs after the passage of the incident wave at the glow plug, a luminescent gas kernel can be observed that already starts growing after it was pushed towards the endwall; ignition area (b) described at the beginning of section 5.1. This gas-dynamic effect was also investigated in the CFD simulations shown later. At 40 µs, the wave reflects off the endwall and the leading front of the reflected wave further heats up the gases. As shown in the simulations below, the gas temperature in the trail of hot gases behind the incident shock wave is approximately 50 K higher

(950 K instead of 900 K) than in the bulk gas behind the reflected shock wave. Because of this increased temperature, the ignition in the wake of the hot spot is accelerated leading to strong luminescence, which indicates the movement of the reflected shock wave from right to left (visible in frame 6–9 in Figure 49). The calculated arrival time of the reflected shock at the glow plug is at 65 µs. The gas at the glow plug, however, has been purged off the hot surface, and the result of reactions caused by the heating from the hot surface are clearly visible from the discontinuity of the signal of the moving front and the signal at the glow-plug position in frame 9 and 10. The following CFD simulations and discussion will show that the local pre-ignition at the glow-plug position relative to the bulk gas can be attributed to the effect of the hot surface, while preheating and the geometry lead to a hot cloud downstream from the hot surface too close to be fully ignored, while the reactive gas purged to the endwall effects the volumetric ignition process only.

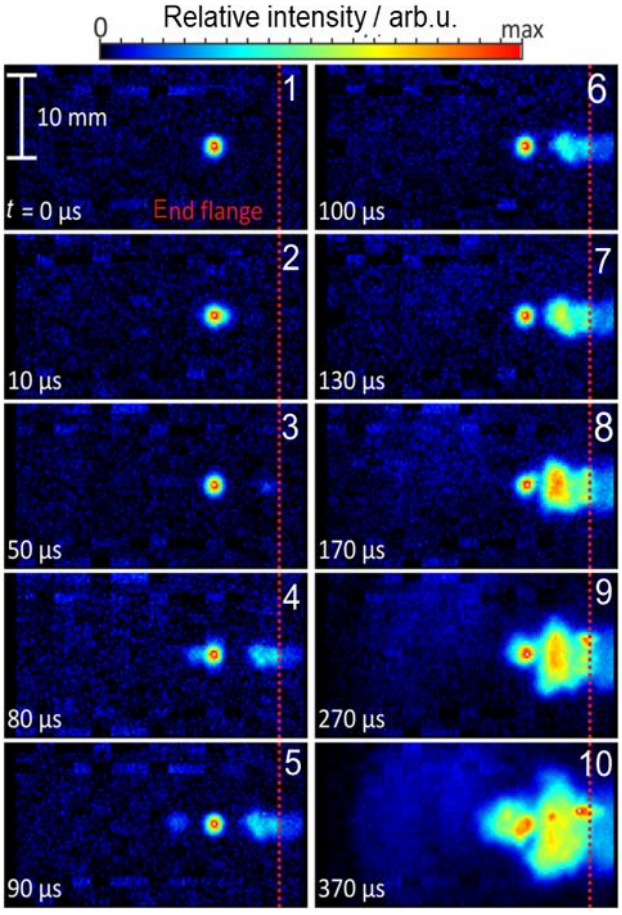

Figure 49: Inhomogeneous ignition of an ethanol/air mixture at $\phi = 1$, $T_5 =$ 850 K, $p_5 = 40$ bar, $T_s = 1200$ K, and $\tau_{ign.} = 2.86$ ms. For signal at the right of the marked end flange position [48].

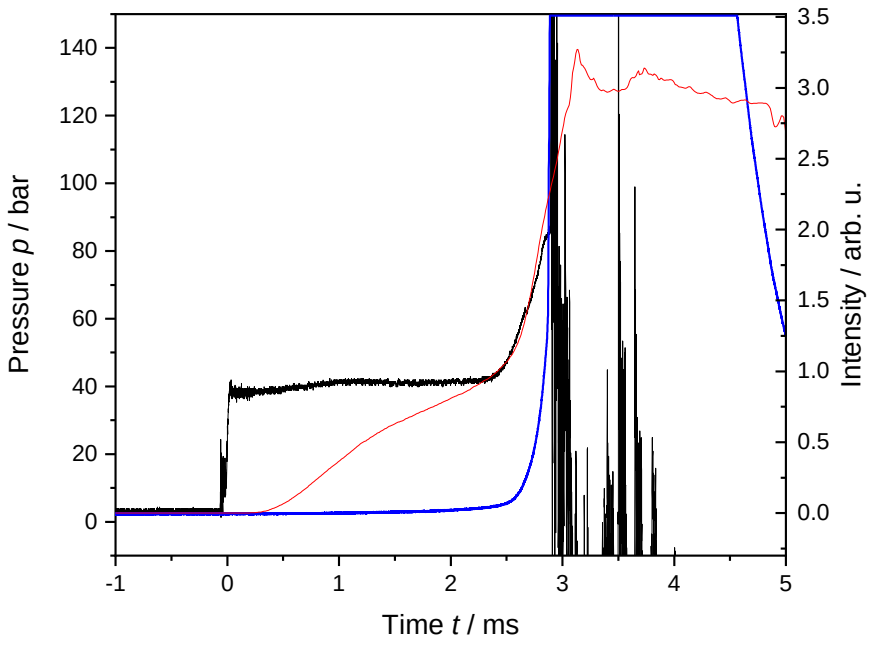

Figure 50: Signal from the high-speed camera detected in the interrogation region as a function of time (red, cf. images Figure 10); Pressure signal of pressure transducer in measuring plane (black); PMT signal (blue); at $\phi = 1$, $T_5 = 850$ K, $p_5 = 40$ bar, $T_S = 1200$ K [48].

In case of ethanol, the results show that the ignition on the hot surface appears in a narrow range of conditions. Ethanol was found to be insensitive to surface ignition for glow-plug temperatures below 1000 K and gas temperatures higher than 900 K. With increased surface temperature, the ignition is obviously seen near the surface.

The experimental observations were supported through simulation to decouple the unwanted side effects of preheating and gas dynamics from the chemical kinetics.

A three-dimensional simulation of the unsteady flow field was conducted, to answer the following questions about the effect of the hot surface as well as its geometric constraints on the flow field:

(a) Do the geometric changes that came along with the installation of the glow plug and the crevices shown in Figure 18 affect the post-shock conditions? Significant temperature or pressure variations due to gas-dynamic effects could interfere with our measurements and also cause a deviation from calculated post-shock conditions and limits the comparability to other ignition delay time measurements.

(b) Can the described interpretation of the various observed local ignition phenomena due to geometric disturbance be supported by (low cost) simulations?

(c) What is the expected gas temperature in the hot gas generated around the glow plug and what are the dimensions of the heated gas cloud and are the observed premature ignition phenomena consistent with the expected reduction in (local) ignition delay time?

(d) Is the gas preheating relevant for the experimental results? What happens with the preheated gas cloud around the glow plug when the shock front passes by?

(e) What are the conditions behind the incident shock in the vicinity of the glow plug (regime C as described in the introduction) and close to the endwall (regime B)?

(f) What are the post-shock conditions of the heated gas cloud close to the plug (regime C) and close to the endwall (regime B)?

Numerical investigations of the unsteady flow in a shock tube are rare,[160] except for one-dimensional, inviscid problems. The latter are for example the Riemann problem, an important object of investigation for hyperbolic partial differential equations, and its numerical benchmark

version: Sod's shock tube [176]. The possibilities for numerical investigations of the three-dimensional flow in shock tubes are usually limited due to the multi-scale and transient nature of the flow. Simulation strategies employed in the recent past are either limited in the geometric description of shock tube features and are usually highly demanding in terms of computational resources. For the latter reason we decided to conduct a limited investigation. All investigations were conducted with the open-source CFD framework OpenFOAM [177] that provides all the necessary numerical schemes. The choice of schemes for a particular step of the simulation strategy is described below. The simulations presented here are not intended to fully reflect the conditions of the performed experiments (including reactions), but to focus on a qualitative assessment of the gas-dynamic effects and their interaction with small perturbations by geometry of the glow plug and the local heating. The (simulated) shock tube is filled with air instead of a real fuel/air mixture, its dimensions correspond to the real shock tube in the lab, but the three-dimensional simulations are limited to the last 100 mm of the test section. In order to reduce the problem's complexity and ensure consistent initial and boundary conditions.

As a first step, the influence on gas dynamics (inserted glow plug without heating /homogeneous wall temperature) needed to be investigated (viscous/inviscid, do boundary effects play a role?) in the simulation. Simulations of the viscid flow, solving the full set of conservation equations, and simulations of the inviscid flow, solving the Euler equation, showed the same *temporal* behavior, which is not surprising, as the gas dynamics are only weakly affected by the viscosity. An effect of boundary layer formation could be observed but was minor. In the viscous case for an unheated glow plug, the pure geometric effect is investigated and results are shown in Figure 51, 100 µs after the shock wave is reflected from the endwall (RW: reflected wave; endwall: right end of image). The simulation shows the temperature distribution (left image) from the central axis (top of the image) to the wall (bottom of the image) for homogeneous wall temperatures.

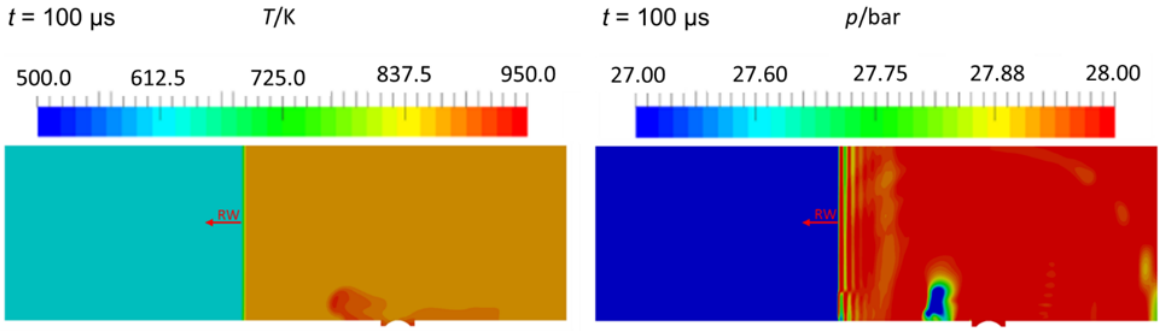

Figure 51: Viscous shock simulation 100 µs after reflection of unheated plug geometry (temperature left; pressure right); at $T_2 = 609.88$ K, $p_2 = 8.626$ bar and $u_{RW} = 469.64$ m/s calculated as 1D solution of the shock tube problem [48].

The simulation predicts a partial heat-up of the gas, by reflections in the crevice between holder and glow plug. Because of these findings, a clear separation between the conditions in the crevice and the ignition situation of area c (explained at the beginning of this section) is necessary. The heat-up results in temperatures close to 1000 K in the crevice and in the gas along the sidewall while the bulk part (area a) is heated to 900 K, simultaneously, the hotter gas especially the formed cloud on the left side of the glow plug (Figure 51) is at a lower pressure level. This reduces the influence on the ignition delay time. Concerning the question (a) the simulation shows an effect of the geometry in post-shock temperature and pressure close to the wall. Compared to the gas volume the effect is minor.

The questions (d)–(f) only plays a role in the heated case shown in Figure 52 and Figure 54. Figure 54 shows the complete sequence of vertical cuts through the glow-plug plane, from the incident wave (IW) running through the measuring plane until the reflected shock passes the measuring plane. The preheated, and possibly already reacting gas is swept completely away from the plug

cavity after the passage of the incident shock waves (Figure 54, image 2 at $t = 10$ µs) the reflected shock wave forms a hot cloud downstream close to the hot surface (Figure 54, image 4 at $t = 80$ µs). This cloud is also shown in the simulations of the unheated surface (geometric imperfection effect), while experiments without heating didn't show any local ignition close to the glow plug position. Therefore, the hot-surface ignition can be observed independently from the gas preheating effect in our experiment (question d), while the formed hot cloud can promote the local ignition in the vicinity of the hot surface. The different scenarios of the effect of the hot surface and the surrounding cloud are discussed using CFD simulations results in Figure 54.
The heated volume after 10 s of preheating (considering of the heating ramp shown in Figure 14) is distributed along the 15 mm sidewall between glow plug and endwall (question (e)). The main part and even the hottest one is at rest close to the endwall (Figure 54, image 3, $t = 50$ µs). Because the CFD simulation neglects reactions, we calculated the residual ethanol concentration over time of each condition using a state-of-the-art reaction mechanism from Curran [195] for the respective temperature conditions. The top graph of Figure 53 displays the ethanol concentration over a time of 10 s after reaching the maximum glow-plug temperature and 2 bar, conditions typical before the arrival of the incident shock. While no ethanol is consumed in the bulk gas, it only takes about 0.8 s for complete reaction of ethanol in the heated cloud close to the plug. Depending on the time when the shock wave arrives, the wave pushes a cloud of reacting ethanol or hot exhaust to the endwall. The reactions in the cloud never result in a volumetric ignition before the shock, in any experiment.
Behind the incident shock, the disturbed flow caused by the crevices around the glow plug as already shown in Figure 51 is important. The shock wave is partially reflected on the edge of the crevice, which heats the gas in the crevice, while the hot cloud in the heated case is spread along the sidewall and fresh cold gas is now in contact with the hot plug (Figure 54, image 2). For the unheated case, this reflection is negligible considering the very short reaction time until the reflected wave arrives. In contrast, the heated case shows harsher conditions in the crevice. Here, the gas in the crevice reacts in a very short period of time (Figure 53, center graph). At this point, the heated case of Figure 53 shows that there are only reaction products left in the crevice when the reflected shock arrives. Until this point, the preheating and the geometric disturbance show no problem for discriminating local from volumetric ignition.

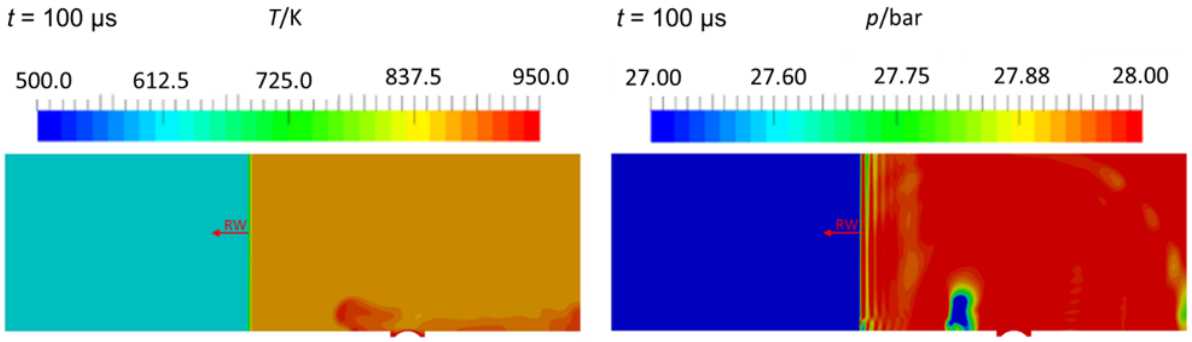

Figure 52: Viscous shock simulation 100 µs after reflection of heated plug geometry (temperature left; pressure right); at $T_2 = 609.88$ K, $p_2 = 8.626$ bar and $u_{RW} = 469.64$ m/s calculated as 1D solution of the shock tube problem [48].

Post-reflected-shock conditions for the heated case are shown in Figure 52. The reflected wave creates a hot gas cloud next to the glow-plug with lower pressure while the pressure in the crevice is similar to the bulk gas (Figure 52)(question (f)). The variations of temperature and pressure result in different ethanol concentrations over time, because of differences in initial conditions predicted by the simulations. However, from the simulation, the gas cloud in the vicinity of the

plug is always similar for both cases (heated and unheated plug). Also, we never observed local chemiluminescence close to the plug for unheated case and behind reflected shock waves.
In the heated case, the reflected shock wave heats up the gas cloud that is pushed close towards the endwall (Figure 54, image 2; regime B, c.f. introduction) again. When running through the measuring plane again the wave pushes the heated gas close to the plug in the other direction, forming a second hot cloud, just beside the plug; cf. the simulations (Figure 54, image 5) and experiments (Figure 49, image 5) 90 µs after the IW. Figure 52 shows that the pressure is locally lower in the area of the second hot cloud and also in the cloud close to the endwall (regime B), while the local maximum temperatures in the cloud is only 50 K higher than the bulk gas, so that the local ignition delay time would be longer than elsewhere even longer than in the bulk gas (Figure 53,bottom graph). The simulations allowed to verify the experimental procedure, reproducing the flow conditions (cf. Figure 49and Figure 54) and yield information about local post-shock temperature and pressure conditions (question (b)). Some qualitative interpretations can be drawn on the basis of the conditions obtained by the numerical simulations: First, the geometric changes clearly show the effect on flow conditions, but we found out that this do not dominate the post-shock conditions in the heated case (question (a)–(d)). Second, in the crevice, the temperature and pressure is much higher which would imply that ignition starts there (Figure 53,bottom graph). However, again we did not observe this, apparently, because the gas mixture is not reactive anymore and contains just burned gases (question (e)). The fresh gas that is around the glow plug transported by the reflected wave has the same conditions as the bulk gas not affected by the procedure or the geometric disturbance (question (a) and (f)).

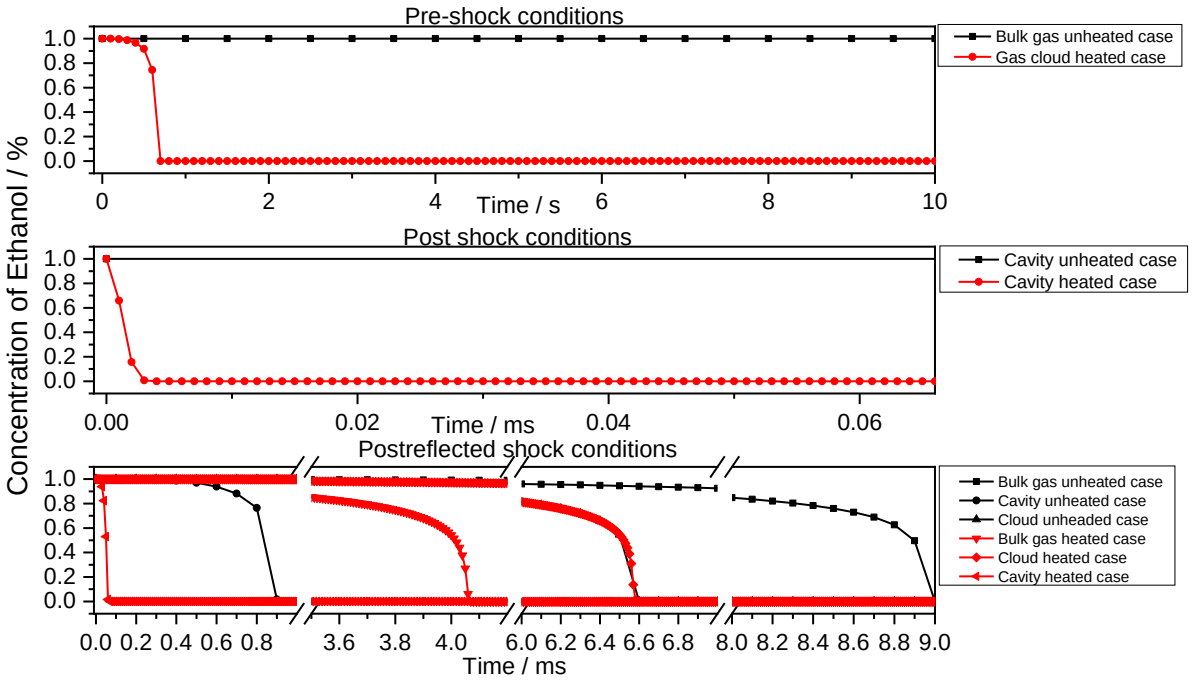

Figure 53: Ethanol concentration in the vicinity of the glow plug over time for the unheated glow plug (black) and heated glow plug (red) at different shock states; pre-shock conditions: at $T_1 = 373$ K, $p_1 = 2.0$ bar, gas cloud $T = 850$ K; post-shock conditions of unheated crevice: $T = 885$ K, $p = 28.5$ bar; post shock conditions of heated crevice: $T = 1600$ K, $p = 17.7$ bar; post-reflected-shock conditions unheated: $T_5 = 885$, $p_5 = 28.8$ bar, $T_{cloud} = 900$ K, $p_{cloud} = 28.8$ bar, $T_{crevice} = 1000$ K, $p_{crevice} = 36.6$ bar; post-reflected-shock conditions heated: $T_5 = 885$ K, $p_5 = 29$ bar, $T_{cloud} = 900$ K, $p_{cloud} = 28.8$ bar, $T_{crevice} = 1200$ K, $p_{crevice} = 34$ bar, ref. [48].

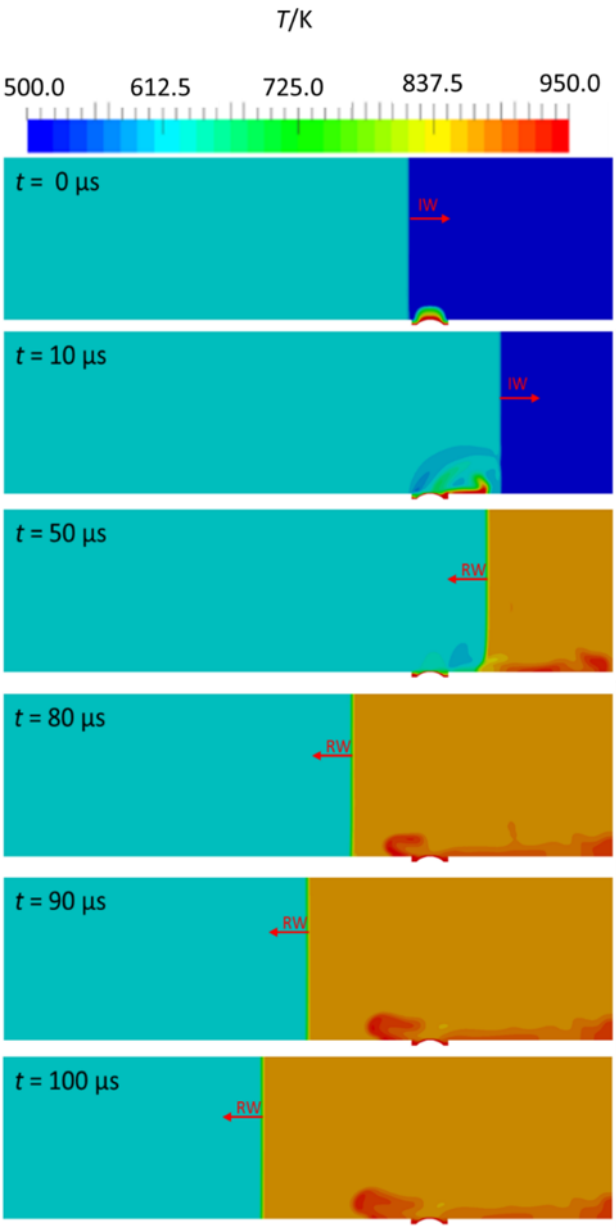

Figure 54: Simulated temperature fields at various times after the incident shock arrives at the glow plug. The time-stamp corresponds to figure 9, the temperature is scale from 500 to 950 K); at $T_2 = 609.88$ K, $p_2 = 8.626$ bar and RW = 469.64 m/s calculated as 1D solution of the shock tube problem [48].

5.1.1 Interpretation of hot surface-induced ignition

The motivation to introduce a hot surface into fuel/air mixture at autoignition conditions focusses on unwanted pre-ignition in internal combustion engines. The results of the study Niegemann et al. [48] support additional data to understand the unwanted effect of membrane particle ignition and the impact on the volumetric ignition.

The impact of the hot surface was not really answered, and no ignition delay times were presented in the publication, because the ignition delay times effected by the hot surface showed extreme scatter that could not be explained by the experiment. Considering the new results from Nativel et al. [160] shown in section 4.2 it is possible to explain the measured ignition delay times. Figure 55 shows the measured ignition delay times for ethanol/air, ethanol/air in the presence of the hot surface and comparison with simulations. The mechanism from Marinov [178] was modified by Cancino et al. [179] to reproduce well the measured data, but the changes that were adopted in the mechanism in Ref. [179] were empirical to fit the data, while the data is affected

by inhomogeneous ignition. Only two of 10 experiments with heated surface show ignition delay times that are shorter than the data simulations from Cancino et al. [179], which represents well the reference measurements (red dots) from this study. The other 8 of 10 experiments scatter around the banded prediction which agrees well to the measured data of mixture #3 in section 4.2.

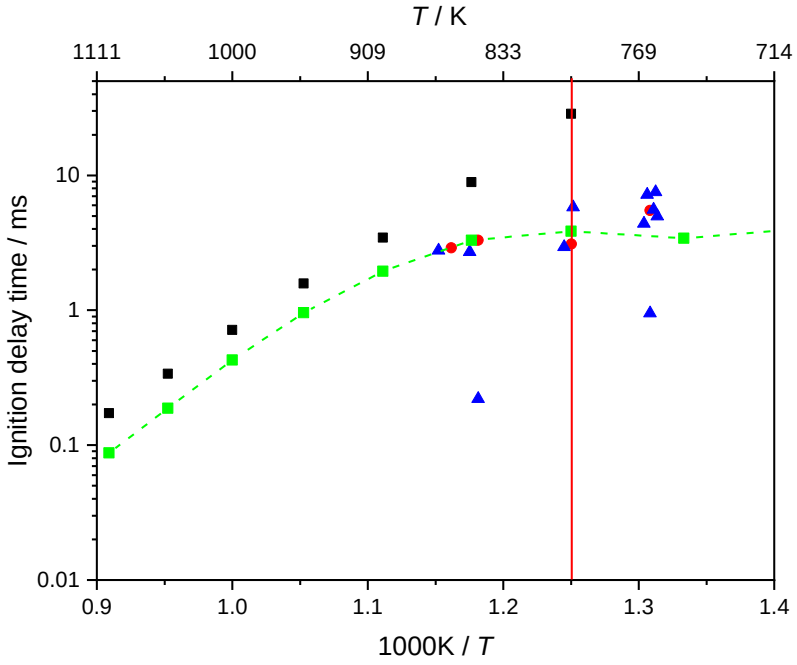

Figure 55: Ignition delay times of ethanol in air at $p_5 = 40$ bar, $\phi = 1$: (■) induction time according to CH* simulated with Ranzi; (■) induction time according to CH simulated with Cancino; (●) ignition delay time for homogeneous conditions; (▲) ignition delay time for the heated surface.

To suppress these effects recent works have shown that the addition of 10 % helium can minimize non-idealities, previously shown in section 4.2. High dilution levels would also work but would reduce the local reactivity too far to be sensitive to the artificial introduced ignition sources.

It was also shown in section 4.2 that hot particles were not present at temperatures below 800 K because the gas temperature is too low. This means that disturbance by hot particles can be avoided at low gas temperatures so that an effect by particles can be excluded from the very low temperature results shown on the right of the red line in Figure 55. Nevertheless, measurements at gas temperatures of 750 K in presence of the hot surface heated to 1200 K did not show any reduction of ignition delay time, although local ignition was clearly observed in the vicinity of the glow plug.

Based on the experimental results in chapter 4 it can be concluded that cleaning and the reduction of particles minimized the promoting effect of particles to reduce the ignition delay times. Based on the observation in section 5.1 where the hot surface was not able to reduce the ignition delay time it is concluded that it is not the heat release from the hot particle which is responsible for the reduction of ignition delay time, but rather the oxidation reactions of the aluminum membrane.

5.2 Pre-ignition triggered by droplets

Abnormal ignition phenomena in IC engines lead to “knock” or “super knock”, which can damage the engine dramatically. Wang et al. [14] summarized the problems to this subject in his review “Knocking combustion in spark-ignition engines”. Engine tests revealed that LSPI occurs randomly

at operation at high load and low engine speed [64]. There is an overall consensus that droplets of engine oil play a predominant role in the process of LSPI. There is a hypothesis that engine oil droplets are splashed into the combustion chamber, initiate early ignition and subsequent flame propagation, which transits to detonation under the right circumstances [3-6]. Often, this first knocking cycle is followed by several alternating knocking cycles. It is assumed that the following alternating knocking cycles are caused by particles that are removed from the piston or fire deck by the detonation wave, remain in the chamber heated by the following normal cycle and trigger local ignition in the compression stroke of the second next cycle [180, 181]. This work focuses on the hypothesis of droplets triggering “super knock”. Until now the latter postulation is not proven, and the mechanism of droplet-initiated ignition is not well understood.

The impact of lubricant oil on the frequency of LSPI events has been shown on engine tests by the use of different oil compositions [7-10]. Engine tests are always dependent on many different parameters and show cycle to cycle variation which is disruptive for investigation of statistically occurring events in single cycles. To control the occurrence of droplets, injectors for lubricant oil were installed in research engines [70]. To reduce the impact factors (parameters) in the experimental oil droplets were injected into RCMs and the ignition was studied [67, 72, 73]. The amount of oil and the number and size of droplets are critical for the heat transfer, evaporation, and ignition of the droplets. Therefore, an injection system for single droplets was developed by Ohtomo et al. [71] to control all parameters of the droplet and inject this droplet into an RCM. The results showed that ignition starts in the trace of the droplet a few ms after injection depending on droplet composition, droplet size, droplet temperature and ambient gas temperature.

This result shows the high relevance of evaporated/decomposed droplet material for the ignition process. Because the evaporation and decomposition can happen on the liner, piston or piston crevice the previous existence of a droplet is not necessary for an engine LSPI event if the ignition only depends on the gas phase products. Likewise, formation of highly reactive gas-phase species in the lubricant oil that are released in the compression stroke is also process hypothesis. This work pursues a three-step strategy to investigate pre-ignition triggered by lubricant oil and the containing additives. The used lubricant oil samples and their composition is shown in Table 2.

1. The samples were studied by TGA/DSC in combination with QMS to understand the thermal decomposition/evaporation behavior and identify released gaseous products
2. Gaseous products (from pyrolysis of the oils) with potential impact on autoignition were added to a fuel/air mixture in realistic concentrations to investigate their potential effect on ignition
3. Droplets were injected into the fuel/air mixture to follow the ignition process under controlled conditions and to determine the impact of the droplets on the ignition delay

Table 2: List of studied samples.

Sample Name	**Composition**	**Role**
Base oil	Pure group I base oil	solvent
ZDDP	Base oil + Zinc diphosphate	Anti wear
Ca-det.	Base oil + Ca based detergent	Detergent
Mg-det.	Base oil + Mg based detergent	Detergent
Mo-Fric.	Base oil + Mo based friction modifier	Friction modifier
Oil A	Group IV base oil + moderate additive package	Fully formulated

Oil B	Group IV base oil + high Mg-det. additive package	Fully formulated
Oil C	Group IV base oil + high Ca-det. additive package	Fully formulated

5.2.1 Decomposition of oil samples

All oil samples were thermally decomposed by heating in a crucible and the mass loss, energy flow, and the exhaust gas composition were analyzed in a TGA/DSC in combination with a QMS. The samples were heated by 10 K/min while the reaction volume was constantly flushed by argon (inert conditions) or synthetic air (oxidation). Both processes were compared, and the mass spectra of the exhaust gas were analyzed for volatile species that could have a promoting impact on local ignition processes.

Base oil has the simplest composition compared to the other samples from Table 2. The mass loss started at 209°C independent from the environment. In inert gas flow, the sample decomposed and evaporated through heating at a temperature of 360°C. In contrast, in air the endothermic oxidation reactions start around 200°C. In Figure 56 it can be seen in the DSC traces (red lines) that the dashed line starts to diverge from the trace under inert conditions (solid red line) and decreases strongly showing two strong exothermic peaks and additional small peaks for over 400°C. The mass loss rate is similar for both. Until 360°C most of the mass is gone. While the pyrolysis is completed with about 2% solid residual mass, the oxidation has higher residual mass of about 10% which slightly decreases at the highest measured temperature of 500°C.

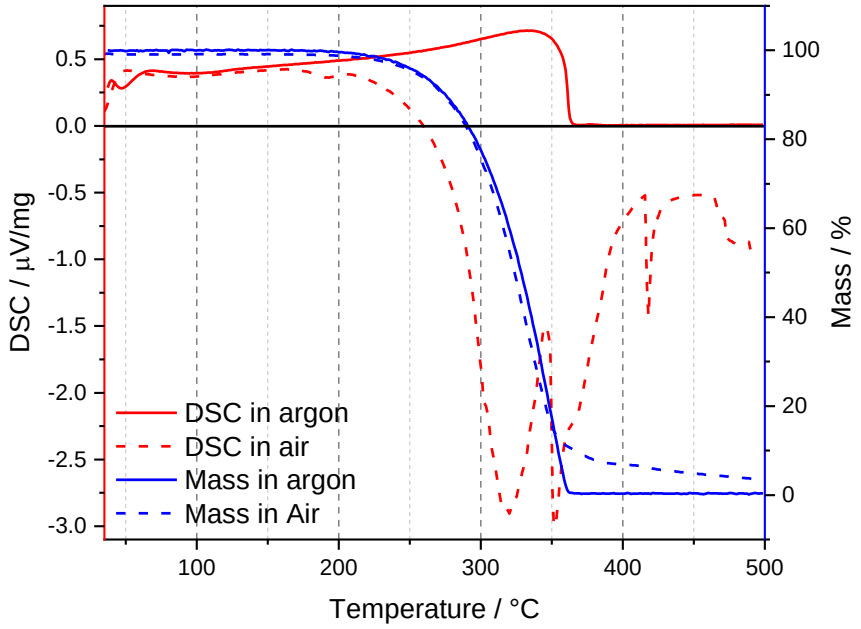

Figure 56: Mass loss and energy flow during the thermal decomposing of the base oil.

The reproducibility of the procedure was tested by running the same sample three times in a row. In Figure 57 the mass loss of the repeated procedure shows the same behavior (two-step oxidation trend) while the traces deviate about 10 K in temperature for DSC measurements at the beginning the two oxidation steps showed better agreement as well as the mass loss. Because the presence of metal could potentially have an impact on the decomposition process or have catalytic effects on the decomposition of base oil, metal flakes were added to the oil to check the hypotheses.

Additionally, the effect of a ZDDP-passivated metal on the decomposition of base oil was tested. Especially the anti-wear additives interact with metallic surfaces for protection reasons. It is known that ZDDP passivates metal surfaces at elevated temperatures to prevent oxidation (corrosion) [182]. When testing the decomposition of base oil in presence of a piece of metal piston ring, the first oxidation step is shifted about 5–10 K to higher temperature and the heat release is less compared to pure base oil. This shift is minor considering the fluctuation for identical sample and the increased heat capacity by the addition of metal. The second oxidation step, however, shifts to lower temperature by about 20 K so that both oxidation peaks move closer. This trend can be found in the mass loss starting later, but higher mass loss rates. Finally, the mass loss drops at lower temperature. If the metal piece is exposed to ZDDP in advance, the base oil shows the same behavior of first oxidation step with largest exothermic energy release and the incursion between the two steps is now in the range of a few percent instead of going down to nearly zero as it was observed in the previous test. The peak of the second oxidation step is two times larger. It is the only case in which the second oxidation step shows larger exothermic energy than in the first step. The higher amount of energy release is due to the high reactivity of the ZDDP as it is shown later in this chapter.

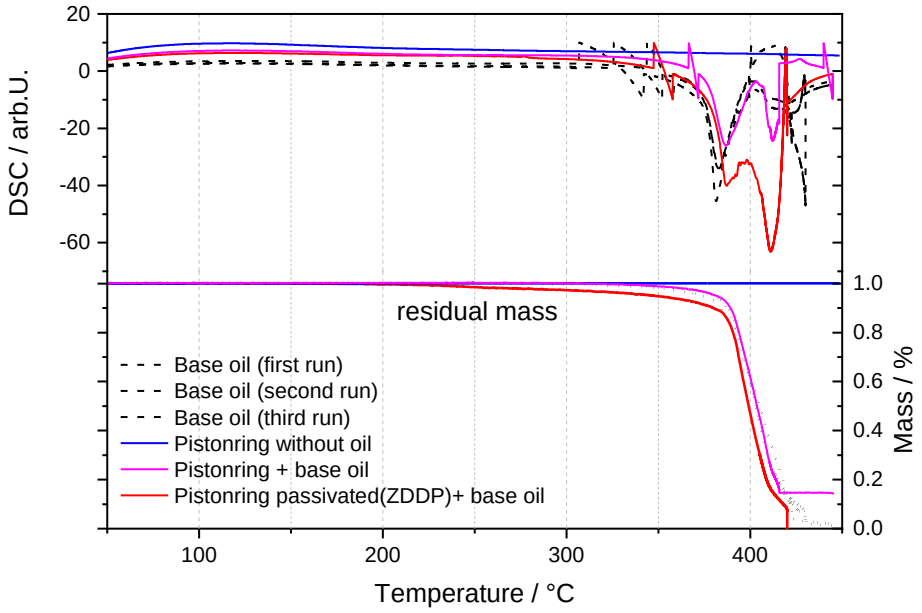

Figure 57: Mass loss of base oil, base oil with metal flake and base oil with metal flake exposed to ZDDP.

The measured mass spectra of base oil showed a characteristic pattern for alkenes. In oxidative environment, the mass spectra showed additional peaks from oxidation products like carbon dioxide. Figure 58 shows the mass spectra of the exhaust gas from base oil heated up to 300°C in argon and air gas flow. The difference in the CH-pattern can be associated to combustion intermediates like alcohols. In contrast, only pyrolysis products were measured in Ar.
The samples containing additives were dissolved in the base oil. Therefore, the decomposition and gaseous products create a baseline for the following results of lubricant additives.

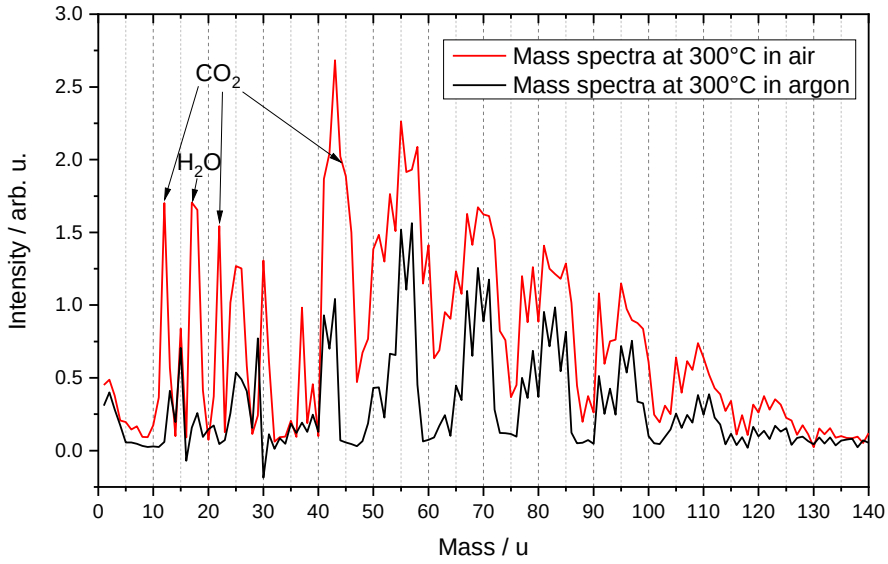

Figure 58: Mass spectrum of exhaust gas from base oil at 300 C in air- or argon flow.

ZDDP anti-wear additive

The additive ZDDP (zinc diphosphate) showed high reactivity in the first test, so it was necessary to further dissolve the ZDDP in base oil to a low concentration similar to the amount of typical additive packages. In an inert environment, the low concentration of ZDDP showed only about 15 % mass loss without strong endothermicity as shown in Figure 59. But in an oxidative gas flow, the sample showed an initial phase of energy release followed by a strong energy release which is three times higher than measured for the pure base oil. The evaporation during the oxidation occurs at lower temperatures and it is of the same magnitude as in the pyrolysis case. Because of the high amount of residual mass, compared to the pure base oil which had less than 10 % of residual mass, it is supposed that the ZDDP interacts with the base oil and hinders the base oil to decompose and evaporate completely.

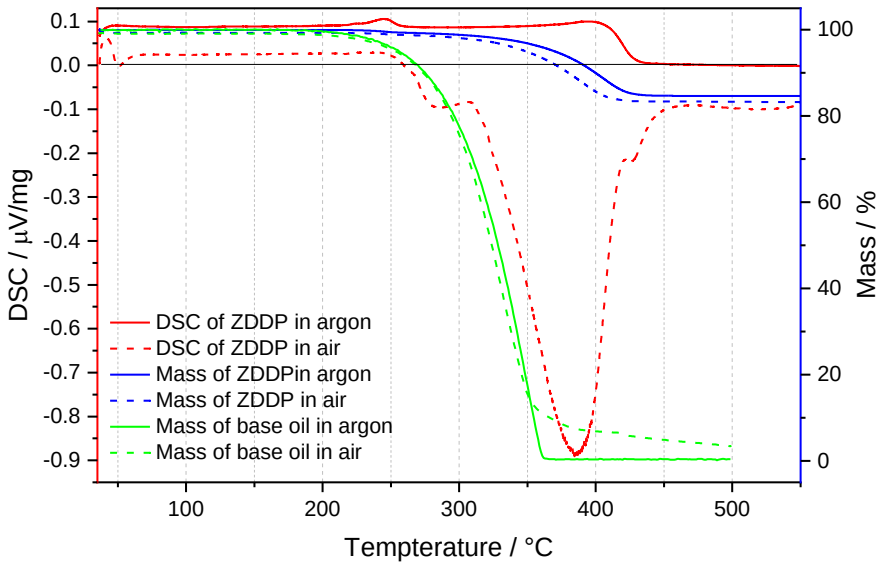

Figure 59: Mass loss and energy flow during the thermal decomposition of the base oil and base oil with ZDDP.

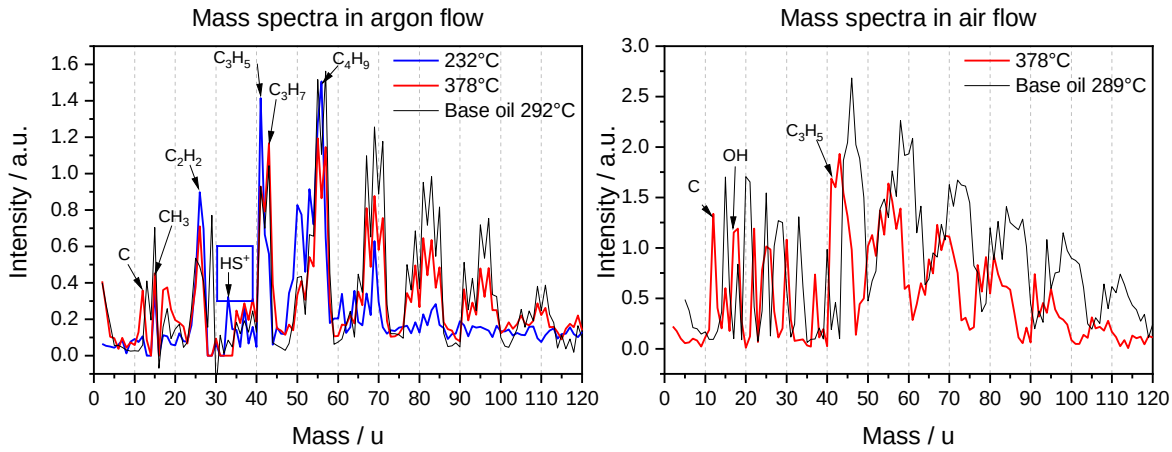

Figure 60: Mass spectra of pyrolysis products of base oil and base oil doped with ZDDP in argon or air flow.

When comparing the mass spectra of base oil and base oil with ZDDP (Figure 60) two trends were observed. First, at inert conditions, a sulfur peak appeared. Second, in an oxygen environment, the overall peak height is lower over the measured temperature range and the C–H progression pattern is shifted by three mass units.

Calcium-based detergent

The detergent additives typically have a metal core like Ca or Mg embedded in a polar head group linked to a negative alkene so it can be dissolved in the base oil. The mass loss starts at 300°C in the inert case with a final residual of 38 %. In the oxidative case, the mass loss already starts at about 270°C followed by a very strong mass loss at 355°C with a strong energy release (Figure 61, red dashed line). The mass loss rate changes (i.e., the slope of the signal) at 400°C indicating a change in the decomposition/oxidation process. This change induces a strong decrease in the energy release. Compared to the pure base oil the onset of decomposition is shifted towards higher temperatures. The residual mass was also about 38 % independent of the gas flow. The residual mass cannot be explained by the remaining metal or products like CaO. Peltier and Duval [183] were the first studying the decomposition of calcium by thermogravimetry analysis. Later Simons and Newkirk studied calcium oxalate monohydrate and the impact of test conditions on the thermogram [135]. For complete decomposition, a temperature of 1000°C is necessary. Therefore, in the present work only the first, and parts of the second decomposition phase was observed. Compared to calcium oxalate monohydrate, the Ca-detergents start to decompose at higher temperatures, because the calcium is bonded to a salicylate and is dissolved in oil. The second decomposition step is observed between 450–500°C. Simons and Newkirk [135] found that CaC_2O_4 decomposes to $CaCO_3$ at this temperature.

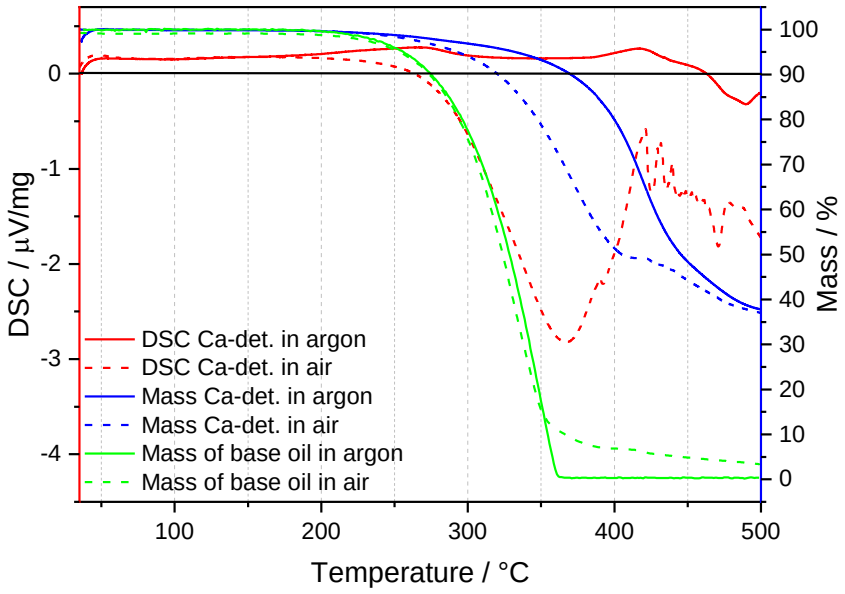

Figure 61: Mass loss and energy flow during the thermal decomposition of base oil and base oil with Ca-based detergent.

The catalytic effect of iron was tested by adding an iron flake to the oil in the crucible. 11 mg of the Ca-detergent sample was investigated in direct contact with a 2.5 mg iron flake taken from a cylinder liner. The results showed that independently of the bath gas, the mass loss in the presence of metallic iron starts earlier (at ~230°C) compared to the standard test without iron (Figure 62). The energy-release signal (oxidation case with vs. without iron) is about 20 % less comparing the red dashed and solid line on the right side of Figure 62. Both the pyrolysis and the oxidation reaction seem to be catalyzed by the iron flakes. The difference in the DSC signal can be associated with the heat capacity of the iron flakes but does not explain the clear shift of the first step in mass loss that appears 60 K earlier, therefore the decomposition is catalyzed by the iron.

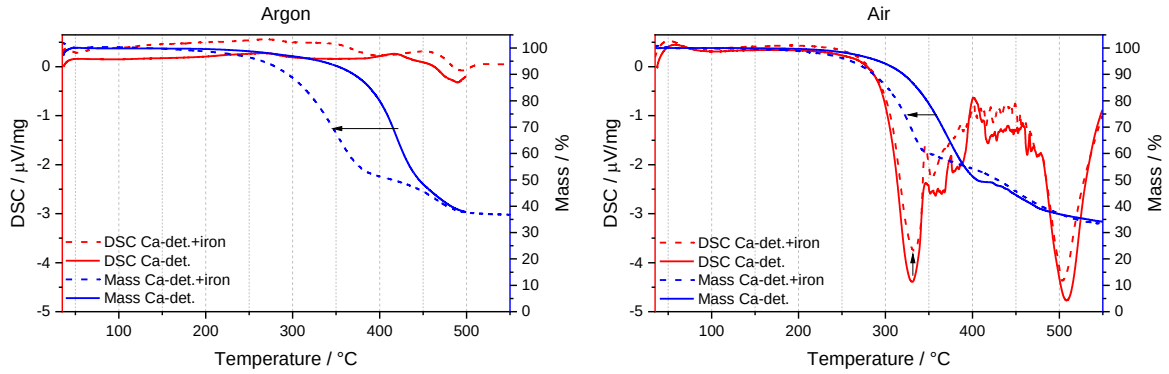

Figure 62: Impact of a cylinder liner iron flake on the decomposition properties of Ca-det. in argon and air.

The mass spectra of the decomposition products of the Ca-detergent sample did not show any difference to the pure base oil besides a shift to higher temperature as discussed in the description of mass loss.

Magnesium based detergent

The decomposition of the Mg-det. starts earlier than with the Ca-det. at ~240°C independently from the bath gas. In airflow the Mg-det. evaporates similarly to the base oil up to a temperature of 320°C with a similar energy release. Only a small mass loss was observed in the 320–380°C range in air before the evaporation at higher temperatures similar to the argon case (see Figure

63, dashed and solid blue line). The solid blue line in Figure 63 shows less than 5% of mass loss in argon. In inert environment Mg-det. seems to decelerate the decomposition. Compared to the Ca-detergent, the Mg-detergent has a reduced impact on the oil decomposition and evaporation. Also, the residual mass is lower (15–18 %), which can be attributed to the reaction products of the metal component.

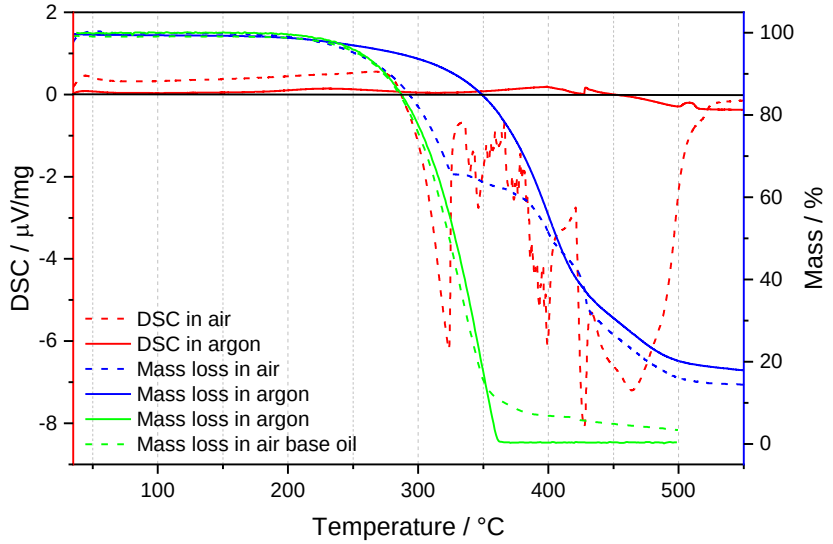

Figure 63: Mass loss and energy flow during the thermal decomposition of Mg-detergent in base oil.

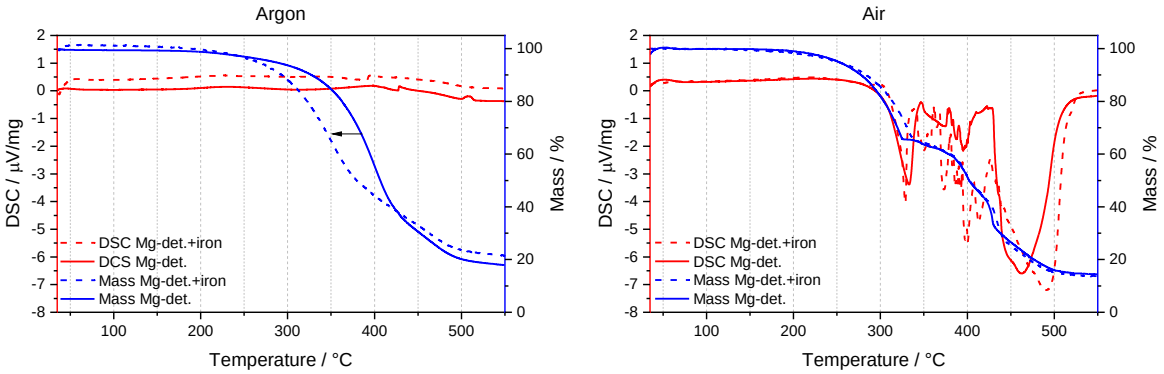

Figure 64: Impact of a cylinder liner metal flake on the decomposition properties of Mg-detergent in Ar and air.

While the iron flake does not affect the Mg-based detergent in air, the start temperature of mass loss is shifted to lower temperature in argon (Figure 64).

Molybdenium-based friction modifier

The Group I base oil containing a Mo-based friction modifier additive (Mo-Fric.) starts to evaporate at 250°C but its evaporation/pyrolysis is retarded compared to the pure base oil independent of the bath gas. At 370°C, the mass loss decreases in air and turns to a constant mass loss rate. In argon, the mass loss is constant up to 400°C. Then the mass loss slows down, reaching a residual mass of ~18 % at 460°C. The mass loss in air approximates to this residual mass. At the highest measured temperature, the residual mass was ~21%.

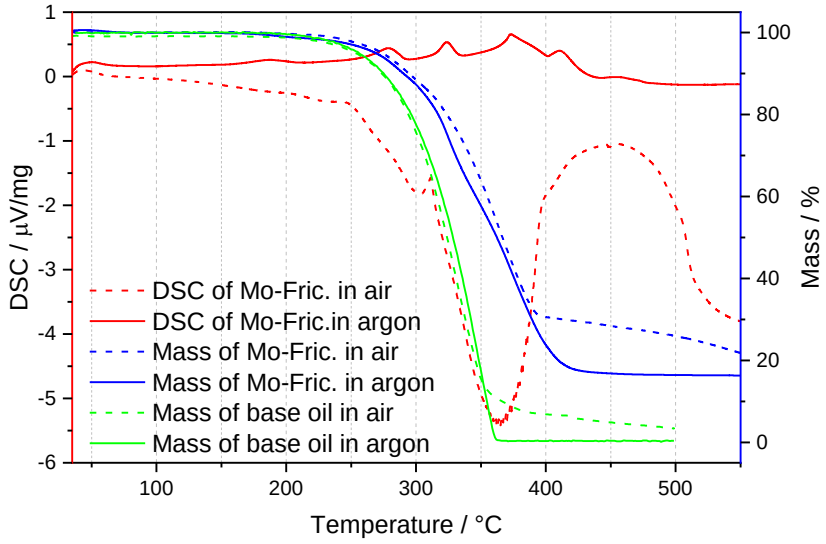

Figure 65: Decomposition of Mo-Fric. in argon and air gas flow.

The shift to lower temperatures observed for detergents in presence of an iron flake was confirmed for the Mo-Fric. too (Figure 65).

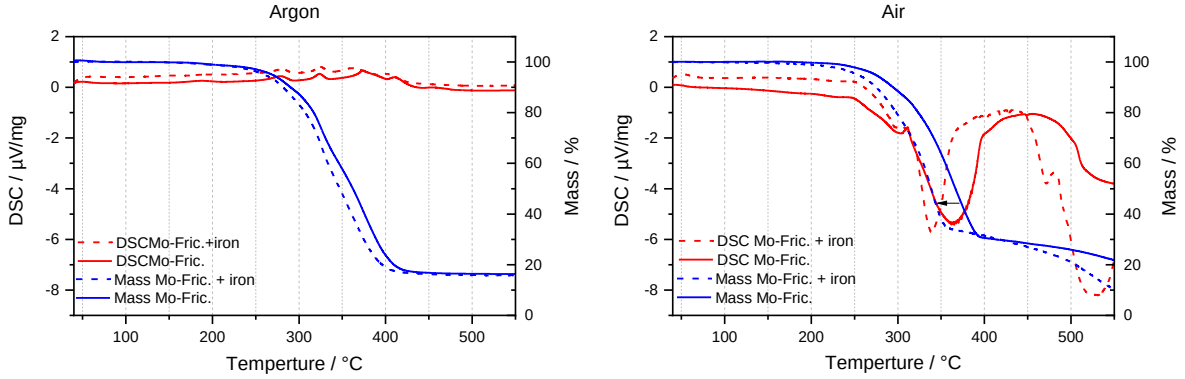

Figure 66: Impact of a cylinder liner metal flakes on the decomposition properties of Mo-Fric. in Ar and air.

The first peaks in the mass spectra were observed at 220–260°C for Mo-Fric. independently from the bath gas. The high sulfur content of the additive leads to the formation of several sulfur-containing products (H_2S, thiols, CS, and CS_2) which are visible in the mass spectra shown in Figure 67.

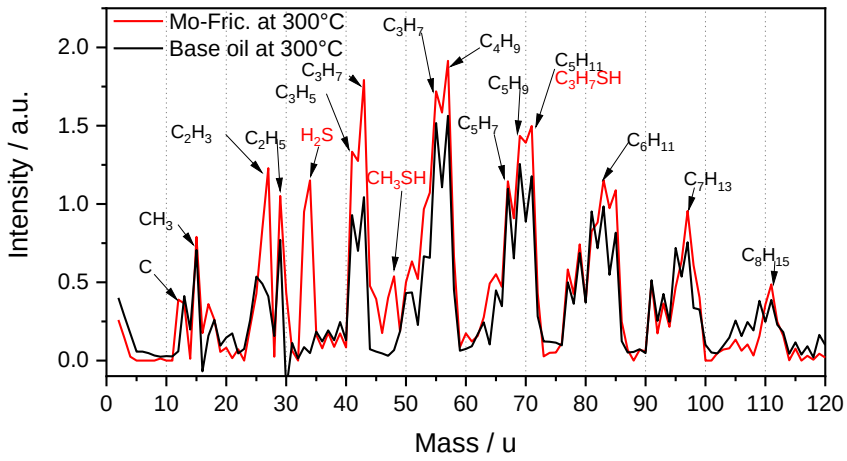

Figure 67: Mass spectrum of exhaust gas from Mo-Fric. at 300°C in argon gas flow.

The fully formulated oils showed a similar decomposition behavior like the base oil, but shifted to higher temperatures by the additive package. The characteristic profiles in the decomposition traces of the single additive were not seen for a fully formulated oil because the single concentration of each additive was too low. The same applies to the analyzed mass spectra.
In engine operation, agglomeration of specific oil materials in the piston cervices is conceivable and abrupt decomposition of this could result in higher concentration of decomposition products in a single cycle [9].
Based on the detected species in the mass spectra, further measurements were performed where species like H_2S, various chain-length thiols and SO_2 were added at a concentration of 1000 ppm to a stoichiometric PRF95 air mixture to identify their effects on the autoignition of gaseous fuels.

5.2.2 Potential impact of oil decomposition products on the autoignition of iso-octane

Several sulfur-based decomposition products were identified as potential gas-phase pre-ignition promoters. Three species were chosen to represent the decomposition products identified in the mass spectra. Hydrogen sulfide, ethyl mercaptane, and sulfur dioxide were added to an isooctane/air mixture of $\phi = 1$ by 1000 ppm.

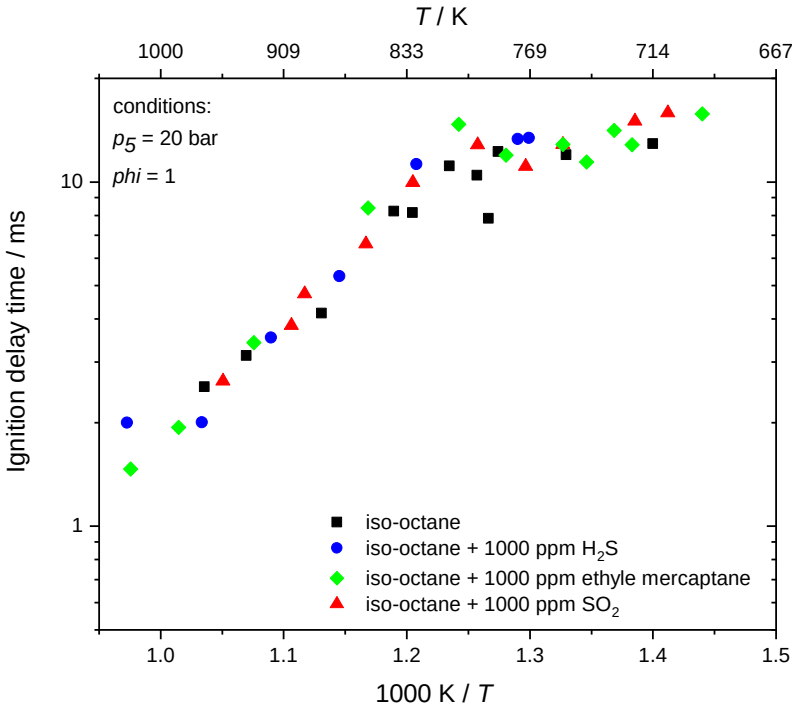

Figure 68: Ignition delay time of iso-octane (■) and iso-octane doped with 1000 ppm of H_2S (●), C_2H_6S (◆), and SO_2 (▲).

Sulfur in combination with hydrogen (H_2S) or oxygen (SO_2) does not show any accelerated ignition of the base mixture of pure iso-octane. Also, effects of H_2S have recently been investigated for temperatures over 1000 K by Mathieu et al. [184], aiming at optimizing the mechanism from Zhou et al. [165]. H_2S is known as a flame inhibitor. Mathieu et al. [185] studied 1 % H_2/1 % O_2 + 100 ppm – 1600 ppm H_2S in argon and found that the increase in ignition delay time is mainly determined by the reaction of $H_2S + H \rightleftarrows SH + H_2$ which consumes H atoms needed in the chain branching reaction $H + O_2 \rightleftarrows OH + O$. The validation of the mechanism was performed at 1045–1860 K [186].

For the different thiols, ethanethiol was chosen as a representative species. *No effect was observed by adding 1000 ppm ethanethiol*.

5.2.3 Impact of single droplets on homogeneous autoignition

Pure gas-phase ignition and the study of lubricant oils decomposition did not lead to results to explain pre-ignition by gas-phase species. Therefore, the complex process of oil sprayed into the combustion chamber was investigated in the shock tube by injecting oil droplets behind the reflected shock wave. Single droplets of 50–200 µm diameter were assumed to be realistic as potential source of pre-ignition in engine combustion based on calculations using equation (44).

5.2.3.1 Characterization of the injector system

To find the best injector settings all liquid samples were previously injected into a high-pressure cell introduced in section 3.2 to generate comparable droplets for different liquids. For example, experiments were conducted with injection of dodecane into nitrogen at 6–8 bar (equivalent densities like post-shock conditions for PRF95 in synthetic air at $\phi = 1$, $p_5 = 20$ bar and temperatures T_5 between 750–1000 K). The base oil and the additive containing samples described in table 2 as well as n-dodecane was injected. n-dodecane was tested additionally as a Diesel surrogate because diesel mixed into the injected gasoline fuel showed similar knocking typical for LSPI in engine tests [187].
The results of droplet injection into the pressurized cell are shown in Figure 69 and Figure 70. The figures show schlieren images of droplets flying horizontally through the observed area directly at the tip of the injector and at a distance of about 45 mm. For n-dodecane 0.016 µl were injected in one injection, which typically results in a number of 3–5 single droplets. The parameters studied in the static cell have shown that the droplet size and speed are mainly sensitive to the setting parameters, “needle lift” and the “falling time”. Likewise, the reservoir pressure has a significant influence on droplet formation. The reservoir pressure must be kept small and equal to the pressure in the reaction chamber. For the experiments in the shock tube, the container pressure was set to 21 bar, while the calculated pressure behind the reflected shock wave was about 20 ± 0.5 bar. The pressure was set slightly higher to avoid any backflow into the injector.
In the frames shown in Figure 69 and Figure 70 the red circles visualize the results of the algorithm tracking droplets, while the figure itself shows raw images.
During all injections independent from the set parameters of the injector, a very short jet is formed at the nozzle that forms larger and smaller droplets where their velocities are in the Rayleigh regime (section 3.3.2). Increasing the dynamic viscosity μ_L of the fluid shifts the regime towards the formation of larger droplets according to the Ohnesorge relationship [90].

$$\mathrm{Oh} = \frac{\eta_L}{\sqrt{\rho_L \, \sigma \, d_0}} \tag{32}$$

n-dodecane has a lower dynamic viscosity compared to other liquids like oils. Smaller droplets with respective smaller masses are so strongly decelerated in the first 15 mm that they fall down and will not reach a distance of 45 mm. Larger droplets, however, will reach this distance quite fast in about 8 ms and then lose their momentum, too. For n-dodecane 2–3 droplets survive the course of 45 mm, thereby the separation of individual droplets was possible.
The separation of the droplets was important because single droplet ignition characteristics are very different from spray ignition which is not the scope of this work.

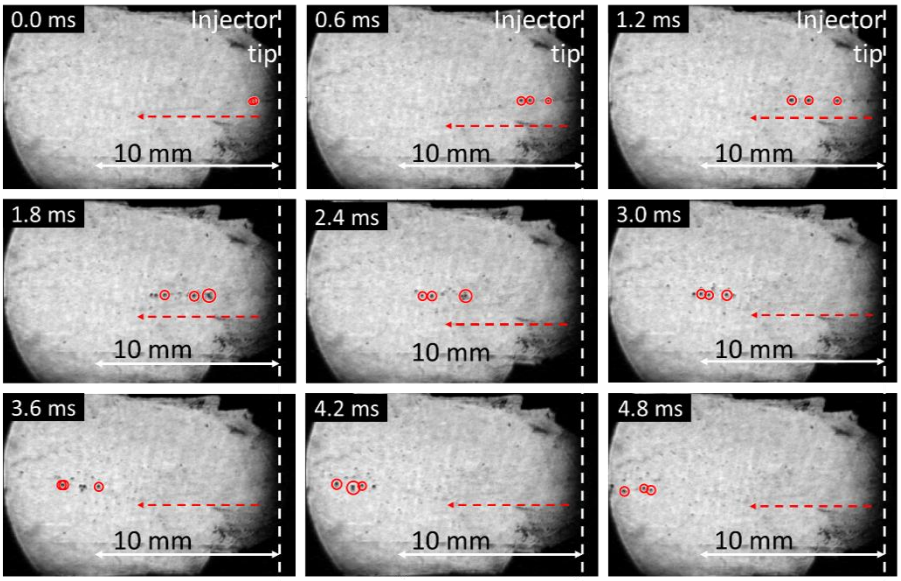

Figure 69: Image sequence of droplets formation of n-dodecane injection into nitrogen at $p = 8$ bar, $T = 293$ K; Falling time: 1 ms; Needle lift: 35% in a distance of 0–15 ms.

Chiu and co-workers [109-111] developed an approach to calculate the limits or regimes for four different combustion processes in a droplet cloud. First the single droplet combustion, the internal group combustion, the external group combustion, and the external sheath combustion. According to Chiu et al. [109], the Chui number G was calculated for dodecane:

$$G = 3\left(1 + 0.276\mathrm{Re}^{1/2}\mathrm{Sc}^{1/3}\right) \leq N^{2/3}\left(\frac{r_l}{d}\right) \tag{44}$$

The Reynolds number Re describes the flow conditions and the Schmidt number Sc the transport properties. The Lewis number *Le* describes the heat transport which is equivalent to the mass transport. *N* is the total number of droplets in the region of interest, r_l is the average droplet radius. For accurate calculations, the variance in droplet size must be small. *d* is the spacing or distance between the droplets.

The droplet speed, size, and distance between the droplets were used to calculate G for post-shock conditions when injecting dodecane in shock-heated air. For density and dynamic viscosity, the values given by Feng et al. [188] were applied at $T = 683.2$ K and $p = 10.04$ bar. These parameters are the closest to the conditions in the shock tube that are published [188].

At a distance of 45 mm $G = 0.0071$ was determined, which is below the critical value for group combustion ($G = 0.1$–1) [109]. The G number was calculated for the first millimeters too, and results in $G = 1.26$, which is in the regime of external group combustion. However, the very small droplets fall down in the first 3–5 ms and the larger ones merge until only a few droplets survive, which makes group combustion unlikely.

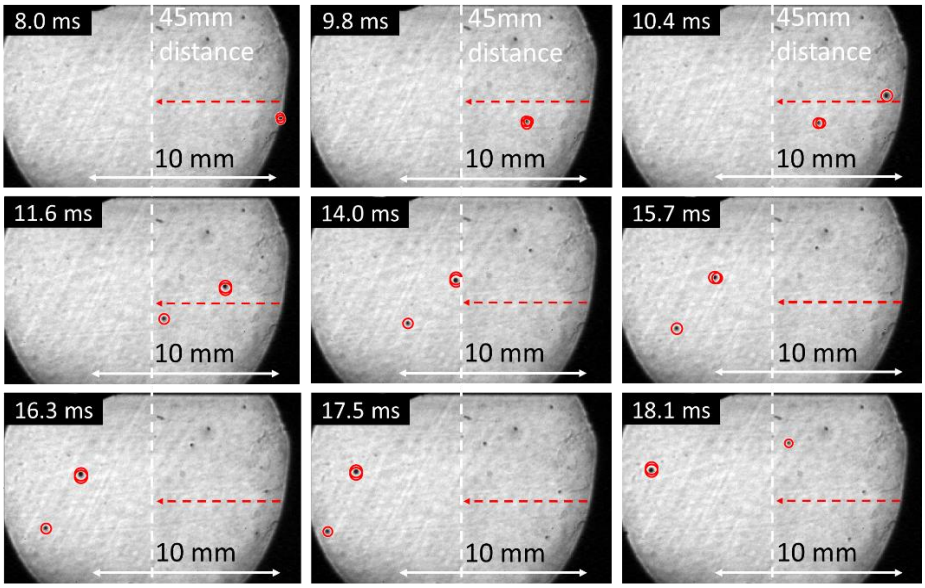

Figure 70: Image sequence of dodecane droplets flowing into ambient gas (N_2) at 8 bar and a distance of 45 mm; $T = 293$ K; Falling time: 1 ms; Needle lift: 35%. The circles depict the trajectory of the released droplets.

According to the work of Chiu [109, 110] and Xiong [189] the aforementioned theory overpredicts the interaction effects. At a distance of five times the nozzle diameter, it is sufficient to avoid interaction between droplets in order for them to behave like a single droplet for the combustion process [189]. Reducing the problem to the diameter spacing ratio (d_0/d), the area close to the tip becomes critical for combustion, but local separation and ignition compete with respect to the combustion regime. All these aspects are summarized in William and Sirignano [190].
These measurements show that the injection of single droplets into high-pressure ambient gas is fast enough to be used behind reflected shock waves in the time of stable post-shock conditions.

5.2.3.2 Injection of droplets into shock heated air

The impact of droplets on the autoignition of fuel/air mixture was one main task of this work. However, one difficulty was faced through the limitation of the observation time that varies with the post-shock conditions. To cover the full available 15 ms observation time in a first step, dodecane was injected in pure shock-heated air.
The ignition of dodecane injected as droplets into air was observed at $p_5 = 20$ bar and temperatures from 750–1400 K. Within 15 ms dodecane could be ignited for temperatures above 900 K. Figure 71 shows an image sequence of dodecane injected into synthetic air at 1390 K without optical filtering. Before injection a few bright spots were seen in frame 1, mainly in the bottom half of the tube. When the injector releases the droplets the dodecane ignites directly around the droplets (frames 2 and 3). Afterwards, the burning droplets fly towards the center of the shock tube. Instead of moving straight, they are deflected by interaction with the boundary layer. When the droplets ignite, the emitted light is of similar wavelength as the burning particles.

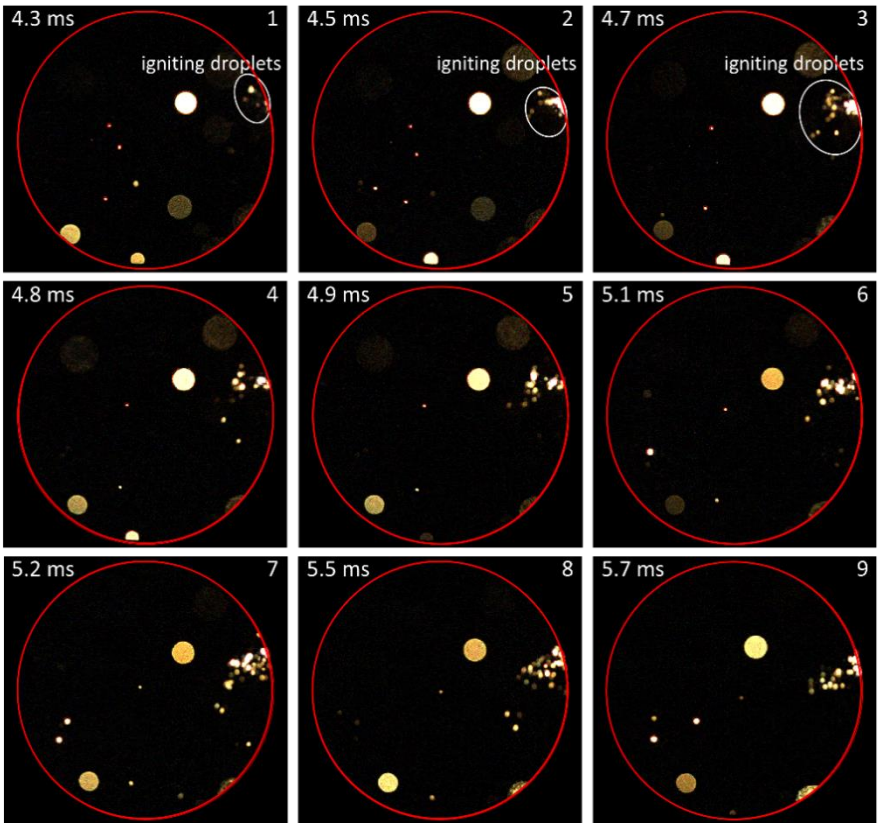

Figure 71: Image sequence of dodecane droplet ignition after injection into synthetic air at $T_5 = 1391$ K and $p_5 = 20$ bar.

Base oil was also injected into pure shock heated air. The imaging showed that oil injected as droplets only ignite for gas temperatures over 900 K, too.
During the injection the presence of particles further complicates the identification of the droplets and local ignition in the direct droplet vicinity. Illumination by laser light was attempted in order to follow the droplets before ignition. But both (particles and droplets) scatter the laser light (discussed in section 4.1). Therefore, the LIF technique described in section 3.1.3.2 was developed.

5.2.3.3 Influence of dodecane droplets on the ignition properties of PRF95/air mixtures

The following section is a reprint of the publication Niegemann et al. 2020 [124]. All results are based on my own work while the final manuscript was written together with my co-authors.
Dodecane was injected behind the reflected shock wave into a mixture of PRF95 and synthetic air ($\phi = 1$) at conditions between 750 and 850 K and 20 bar. The conditions were chosen to mimic the gas conditions in an IC engine at the end of compression. The minimum temperature was limited by the observation time of 15 ms. A further increase in pressure seems not to be useful because the influence of pressure on the ignition kinetics is relatively weak and also because the injection into higher pressure becomes increasingly difficult. The ignition of the gas mixture with an injection of dodecane shows significant differences in flame color, structure, and propagation, while in addition, the starting point of ignition changes in time and location. The strength of the effect depends on the amount of injected liquid. While the best results for single-droplet injection were obtained for injector settings with low needle lift, the effect on ignition was stronger with higher needle lift. Higher momentum of the droplets was necessary to overcome the boundary layer. Figure 72 shows an example with high needle lift (80 %) when the droplets penetrate deep into the shock tube. The images are cropped to the area close to the injector tip with a dynamic intensity scale.

The first and third frame shows two droplets before ignition, while the second frame only shows low-intensity noise in absence of LIF signal (the laser is off in all frames with even numbers). The ignition starts in the fourth frame in the path of the droplets. Although the exact position of the droplets is not shown in this frame, their position can be estimated based on the trajectory in the previous frames. In the next frame, the flame-edge detection algorithm detects an area with weak chemiluminescence, thus, early-stage ignition (red contour). Later, the bulk of dodecane penetrates the center area of the shock tube, which correlates well with the timing of the injector. The appearance of the first droplets at 2.60 ms reveals that the injection starts with the beginning of the needle falling. Frame 6 shows the first two droplets caught up by the luminescing reaction zone and the following injected liquid is injected into the reaction zone. Therefore, droplet evaporation and fuel decomposition and ignition are accelerated. Within the area emitting chemiluminescence, the droplet LIF signal is too weak to be identified.

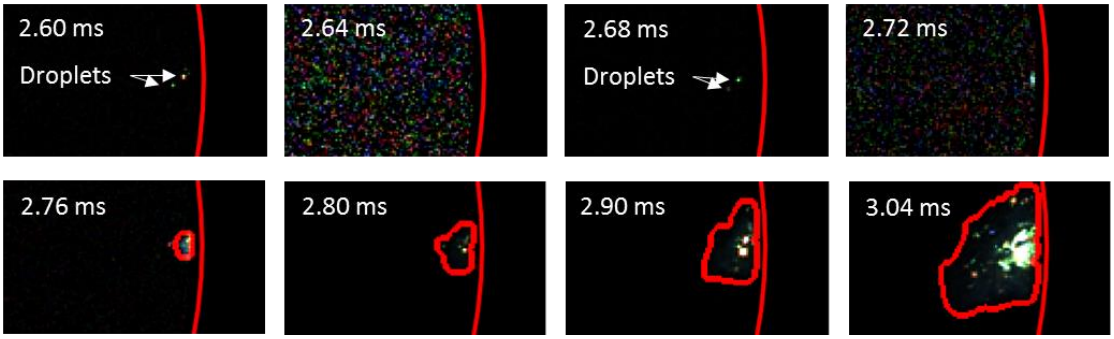

Figure 72: Droplet reaching the observation area before ignition at T_5 = 830 K, needle lift: 80 %.

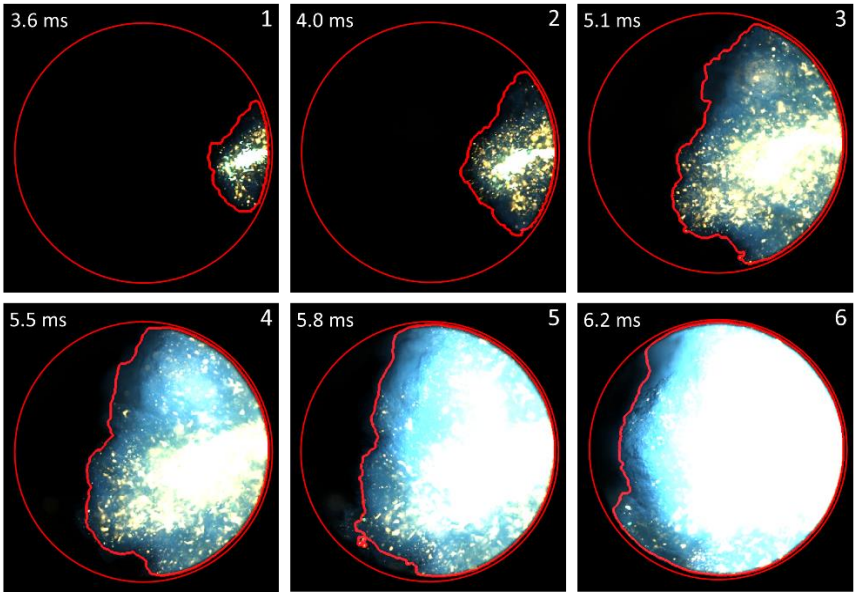

Figure 73: Combustion of PRF95 triggered by dodecane droplets at T_5 = 830 K, needle lift: 80 % [124].

The liquid injected into the reaction zone appears green in the images shortly after injection (frame 1, 2, and 3 of Figure 73). When dodecane evaporates and burns, locally rich regions lead to soot formation. Therefore, the color changes to yellow due to soot incandescence. With the camera settings chosen for maximum sensitivity aiming at observing the early phase of ignition, the signal from the jet center region leads to saturation of all three-color channels early after the start of ignition. Chemiluminescence from PRF95/air combustion was observed in the outer region especially in the top half of the shock tube where only the fuel/air mixture burns. In contrast, the propagation of the luminescing reaction zone towards the bottom half is driven by the penetration depth of the injected droplets. The injection of a droplet spray strongly influences the

trace of chemiluminescence and pressure. Figure 74 shows that the signal intensities rise directly after injection. No clear ignition delay can be defined. More or less different types of combustion of the spray followed by a first and second ignition steps were identified. The flame-edge detection algorithm shows that the luminescing reaction zone fills the entire observed plane before the main gas in the front or back of the imaging plane ignites.

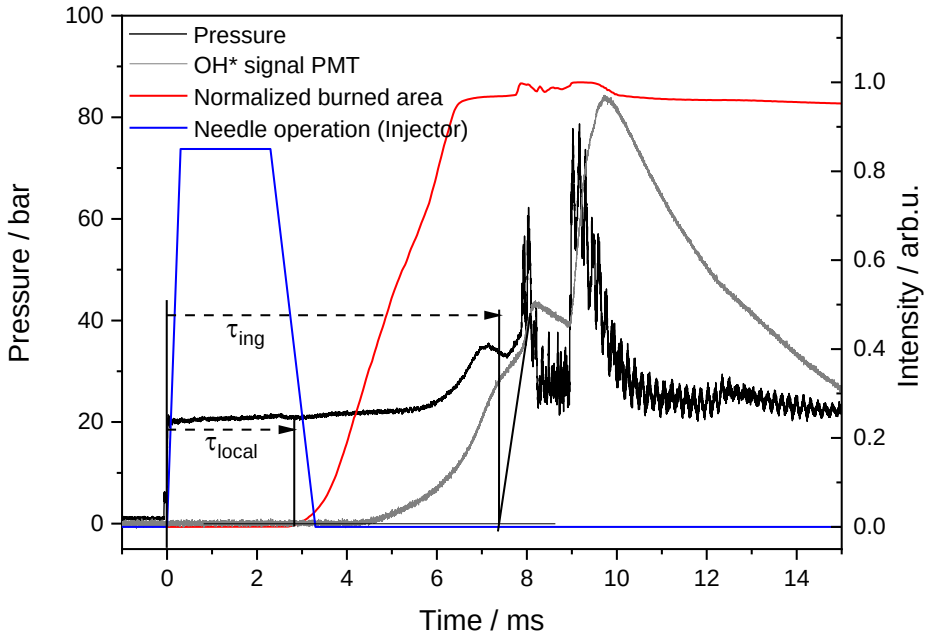

Figure 74: Detected signals over time corresponding to Figure 72 and Figure 73 at $T_5 = 830$ K, needle lift: 80 % [124].

In comparison to the injection with high droplet mass, cases with injection of less droplet mass look similar to the ignition of pure PRF95 in synthetic air. Figure 75 shows the local ignition of PRF95 in synthetic air triggered by two different sources. The first three frames show two droplets flying through the combustion chamber, igniting the surrounding fuel/air mixture at 6 and 7.5 ms respectively. At the same time, particles from the diaphragm trigger the ignition far upstream from the endwall in the bottom half of the tube as described by Tulgestke et al. [154] and Troutman et al. [191]. All ignition spots initiate propagation of the reaction zone through the unburned gas.

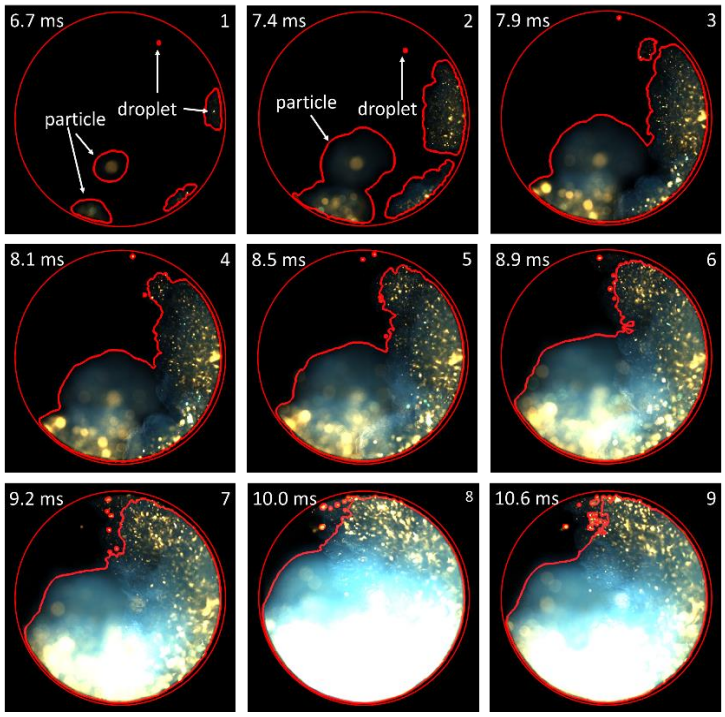

Figure 75: Ignition of PRF95/air triggered by particles and droplets at different locations in the tube on a similar time scale at T_5 = 780 K, needle lift = 35 % [124].

The effect of droplets on the ignition process with respect to the ignition delay times can be seen in Figure 76 comparing the traces of pressure and OH* emission of PRF95/air ignition without and with injection at different needle lifts at one temperature. The temperatures of 770 and 780 K selected in Figure 76 with a 10 K difference have a negligible influence on the ignition delay time in the NTC regime. In case of injection, the ignition delay time decreases as seen from both the pressure and the OH* signal trace. Injecting more droplets does not decrease the ignition delay time much further. The amount of dodecane injected has less influence on the ignition than the fact that droplets were injected at all. The pressure response is a better indicator for pre-ignition than OH* because of the narrow detection angle and thus the localized information detected by the latter. The pressure trace shown on the left side of Figure 76 indicates that an increase of injected liquid increases the pre-ignition intensity. Because the pressure response is comparably weak and chemiluminescence signal is recorded through a spatially confined view the location of ignition the local impact of the droplets should be followed by imaging. For the impact on ignition delay time the classic pressure and chemiluminescence techniques are sufficient.

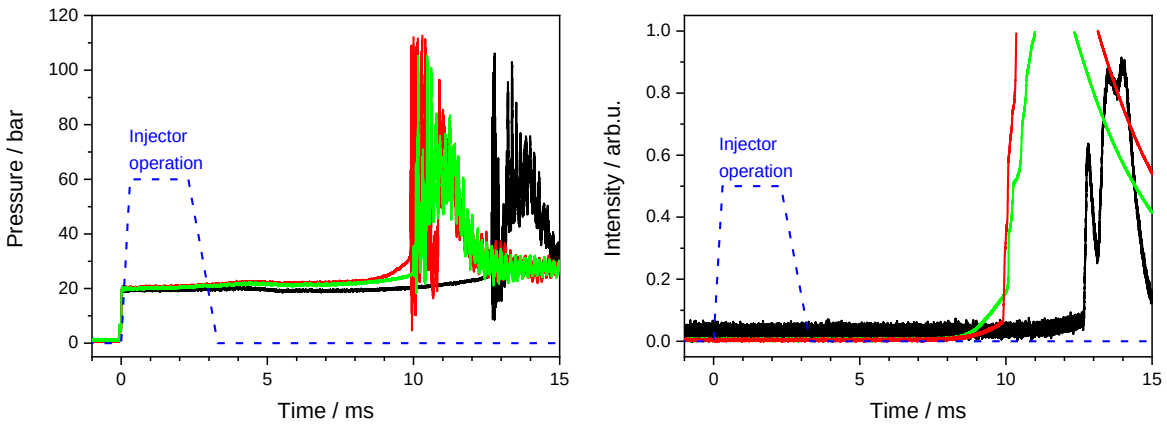

Figure 76: Pressure and OH* signals at comparable conditions with variation of the injected liquid volume. (—) PRF95/air ignition T_5 = 770 K, (—) PRF95/air ignition with injection of dodecane at needle lift = 40% and T_5 = 780 K, (—) PRF95/air ignition with injection of dodecane at needle lift = 80 % and T_5 = 780 K [124].

Figure 77 shows the ignition delay times determined by the extrapolation of the steepest rise of the OH* chemiluminescence signal to the background level of PRF95/air at $\phi = 1$ and the effect of droplets. The dashed black line shows the ignition delay time simulated for a zero-dimensional batch reactor with constant pressure in Chemkin [123] using the mechanism from Cai and Pitsch [148]. The solid black line considers a dp/dt of 2%/ms in the first 3 ms typical for these conditions in this shock tube. Symbols represent results from single experiments. The black open squares are experiments with a PRF95/synthetic air mixture at $\phi = 1$ without injection (reference case). The ignition delay times without injection agree to the predictions of the mechanism and data measured in the past published in refs. [192-194].

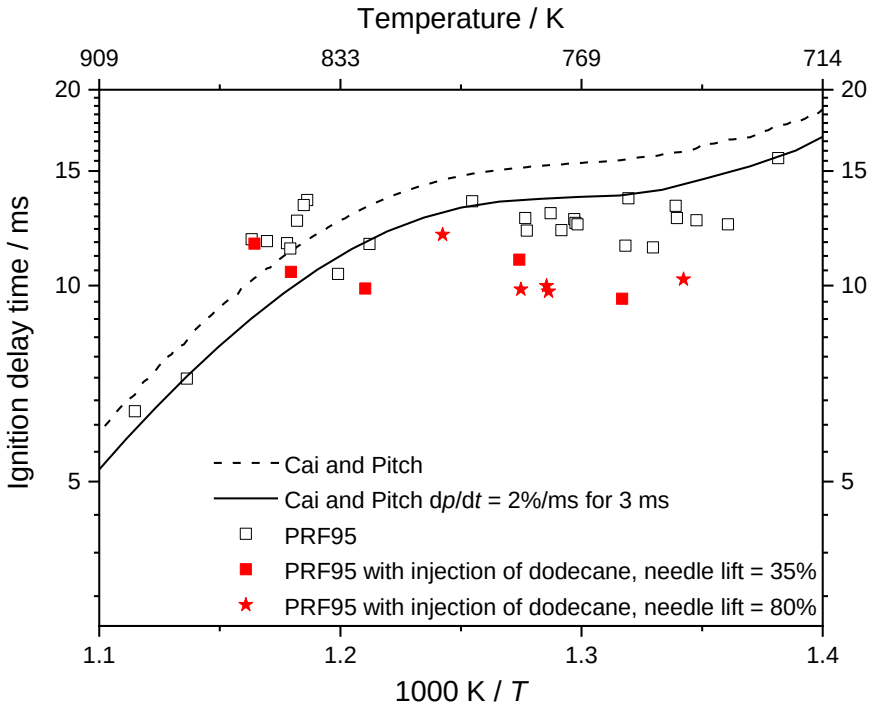

Figure 77: Simulated and experimental ignition delay time of PRF95/air mixtures ($\phi = 1$) and 20 bar and the impact of droplets on the ignition delay time [124].

The red squares and stars represent the ignition delay time with injection of dodecane. Solid squares are results with minor needle lift of 35 or 40% and stars with 80% needle lift. The influence on the ignition delay time by the amount of injected liquid is minor: Small trend of more

droplets lead to little faster ignition. The Arrhenius plot shows that the effect of the droplets is small at gas temperatures higher than 800 K. Through injection, the NTC-region becomes more pronounced and widen as it is for homogenous gas mixtures. At 750 K the local minimum in ignition delay time is reached. Lower gas temperatures do not decrease the ignition delay time furthermore. Injection of base oil (blue squares in Figure 83) shows the same trend as the dodecane but less impact on ignition delay time. This behavior can be explained by higher boiling point of the base oil meaning lower evaporation rates but the difference in the chemical composition might be also the cause.

5.2.3.4 Impact of base oil and base oil/fuel droplets on the autoignition of PRF/air mixture

Base oil, the main component in lubricant engine oil, was investigated and the results of this study were published in a SAE technical paper contributed for the JSAE/SAE Powertrains, Fuels and Lubricants International meeting (2019) [152] and additional work on this topic was presented at the "Flammentag" 2019. The following section is a reprint of different parts of both works. All results are based on my own work.

The influence of injected base oil was investigated for a temperature range of 750–950 K at a pressure of 20 bar. Figure 78 shows one image sequence of the ignition of PRF95 with injection of oil. Figure 78, frame 1, label (a) shows local droplet ignition at the top of the tube in the focal plane, after the droplet was distracted while crossing the turbulent interface. The flame area (b) next to area (a) is further away from the endwall having less intensity that was only detected by the blue channel of the RGB-camera detector without bright spots and a less sharp structure. Because of the position of the ignition spot we can conclude that this spot originates from gas ignition.

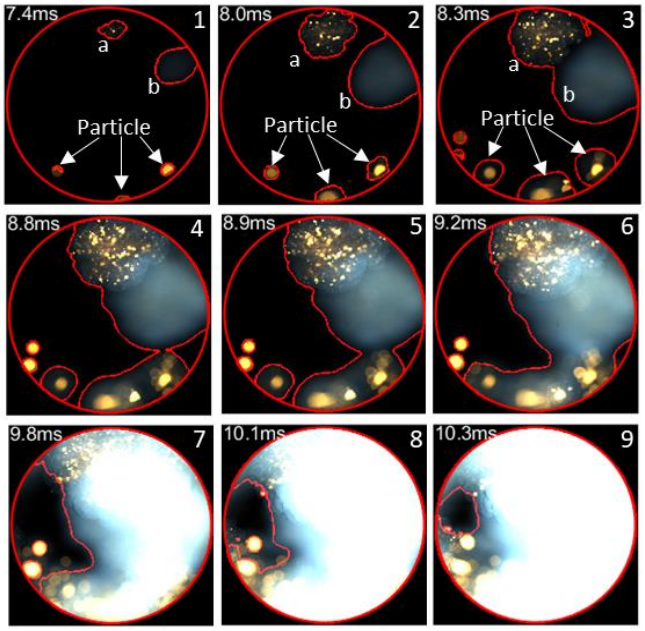

Figure 78: Local ignition of droplets of base oil injected into PRF95/air. $\phi = 1$, $p_5 = 20.8$ bar, $T_5 = 760$ K [152].

In the bottom area, several yellow spots simultaneously appear that transit into flame propagation (Figure 78, frame 1–5). Because these spots are all behind the measurement plane, they are out of focus. We presume that these are small particles from the aluminum diaphragm as also reported by Tulgestke et al. [145] and discussed in section 4. Since flame area (a) is in the field of view of the photomultiplier, the chemiluminescence signal (Figure 79, red trace) increases

starting with the first frame shown in Figure 78 (frame 1). The pressure signal (Figure 79, black trace) also starts to rise with image 6 due to the heat release of the early combustion.

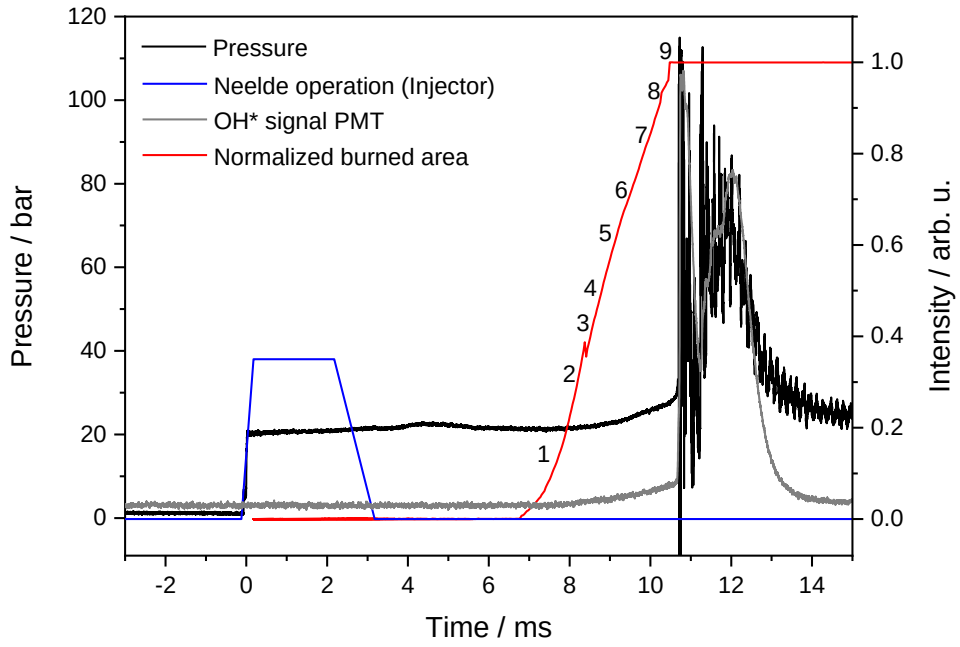

Figure 79: Variation of pressure and chemiluminescence intensity for the measurements shown in Figure 78 [152].

UV/VIS high-repetition-rate imaging was used to distinguish between various ignition effects in time and space. Processes of interest are the volumetric ignition in the gas phase and local ignition initiated by the injected liquid.

The following results were generated with the experimental setup shown in Figure 12 combining the injector, the LIF technique and the simultaneous imaging in the UV/VIS through the transparent endwall described in chapter 3.

The frames before the onset of the local ignition were examined for intensity fluctuations, which originates from the alternating LIF pulses. As an example of the observed ignition phenomena color images from an experiment at $T_5 = 760$ K and $p_5 = 21$ bar are presented in Figure 80 which shows ignition close to the injector triggered by a droplet. The frames are cropped images that are background-corrected and displayed with a dynamic intensity scale maximizing the contrast in each frame. In the first row of Figure 80, LIF from a droplet can be seen in frame 1, 3, and 5 (denoted with arrows). In Frame 7, the droplet can no longer be observed. 5.28 ms after the reflected shock wave has passed the measuring plane ignition was detected at the position where the droplet was seen before. 500 µs later the flame area is large and the intensity is strong enough to be detected by the flame edge detection algorithm that uses the blue channel of the RGB color sensor, which is shown in Figure 81.

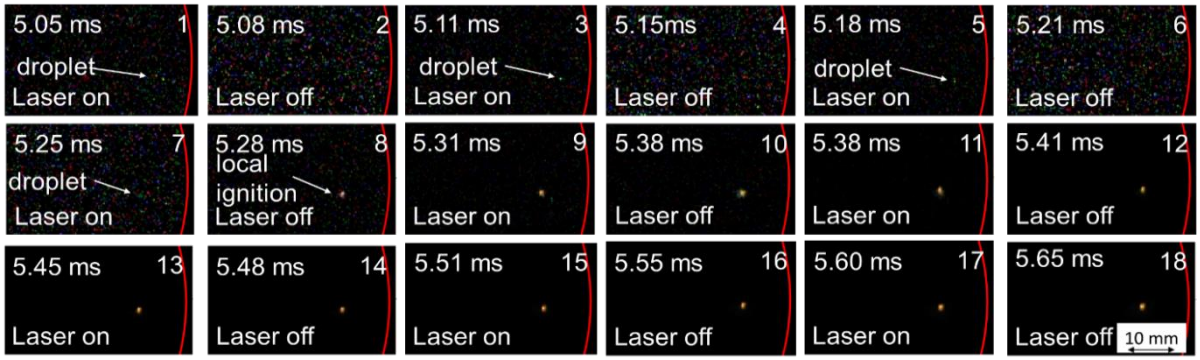

Figure 80: Images sequence with dynamic intensity scaling showing local ignition of an oil droplet in PRF95/air mixture at $\phi = 1$, $T_5 = 760$ K, and $p_5 = 21$ bar, [195].

Ignition was recorded by the color camera and the OH* imaging system simultaneously. While the color images are background-corrected only, the OH* images are also white-field corrected. The left side (the first three columns) of Figure 81 shows the blue channel from the color camera. It collects mainly emission from CH* and CO_2* that are formed in the flame. Both sequences are shown in false color. The results of the edge detection are shown by the red contours in Figure 81.

In the first frame at 5.3 ms, the local ignition at the droplet position as already seen in Figure 80. On the right side of Figure 81, the corresponding OH* images are shown. The sensitivity of the intensified camera is much higher than that of the RGB camera. In the following frames, the OH* images show areas of flame before these appear in the images of the blue channel of the color camera.

While the flame triggered by the droplet propagates into the unburned gas, additional bright spots appear on the left. The origin of these spots cannot be clarified because their starting point is not in the field of view. Three local flames (denoted with indexes a, b, c) propagate through the unburned gas, and they propagate faster tangentially than in the radial direction. The different flames merge and finally, when the volumetric ignition starts after 9.9 ms, the flames cover the whole focal plane. The intensity of volumetric ignition saturates the camera sensors. The first formation features of OH* were of interest in this study, therefore, the gain of the image intensifier was increased with the drawback of saturation in the late stage of the process. In contrast, the images from the color-camera contain useful information for a longer time. The wide spectral range separated into three channels enabled distinction of different phenomena: The blue channel shows flame chemiluminescence (mainly CH* and CO_2*). The green channel shows the LIF signal from the droplets and the red channel the incandescence from hot particles like soot. The signal from the blue channel was used for flame edge detection for a comparison between the imaging systems shown in Figure 82.

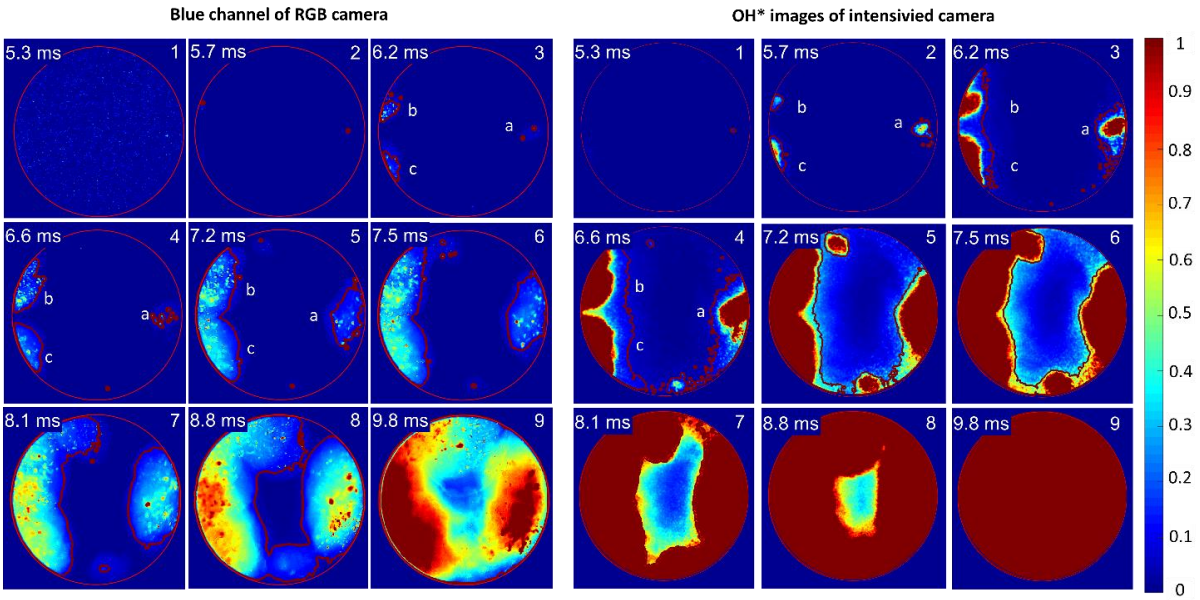

Figure 81: Simultaneous images sequence from the blue channel of the color camera (left) and the OH* imaging (right) of PRF95/air ignition triggered by an oil droplet [195]. Same experiment as in Figure 80.

The traces of the normalized burned area from both image sequences (solid and dashed red lines in Figure 82) are similar in shape, however, the trace from the OH* camera is slightly shifted in time. The shift is due to the threshold-based algorithm that uses the background signal to set the threshold.

For the two image sequences shown in Figure 81 the image intensity was integrated over each frame (solid and dashed green lines in Figure 82). The integrated intensity starts to increase after 6 ms and the volumetric ignition takes place at 9.8 ms accompanied with strong light emission. The normalized burned area (defined in section 3.1.3) contains information on the spatial progress of ignition, while the integrated signal considers the intensity of light emission. This intensity is the light emission integrated over the observed volume. For comparison, the pressure trace, the OH* signal detected by the photomultiplier, and the injector timing are shown in Figure 82 as well. Comparing the signal traces of the cameras with the pressure and OH* from the PMT, the integrated intensity of the blue channel fits much better to the pressure trace. The progress of ignition is well described by the integrated intensity. The heat release from the early local ignition is not high enough to lead to a measurable rise in pressure. In contrast, the OH* signal from the PMT only rises when the local flame reaches its field of view (limited by the small optical access), which is narrow compared to the UV camera that detects nearly the entire volume of the shock tube. The camera system allows determining the onset of the local ignition.

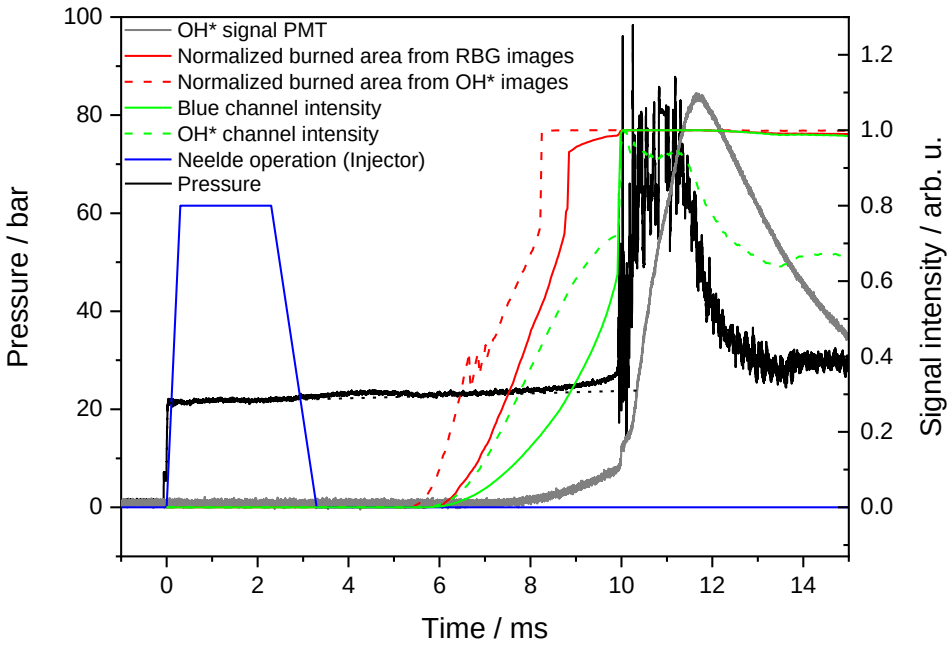

Figure 82: Comparison of OH* high-speed imaging and blue channel of color high-speed imaging over time correlated with pressure and PMT response [195].

Figure 83 shows the ignition delay times for the PRF95/air mixture in an Arrhenius plot. The black squares show τ_{ign} for the gas mixture without injection and the solid line the simulated results as already shown in Figure 26. By chance, the first experiments without oil injection were performed after other, unrelated experiments that produced much soot. Despite thorough cleaning afterwards, with each successive experiment, the shock tube became cleaner still. Therefore, additional experiments in this critical temperature range from 800–870 K were performed and it was decided to include all data points in Figure 83 red square, and indeed the later experiments show less scatter.

Figure 83 shows that the ignition delay time is not sensitive to the presence of droplets (blue squares) for temperatures above 800 K. Below this temperature the ignition delay time is in the range of shortest ignition delay times measured for pure PRF95/air mixtures. In absence of oil droplets, the mixture exhibits slight NTC behavior (dashed black line), while in the presence of these droplets the NTC becomes more pronounced (dashed blue line). The simulations underpredict both trends of NTC behavior.

In contrast to the ignition delay time of volumetric ignition, which exhibits a clear trend, the local ignition delay times without injection show strong scatter. The injection of base oil has no influence on τ_{local} over the entire temperature range (solid blue and black circles). The local ignition delay times are in the scatter without injection. A direct comparison of the black circles and the blue ones is not possible because the ignition process proceeds in two different ways. The black circles show local ignition in the gas triggered by gas-dynamic effects discussed in chapter 4.1, while the blue circles show local ignition triggered by droplets. Although the local ignition sources are totally different, they appear nearly simultaneous.

In case of base oil injection, local ignition in the vicinity of the droplet was observed for gas temperatures down to 750 K which is much lower than the local ignition of base oil in shock heated air observed for temperatures down to 900 K. Therefore, an interaction of the droplet with the surrounding gas is likely.

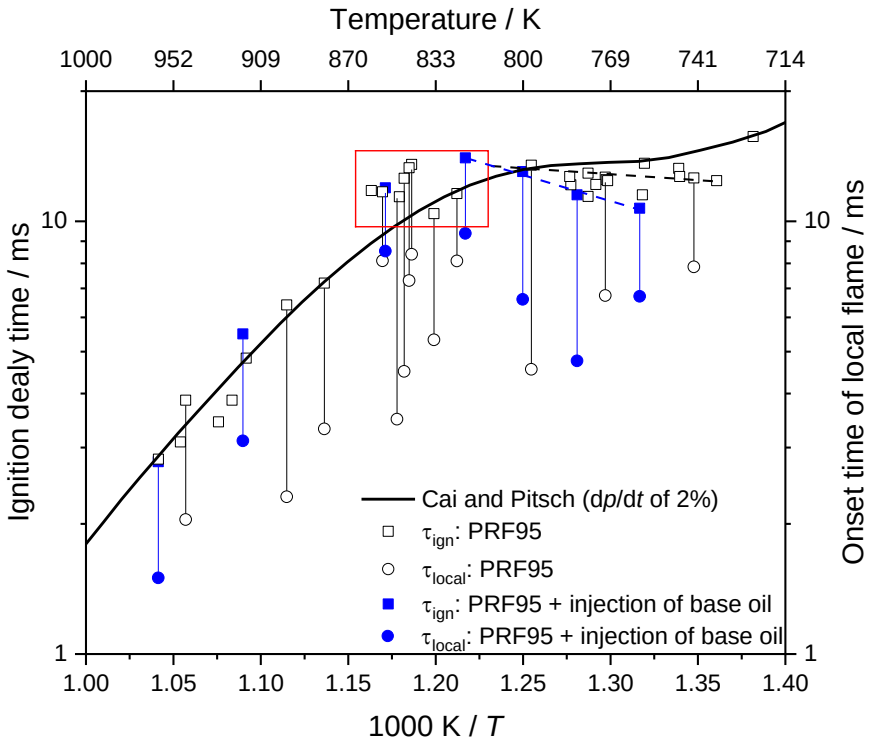

Figure 83: Ignition delay times and time until local flame occurs for PRF95/air with $\phi = 1$ and $p_5 = 20$ bar with injection of the base oil. Blackline: $\tau_{ign.}$ from a constant-pressure simulation with the mechanism from Cai and Pitsch [148]. The two dashed trend lines and the red box are discussed in the text [152].

The large scatter of the local ignition delay makes it difficult to find a correlation between local and global ignition delay. Nevertheless, it has to be assumed that the evaporated droplet molecules might interact in the fuel reaction pass by enrichment, enhances the chain-branching process causing faster volumetric ignition at low temperatures. This is in line with the results by Kuti et al. [76] who found that in an ignition quality tester, base oil reduced the ignition delay time of iso-octane. With decreasing temperature, the promoting effect of base oil increases and reinforces the NTC behavior. Further investigations should be carried out to explain this effect.
Previous studies have shown that fuel from direct injection wetting the liner has an influence on the LSPI frequency [63, 72]. To understand whether this is due to a chemical effect, the base oil was mixed with PRF95 1:1 by volume. This was also done for all samples containing a single lubricant additive. In this series of measurements, in most cases the ignition of the mixture starts locally at the droplet itself. With increased temperature, the reactivity of bulk gas mixture increases and promotes *local gas ignition* that starts somewhere in the end gas and competes with the *local droplet ignition*. In other cases, like that shown in Figure 84, combustion starts at the droplet (denoted with red contour in image 1) and a flame propagates from there through the fuel/air mixture.

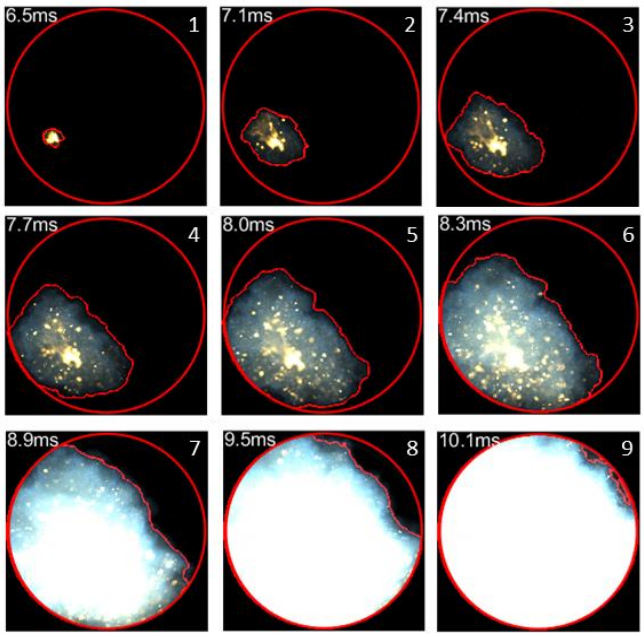

Figure 84: Local ignition of droplets of a mixture of base oil and PRF95 in a gas mixture of PRF95/air. $\phi = 1$, $p_5 = 20.4$ bar and $T_5 = 856$ K, injection of base oil + PRF95. The pressure trace of this experiment is shown in Figure 85 [152].

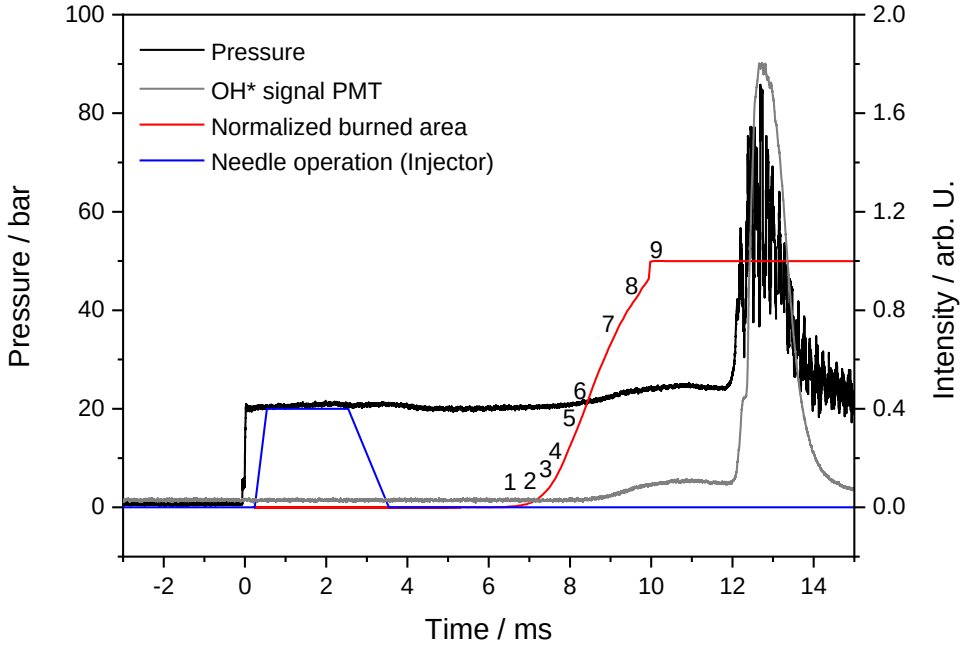

Figure 85: Variation of pressure and chemiluminescence intensity during the measurements shown in Figure 84 [152].

In the local ignition area of the evaporated droplet (oil/fuel mixture), at first, soot is produced as indicated in Figure 84, image 1, by the yellow luminescence, while the later flame propagation emits blue light (image 2-9). After 10.1 ms (Figure 84, frame 9) the flame already covers the field of view. Figure 85 shows the accompanying weak OH* emission and pressure rise at about 10 ms, prior to volume ignition at $\tau_{ign.} = 12.3$ ms.

In general, over the whole investigated temperature range, $\tau_{ign.}$ with injection (Figure 86, red filled squares) is slightly reduced compared to that without injection (black open squares), while the stronger NTC behavior is the same as for the injection of base oil. The experiment in the red box in Figure 86 is an outlier and does not follow this trend. In terms of local ignition delay,

injection of the fuel/oil-mixture shows the same lack of effect that injection of pure base oil shows (Figure 86). A closer look at Figure 86 shows one outlier at 770–780 K marked by the blue box. Here, the droplets ignited earlier (red filled circle) compared to local gas-ignition for premixed PRF95 only (black open circle), but the volume ignition delay is not reduced to the same extent. In this case, flame propagation was found to be very slow in case of injection compared to the corresponding experiment without injection. In an engine, such an outlier showing extreme early local ignition could act as a trigger for a (rare) LSPI event. It is expected that the following flame propagation and volumetric ignition would be faster in an engine as the local ignition occurs in the compression stroke, will show strong pressure response.

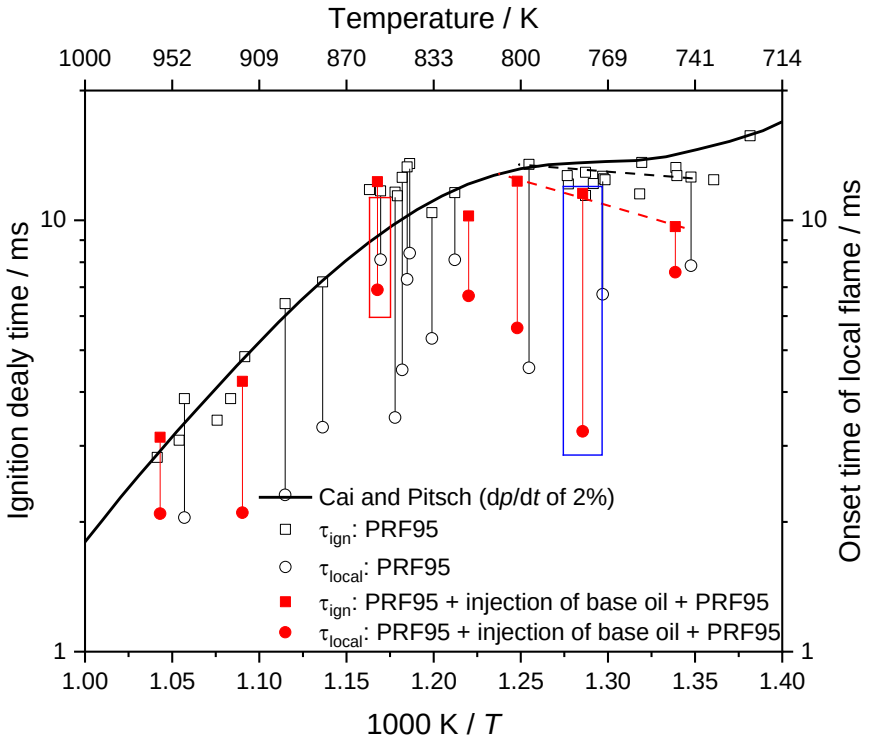

Figure 86: Ignition delay times and time until local flame occurs for PRF95/air with $\phi = 1$ and $p_5 = 20$ bar with injection of the base oil mixed with PRF 95 50:50 v/v%. Black line: $\tau_{ign.}$ simulated with the mechanism from Cai and Pitsch [148]. The two dashed trend lines and the boxes are discussed in the text [152].

Figure 87 shows a comparison of local ignition τ_{local} for the injection of pure base oil and base oil mixed with PRF95. These data were already contained in Figure 83 and Figure 86, but the direct comparison here shows two trends more clearly. First, the presence of liquid PRF95 clearly enhances the reactivity, resulting in shorter local ignition delay. Only for one set of experiments at the highest temperature of about 960 K the droplets without PRF95 ignited before those in the corresponding experiment with pure base oil. Second, τ_{local} shows a local minimum at low temperatures that appears like a strong instance of the classic NTC behavior of large hydrocarbons. The ignition of a locally spatio-temporally inhomogeneous mixture of air, PRF95, and evaporated oil components may be more complex than the homogeneous ignition experiments yielding the NTC region in an Arrhenius plot, but at least the phenomenological similarity is striking and warrants further investigation.

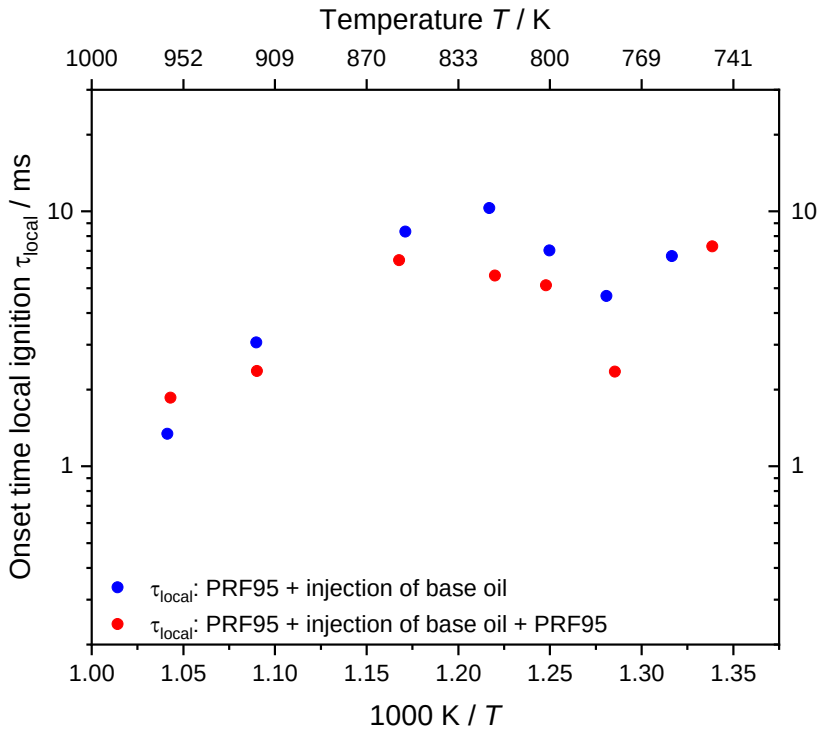

Figure 87: Comparison of time until local ignition occurs for injection of base oil vs. injection of base oil mixed with PRF95 50/50 vol.%. Bulk gas: PRF95/air, $\phi = 1$, $p_5 = 20$ bar [152].

5.2.3.5 Impact of ZDDP and fuel in base oil droplets on PRF95 ignition

Adding a single additive component to the base oil in very high concentration compared to the amount in a fully formulated oil should be noticeable (if it had an impact) and reveal the role the component would play in the ignition process. The results shown in section 5.2.1 indicate that ZDDP is very reactive, especially at high concentrations like in the tested sample. The ignition delay times with injection of base oil droplets containing ZDDP into the PRF95/air mixture shown in Figure 88 confirm this finding, where shorter ignition delay times were obtained. At low temperatures, the ignition delay time is shorter and at temperatures over 850 K very short ignition delay times were randomly observed. Furthermore, when the fuel was added to the sample by 1:1 vol.%, the ignition delay time was less reduced again and is in-between the delay of pure gas and that of the results without added fuel.

The findings showed that the overall reactivity is driven by the amount of ZDDP and that the dilution of the sample extend the ignition delay time.

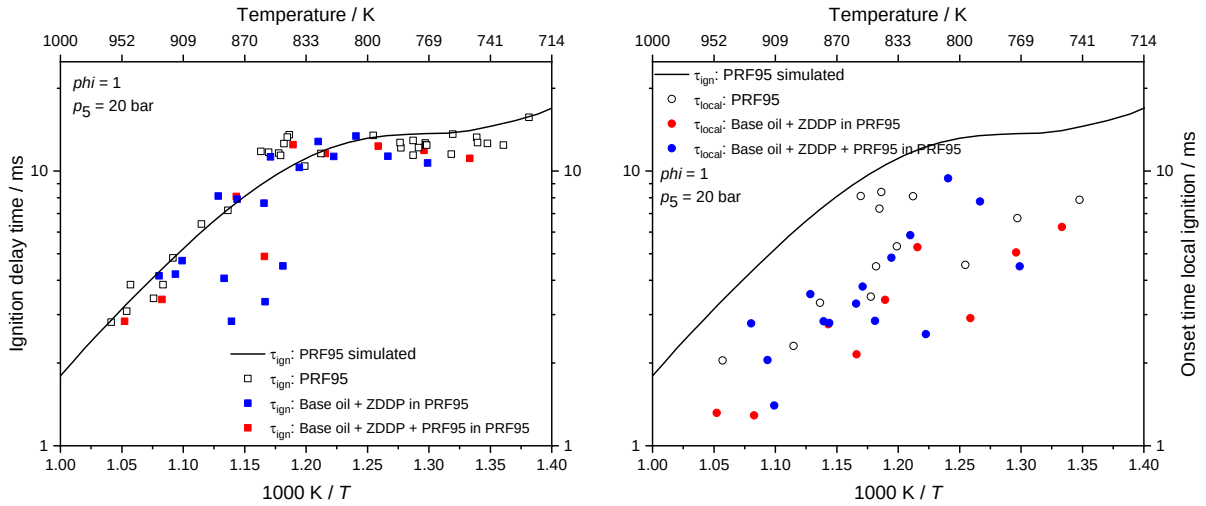

Figure 88: Ignition delay time and local ignition delay of base oil mixed with ZDDP, base oil mixed with ZDDP + 50 vol.% PRF95 in PRF95.

RGB-imaging was performed for all tests with Zinc diphosphate (ZDDP). Figure 89 shows an example of local ignition induced by a droplet of base oil + ZDDP + fuel. The high reactivity of the droplet leads to very early local ignition while the injection process is not fully completed. The first released droplet (1.6 ms) initiates the ignition followed by flame propagation. Although this process started early, the impact on the volumetric ignition was found to be minor. The trace of OH* and pressure shown in Figure 90 match with an early strong pre-ignition with a volumetric ignition after 7.8 ms.

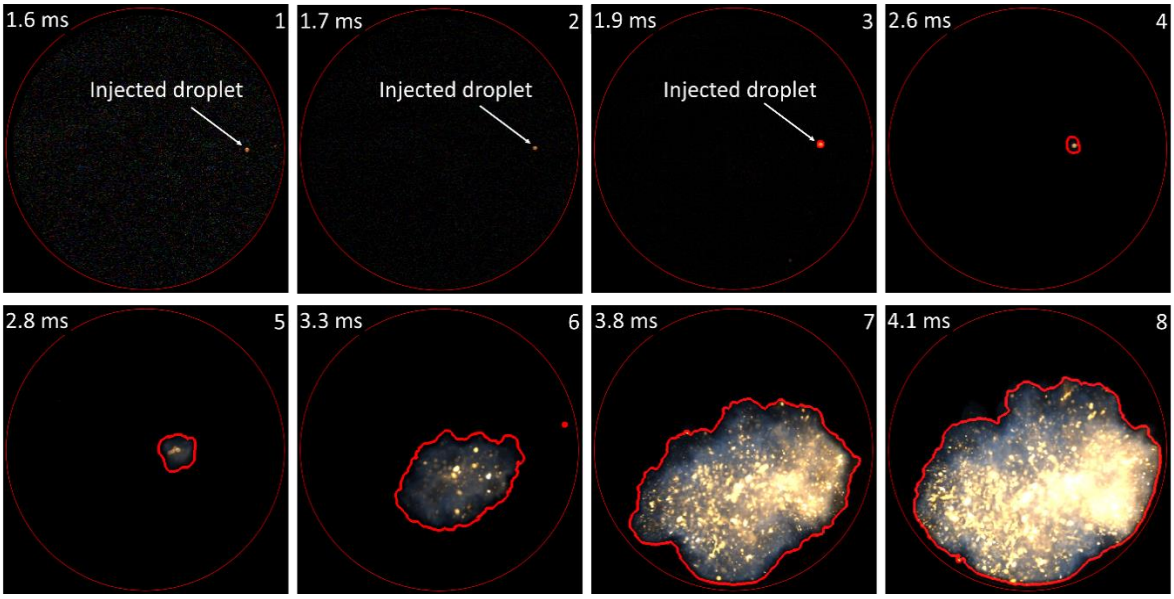

Figure 89: Ignition process in the shock tube after injection of ZDDP dissolved in base oil mixed with PRF95. Conditions: Mixture: PRF95/air at $\phi = 1$; $T_5 = 870$ K.

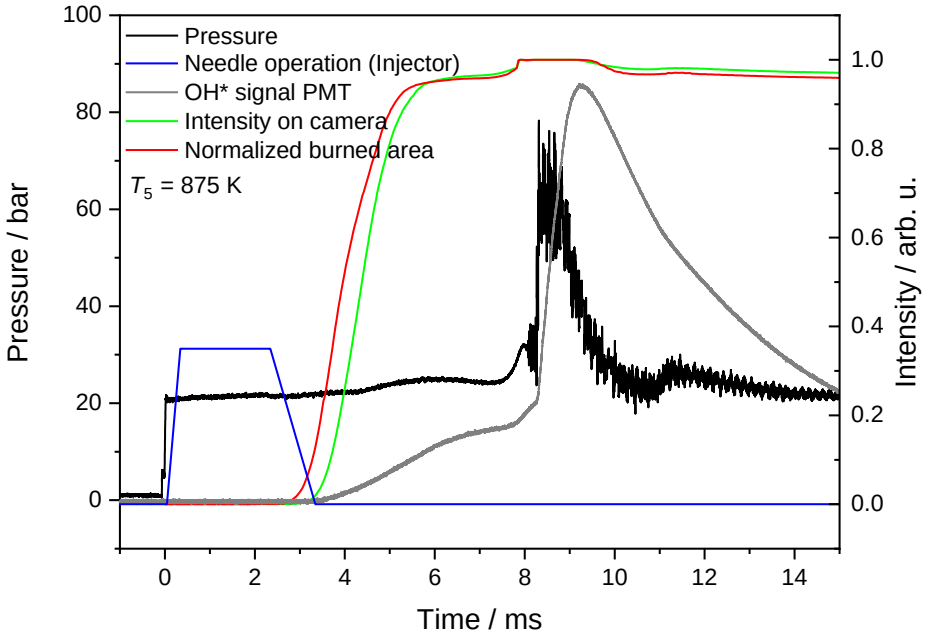

Figure 90: Pressure, chemiluminescence, and intensity traces evaluated from the image sequence shown in Figure 89.

5.2.3.6 Impact of detergents containing Ca or Mg on the ignition of PRF95/air

Besides the anti-wear additive ZDDP, detergents are a major component of lubricant additive package and are known to impact the LSPI process [7-10]. The sample in this study called “Ca-detergent” consists of base oil containing only one single Ca-based detergent. The Ca-based detergent reduces the ignition delay time of the multiphase mixture shown in Figure 91 (blue and red symbols) more than any other tested sample. The reduction of ignition delay time was significant over the whole temperature range. Fuel was added to the sample in the same manner as before to evaluate whether the interaction oil/fuel enhances the reactivity of the Ca-based detergent, but the opposite was found. The dilution of the Ca-based detergent in the sample through fuel addition causes a decrease of the reactivity of the sample.

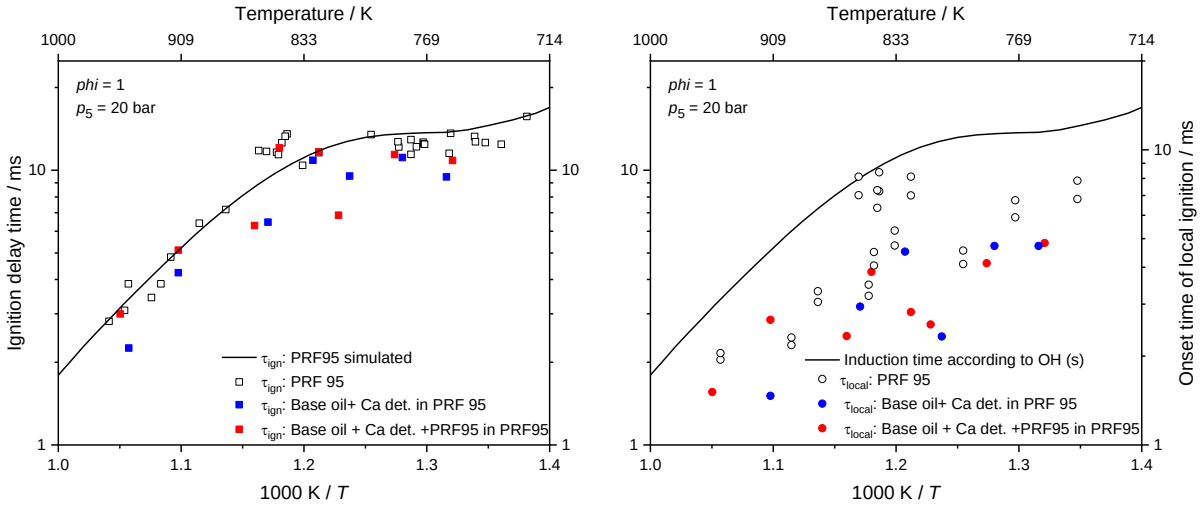

Figure 91: Ignition delay time and local ignition delay of Ca-detergent /+ 50 vol.% PRF95 in PRF95.

An example of an observed ignition of a droplet containing Ca-based detergent was performed at a gas temperature of 800 K. The image sequence in Figure 92 shows local droplet ignition occurring on the bottom right labeled by the index *a*. Local ignition was first triggered by a hot membrane particle marked *b* far upstream the shock tube. After 5.8 ms (frame 3), another

droplet marked *c* appears in the images that causes ignition in the following frames. The color of the burning droplet is shifted to the red (frame 7 and 8) compared to the observations made for the other samples shown in Figure 84 and Figure 89.
Local ignition is detected as pre-ignition in pressure and OH* traces after the droplet ignition when the flame reaches the observation area of the PMT and the pressure transducer.

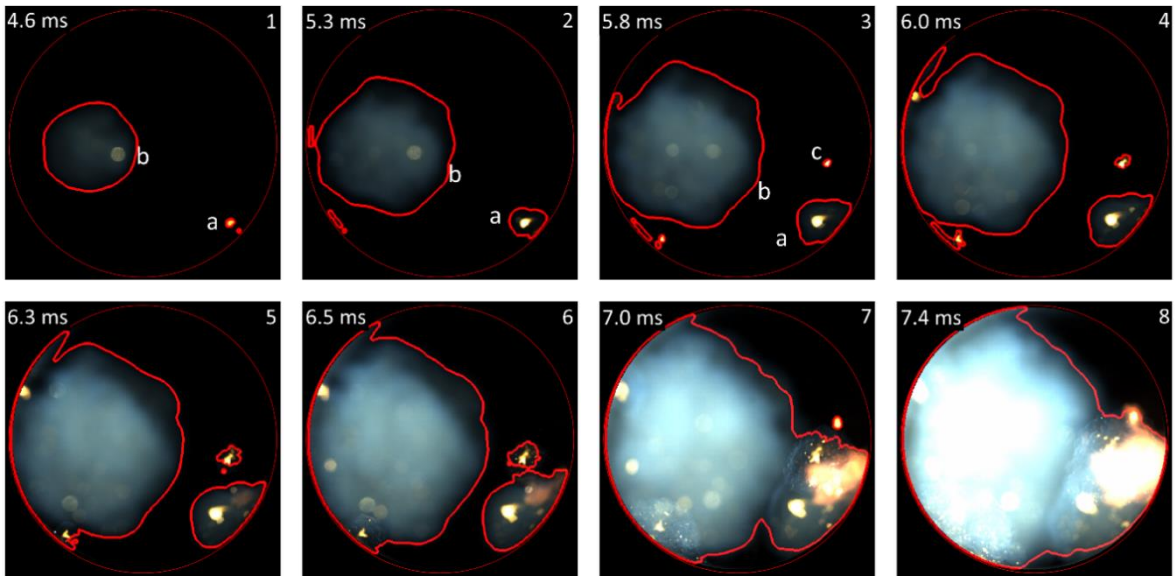

Figure 92: Ignition process in the shock tube after injection of Ca-containing detergent dissolved in base oil. Conditions: Mixture: PRF95/air; $\phi = 1$; $T_5 = 810$ K.

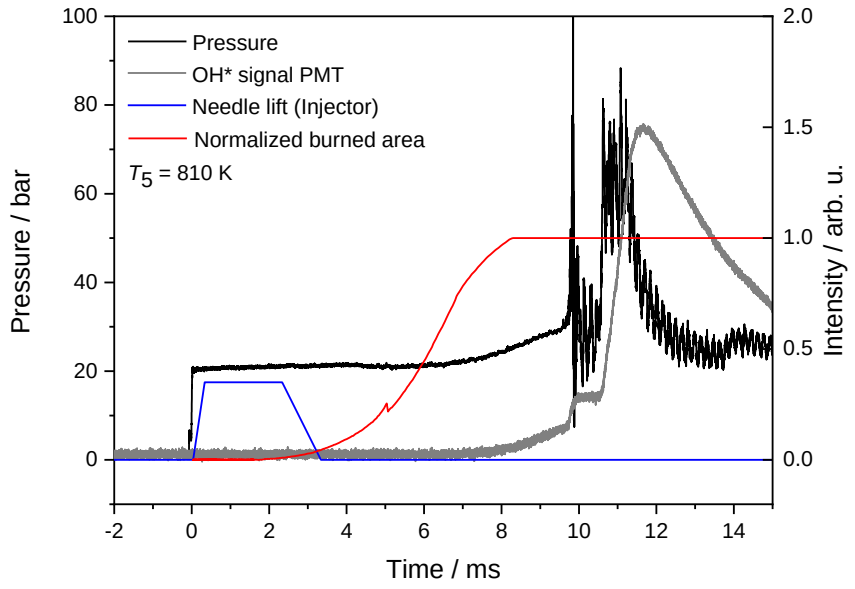

Figure 93: Pressure, chemiluminescence, and intensity traces evaluated from the image sequence shown in Figure 92

There are two types of detergents that are always in discussion when talking about LSPI. The Ca-detergent that promotes LSPI and the Mg-based detergent that seems to have no effect and can be used as an additional component to reduce the concentration of Ca-based detergent in the additive package. Besides the engine test results in [7, 10, 67, 72, 196] and the study of Yuusuke et al. [73] using a RCM, there is no study that directly measures the relative reactivity in a single cycle.

Figure 94 shows high-repetition-rate image series during the ignition of a droplet containing Mg-based detergent and PRF95 in a mixture of 1:1 vol.%. The flame of the droplet appears dark red, even darker than the flame of the Ca-based detergent shown in Figure 92.

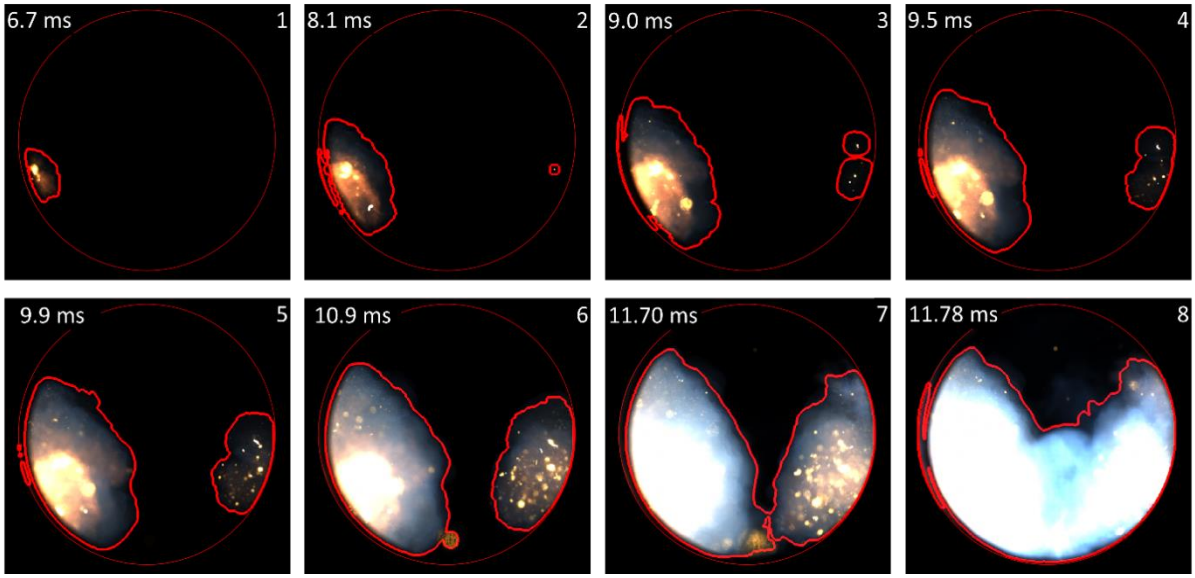

Figure 94: Ignition process in the shock tube after injection of Mg-containing detergent dissolved in base oil in mixture with PRF95. Conditions: Mixture: PRF95/air at $\phi = 1$, $T_5 = 760$ K.

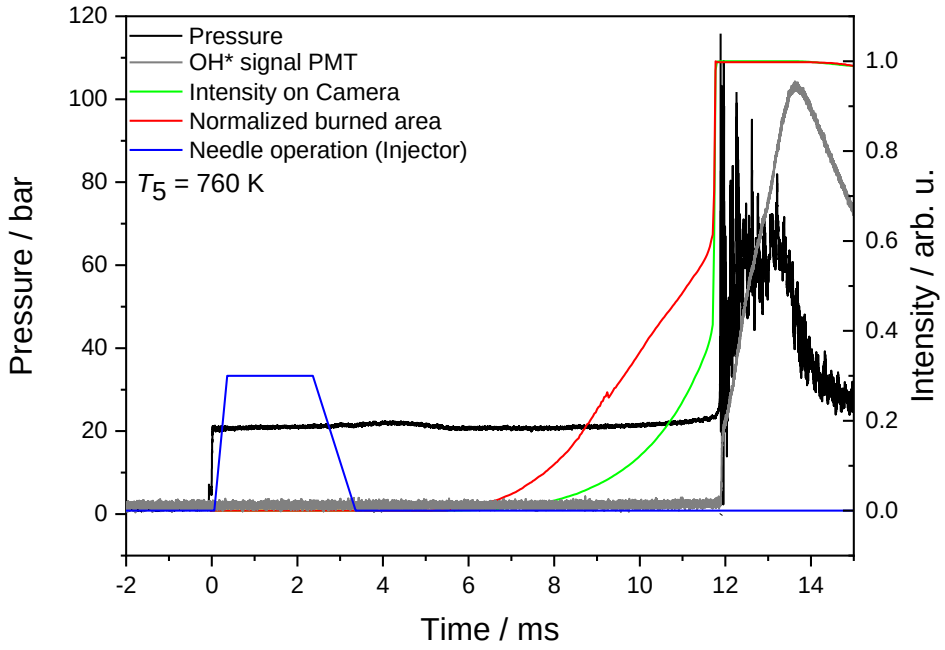

Figure 95: Pressure, chemiluminescence, and intensity traces evaluated from the image sequence shown in Figure 94.

The local ignition delay time is in the typical range as it would be without injection (Figure 96). The local ignition initiates flame propagation, but the overall reactivity was slow compared to the other additives. No pre-ignition signal by the PMT prior the global ignition of fuel/air was observed in Figure 95 because the emission from local ignition could not be detected by the detectors due to the confined optical access.

The same was observed for the local ignition delay time, which was in the range of the cases without injection. The most striking observation is the occurrence of pre-ignition that was observed more often when the liquid fuel was present. In this test, no longer ignition delay times

than those known for the pure gas mixture were observed, which is attributed to the test method. The local intrusion of ignition sources can trigger local processes that accelerate the global process but cannot have a contrary effect on the global gas reaction.

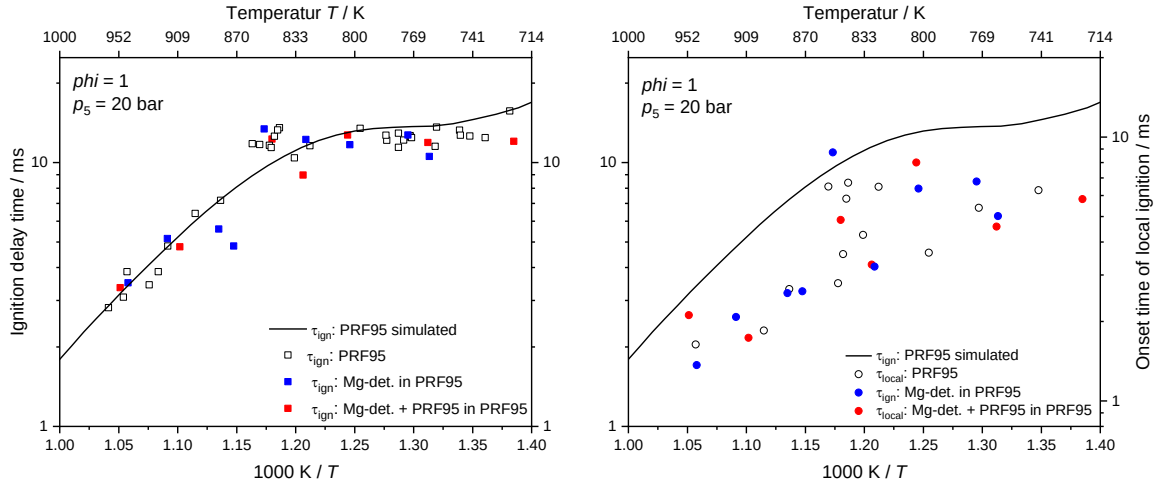

Figure 96: Ignition delay time and local ignition delay of Mg-detergent /+ 50 vol.% PRF95 in PRF95.

Mg-based detergent in a droplet was able to initiate local ignition of the droplet. But the Mg-based detergent has no crucial effect on the ignition delay time of the mixture. Adding fuel to the oil droplet did not enhance the overall reactivity of the mixture. This means that the Mg-based detergent inhibits the reactivity of the lubricant oil with the surrounding fuel mixtures. In the context of LSPI, the results confirm that the Mg-based detergent should be added to reduce the amount of Ca-based detergent in the oil.

5.2.4 Discussion and outcomes of the impact of lubricant oil/compounds or droplets on the ignition of PRF95/air

An impact of lubricant oil on pre-ignition was observed in several IC-engine studies [7-10, 76, 197] but the process is not fully understood. It is generally assumed that oil droplets are splashed into the reaction chamber and initiate local ignition, but there is no evidence for this at all. Therefore, evaporation and decomposition products in the gas phase are potential ignition sources, too.

Analysis of decomposition and evaporation products of oil additives result in hydrocarbons and different sulfur-containing species, which were tested for their potential on pre-ignition in combination with fuel surrogates. No change in ignition delay time was found, even for very high concentrations of 1000 ppm. It is unlikely that pre-ignition in engines is a pure gas-phase phenomenon. Gas-phase reactions can play a role when locally enriching the mixture by evaporation of oil on hot surfaces in the combustion chamber. This would have the same effect as ignition in the trace of a droplet as it was observed by Ohtomo et al. in an RCM [71].

With injection of lubricant oil droplets into fuel/air mixtures behind reflected shock waves, this work investigated both, surface reactions on the droplet as well as ignition in the evaporated trace. The presented results of different droplets influencing the ignition delay time was found to depend on the sample composition. But scatter in the data of all reference experiments and those with injection makes it difficult to clearly conclude whether there is an effect. The uncertainty in temperature is discussed in Appendix A. But the repeatability to match the conditions is much higher than the accuracy of temperature determination of a single experiment. The measured ignition delay times scatter slightly. Detailed analysis of images and signal traces have shown that the ignitions scatter because of non-ideal effects. These effects are less strong for PRF95/air

mixtures in comparison to the results of ethanol, but are verifiable. One way would be to identify all data points that suffer from non-ideality and delete those to generate a clean reference line. But then the same must be done for cases with the injection of droplets. Here the identification is more difficult because the origin of the effect in pressure or chemiluminescence must be clarified whether it is due to the droplet or non-ideality. Both phenomena coexist and appear in one experiment like local ignition in the gas and local ignition around a droplet.

Do the droplets impact the ignition delay time?
All data points were considered, those with and without non-ideal behavior. The non-ideal behavior underlies statistics for each specific condition. The experiments with injection of droplets follow the same statistical behavior, and are additionally affected by the impact of the droplets. By running a significance test for the different injection samples, it was possible to prove whether the difference in ignition delay time is due to the statistics of non-ideality or whether the difference is too large so that it could not be covered within a 95 % confidence interval. Table 3: Significance table for all injected samples ($\alpha = 0.05$) shows the result of two different significance tests for the injected samples. The *t*-test is more restricted than the *u*-test. For more information about the tests see Appendix B.

Table 3: Significance table for all injected samples ($\alpha = 0.05$).

Sample	*t*-test	*u*-test
Dodecane	Significant impact	Significant impact
Base oil	No impact	No impact
Base oil + PRF95	No impact	No impact
ZDDP	Significant impact	Significant impact
ZDDP + PRF95	No impact	No impact
Ca-detergent	Significant impact	Significant impact
Ca-detergent + PRF95	Significant impact	No impact
Mg-detergent	No impact	No impact
Mg-detergent + PRF95	No impact	No impact

n-Dodecane is a mid-length alkene while base oil mainly consists of comparably long alkenes. The impact on the ignition delay time of n-dodecane was higher than it was for base oil. Statistically, base oil did not show an effect. Nevertheless, it seems that the base oil shows ignition delay times in-between the pure PRF95 and the n-dodecane. An explanation could be the needed evaporation energy of base oil compared to n-dodecane while the structure of the species is similar and distinct mainly in length.
In contrast to the n-dodecane, the samples containing additives like ZDDP or Ca-detergent showed an impact, which is clearly linked to the chemistry of individually components. The TGA/DSC measurements showed extreme reactivity of ZDDP when heating over 200°C. The pure base oil starts to decompose at temperatures over 230°C. Although base oil containing Ca-detergent evaporates/decomposes at much higher temperatures, it has an impact on the ignition. Only an interaction of the Ca-detergent with its gas phase environment can explain this observation. Mixing fuel to the samples decreases the effect, which means that the concentration of the additive is important for the impact on the ignition delay time. Also, the observed effect of liner wetting is more a mechanical one of washing the oil from the line, which promotes accumulation of oil in the crevice and changes the surface tension.

The Mg-detergent is very similar to the Ca-detergent in structure, but thermo-analysis showed that more heat is necessary for evaporation and decomposition which can be the more critical parameter for the inhibition properties.
Some droplets have an influence on the ignition delay time and others do not. All droplets ignite locally which is followed by a flame propagating through the gas mixture, resulting in volumetric ignition. Because the volumetric ignition delay time differs for different injected samples the mechanism of action for the transition from local to volumetric ignition should be further investigated.
Therefore, the time until local ignition occurs for the different droplet samples was compared. The local ignition of the pure gas phase cannot be referred to as a reference, because the mechanism of action is different from that of droplets. Instead, base oil that was used as a solvent in all samples was chosen as a baseline for comparison of local droplet ignition delay times.

1. Only base oil containing ZDDP or Ca-detergent mixed with PRF95 showed significantly shorter local ignition delay times than pure base oil droplets using the *u*-test. Absolute times are shown in Figure 97. For these cases, a significant influence on the volumetric ignition delay time was found in the *t*- and *u*-test.

2. The local ignition delay times of dodecane droplets are in-between the local onset of base oil droplet ignition and those of ZDDP or Ca-detergent. samples and are still significantly shorter. The volumetric ignition was significantly affected by the injection of dodecane, too.

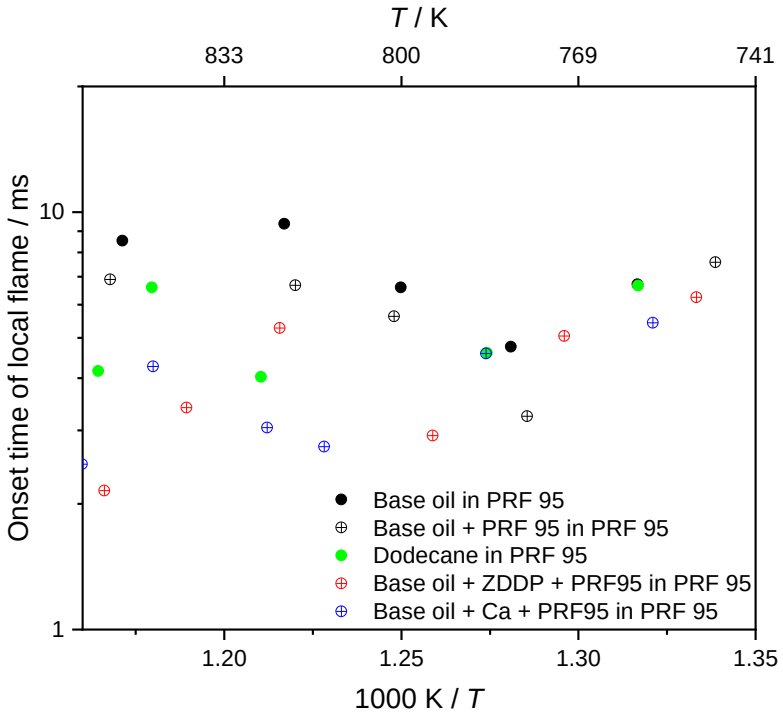

Figure 97: Onset times of local flame for all samples that show a significant difference to injection of base oil and the onset times of base oil mixed with PRF95.

The good agreement of the significant difference in local ignition delay time and the volumetric ignition delay time indicates that the timing of local ignition is important for the volumetric ignition. Because different effects impact the volumetric ignition delay time the onset of local droplet ignition is potentially the better indicator to study the likelihood of an additive in context of LSPI.

6 Conclusions and outlook

This work combines different high-repetition-rate imaging approaches and new shock-tube techniques to study homogeneous and inhomogeneous ignition of fuel/air mixtures at engine relevant conditions. Inhomogeneous ignition in the context of engine application was studied under idealized conditions in a high-pressure shock tube. Therefore, defined inhomogeneities in temperature and mixture composition were introduced to trigger local ignition behind the reflected shock wave. The ignition was followed by non-intrusive measurement techniques with spatial and high-temporal resolution.

High-repetition-rate imaging through a 10-mm diameter optical access in the sidewall was performed using endoscopic optics. Imaging from the endwall was performed in addition through a transparent endwall with an aperture of 80 mm endwall. The special feature of the optical endwall is the large aperture sustaining extremely harsh conditions; endwall pressures in p_5 of 20 bar at temperatures up to 1400 K. Peak pressures in the ignition of up to 150 bar were measured for experiments while the optical endwall was installed. Endwall imaging with such a wide angle of view at these high pressures is unique.

Simultaneous high-speed imaging in the UV and visible range enabled detailed ignition studies of homogeneous fuel mixtures. PRF95 and ethanol were studied in air to identify non-idealities resulting in different ignition modes. It was found that local ignition around particles has no impact on the volumetric ignition delay time when the number of particles is reduced by cleaning.

Pre-ignition takes place at low temperatures due to gas dynamic effects that lead to non-uniformity in temperature. Bifurcation of the shock wave was not observed in the pressure traces. However, the formation of vortex close to the sidewall with strong pressure and temperature gradients are potential local ignition sources. This fits well to the observed local gas ignition close to the sidewall and is confirmed by the finding that an increase of thermal dissipation by dilution with nitrogen or helium helps to suppress local ignition.

The impact of a hot surface on the ignition delay time underlines the findings of local ignition around hot particles. The local ignitions depended on the temperature T_5 and the surface temperature T_s. The energy dissipation of the hot surface is small compared to the energy content of the reactive volume. Therefore, the local ignition kernels have no significant impact in the volumetric ignition on short time scales up to 15 ms.

Injection of single droplets behind reflected shock waves was realized by modification of a microdispensing injector. The droplets were visualized by high-repetitive alternating LIF imaging to distinguish between LIF signal from droplets that are present in every second image and burning particles that are present in all frames and emit in the similar wave length. This was applied to the high-pressure shock tube for the first time. The injection of droplets showed that the low-temperature range is affected when the chemistry is comparably slow and therefore, the droplets have time to locally ignite and accelerate the volumetric ignition. The scatter in the data in combination with low effects necessitates statistical analysis.

Droplets of n-dodecane as well as base oil containing high concentration of ZDDP or Ca-detergent was found to significantly reduce the ignition delay time.

The onset of local ignition was introduced to describe the local reactivity of the droplet and the initiation of the flame. Differences to the pure (local) gas-phase ignition and droplet induced ignition were found. The ZDDP and Ca-detergents containing samples show a significant reduction in local ignition delay time. Droplets of n-dodecane as well as base oil containing high concentration of ZDDP or Ca-detergent were additionally found to significantly reduce the volumetric ignition delay time.

Additive concentration was important for the impact on volumetric ignition. Therefore, local ignitability of the droplets in combination with the impact on the volumetric ignition process is a good criterion to rate the relevance of the additive for LSPI.

The results of this work point out a possible to suppress non-ideality effects in the shock tube in further studies. This will be beneficial to separate inhomogeneous ignition triggered by non-idealities from the local ignition triggered by the artificially introduced ignition sources.
CFD simulations would further help to understand non-ideal effects in shock tubes. With increasing computational power, high-pressure shock-tube simulations will further promote the understanding of the observed processes to optimize facility-dependent effects. The further development of simulation and shock-tube experiments is thus a mutually influencing process that needs to be focused in the near future.
To fully understand the impact of droplets on the local ignition, conditions must be found where the gas ignition is ideal but still sensitive to intentionally introduced ignition sources. At these conditions, the experiments of this work should be verified and further optimized. In a next step, the injector should be moved to the top position and the laser should be coupled in from the bottom to improve the separation of the droplets and their deflection. In addition, alternative optical methods should be brought back into discussion.
Subject of future investigations should be a model liquid like n-dodecane with well-known properties in evaporation and ignition to verify the experimental results with known models. In further steps the studies should be supported by CFD simulations implementing reaction chemistry.
Based on the findings using helium as a diluent to suppress pre-ignition in homogeneous shock tube experiments the potential of CO_2 is interesting and has the benefit to be close to the EGR application in IC engines.
The results of this work are a milestone in shock-tube technique, fundamental for further development of advances liquid fuels and lubricant oils based CO_2 neutral components for meeting future environmental requirements.

7 Publications

Peer-reviewed publications

- P. Niegemann, M. Fikri, I. Wlokas, M. Röder, C. Schulz, "Methodology for the investigation of ignition near hot surfaces in a high-pressure shock tube", *Review of Scientific Instruments* 89 (2018) 1-13.
- P. Niegemann, M. Fikri, S. A. Kaiser, C. Schulz, "Ignition of individual droplets in a reactive fuel/air mixture behind reflected shock waves", SAE Technical paper 2019-01-2162 (2019) also in SAE International Journal of Advances and Current Practices in Mobility-V129-99EJ.
- D. Nativel, P. Niegemann, J. Herzler, M. Fikri, C. Schulz, "Ethanol ignition in a high-pressure shock tube: Ignition delay time and high-repetition-rate imaging measurements", *Proc. Combust. Inst.* (2021) DOI: 10.1016/j.proci.2020.07.021.
- P. Niegemann, J. Herzler, M. Fikri, C. Schulz, "Studying the influence of single droplets on fuel/air ignition in a high-pressure shock tube", *Review of Scientific Instruments* 91 (2020) 105-107.

Conference contributions

- P. Niegemann, M. Fikri, S. A. Kaiser, C. Schulz, "Investidation of lubricant oil/fuel/air ignition behind reflected shock waves at elevated pressure and moderate temperatures", in: *29th Deutscher Flammentag*, Bochum, Germany (2019) 1-6.

8 References

1. A. Königstein, U. D. Grebe, K.-J. Wu, P.-I. Larsson, "Differentiated analysis of downsizing concepts", *MTZ worldwide* 69 (2008) 4-11.
2. M. Rothe, K.-M. Han, U. Spicher, "Untersuchungen zur Ursache von Extremklopfen bei Motoren mit Direkteinspritzung", in: *15th Aachen Colloquium on Automobile and engine technology*, Aachen (2006).
3. C. Dahnz, U. Spicher, "Irregular combustion in supercharged spark ignition engines – pre-ignition and other phenomena", *Int. J. Engine Res.* 11 (2010) 485-498.
4. C. Dahnz, K. Han, U. Spicher, R. Schießl, U. Maas, M. Magar, "Investigations on Pre-Ignition in Highly Supercharged SI Engines", *SAE Int. J. Engines* 3 (2010) 214-223.
5. M. Amann, D. Mehta, T. Alger, "Engine Operating Condition and Gasoline Fuel Composition Effects on Low-Speed Pre-Ignition in High-Performance Spark Ignited Gasoline Engines", *SAE Int. J. Fuels Lubr.* 4 (2011) 274-285.
6. M. Amann, T. Alger, B. Westmoreland, A. Rothmaier, "The Effects of Piston Crevices and Injection Strategy on Low-Speed Pre-Ignition in Boosted SI Engines", *SAE Int. J. Eng.* 5 (2012) 1216-1228.
7. K. Takeuchi, K. Fujimoto, S. Hirano, M. Yamashita, "Investigation of Engine Oil Effect on Abnormal Combustion in Turbocharged Direct Injection - Spark Ignition Engines", *SAE Int. J. Fuels Lubr.* 5 (2012) 1017-1024.
8. K. Fujimoto, M. Yamashita, S. Hirano, K. Kato, I. Watanabe, K. Ito, "Engine oil development for preventing pre-ignition in turbocharged gasoline engine", *SAE Int. J. Fuels Lubr.* 7 (2014) 869-874.
9. S. Hirano, M. Yamashita, K. Fujimoto, K. Kato, "Investigation of Engine Oil Effect on Abnormal Combustion in Turbocharged Direct Injection Spark Ignition Engines (Part 2)", *SAE Technical Paper* 2013-01-2569 (2013).
10. T. Miyasaka, K. Miura, N. Hayakawa, T. Ishino, A. Iijima, H. Shoji, K. Tamura, T. Utaka, H. Kamano, "A Study on the Effect of a Calcium-Based Engine Oil Additive on Abnormal SI Engine Combustion", *SAE Int. J. Eng.* 8 (2015) 208-213.
11. Y. Moriyoshi, T. Yamada, D. Tsunoda, M. Xie, T. Kuboyama, K. Morikawa, "Numerical Simulation to Understand the Cause and Sequence of LSPI Phenomena and Suggestion of CaO Mechanism in Highly Boosted SI Combustion in Low Speed Range", *SAE Technical Paper* 2015-01-0755 (2015).
12. G. T. Kalghatgi, "Developments in internal combustion engines and implications for combustion science and future transport fuels", *Proc. Combust. Inst.* 35 (2015) 101-115.
13. C. Pera, S. H. Won, F. L. Dryer, F. Haas, "LSPI and lubricant auto-ignition", *INSIGHT* form Infineum Ldt. (2017).
14. Z. Wang, H. Liu, R. D. Reitz, "Knocking combustion in spark-ignition engines", *Prog. Energ. Combust.* 61 (2017) 78-112.
15. J. D. Colwell, A. Reza, "Hot Surface Ignition of Automotive and Aviation Fluids", *Journal of Fire Technology* 41 (2005) 105-123.
16. N. R. LaPointe, C. T. Adams, J. Washington, "Autoignition of Gasoline on Hot Surfaces", *Fire and Arson Investigator* 56 (2005) 18-21.
17. L. J. Hamilton, M. G. Rostedt, P. A. Caton, J. S. Cowart, "Pre-Ignition Characteristics of Ethanol and E85 in a Spark Ignition Engine", *SAE Int. J. Fuels Lubr.* 1 (2009) 145-154.
18. M. Figueroa-Labastida, J. Badra, A. M. Elbaz, A. Farooq, "Shock tube studies of ethanol preignition", *Combust. Flame* 198 (2018) 176-185.

19. J. Warnatz, U. Maas, R. W. Dibble, "Combustion", *Springer*, Berlin, Heidelberg, New York, (2006).
20. U. Maas, J. Warnatz, "Ignition processes in hydrogen - oxygen mixtures", *Combust. Flame* 74 (1988) 53-69.
21. H. C. Bailey, R. G. W. Norrish, "The oxidation of hexane in the cool-flame region", *Proc. R. Soc. London, Ser. A* 212 (1952) 311-330.
22. J. F. Griffiths, B. F. Gray, P. Gray, "Multistage ignition in hydrocarbon combustion: Temperature effects and theories of nonisothermal combustion", *Symposium (International) on Combustion* 13 (1971) 239-248.
23. N. N. Semenov, I. I. Frenkel', "Chemical kinetics and chain reactions", *Clarendon Press*, Oxford, (1935).
24. M. J. Pilling, "Low-temperature combustion and autoignition", *Elsevier*, Amsterdam; New York, (1997).
25. P. Zhang, W. Ji, T. He, X. He, Z. Wang, B. Yang, C. K. Law, "First-stage ignition delay in the negative temperature coefficient behavior: Experiment and simulation", *Combust. Flame* 167 (2016) 14-23.
26. H. K. Ciezki, G. Adomeit, "Shock-tube investigation of self-ignition of n-heptane-air mixtures under engine relevant conditions", *Combust. Flame* 93 (1993) 421-433.
27. C. Chevalier, W. J. Pitz, J. Warnatz, C. K. Westbrook, H. Melenk, "Hydrocarbon ignition: Automatic generation of reaction mechanisms and applications to modeling of engine knock", in: *24th Symposium (International) on Combustion*, (1992) 93-101.
28. C. Chevalier, P. Louessard, U. C. Müller, J. Warnatz, "A Detailed Low-Temperature Reaction Mechanism of n-Heptane Auto-Ignition", in: *90th International Symposium COMODIA*, Kyoto (1990) 93-97.
29. F. A. Williams, "Combustion Theory", *The Benjamin/Cummings Publishing Company Inc.*, Menlo Park, California, Reading, Massachusetts, Don Mills, Ontario, Wokingham, U.K., Amsterdam, Sydney, Singapore, Tokyo, Mexico City, Bogota, Santiago, San Juan, (1985).
30. I. Glassman, R. A. Yetter, "Combustion", *Academic Press*, Amsterdam, Boston, Heidelberg, London, New York, Oxford, Paris, San Diego, San Francisco, Singapore, Sydney, Tokyo, (2008).
31. S. R. Turns, "An Introduction to Combustion: Concepts and Application", *McGrawHill*, Boston, Burr Ridge, Dubuque, Madison, New York, San Francisco, St. Louis, Bangkok, Bogota, Cacacas, Lisbon, London, Madrid, Mexico City, Milan, New Delhi, Seoul, Singapore, Sydney, Taipei, Toronto, (2000).
32. S. P. M. Bane, "Spark Ignition: Experimental and Numerical Investigartion With Application to Aviation Safety", California Institute of Technology Pasadena, Passedian, California, (2010).
33. H. Hugoniot, "Mémoire sur la propagation du mouvement dans un fluide indéfini (seconde Partie)", *Journal de Mathématiques Pures et Appliquées* 4 (1888) 153-168.
34. W. M. Rankine, "On the thermodynamic theory of waves of finite longitudinal disturbance", *Philos. Trans. R. Soc. London, Ser. A* 160 (1870) 277-288.
35. H. Oertel, "Stoßrohre", *Springer*, Wien, New York, (1996).
36. A. G. Gaydon, I. R. Hurle, "The shock tube in high-temperature Chemical physics", *Springer*, London, (1963).
37. H. B. Palmer, B. E. Knox, "Contact surface tailoring in a chemical shock tube", *ARS J.* 31 (1961) 1-6.
38. H. Mirels, "Attenuation in a shock tube due to unsteady-boundary-layer action", National Advisory Committee for Aeronautics, NACA-TR-1333 (1957).

39. D. Nativel, S. P. Cooper, J. T. Lipkowicz, M. Fikri, E. L. Petersen, C. Schulz, "Impact of shock-tube facility-dependent effects on incident- and reflected-shock conditions over a wide range of pressures and Mach numbers", *Combust. Flame* 217 (2020) 200-211.
40. D. He, L. Shi, D. Nativel, J. Herzler, M. Fikri, C. Schulz, "CO-concentration and temperature measurements in reacting CH4/O2 mixtures doped with diethyl ether behind reflected shock waves", *Combust. Flame* 216 (2020) 194-205.
41. H. Mark, "The interaction of a reflected shock wave with the boundary layer in a shock tube.", *J. Aeronaut. Sci.* 24 (1958) 304–306.
42. A. Khokhlov, J. Austin, A. Knisely, "Development of Hot Spots and Ignition Behind Reflected Shocks in 2H2 + O2.", in: *25th ICDERS*, Leeds, UK (2015).
43. J. T. Lipkowicz, I. Wlokas, A. M. Kempf, "Analysis of mild ignition in a shock tube using a highly resolved 3D-LES and high-order shock-capturing schemes", *Shock Waves* 29 (2019) 511-521.
44. K. Fieweger, R. Blumenthal, G. Adomeit, "Shock-tube investigations on the self-ignition of hydrocarbon-air mixtures at high pressures", in: *25th Symp. Int. Comb.*, California, USA (1994) 1579-1585.
45. C. J. Aul, E. L. Petersen, H. J. Curran, M. Fikri, C. Schulz, "Interpretation of Low-Temperature, High-Pressure Ignition Data from a Shock Tube with Significant PreIgnition Pressure Rise", in: *23rd ICDERS*, Irvine, USA (2011).
46. R. K. Hanson, G. A. Pang, S. Chakraborty, W. Ren, S. Wang, D. F. Davidson, "Constrained reaction volume approach for studying chemical kinetics behind reflected shock waves", *Combust. Flame* 160 (2013) 1550-1558.
47. D. Downs, F. B. Theobald, "The Effect of Fuel Characteristics and Engine Operating Conditions on Pre-Ignition", *ProcInstMechEng:Automobile Division* 178 (1963) 20.
48. P. Niegemann, M. Fikri, I. Wlokas, M. Röder, C. Schulz, "Methodology for the investigation of ignition near hot surfaces in a high-pressure shock tube", *Rev. Sci. Instrum.* 89 (2018) 1-13.
49. G. R. Astbury, S. J. Hawksworth, "Spontaneous ignition of hydrogen leaks: A review of postulated mechanisms", *Int. J. Hydrogen Energy* 32 (2007) 2178-2185.
50. L. R. Boeck, M. Meijers, A. Kink, R. Mével, J. E. Shepherd, "Ignition of fuel–air mixtures from a hot circular cylinder", *Combust. Flame* 185 (2017) 265-277.
51. M. Koban, B. Minor, P. Coughlan, N. Gray, "Hot Surface Ignition Testing of Low GWP 2L Refrigerants", in: *International Refrigeration and Air Conditioning Conference*, (2016).
52. R. E. Ebersole, L. C. Matusz, M. S. Modi, R. E. Orlando, "Hot Surface Ignition of Gasoline-Ethanol Fuel Mixtures", *SAE Int. J. Eng.* 2 (2009) 1-8.
53. V. Somandepalli, S. Kelly, S. Davis, "Hot Surface Ignition of Ethanol-blended Fuels and Biodiesel", *SAE Technial Paper* 2008-01-0402 (2008).
54. J. Melguizo-Gavilanes, L. Boeck, R. Mével, J. E. Shepherd, "Hot surface ignition of stoichiometric hydrogen-air mixtures", *Int. J. Hydrogen Energy* 42 (2017) 10.
55. D. Roth, T. Häber, H. Bockhorn, "Experimental and numerical study on the ignition of fuel/air mixtures at laser heated silicon nitride particles", *Proc. Combust. Inst.* 36 (2017) 1475-1484.
56. C. A. Bergeron, W. L. Hallett, "Ignition characteristics of liquid hydrocarbon fuels as single droplets", *Can. J. Chem. Eng.* 67 (1989) 142-149.
57. C. A. Bergeron, "A study of the auto-ignition of single droplets of liquid fuel", University of Ottawa (Canada), (1987).
58. P. Adomeit, M. Jakob, A. Kolbeck, S. Pischinger, "Glow-plug Ignition of Ethanol Fuels under Diesel Engine Relevant Thermodynamic Conditions", *SAE Technical Paper* 2011-01-1391 (2011).

59. S. K. Menon, P. A. Boettcher, B. Ventura, G. Blanquart, "Hot surface ignition of n-hexane in air", *Combust. Flame* 163 (2015) 42-53.
60. G. Blanquart, P. Pepiot-Desjardins, H. Pitsch, "Chemical mechanism for high temperature combustion of engine relevant fuels with emphasis on soot precursors", *Combust. Flame* 156 (2009) 588-607.
61. R. v. Basshuysen, F. Schäfer, "Handbuch Verbrennungsmotor: Grundlagen, Komponenten, Systeme, Perspektive", *Springer Vieweg*, (2005) Kapitel 13.2,.
62. O. Budak, F. Hoppe, B. Heuser, S. Pischinger, U. Burke, A. Heufer, "Hot surface pre-ignition in direct-injection spark-ignition engines: Investigations with Tailor-Made Fuels from Biomass", *Int. J. Engine Res.* 19 (2017) 45-54.
63. A. Zahdeh, P. Rothenberger, W. Nguyen, M. Anbarasu, S. Schmuck-Soldan, J. Schaefer, T. Goebel, "Fundamental Approach to Investigate Pre-Ignition in Boosted SI Engines", *SAE Int. J. Eng.* 4 (2011) 246-273.
64. N. Sasaki, K. Nakata, K. Kawatke, S. Sagawa, M. Watanabe, T. Sone, "Effect of Fuel Components on Engine Abnormal Combustion", *SAE Technical Paper* 2012-01-1276 (2012).
65. G. T. Kalghatgi, D. Bradley, "Pre-ignition and 'super-knock' in turbo-charged spark-ignition engines", *Int. J. Engine Res.* 13 (2012) 399-414.
66. G. T. Kalghatgi, D. Bradley, J. Andrae, A. J. Harrison, "The nature of "superknock" and its origins in SI engines", in: *Conference on Internal combustion engines: Performance, Fuel Economy and Emissions*, London (2009) 1-14.
67. Y. Long, Z. Wang, Y. Qi, S. Xiang, G. Zeng, P. Zhang, X. He, A. Gupta, H. Shao, Y. Wang, "Effect of Oil and Gasoline Properties on Pre-Ignition and Super-Knock in a Thermal Research Engine (TRE) and an Optical Rapid Compression Machine (RCM)", *SAE Technical Paper* 2016-01-0720 (2016).
68. Z. Wang, Y. Qi, H. Liu, P. Zhang, X. He, J. Wang, "Shock wave reflection induced detonation (SWRID) under high pressure and temperature condition in closed cylinder", *Shock Waves* 26 (2016) 687-691.
69. Y. Qi, Z. Wang, J. Wang, X. He, "Effects of thermodynamic conditions on the end gas combustion mode associated with engine knock", *Combust. Flame* 162 (2015) 4119-4128.
70. S. F. Dingle, A. Cairns, H. Zhao, J. Williams, O. Williams, R. Ali, "Lubricant Induced Pre-Ignition in an Optical SI Engine", *SAE Technical Paper* 2014-01-1222 (2014).
71. M. Ohtomo, H. Miyagawa, M. Koike, N. Yokoo, K. Nakata, "Pre-Ignition of Gasoline-Air Mixtures Triggered by a Lubricant Oil Droplet", *SAE Int. J. Fuels Lubr.* 7 (2014) 673-682.
72. M. Kassai, T. Shiraishi, T. Noda, M. Hirabe, Y. Wakabayashi, J. Kusaka, Y. Daisho, "An Investigation on the Ignition Characteristics of Lubricant Component Containing Fuel Droplets Using Rapid Compression and Expansion Machine", *SAE Int. J. Fuels and Lubr.* 9 (2016) 469-480.
73. W. Yuusuke, I. Kazuki, T. Kotaro, K. Mitsuru, J. Ying, S. Yasuyuki, "Experimental Study on the Effect of Lubricant Oil on Ignition Characteristics of Hydrocarbons Using a Rapid Compression Machine", in: *11thASPACC*, Sydney, Australia (2017).
74. D. Distaso, R. Amirante, G. Calò, P. D. Palma, P. Tamburrano, R. D. Reitz, "Investigation of Lubricant Oil influence on Ignition of Gasoline-like Fuels by a Detailed Reaction Mechanism", *Energy Procedia* 148 (2018) 663-670.
75. S. M. Sarathy, C. K. Westbrook, M. Mehl, W. J. Pitz, C. Togbe, P. Dagaut, H. Wang, M. A. Oehlschlaeger, U. Niemann, K. Seshadri, P. S. Veloo, C. Ji, F. N. Egolfopoulos, T. Lu, "Comprehensive chemical kinetic modeling of the oxidation of 2-methylalkanes from C7 to C20", *Combust. Flame* 158 (2011) 2338-2357.

76. O. A. Kuti, S. Y. Yang, N. Hourani, N. Naser, W. L. Roberts, S. H. Chung, S. M. Sarathy, "A fundamental investigation into the relationship between lubricant composition and fuel ignition quality", *Fuel* 160 (2015) 605-613.
77. J. N. Ziemer, K. R. Krishna, "Lube Base Oil Hydrofinishing", *Springer*, Berlin, Heidelberg, (2014).
78. R. M. Mortier, M. R. Fox, S. T. Orszulik, "Chemistry and Technology of Lubricants", *Springer*, Heidelberg, London, New York, (2010).
79. A. P. Institute, "Engine Oil Licensing and Certification System", API 1509, (2019).
80. L. R. Rudnick, "Lubricant Additives: chemistry and application", *CRC Press*, (2009).
81. M. Houben, "Friction analysis of modern gasoline engines and new test methods to determine lubricant effects", in: *10th International Colloquium*, Esslingen (1996).
82. W. C. Gergel, "Lubricant additive chemistry", in: *International Symosium on Technical Organic Additives and Environment*, Interlaken, Switzerland (1984).
83. L. E. King, "Basic alkali metal sulfonate dispersions, process for their preparation, and lubricants containing same", US5037565A, August 6th, (1991).
84. A. H. Lefebvre, V. G. McDonell, "Atomization and sprays", *CRC Press*, (2017).
85. G. Bidone, "Expériences sur la Frome et sur la Direction des Veines et des Courants d'Eau Lancespar Diveres Ouvertures", *Imprimerie Royale*, Turin, (1829).
86. F. Savart, "Wemoire sur la constitution des veines liquids lancees par des orifices circulaires en mince paroi", *Ann. de chim.* 53 (1833) 49.
87. L. Rayleigh, "On The Instability Of Jets", *Proc. London Math. Soc.* s1-10 (1878) 4-13.
88. E. Tyler, "XL. Instability of liquid jets", *The London, Edinburgh, and Dublin Philosophical Magazine and Journal of Science* 16 (1933) 504-518.
89. C. Weber, "Disintegration of Liquid Jets", *Z. Angew. Math. Mech.* 1 (1931) 136-159.
90. W. Ohnesorge, "Formation of Dropsby Nozzles and the Breakup of Liquid Jets", *Z. Angew. Math. Mech.* 16 (1936) 3.
91. R. D. Reitz, "Atomization and other breakup regimes of a liquid jet", Princeton, (1978).
92. E. Giffen, A. Muraszew, "The atomisation of liquid fuels", *Chapman & Hall*, (1953).
93. A. Haenlein, "Disintegration of a liquid jet", Washington, No. 659 (1932).
94. C. Dumouchel, "On the experimental investigation on primary atomization of liquid streams", *Experiments in Fluids* 45 (2008) 371-422.
95. S. Leroux, C. Dumouchel, M. Ledoux, "The stability curve of Newtonian liquid jets", *Atomization and sprays* 6 (1996).
96. J. O. Hinze, "Fundamentals of the hydrodynamic mechanism of splitting in dispersion processes", *AIChE Journal* 1 (1955) 289-295.
97. B. J. Meister, G. F. Scheele, "Drop formation from cylindrical jets in immiscible liquid systems", *AIChE Journal* 15 (1969) 700-706.
98. G. I. Taylor, "The formation of emulsions in definable fields of flow", *Proc. R. Soc. London, Ser. A* 146 (1934) 501-523.
99. F. D. Rumscheidt, S. G. Mason, "Particle motions in sheared suspensions XII. Deformation and burst of fluid drops in shear and hyperbolic flow", *J. Colloid Sci.* 16 (1961) 238-261.
100. P. Clay, "The mechanism of emulsion formation in turbulent flow", *Proc. Sec. Sci.* 43 (1940) 852-965.
101. M. Sevik, S. H. Park, "The Splitting of Drops and Bubbles by Turbulent Fluid Flow", *J. Fluids Eng.* 95 (1973) 53-60.
102. W. A. Sirignano, "Droplet-Model Summary", in: "Fluid Dynamics and Transport of Droplets and Sprays", *Cambridge University Press*, Cambridge, (2010).
103. G. M. Faeth, "Current status of droplet and liquid combustion", *Prog. Energ. Combust.* 3 (1977) 191-224.

104. M. Goldsmith, "On the Burning of Single Drops of Fuel in an Oxidizing Atmosphere", *J. Jet Prop.* 24 (1954) 245-251.
105. A. M. Kanury, "Introduction to Combustion Phenomena", *Taylor & Francis*, (1975).
106. D. B. Spalding, "Some Fundamentals of Combustion", *Academic Press*, New York, London, (1955).
107. A. Williams, "Fundamentals of oil combustion", *Prog. Energ. Combust.* 2 (1976) 167-179.
108. W. Ranz, W. Marshall, "Evaporation from Drops.", *Chem. Eng. Prog.* 48 (1952) 141-146.
109. H. H. Chiu, H. Y. Kim, E. J. Croke, "Internal group combustion of liquid droplets", in: *19th Symposium (International) on Combustion*, Haifa, Isreal (1982) 971-980.
110. H. H. Chiu, T. M. Liu, "Group Combustion of Liquid Droplets", *Combust. Sci. Technol.* 17 (1977) 127-142.
111. T. Suzuki, H. H. CHiu, "Multi Droplet Combustion on Liquid Propellants", in: *Proc. of the 19th Int. Symp. on Space Technology and Science*, Tokyo, Japan (1971) 9.
112. M. Labowsky, D. Rosner, "Group combustion of droplets in fuel clouds, I. Quasi-steady predictions", *Evaporation-combustion of fuels* 166 (1978) 63-79.
113. T. Kathrotia, U. Riedel, A. Seipel, K. Moshammer, A. Brockhinke, "Experimental and numerical study of chemiluminescent species in low-pressure flames", *Appl. Phys. B* 107 (2012) 571-584.
114. T. Kathrotia, M. Fikri, M. Bozkurt, M. Hartmann, U. Riedel, C. Schulz, "Study of the H+O+M reaction forming OH∗: Kinetics of OH∗ chemiluminescence in hydrogen combustion systems", *Combust. Flame* 157 (2010) 1261-1273.
115. M. Bozkurt, M. Fikri, C. Schulz, "Investigation of the kinetics of OH* and CH* chemiluminescence in hydrocarbon oxidation behind reflected shock waves", *Appl. Phys. B* 107 (2012) 515-527.
116. J. R. Lakowicz, "Principles of Fluorescence Spectroscopy", *Springer*, (2006).
117. G. Gauglitz, T. Vo-Dinh, "Applications", in: "Handbook of Spectroscopy", *Wiley-VCH*, (2014).
118. C. Schulz, V. Sick, "Tracer-LIF diagnostics: quantitative measurement of fuel concentration, temperature and fuel/air ratio in practical combustion systems", *Prog. Energ. Combust.* 31 (2005) 75-121.
119. W. Koban, J. D. Koch, R. K. Hanson, C. Schulz, "Toluene LIF at elevated temperatures: implications for fuel–air ratio measurements", *Appl. Phys. B* 80 (2005) 147-150.
120. S. Faust, G. Tea, T. Dreier, C. Schulz, "Temperature, pressure, and bath gas composition dependence of fluorescence spectra and fluorescence lifetimes of toluene and naphthalene", *Appl. Phys. B* 110 (2013) 81-93.
121. J. H. Christensen, A. B. Hansen, J. Mortensen, O. Andersen, "Characterization and Matching of Oil Samples Using Fluorescence Spectroscopy and Parallel Factor Analysis", *Anal. Chem.* 77 (2005) 2210-2217.
122. T. Benzler, S. Faust, T. Dreier, C. Schulz, "Low-pressure effective fluorescence lifetimes and photo-physical rate constants of one- and two-ring aromatics", *Appl. Phys. B* 121 (2015) 549-558.
123. R. J. Kee, F. M. Rupley, J. A. Miller, M. E. Coltrin, J. F. Grcar, E. Meeks, H. K. Moffa, A. E. Lutz, G. Dixon-Lewis, M. D. Smooke, J. Warnatz, G. H. Evans, R. S. Larson, R. E. Mitchell, L. R. Petzold, W. C. Reynolds, M. Caracotsios, W. E. Stewart, P. Glarborg, C. Wang, O. Adigun, "CHEMKIN Collection, Release 3.6", in: *CHEMKIN Collection, Reaction Design, Inc.*, San Diego, CA (2000).
124. P. Niegemann, J. Herzler, M. Fikri, C. Schulz, "Studying the influence of single droplets on fuel/air ignition in a high-pressure shock tube", *Rev. Sci. Instrum.* 91 (2020) 105107.
125. Federal-Mogul Aftermarket GmbH, "Alles über Glühkerzen", 4, (2014).

126. N. M. Ravindra, S. Abedrabbo, C. Wei, F. M. Tong, A. K. Nanda, A. C. Speranza, "Temperature-dependent emissivity of silicon-related materials and structures", *IEEE Transactions on Semiconductor Manufacturing* 11 (1998) 30-39.
127. E. K. Dabora, K. W. Ragland, J. A. Nicholls, "A Study of Heterogeneous Detonations", in: *3rd Aerospace Sciences Meeting*, New York, USA (1966) 66-109.
128. A. R. Hanson, E. G. Domich, H. S. Adams, "Shock tube investigation of the breakup of drops by air blasts", *The Physics of Fluids* 6 (1963) 1070-1080.
129. B. Thirouard, T. Tian, "Oil Transport in the Piston Ring Pack (Part I): Identification and Characterization of the Main Oil Transport Routes and Mechanisms", *SAE Technical Paper* 2003-01-1952 (2003).
130. N. Otsu, "A Threshold Selection Method from Gray-Level Histograms", *IEEE Trans. Syst. Man Cybern.* 9 (1979) 62-66.
131. S. Shawal, M. Goschutz, M. Schild, S. Kaiser, M. Neurohr, J. Pfeil, T. Koch, "High-Speed Imaging of Early Flame Growth in Spark-Ignited Engines Using Different Imaging Systems via Endoscopic and Full Optical Access", *SAE Int. J. Eng.* 9 (2016) 704-718.
132. S. Gordon, "Encyclopedia of Science and Technology", *MCGraw-Hill Book Co. Inc.*, New York, Toronto, London, (1960).
133. A. W. Coats, J. P. Redfern, "Thermogravimetric analysis. A review", *Analyst* 88 (1963) 906-924.
134. G. Gulochon, "Thermogravimetric Measurements", *Anal. Chem.* 33 (1961) 1124-1125.
135. E. L. Simons, A. E. Newkirk, "New studies on calcium oxalate monohydrate: A guide to the interpretation of thermogravimetric measurements", *Talanta* 11 (1964) 549-571.
136. C. D. Doyle, "Estimating Thermal Stability of Experimental Polymers by Empirical Thermogravimetric Analysis", *Anal. Chem.* 33 (1961) 77-79.
137. J. Pellon, W. G. Carpenter, "Polyamides containing phosphorus. I. Preparation and properties", *J. Polym. Sci., Part A: Polym. Chem.* 1 (1963) 863-876.
138. E. s. Watson, M. J. O'neill, "Differential microcalorimeter", US3263484A, (1966).
139. R. Ekman, J. Silberring, A. Westman-Brinkmalm, A. Kraj, "Mass Spectrometry Instrumentation, Interpretation, and Applications", *John Wiley & Sons Inc.*, New Jersey, (2009).
140. C. Pera, V. Knop, "Methodology to define gasoline surrogates dedicated to auto-ignition in engines", *Fuel* 96 (2012) 59-69.
141. A. S. Roger, C. Arthur, "Limitations of the Reflected Shock Technique for Studying Fast Chemical Reactions and Its Application to the Observation of Relaxation in Nitrogen and Oxygen", *J. Chem. Phys.* 30 (1959) 257-265.
142. M. Honda, K. Takayama, O. Onodera, Y. Kohama, "Motion of reflected shock waves in shock tube", in: *Proc. of the 10th Intern. Shock Tube Symp.*, Kyoto, Japan (1975) 312–319.
143. E. L. Petersen, R. K. Hanson, "Measurement of Reflected-shock Bifurcation Over a Wide Range of Gas Composition and Pressure", *Shock Waves* 15 (2006) 333-340.
144. K. Grogan, Q. Wang, M. Ihme, "Modeling Gas Dynamic Effects in Shock-Tubes for Reaction Kinetics Measurements", *Bull. Am. Phys. Soc.* 59 (2014).
145. A. M. Tulgestke, S. E. Johnson, D. F. Davidson, R. K. Hanson, "High Speed Imaging of Inhomogeneous Ignition in a Shock Tube", in: *26th International Colloquium on the Dynamics of Explosions and Reactive Systems*, Boston, MA, USA (2017) 1-6.
146. O. Mathieu, L. T. Pinzón, T. M. Atherley, C. R. Mulvihill, I. Schoel, E. L. Petersen, "Experimental study of ethanol oxidation behind reflected shock waves: Ignition delay time and H2O laser-absorption measurements", *Combust. Flame* 208 (2019) 313-326.

147. L. T. Pinzón, O. Mathieu, C. R. Mulvihill, I. Schoegl, E. L. Petersen, "Ignition delay time and H2O measurements during methanol oxidation behind reflected shock waves", *Combust. Flame* 203 (2019) 143-156.
148. L. Cai, H. Pitsch, "Optimized chemical mechanism for combustion of gasoline surrogate fuels", *Combust. Flame* 162 (2015) 1623-1637.
149. M. Deminsky, V. Chorkov, G. Belov, I. Cheshigin, A. Knizhnik, E. Shulakova, M. Shulakov, I. Iskandarova, V. Alexandrov, A. Petrusev, I. Kirillov, M. Strelkova, S. Umanski, B. Potapkin, "Chemical Workbench", *Comp. Mater. Sci.* 28 (2003) 169-178.
150. D. F. Davidson, R. K. Hanson, "Recent advances in shock tube/laser diagnostic methods for improved chemical kinetics measurements", *Shock Waves* 19 (2009) 271-283.
151. G. A. Pang, D. F. Davidson, R. K. Hanson, "Experimental study and modeling of shock tube ignition delay times for hydrogen–oxygen–argon mixtures at low temperatures", *Proc. Combust. Inst.* 32 (2009) 181-188.
152. P. Niegemann, M. Fikri, S. A. Kaiser, C. Schulz, "Ignition of individual droplets in a reactive fuel/air mixture behind reflected shock waves", *SAE Technical Paper* 2019-01-2162 (2019).
153. R. Friedman, A. Maček, "Ignition and combustion of aluminium particles in hot ambient gases", *Combust. Flame* 6 (1962) 9-19.
154. A. M. Tulgestke, S. E. Johnson, D. F. Davidson, A. R. Hanson, "High-speed imaging of inhomogeneous ignition in a shock tube", *Shock Waves* 28 (2018) 1089–1095.
155. C. Lee, S. Vranckx, K. A. Heufer, S. V. Khomik, Y. Uygun, H. Olivier, R. X. Fernandez, "On the Chemical Kinetics of Ethanol Oxidation: Shock Tube, Rapid Compression Machine and Detailed Modeling Study", *Zeitschrift für Physikalische Chemie* 226 (2012) 1-28.
156. S. Barak, O. Pryor, J. Lopez, E. Ninnemann, S. Vasu, B. Koroglu, "High-Speed Imaging and Measurements of Ignition Delay Times in Oxy-Syngas Mixtures With High CO2 Dilution in a Shock Tube", *J. Eng. Gas Turbines Power* 139 (2017).
157. Y. Zhang, H. El-Merhubi, B. Lefort, L. Le Moyne, H. J. Curran, A. Kéromnès, "Probing the low-temperature chemistry of ethanol via the addition of dimethyl ether", *Combust. Flame* 190 (2018) 74-86.
158. K. A. Heufer, H. Olivier, "Determination of ignition delay times of different hydrocarbons in a new high pressure shock tube", *Shock Waves* 20 (2010) 307-316.
159. L. R. Cancino, M. Fikri, A. A. M. Oliveira, C. Schulz, "Ignition delay times of ethanol-containing multi-component gasoline surrogates: Shock-tube experiments and detailed modeling", *Fuel* 90 (2011) 1238-1244.
160. D. Nativel, P. Niegemann, J. Herzler, M. Fikri, C. Schulz, "Ethanol ignition in a high-pressure shock tube: Ignition delay time and high-repetition-rate imaging measurements", *Proc. Combust. Inst.* 91 (2020) 1-9.
161. L. R. Cancino, M. Fikri, A. A. M. Oliveira, C. Schulz, "Measurement and chemical kinetics modeling of shock-induced ignition of ethanol− air mixtures", *Energ. Fuel.* 24 (2010) 2830-2840.
162. R. K. Hanson, D. F. Davidson, "Recent advances in laser absorption and shock tube methods for studies of combustion chemistry", *Prog. Energ. Combust.* 44 (2014) 103-114.
163. H. Li, Z. C. Owens, D. F. Davidson, R. K. Hanson, "A simple reactive gasdynamic model for the computation of gas temperature and species concentrations behind reflected shock waves", *Int. J. Chem. Kinet.* 40 (2008) 189-198.
164. A. Frassoldati, A. Cuoci, T. Faravelli, E. Ranzi, "Kinetic Modeling of the Oxidation of Ethanol and Gasoline Surrogate Mixtures", *Combust. Sci. Technol.* 182 (2010) 653-667.
165. C. Zhou, K. Sendt, B. S. Haynes, "Experimental and kinetic modelling study of H2S oxidation", *Proc. Combust. Inst.* 34 (2013) 625-632.

166. E. Ninnemann, B. Koroglu, O. Pryor, S. Barak, L. Nash, Z. Loparo, J. Sosa, K. Ahmed, S. Vasu, "New insights into the shock tube ignition of H2/O2 at low to moderate temperatures using high-speed end-wall imaging", *Combust. Flame* 187 (2018) 11-21.
167. A. M. Ferris, A. J. Susa, D. F. Davidson, R. K. Hanson, "High-temperature laminar flame speed measurements in a shock tube", *Combust. Flame* 205 (2019) 241-252.
168. S. S. Merola, B. M. Vaglieco, "Knock investigation by flame and radical species detection in spark ignition engine for different fuels", *Energy convers. Manag.* 48 (2007) 2897-2910.
169. S. Palaveev, M. Magar, H. Kubach, R. Schiessl, U. Spicher, U. Maas, "Premature Flame Initiation in a Turbocharged DISI Engine-Numerical and Experimental Investigations", *SAE Int. J. Eng.* 6 (2013) 54-66.
170. J. H. Van't Hoff, E. Cohen, T. Ewan, "Studies in chemical dynamics", *Williams & Norgate, Muller F.*, London, Amsterdam, (1896).
171. N. M. Laurendeau, "Thermal ignition of methane air mixtures by hot surfaces: A critical examination", *Combust. Flame* 46 (1982) 29-49.
172. A. Alkidas, P. Durbetaki, "Ignition of a Gaseous Mixture by a Heated Surface", *Combust. Sci.Technol.* 7 (1973) 135-140.
173. A. Alkidas, P. Durbetaki, "A Simplified Model for Stagnation Heat Transfer and Ignition of a Gaseous Mixture", *J. Heat Transfer* 95 (1973) 564-566.
174. C. K. Law, "On the stagnation-point ignition of a premixed combustible", *Int. J. Heat Mass Transfer* 21 (1978) 1363-1368.
175. L. D. Chen, G. M. Faeth, "Ignition of a combustible gas near heated vertical surfaces", *Combust. Flame* 42 (1981) 77-92.
176. G. A. Sod, "Survey of Several Finite-Difference Methods for Systems of Non-Linear Hyperbolic Conservation Laws", *J Comput Phys* 27 (1978) 1-31.
177. H. Jasak, A. Jemcov, Z. Tukovic, "OpenFOAM: A C++ library for complex physics simulations.", in: *International workshop on coupled methods in numerical dynamics*, IUC Dubrovnik, Croatia (2007) 1-20.
178. N. M. Marinov, "A detailed chemical kinetic model for high temperature ethanol oxidation", *Int. J. Chem. Kinet.* 31 (1999) 183-220.
179. L. R. Cancino, M. Fikri, A. A. M. Oliveira, C. Schulz, "Thermal Oxidation of Ethanol: Experimental and Numerical Analysis of Ignition Chemistry of Ethanol-Air Mixtures in Shock Heated Gases", in: *27th International Symposium on Shock Waves*, St. Petersburg, Russia (2009).
180. T. Kuboyama, Y. Moriyoshi, K. Morikawa, "Visualization and Analysis of LSPI Mechanism Caused by Oil Droplet, Particle and Deposit in Highly Boosted SI Combustion in Low Speed Range", *SAE Int. J. Eng.* 8 (2015) 529-537.
181. I. Takahiro, A. Yoshikazu, T. Junya, "Lubricant Oil Droplets in Cylinder on Abnormal Combustion in Supercharged SI Engien", *SAE Technical Paper* 2018-32-0008 (2018).
182. W. Hongxia, S. Dongdong, L. Xiaogang, Z. Dawei, G. Jin, D. Cuiwei, "Effect of Zinc Phosphate on the Corrosion Behavior of Waterborne Acrylic Coating/Metal Interface", *Materials* 10 (2017) 654-667.
183. S. Peltier, C. Duval, "Sur la thermogravimétrie des précipités analytiques: Dosage du calcium", *Anal. Chem. Acta* 1 (1947) 345-354.
184. O. Mathieu, C. Mulvihill, E. L. Petersen, "Shock-tube water time-histories and ignition delay time measurements for H2S near atmospheric pressure", *Proc. Combust. Inst.* 36 (2017) 4019-4027.
185. O. Mathieu, J. W. Hargis, E. L. Petersen, J. Bugler, H. J. Curran, F. Güthe, "The Effect of Impurities on Ignition Delay Times and Laminar Flame Speeds of Syngas Mixtures at Gas

Turbine Conditions", in: *ASME Turbo Expo 2014: Turbine Technical Conference and Exposition*, Düsseldorf, Germany (2014) 1-15.
186. O. Mathieu, J. Hargis, A. Camou, C. Mulvihill, E. L. Petersen, "Ignition delay time measurements behind reflected shock-waves for a representative coal-derived syngas with and without NH3 and H2S impurities", *Proc. Combust. Inst.* 35 (2015) 3143-3150.
187. B. Baral, R. Raine, "Knock in a Spark Ignition Engine Fuelled with Gasoline-Kerosene Blends", *SEA Technical Paper* 2008-01-2417 (2008).
188. S. Feng, Z. Liu, Q. Bi, H. Pan, "Viscosity Measurements of n-Dodecane at Temperatures between 303 K and 693 K and Pressures up to 10 MPa", *J. Chem. Eng. Data* 63 (2018) 671-678.
189. T. Y. Xiong, C. K. Law, K. Miyasaka, "Interactive vaporization and combustion of binary droplet systems", in: *20th Symposium (International) on Combustion*, Ann Arbor, Michigan (1984) 1781-1787.
190. W. A. Sirignano, "Droplet Arrays and Groups", in: "Fluid Dynamics and Transport of Droplets and Sprays", *Cambridge University Press*, Cambridge, (2010).
191. V. Troutman, C. Strand, M. Campbell, A. Tulgestke, V. Miller, D. Davidson, R. Hanson, "High-speed OH* chemiluminescence imaging of ignition through a shock tube end-wall", *Appl. Phys. B* 122 (2016) 1-7.
192. M. Hartmann, M. Fikri, R. Starke, C. Schulz, "Shock-Tube Investigation of Ignition Delay Times of Model Fuels", in: *3th ECM* Crete, Greece (2007) 1-3.
193. M. Fikri, Y. Sakai, J. Herzler, C. Schulz, "Experimental and numerical study of the ignition delay times of primary reference fuels containing diethyl ether", in: *26th ICDERS*, Boston, USA (2017) 1-6.
194. M. Fikri, J. Herzler, R. Starke, C. Schulz, P. Roth, G. T. Kalghatgi, "Autoignition of gasoline surrogates mixtures at intermediate temperatures and high pressures", *Combust. Flame* 152 (2008) 276-281.
195. P. Niegemann, M. Fikri, S. A. Kaiser, C. Schulz, "Investidation of lubricant oil/fuel/air ignition behind reflected shock waves at elevated pressure and moderate temperatures", in: *29th Deutscher Flammentag*, Bochum, Germany (2019) 1-6.
196. S. Fujikawa, "Vapor-Liquid Interfaces, Bubbles and Droplets: Fundamentals and Applications", *Springer-Verlag*, Berlin, Heidelberg, (2011).
197. F. Mounce, "Development of a Standardized Test to Evaluate the Effect of Gasoline Engine Oil on the Occurrence of Low Speed Pre-Ignition - The Sequence IX Test", *SAE Technical Paper* 2018-01-1808 (2018).
198. E. L. Petersen, M. J. A. Rickard, M. W. Crofton, E. D. Abbey, M. J. Traum, D. M. Kalitan, "A facility for gas- and condensed-phase measurements behind shock waves", *Meas. Sci. Technologie* 16 (2005) 1716-1729.
199. J. T. Herbon, "Shock tube measurements of CH3+O2 kinetics and the heat of formation of the OH radical", Stanford, California, TSD-153 (2004).
200. M. Rouaud, "Probability, Statistics and Estimation", *Creative Commons*, (2013).
201. A. Ghasemi, S. Zahediasl, "Normality tests for statistical analysis: a guide for non-statisticians", *Int J Endocrinol Metab* 10 (2012) 486-489.
202. C. T. Armitage P, "Encyclopedia of Biostatistics", *Wiley*, New York, (1998) 3075-3079.

9 Appendices

9.1 Appendix A: Uncertainty and error calculation

Uncertainty of temperature determination

Reaction kinetics are strongly temperature-dependent, therefore, an accurate determination of the temperature behind the reflected shock wave is essential for analyzing the experimental results. The temperature behind the reflected shock wave depends on the initial temperature T_1, the Mach number M and the isentropic exponent κ.

$$T_5 = T_1 \frac{[2(\kappa-1)\mathrm{M}^2 + (3-\kappa)][(3\kappa-1)\mathrm{M}^2 - 2(\kappa-1)]}{(\kappa+1)^2\mathrm{M}^2} \tag{48}$$

The initial temperature T_1 is very well known because the shock tube and the vessel are heated by regulated heating wires with thermocouples. The Mach number depends on the velocity of the incident shock wave u_1 and temperature T_1 as shown in equation (49).

$$\mathrm{M} = \frac{u_1}{\sqrt{\kappa R T_1}} \tag{49}$$

The κ depends on the specific speed of sound in the gas *a*, the specific mass *m,* the universal gas constant *R* and T_1.

$$\kappa = \frac{a^2 m}{1000\ R T_1} = \frac{c_p}{c_V} \tag{50}$$

The uncertainty in T_5 is strongly dependent on the uncertainty of the Mach number, which mainly depends on the velocity of the incident shock wave which is measured in each experiment. To calculate the error of a measured value, the sum of each error in the measurement propagates in the total error. The velocity is not measured directly; instead, the velocity is calculated over three distances by:

$$u_\mathrm{i} = \frac{dx_\mathrm{i}}{dt_\mathrm{i}} \tag{51}$$

The error of the velocity in each point depends on the uncertainty of d*x* and d*t*. Eric Petersen published the characterization of a shock tube in 2005 including an uncertainty calculation for the measured d*x*/d*t* [198]. The uncertainty of dx depends on the precision of the tool used to measure the distance between the pressure transducers, which was below 0.1 mm. A maximum error was assumed δ_{dx} = 0.1 mm. The uncertainty of time measurements is the sum of used devices. This method does not make sense here because *d*t is relative. The rising time in the pressure trace was about 4 µs with a sampling rate of 1 µs. In a worst-case scenario, a max error δ_{dt} of 2 µs is extremely conservative. The standard deviation of the velocity u_i can be calculated as:

$$\sigma_{u_\mathrm{i}} = \sqrt{\left(\frac{\partial u_1}{\partial(\mathrm{d}x)}\delta_{\mathrm{d}x}\right)^2 + \left(\frac{\partial u_1}{\partial(\mathrm{d}t)}\delta_{\mathrm{d}t}\right)^2} = \sqrt{\left(\frac{1}{\mathrm{d}t}\delta_{\Delta x}\right)^2 + \left(\frac{-\mathrm{d}x}{\mathrm{d}t^2}\delta_{\mathrm{d}t}\right)^2} \tag{52}$$

This is the uncertainty of each measured velocity between the pressure transducers. To consider the attenuation of the shock wave, the velocity is linearly extrapolated using the method of minimized weighted sum of squares as shown in equations (53), (54), and (55).

$$\Delta = \sum_i \frac{1}{\sigma_\mathrm{i}^2} \sum_i \frac{x_\mathrm{i}^2}{\sigma_\mathrm{i}^2} - \left(\sum_i \frac{x_\mathrm{i}}{\sigma_\mathrm{i}^2}\right)^2 \tag{53}$$

$$a = \frac{1}{\Delta}\left(\sum \frac{x_\mathrm{i}^2}{\sigma_\mathrm{i}^2}\sum \frac{u_\mathrm{i}}{\sigma_\mathrm{i}^2} - \sum \frac{x_\mathrm{i}}{\sigma_\mathrm{i}^2}\sum \frac{x_\mathrm{i}u_\mathrm{i}}{\sigma_\mathrm{i}^2}\right) \tag{54}$$

$$b = \frac{1}{\Delta}\left(\sum \frac{1}{\sigma_i^2}\sum \frac{x_\mathrm{i}u_\mathrm{i}}{\sigma_\mathrm{i}^2} - \sum \frac{x_\mathrm{i}}{\sigma_\mathrm{i}^2}\sum \frac{u_\mathrm{i}}{\sigma_\mathrm{i}^2}\right) \tag{55}$$

The uncertainty of the factors a and b of the linear regression can be calculated with reference to Herbon [199]:

$$\sigma_\mathrm{a}^2 = \frac{1}{\Delta}\sum \frac{x_\mathrm{i}}{\sigma_\mathrm{i}^2} \tag{56}$$

$$\sigma_\mathrm{b}^2 = \frac{1}{\Delta}\sum \frac{1}{\sigma_\mathrm{i}^2} \tag{57}$$

The standard deviation for the fit σ can be calculated based on the scatter in the linear regression:

$$\sigma^2 = \frac{1}{N-2}\sum (u_\mathrm{i} - a - bx_\mathrm{i})^2 \tag{58}$$

The number of data points is *N*. Beside the standard deviation a goodness-of-fit parameter χ^2 can be used. Using the optimum regression, the goodness-of-fit factor can be used to recheck the estimated uncertainty for d*t* and d*x*. As the influence of d*x* is negligible, the overestimated d*t* was adjusted to meet the goodness-of-fit factor.

$$\mathrm{X}^2 = \sum_\mathrm{i}\left[\frac{1}{\sigma_\mathrm{i}^2}\left(u_\mathrm{i} - (a - bx_\mathrm{i})\right)\right] \tag{59}$$

If $\chi^2 < (N - 2)$ the uncertainty of one or more parameters has been overestimated. Using the uncertainty described above $\chi^2 = 0.04$. Therefore, the uncertainty in d*t* was reduced to 0.4 µs. This results in $\chi^2 = 0.92$. This is more realistic than the worst case of 2 µs.
Based on this an uncertainty in extrapolated velocity at the endwall can be calculated:

$$\sigma_{\mathrm{u}_\mathrm{endwall}}^2 = \sigma_\mathrm{a}^2 + \sigma_\mathrm{b}^2 x_\mathrm{endwall}^2 + (\delta x_\mathrm{endwall})^2 b^2 \tag{60}$$

The uncertainty of the velocities is dependent on the position and the speed of the shock wave, which is proportional to the temperature T_5. The uncertainty is shown over distance in Figure 98.

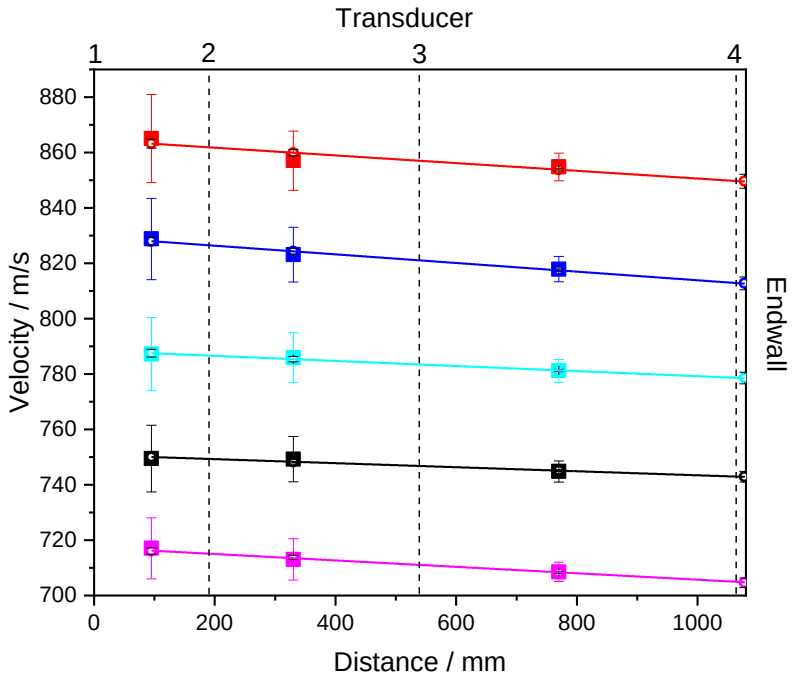

Figure 98: Uncertainty of velocity over distance for the used temperature range.

For an experiment κ is constant as well as the speed of sound a, so the equation(48) can be simplified to:

$$\delta_{T_5} = \frac{\partial T_5}{\partial \mathrm{M}} \delta_{\mathrm{M}} = (281.72\mathrm{M} + 149.71\mathrm{M}^{-3}) \frac{\delta u_1}{\sqrt{\kappa R T_1}} \tag{61}$$

The uncertainty is temperature-dependent and was calculated for the temperature range of 750–950 K as shown in Figure 99.

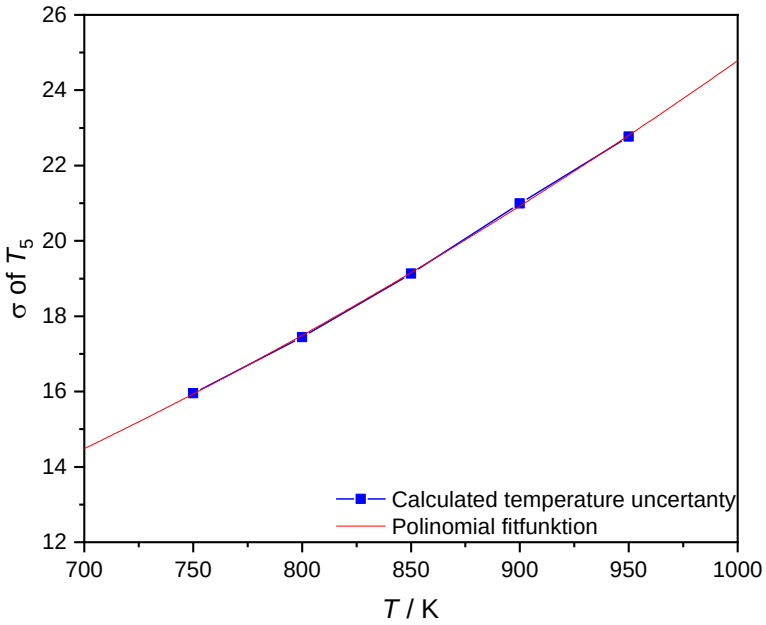

Figure 99: Uncertainty of calculated temperature behind the reflected shock wave over temperature.

Uncertainty in ignition delay time

Shock-tube experiments are discontinuous with low repetition rates, which prevents the use of classic statistical analysis tools/corrections. An increase in diameter is beneficial to minimize boundary layer effects and an increase in length is beneficial for the test duration, which means

constant conditions for longer times behind the reflected shock wave. On the other hand, an increase in volume (increase of diameter/length of shock tube) is a disadvantage for pumping duration and gas consumption because of costs for a single experiment. Therefore, the quantity of experiments is extremely limited. The calculated uncertainty in temperature was used as a dynamic lowpass filter in temperature to group more data points to one temperature. An example is shown in Figure 100.

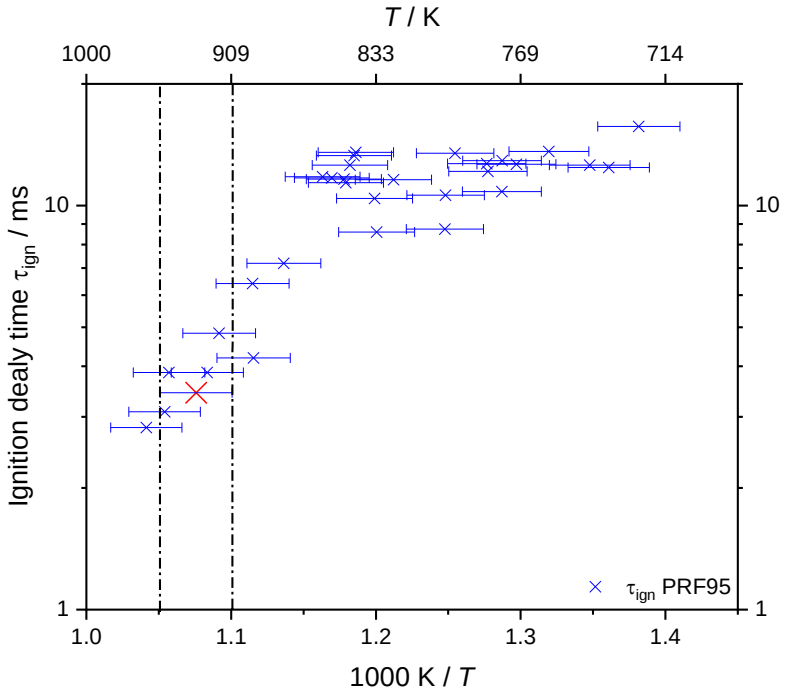

Figure 100: Temperature uncertainty of PRF95/air mixture experiments.

Using this method, an averaged ignition delay time and a standard deviation can be calculated as a function of temperature. The data used for this statistic were measured over several years, including different batches of fuel mixture and vessel mixture. Figure 101 shows the mean ignition delay time over inverted temperature with black error bars for 1 σ and 2 σ, which corresponds to the 95 % confidence interval.

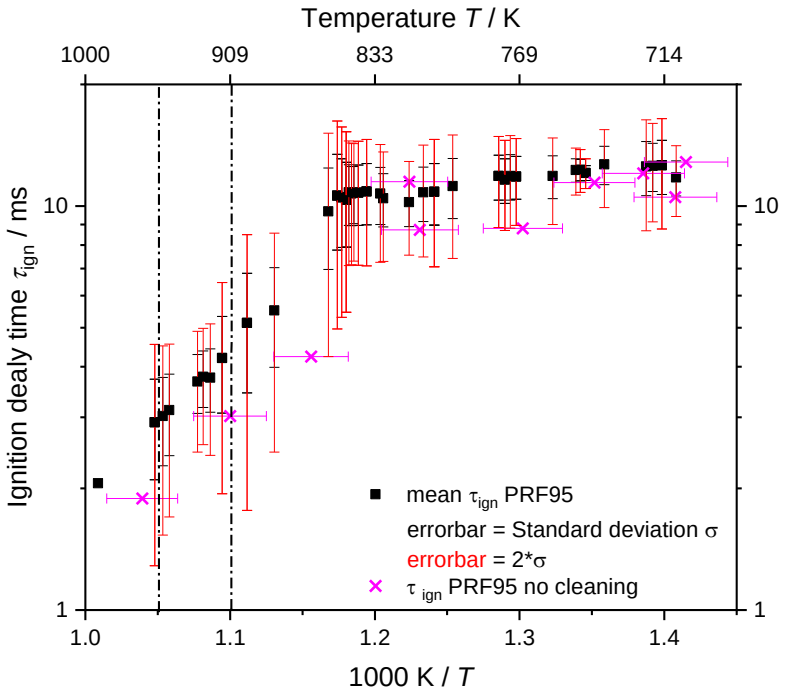

Figure 101: Mean ignition delay time over temperature and measured ignition delay time of PRF95 without cleaning between each experiment.

It is conspicuous that temperature ranges with missing data or minor amounts of data result in an increase in standard deviation. Therefore, statistics in the border areas at low and high temperatures are not representative.
The magenta-colored crosses are ignition delay times measured before starting the regular cleaning between each experiment. Previously, the shock tube was cleaned in-between each set of experiments, so that the first measured data points were performed in a clean tube. Typically, each series starts at low-temperature conditions, going to high temperature. Therefore, the ignition delay time at low temperatures fits well to the statistics. With an increasing number of experiments, the shock tube becomes unclean through enrichment of particles and the ignition delay times are below 1 σ but within the 2 σ confidence interval.
The question whether particles affect ignition is obvious: However, a relative comparison of fuels measured by the same procedure is reliable. But if the absolute value is relevant, cleaning is very important, especially if local ignition is of interest and is observed by imaging.

9.2 Appendix B: Significance analysis of ignition delay times

Ignition delay times of PRF95/air mixture at $\phi = 1$ is the reference mixture for comparison with other fuel mixtures and cases with intentionally introduced ignition sources. Because of the limited data for the different test samples, significant tests can be used to prove if the results stem from the same population. The statistics tools were only used in the temperature range from 710–860 K because of the strong temperature dependence above that range.
The most known significance test is the *t-test*, which is a distribution-based test requiring normally distributed test data. The *t*-test is robust for sample sizes > 30 based on the central limit theorem (which says: "Within a population, we collect random samples of size *n*. The mean of the samples $\bar{x}$ varies around the mean of the population μ with a standard deviation $\sigma/\sqrt{n}$, where σ is the standard deviation of the population. As *n* increases, the sampling distribution of $\bar{x}$ is increasingly concentrated around μ and becomes closer and closer to a Gaussian distribution."[200]). But the data collected from ignition delay time tests is temperature-dependent and

for a specific temperature only one result exists. For temperature ranges (such as 50 K intervals), the amount of data points is far below 30, so the central limit theorem cannot be used. The Gaussian distribution is defined by equation (62):

$$\int_{-\infty}^{\infty} \frac{1}{\sigma\sqrt{2\pi}} e^{-(x-\mu)^2/2\sigma^2} \mathrm{d}x = 1 \tag{62}$$

The deviation of shock tube data in a range that is not strongly temperature-dependent, i.e. for instance 710–860 K, is shown as a histogram in Figure 102. The histogram does not look like a Gaussian bell. Two reasons can be mentioned for this: first, the number of data is too low, second while the measurement error is Gaussian distributed, non-idealities in the reactor will influence the ignition delay time to shorter times, while the ignition delay time will never surpass the τ_{ign} for ideal conditions.

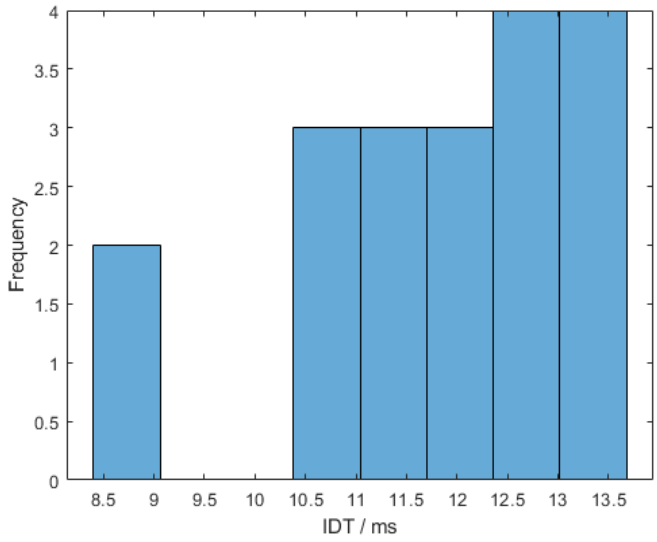

Figure 102: Histogram of 19 ignition delay times from T_5 = 710–860 K.

Additionally to the optical test the most used test for normal distribution is the Kolmogorow-Smirnov test [201]. This test (KS-Test) compares the empirical distribution function of the data with the theoretical cumulative distribution function of the test distribution as shown in equation (63) [202]:

$$D = \sup_x |F_n(x) - F(x, \mu, \sigma) \tag{63}$$

$F(x, \mu, \sigma)$ is the theoretical function of a normal distribution. In the case of PRF95/air τ_{ign} the mean value μ_{PRF95} is 11.8 ms with a standard deviation of $\sigma = 1.47$. The null hypothesis is that the data comes from a normal distribution with a mean of 11.8 and a standard deviation of 1.47.
The KS-Test proves that the null hypothesis is true as shown in Figure 103 by the comparison of the empirical cumulative distribution function (CDF).

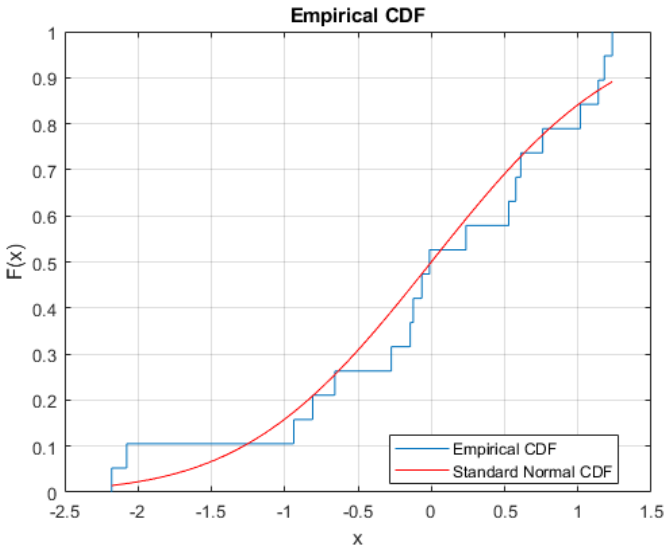

Figure 103: Comparison of the empirical Cumulative Distribution Function (CDF) with the Standard Normal CDF.

The result of the KS–Test permits the Student's *t* test as a significance test. The basic equation for any confidence interval is shown in equation (64):

$$\mu = \bar{x} \pm t\frac{s}{\sqrt{n}} \tag{64}$$

With μ as the mean of the population, $\bar{x}$ the mean of the samples, *s* the standard deviation of the samples, *n* the number of samples and *t* is the *t*-value according to the significance level. The Student's *t*-test assumes that the mean of the population χ is known as μ as well as the standard deviation σ. Now a set of samples of n size is picked and proofed for the same mean:
The hypothesis H0 is: $\bar{x} > \mu - t_\infty \frac{\sigma}{\sqrt{n}}$ and $\bar{x} < \mu + t_\infty \frac{\sigma}{\sqrt{n}}$
Because the true mean value μ is not known all samples of the reference case (PRF95/air) were used to calculate $\bar{x}_{PRF}$ as μ. The later test samples that were injected were tested as picked data against this μ_{PRF}. The tested significance level was 95%.
Beside the Student's *t-test*, the Mann Whitney *U* test was used because it is a distribution-free rank-sum test. The test asks: "Are the medians of the two distributions the same?"
H_0: The measured τ_{ign} data x_n stem from the same population x_{PRF95} ($\mu_{x_n} = \mu_{x_{PRF}}$). H_1 declines H_0 ($\mu_{x_n} \neq \mu_{x_{PRF}}$).
Two ways exist to calculate the U_x value, while the significance value can be looked up for the different levels. Only the more convenient method of computation is presented here. The data of N_x and Ny are ranked, and the rank sum of *x* data R_x is calculated:

$$R_x = \sum_{x_1}^{x_n} \mathrm{rank}(x) \tag{65}$$

$$U_x = N_x N_y + N_x \frac{(N_x + 1)}{2} - R_x \tag{66}$$

Both tests were performed for all injected test samples to prove whether the injected droplets have a significant impact on the τ_{ign}.
Regression analysis was excluded as an alternative because the limitation in data points necessitates the KS test to prove for normal distribution. The assumption that the normal distribution is equal over temperature is not testable based on the available data.

DOI: 10.17185/duepublico/74916
URN: urn:nbn:de:hbz:464-20211111-155034-7